

Miami University

The Graduate School

Certificate for Approving the Dissertation

We hereby approve the Dissertation

of

Shengqian Ma

Candidate for the Degree:

Doctor of Philosophy

Hongcai Zhou, Research Director

Michael W. Crowder, Committee Chair

Benjamin W. Gung, Reader

André J. Sommer, Reader

Qingshun Li,
Graduate School Representative

ABSTRACT

GAS ADSORPTION APPLICATIONS OF POROUS METAL-ORGANIC FRAMEWORKS

By Shengqian Ma

Porous metal-organic frameworks (MOFs) represent a new type of functional materials and have been found to exhibit great potential in various applications such as catalysis, magnetism, gas storage/separation etc. This dissertation details the investigation of porous MOFs for gas adsorption applications, including hydrogen storage, methane storage, and selective gas adsorption.

The first section evaluates porous MOFs as promising candidates for hydrogen storage application. It discusses various strategies to improve hydrogen uptakes in porous MOFs, which includes mimicking hemoglobin to create entatic metal centers in PCN-9 resulting in a high hydrogen heat of adsorption of 10.1 kJ/mol, functionalizing the organic ligand with fused aromatic rings to achieve high hydrogen adsorption capacity of 2.7 wt% in PCN-14 at 77 K and 1 bar, and utilizing catenation to generate PCN-6 with a hydrogen uptake of 9.5 wt% (absolute, at 77 K and 50 bar) as well as a surface area of 3800 m²/g in.

The second section discusses methane storage applications of porous MOFs. Constructed from a pre-designed ligand, the porous MOF, PCN-14 exhibits the highest methane uptake capacity among currently reported materials with a value of 230 v/v (absolute, at ambient temperature and 35 bar), which is 28% higher than the US DOE target (180 v/v) for methane storage.

The third section addresses microporous MOFs as molecular sieves for selective gas adsorption application. Increasing the bulkiness of the struts and introducing coordinatively linked interpenetration restrict the pore sizes of PCN-13 and PCN-17

respectively to selectively adsorb oxygen and hydrogen over nitrogen and carbon monoxide. Based on some amphiphilic ligands, a series of mesh-adjustable molecular sieves, whose pore sizes can be continuously tuned from 2.9 to 5.0 Å, have been designed for various gas separation applications.

GAS ADSORPTION APPLICATIONS OF POROUS METAL-ORGANIC
FRAMEWORKS

A DISSERTATION

Submitted to the Faculty of
Miami University in partial
fulfillment of the requirements
for the degree of
Doctor of Philosophy
Department of Chemistry and Biochemistry

by

Shengqian Ma
Miami University
Oxford, Ohio
2008

Dissertation Director: Hongcai Zhou

©

Shengqian Ma

2008

Table of Contents

List of Tables	vii	
List of Figures	viii	
List of Schemes	xiii	
List of Abbreviations	xiv	
Acknowledgements	xv	
Chapter 1	Introduction to Porous Metal-Organic Frameworks	
1.1	Background of Porous Materials	1
1.2	Porous Metal-Organic Frameworks	2
1.3	Synthetic Considerations of Porous MOFs	6
1.4	Characterizations of Porous MOFs	8
1.5	Applications of Porous MOFs	10
1.6	References	12
Section I	Porous MOFs as Promising Candidates for Hydrogen Storage Application	
Chapter 2	Introduction to Hydrogen Storage in Porous Metal-Organic Frameworks	
2.1	Hydrogen Storage Targets and Current Storage Methods	15
2.2	Hydrogen Storage in Porous MOFs	
2.2.1	Low pressure cryo-temperature hydrogen adsorption studies	16
2.2.2	Hydrogen saturation at cryo-temperatures and high pressure hydrogen adsorption studies at room temperature	21
2.2.3	Hydrogen adsorption enthalpy	24
2.2.4	Tools to investigate the interactions between hydrogen molecules and frameworks	26
2.2.5	Hydrogen spillover	27
2.3	Summary	28
2.4	References	28
Chapter 3	A Metal-Organic Framework with Entatic Metal Centers	

	Exhibiting High Gas Adsorption Affinity	
3.1	Introduction	32
3.2	Experimental Details	33
3.3	Results and Discussion	37
3.4	References	45
Chapter 4	Hydrogen Adsorption in Porous Metal-Organic Frameworks Based on an Anthracene Derivative	
4.1	Introduction	48
4.2	Experimental Details	49
4.3	Results and Discussion	51
4.4	References	61
Chapter 5	Framework-Catenation Isomerism in Metal-Organic Frameworks and Its Impact on Hydrogen Uptake	
5.1	Introduction	64
5.2	Experimental Details	64
5.3	Results and Discussion	68
5.4	References	73
Chapter 6	Investigation of Hydrogen Binding in MOF Catenation Isomers by Inelastic Neutron Scattering and High Pressure Hydrogen Adsorption Properties of the Isomers	
6.1	Introduction	75
6.2	Experimental Details	77
6.3	Results and Discussion	79
6.4	References	91
Section II	Methane Storage Application of Porous MOFs	
Chapter 7	Introduction to Methane Storage in Porous Metal-Organic Frameworks	
7.1	Methane Storage Goals	96
7.2	Methane Storage in Porous MOFs	97
7.3	References	98
Chapter 8	Metal-Organic Framework from an Anthracene Derivative	

	Containing Nanoscopic Cages Exhibiting High Methane Uptake	
8.1	Introduction	99
8.2	Experimental Details	101
8.3	Results and Discussion	104
8.4	References	109
Section III	Microporous MOFs as Molecular Sieves for Selective Gas Adsorption Application	
Chapter 9	Introduction to Selective Gas Adsorption in Porous Metal-Organic Frameworks	
9.1	Molecular Sieving Effect in Porous Metal-Organic Frameworks	114
9.2	Porous Metal-Organic Frameworks for Kinetic Separation Application	115
9.3	References	116
Chapter 10	Ultramicroporous Metal-Organic Framework Based on 9,10-Anthracenedicarboxylate for Selective Gas Adsorption	
10.1	Introduction	118
10.2	Experimental Details	119
10.3	Results and Discussion	121
10.4	References	125
Chapter 11	A Coordinatively Linked, Doubly Interpenetrated, Yb Metal-Organic Framework Demonstrates High Thermal Stability and Uncommon Gas-Adsorption Selectivity	
11.1	Introduction	128
11.2	Experimental Details	129
11.3	Results and Discussion	131
11.4	References	138
Chapter 12	A Mesh-Adjustable Molecular Sieve for General Use in Gas Separation	
12.1	Introduction	142
12.2	Experimental Details	144
12.3	Results and Discussion	146

12.4	References	157
Chapter 13	The Discovery and Gas Adsorption Studies of Mesh-Adjustable Molecular Sieves	
13.1	Introduction	159
13.2	Experimental Details	160
13.3	Results and Discussion	163
13.4	References	181
Chapter 14	Conclusions	
14.1	Porous MOFs as Promising Hydrogen Storage Candidates	184
14.2	Methane Storage Applications of Porous MOFs	185
14.3	Selective Gas Adsorption Applications of Porous MOFs	186
14.4	Outlook	187
14.5	References	187
Vita		189
Appendix	Tables of Crystal Structure	195

List of Tables

Table 1.1	Classification of pores	1
Table 3.1	Crystal data of PCN-9	36
Table 3.2	Selected bond lengths (Å) and angles (deg) for PCN-9	37
Table 4.1	Crystal data and structure refinement of PCN-14 and PCN-15	52
Table 4.2	Physical characteristics and hydrogen adsorption properties of NbO-typed porous MOFs based on tetracarboxylate ligands and dicopper paddlewheel SBU	60
Table 5.1	Crystal data for PCN-6, PCN-6', MOF-HTB, and MOF-HTB'	67
Table 6.1	Tentative assignments of bands in the INS spectra of PCN-6 and PCN-6' according to the model used in ref. 20	82
Table 6.2	Hydrogen adsorption data of PCN-6 and PCN-6'	89
Table 6.3	Hydrogen adsorption data of PCN-6 and some reported MOFs	90
Table 12.1	Crystal data of MAMS-1	146
Table 13.1	Crystal data and structure refinements of MAMS-2, MAMS-3, and MAMS-4	164
Table 13.2	Selected bonding distances in MAMS-2, MAMS-3, and MAMS-4	165

List of Figures

Figure 1.1	IUPAC classification of adsorption isotherms	2
Figure 1.2	Commonly occurring SBUs and examples of organic linkers utilized for the construction of porous MOFs	3
Figure 1.3	Expansion of pore sizes through extension of triangular coplanar carboxylate ligands	4
Figure 1.4	Nanotubular porous MOFs regulated by ADC ligand with trigonal prismatic $M_3(\mu_3-O)(COO)_6$ SBU	5
Figure 1.5	Different structures assembled from TATB ligand with the hour-glass $Zn_3(COO)_6$ SBU	7
Figure 2.1	Different conformations of tcppda ligand lead to two porous MOFs with different topologies	20
Figure 2.2	Correlation between surface area and hydrogen saturation at 77 K	23
Figure 3.1	Schematic drawing of the active center of hemoglobin and the $Co_4(\mu_4-O)(carboxylate)_4$ SBU found in PCN-9	33
Figure 3.2	Crystal structures of PCN-9	38
Figure 3.3	N_2 sorption isotherm of PCN-9	39
Figure 3.4	O_2 adsorption isotherms for PCN-9 at different temperatures	39
Figure 3.5	Enthalpy of adsorption of O_2 for PCN-9	40
Figure 3.6	CO adsorption isotherms for PCN-9 at different temperatures	40
Figure 3.7	Enthalpy of adsorption of CO for PCN-9	41
Figure 3.8	H_2 sorption isotherms of PCN-9	41
Figure 3.9	H_2 adsorption isotherms for PCN-9 at different temperatures	42
Figure 3.10	Enthalpy of adsorption of H_2 for PCN-9	42
Figure 3.11	CH_4 adsorption isotherms for PCN-9 at different temperatures	43
Figure 3.12	Enthalpy of adsorption of CH_4 for PCN-9	43
Figure 3.13	IR spectra of PCN-9	44
Figure 3.14	IR spectra of PCN-9 with CO attached	45

Figure 4.1	H ₄ adip ligand and M ₂ (COO) ₄ (H ₂ O) ₂ (M = Cu, Fe) paddlewheel SBU	49
Figure 4.2	Nanoscopic cage in PCN-14 and one-dimensional hexagonal channels of PCN-15 viewing from (0 0 1) direction	53
Figure 4.3	Chlorine anions residing in the one-dimensional hexagonal channels of PCN-15 viewing from (0 0 1) direction	53
Figure 4.4	Dihedral angles between the anthracene plane and the phenyl ring plane of the adip ligand	54
Figure 4.5	N ₂ sorption isotherms of PCN-14 at 77 K	55
Figure 4.6	N ₂ sorption isotherms of PCN-15 at 77 K	55
Figure 4.7	Low-pressure and high-pressure H ₂ sorption isotherms of PCN-14 at 77 K	56
Figure 4.8	H ₂ adsorption isotherms of PCN-14 at 77, 80, and 87 K	58
Figure 4.9	Isosteric heats of adsorption of H ₂ for PCN-14	59
Figure 5.1	Structures of PCN-6 and PCN-6'	68
Figure 5.2	Nanocages in PCN-6	69
Figure 5.3	HTB ligand and structures of MOF-HTB' and MOF-HTB view from (001) direction	70
Figure 5.4	Gas sorption isotherms (77 K) of PCN-6' and PCN-6 activated at 50 °C for N ₂ and H ₂	71
Figure 5.5	Powder X-ray diffraction patterns	71
Figure 5.6	H ₂ sorption isotherms of PCN-6' and PCN-6 activated at 50 °C and 150 °C	72
Figure 6.1	Catenated PCN-6 and non-catenated PCN-6'	76
Figure 6.2	Isosteric heats of adsorption vs H ₂ uptake for PCN-6 and PCN-6'	80
Figure 6.3	H ₂ adsorption isotherms at 77 and 87 K fitted with Langmuir-Freundlich equation	80
Figure 6.4	INS spectra (15 K) for H ₂ adsorbed in PCN-6 at loadings of 0.5, 1, 2, and 3 molecules per Cu	83

Figure 6.5	INS spectra (15K) for H ₂ adsorbed in PCN-6' at loadings of 0.5, 1, and 2 molecules per Cu site	83
Figure 6.6	Excess hydrogen sorption isotherms of PCN-6 and PCN-6' at 77 K and 298 K	86
Figure 6.7	Excess hydrogen adsorption isotherms of HKUST-1 at 77 and 298 K	87
Figure 6.8	Total hydrogen sorption isotherms of PCN-6 and PCN-6' at 77 K and 298 K	87
Figure 8.1	Methane adsorption isotherms for PCN-13 and PCN-14 at 195 K	100
Figure 8.2	TGA plot of PCN-14	102
Figure 8.3	Nanoscopic cages in PCN-14	105
Figure 8.4	The 3D framework of PCN-14 viewed from the (2 1 1) and (1 0 0) directions	105
Figure 8.5	The 3D framework of PCN-14 viewed as a cuboctahedral net	106
Figure 8.6	PXRD patterns of PCN-14	106
Figure 8.7	Nitrogen gas adsorption isotherm at 77 K of PCN-14	107
Figure 8.8	High pressure methane sorption isotherms at various temperatures	108
Figure 8.9	Isosteric heats of adsorption of methane for PCN-14	109
Figure 10.1	The adc ligand and the Zn ₄ O(H ₂ O) ₃ (COO) ₆ SBU	119
Figure 10.2	TGA for PCN-13	121
Figure 10.3	Structures of PCN-13	122
Figure 10.4	Gas adsorption isotherms of the desolvated PCN-13	123
Figure 10.5	N ₂ and CO adsorption isotherms at 77 K for desolvated and dehydrated (aqua ligands removed) PCN-13	124
Figure 10.6	H ₂ adsorption isotherms for desolvated and dehydrated PCN-13	125
Figure 11.1	Structures of PCN-17 (Part I)	132
Figure 11.2	Structures of PCN-17 (Part II)	133
Figure 11.3	Yb ₄ (μ ₄ -H ₂ O) SBU connecting with four sulfate ligands bridging	

	four other $\text{Yb}_4(\mu_4\text{-H}_2\text{O})$ SBUs	133
Figure 11.4	A single (8,3)-net, doubly-interpenetrated nets and coordinatively linked interpenetration through sulfate bridges	134
Figure 11.5	TGA plot of PCN-17	135
Figure 11.6	PXRD patterns of PCN-17	135
Figure 11.7	Gas adsorption isotherms of the activated PCN-17	137
Figure 11.8	H_2 adsorption isotherms of PCN-17 treated at different conditions	138
Figure 12.1	Crystal structure of MAMS-1	147
Figure 12.2	H_2 adsorption isotherms of MAMS-1 at 77K	148
Figure 12.3	CO_2 adsorption isotherms of MAMS-1	149
Figure 12.4	TGA plot of MAMS-1	149
Figure 12.5	X-ray powder diffraction patterns for fresh sample and the sample activated at 200 °C	150
Figure 12.6	N_2 adsorption isotherm at 77 K of MAMS-1 activated at 120 °C	150
Figure 12.7	Gas adsorption isotherms at different temperatures	152
Figure 12.8	A schematic representation of the mechanism of the gating effect in MAMS-1	153
Figure 12.9	Cell parameters of MAMS-1 measured at different temperatures	154
Figure 12.10	iso- C_4H_{10} and SF_6 adsorption isotherms of MAMS-1 at 298 K	155
Figure 12.11	Temperature-dependent gate opening of MAMS-1	156
Figure 13.1	Two-dimensional trilayer sandwich structure	165
Figure 13.2	Hydrophilic holes and hydrophobic cages in a single layer	166
Figure 13.3	Hydrophobic cages in MAMS-2,3,4	166
Figure 13.4	Two adjacent layers connect with each other through the van der Waals interactions	167
Figure 13.5	Hydrophilic channels and hydrophobic cages viewed along c direction	168
Figure 13.6	TGA plots of MAMSs	169
Figure 13.7	H_2 adsorption isotherms of MAMS-2 activated at different	

	conditions	170
Figure 13.8	Gas adsorption isotherms of MAMS-2 at different temperatures	170
Figure 13.9	H ₂ adsorption isotherms of MAMS-3 activated at different conditions	172
Figure 13.10	Gas adsorption isotherms of MAMS-3 at different temperatures	172
Figure 13.11	H ₂ adsorption isotherms of MAMS-4 activated at different conditions	173
Figure 13.12	Gas adsorption isotherms of MAMS-4 at different temperatures	174
Figure 13.13	Temperature gate opening of MAMS-2	175
Figure 13.14	Crystal lattice parameters of MAMSs at different temperatures	176
Figure 13.15	PXRD patterns of MAMS-3 at different temperatures	176
Figure 13.16	PXRD patterns of MAMS-4 at different temperatures	177
Figure 13.17	Iso-butane and SF ₆ adsorption isotherms of MAMS-2 at 295 K	178
Figure 13.18	Iso-butane adsorption isotherm of MAMS-3 at 295 K	178
Figure 13.19	Iso-butane adsorption isotherm of MAMS-4 at 295 K	179
Figure 13.20	Schematic representation of the mechanism of the gate effects in MAMSs	180

List of Schemes

Scheme 4.1	Tetracarboxylate ligands employed for the construction of NbO type MOFs	57
Scheme 8.1	The carboxylate linkers	101
Scheme 11.1	A single net, two doubly interpenetrated nets, and interpenetrated nets linked by coordination bonds	128
Scheme 13.1	<i>tert</i> -butyl carboxylate ligands	160

List of Abbreviations

MOF	metal-organic framework.
SBU	second building unit.
TATB	4,4',4''- <i>s</i> -triazine-2,4,6-triyl-tribenzoate.
H ₂ ADC	9,10-anthracene dicarboxylic acid.
H ₄ ADIP	5,5'-(9,10-anthracenediyl)di-isophthalic acid.
H ₂ BBPDC	4'- <i>tert</i> -butyl-biphenyl-3,5-dicarboxylic acid.
BTC	bezenetricarboxylate.
HTB	<i>s</i> -heptazine tribenzoate.
BBDC	5- <i>tert</i> -butyl-1, 3-benzenedicarboxylate.
IRMOF	isorecticular metal-organic framework.
DMF	dimethyl formamide.
DMA	dimethylacetamide.
DEF	diethylformamide.
DMSO	dimethyl sulfoxide.
PCN	porous coordination network.
UMC	unsaturated metal center.
EMC	entatic metal center.
ZIF	zeolitic imidazolate frameworks.
MS	molecular sieve.
MAMS	mesh-adjustable molecular sieve.
DOE	Department of Energy.
CSD	Cambridge Structural Database.
INS	inelastic neutron scattering.
PXRD	powder X-ray diffraction.
BET	Brunauer-Emmett-Teller.
TGA	thermogravimetric analysis.
IR	Infrared spectroscopy.
NMR	Nuclear magnetic resonance spectroscopy.

Acknowledgements

First of all, I would like to express my deepest gratitude to my research advisor Dr. Hongcai Zhou for his full support from the first day I joined the group. He is an outstanding role model not only as a scientist with a strong work ethic but as a person with a great personality. I know what I have learned from him will benefit me throughout my career.

I would like to thank the entire Zhou research group both past and present. In particular, I must thank the postdocs, Dr. Xi-Sen Wang for his help on refining some crystal structures and Dr. Daqiang Yuan for his assistance in drawing some beautiful structure pictures; as well as the undergraduate students, Christopher Collier, Erika Manis, Michael Ambrogio, Jacqueline Fillinger, and Laura Wright for their assistance and help on my research projects.

I would like to thank my collaborators, Dr. Paul Forster at the University of Nevada, Los Vegas for his great help on the inelastic neutron scattering experiments, Dr. Jong-San Chang at the Korea Research Institute of Chemical Technology and Jason Simmons at the National Institute of Standards and Technology for measuring the high pressure gas sorption data, and Dr. Juergen Eckert at the University of California, Santa Barbara for his help on analyzing the inelastic neutron scattering data.

I would also like to thank my committee professors Dr. Crowder, Dr. Gung, Dr. Sommer, and Dr. Li for listening to my presentations, reading my dissertations and giving some wonderful suggestions. I am particularly grateful to Dr. Gung, who has given me great help and support in the past five years.

It has been said that behind every accomplished man is a good woman so, finally but foremost, I must recognize the contributions of my wife Rong. Without her understanding, support, and encouragement, I would never have accomplished what I have.

Chapter 1

Introduction to Porous Metal-Organic Frameworks

1.1 Background of Porous Materials

Porous materials have drawn increasing scientific and technological interest due to their widespread applications in petrochemistry, catalysis, separation, and ion exchange. Traditional porous materials mainly include zeolites, activated carbon, and sol-gel compounds, and they are claimed to account for more than 20% of the Gross Domestic Product of the industrial countries for the applications they imply, directly or indirectly.¹⁻³

The ability of porous materials to perform the desired function in a particular application is directly related to the size, shape, and volume of their pores.⁴ According to size, the pores of solids can be classified into four categories: ultramicropores, micropores, mesopores, and macropores as shown in Table 1.1. They exhibit different adsorption behaviors as illustrated by different adsorption isotherm types classified by IUPAC in Figure 1.1.⁵

Table 1.1 Classification of pores.

<i>Pore type</i>	<i>Pore size (Å)</i>
Ultramicropore	<5
Micropore	5-20
Mesopore	20-500
Macropore	>500

There are six major representative adsorption isotherms that reflect the relationship between porous structure and sorption type, and these adsorption isotherms are also characteristic of different adsorbent materials.⁶ The type I isotherm is typical of microporous and ultramicroporous solids, while type VI and V feature a hysteresis loop generated by the capillary condensation of the adsorbate in the mesopores of the solid. Types II, III, and VI are shown by nonporous and macroporous solids. The adsorption in

the micropore can be considered as the filling of molecules into a nanospace where a deep potential field is generated by the overlapping of all the wall potentials thus leading to the adsorption isotherm with a steep rise at very low relative pressure and a plateau after saturation. The adsorption by a mesopore, however, is not attributable to molecule–solid interactions but instead is dominated by capillary condensation, which is responsible for a sharp adsorption rise around the mid relative-pressure region. As to adsorption by a macropore and adsorption onto a nonporous surface, there is no essential difference between them. The differences between types II and III and between types IV and V can be ascribed to the relative strength of fluid–solid and fluid–fluid attractive interactions. The stronger fluid–solid attractive interaction compared to that of fluid–fluid results in the adsorption isotherms of types II and IV, while opposite situation leads to types III and V behaviors. The type VI isotherm represents adsorption on nonporous or macroporous solid surfaces where stepwise multiplayer adsorption occurs.⁴

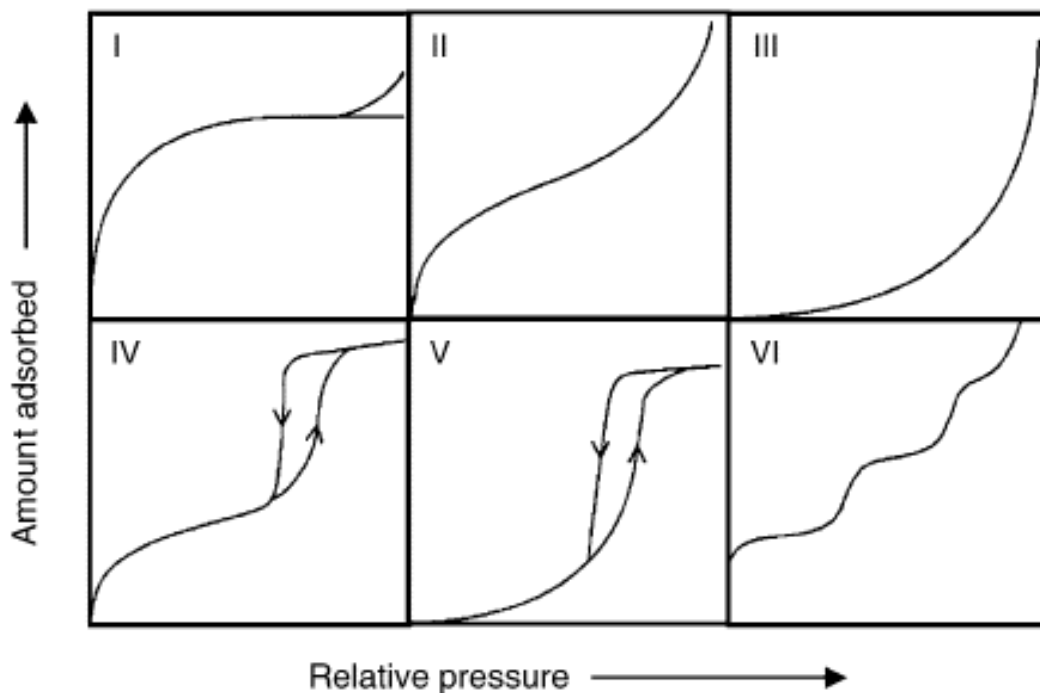


Figure 1.1 IUPAC classification of adsorption isotherms.⁴

1.2 Porous Metal-Organic Frameworks

Over the past two decades, there emerged a new type of functional materials—metal-organic frameworks, and particularly the latest ten years has witnessed the explosive development and rapid progress in this new field.^{4,7-10} Metal-organic frameworks (MOFs), also known as coordination polymers or coordination networks, are highly crystalline inorganic-organic hybrids constructed by assembling metal ions or small metal-containing clusters with multidentate organic ligands (such as carboxylates, tetrazolates, sulfoxolates) via coordination bonds. They can be one, two, or three-dimensional infinite networks. Of those, three-dimensional MOFs with permanent porosity, which can also be termed as porous MOFs, are of the greatest interest because the voids inside the frameworks can accommodate guest molecules for a number of applications.^{2,4,11}

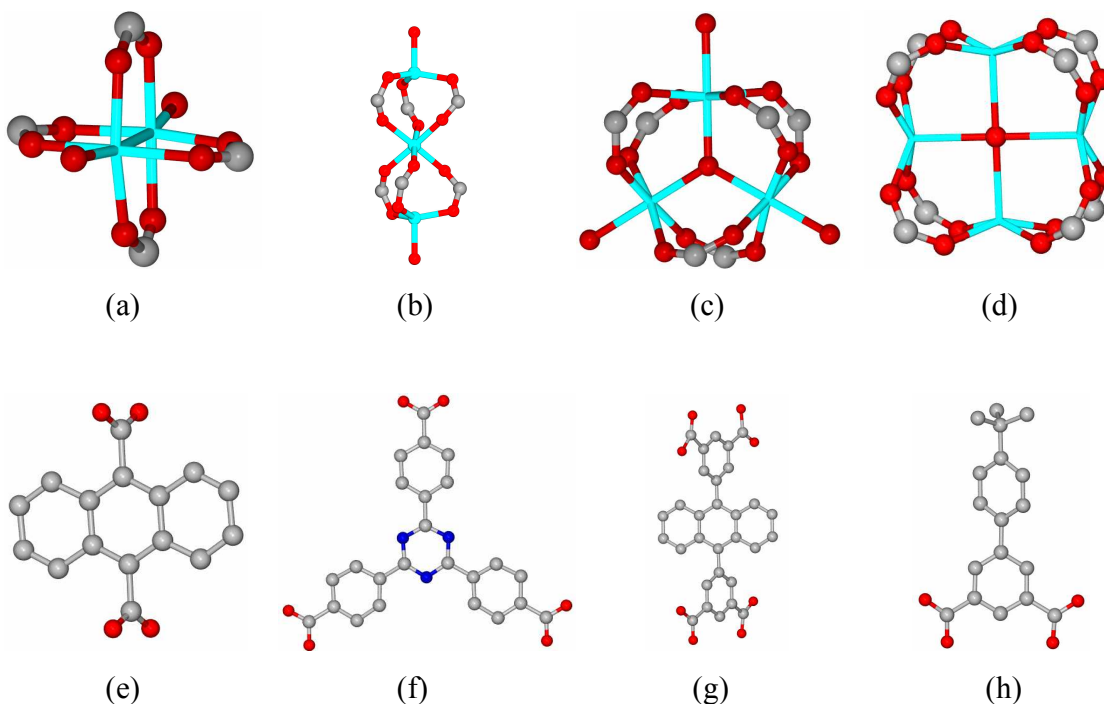


Figure 1.2 Commonly occurring SBUs and examples of organic linkers utilized for the construction of porous MOFs: (a) square paddlewheel SBU; (b) hour-glass SBU; (c) trigonal prismatic SBU; (d) square-planar SBU; (e) 9,10-anthracene dicarboxylate acid (H_2ADC); (f) 4,4',4''-*s*-triazine-2,4,6-triyl-tribenzoate acid (H_3TATB) (g) 5,5'-(9,10-

anthracenediyl)di-isophthalate acid (H_4ADIP) (h) 4'-*tert*-butyl-biphenyl-3,5-dicarboxylate acid (H_2BBPDC).

In the construction of a porous MOF, a multidentate organic ligand is selected as the linker, while a metal cluster, known as secondary building unit (SBUs), serves as the connector. The concept of SBUs was adopted from zeolites in order to aid the structural analysis and prediction of porous MOFs. Thus, porous MOFs are usually considered a new type of zeolite analogues. Examples of some SBUs and organic linkers utilized in porous MOFs are shown in Figure 1.2.

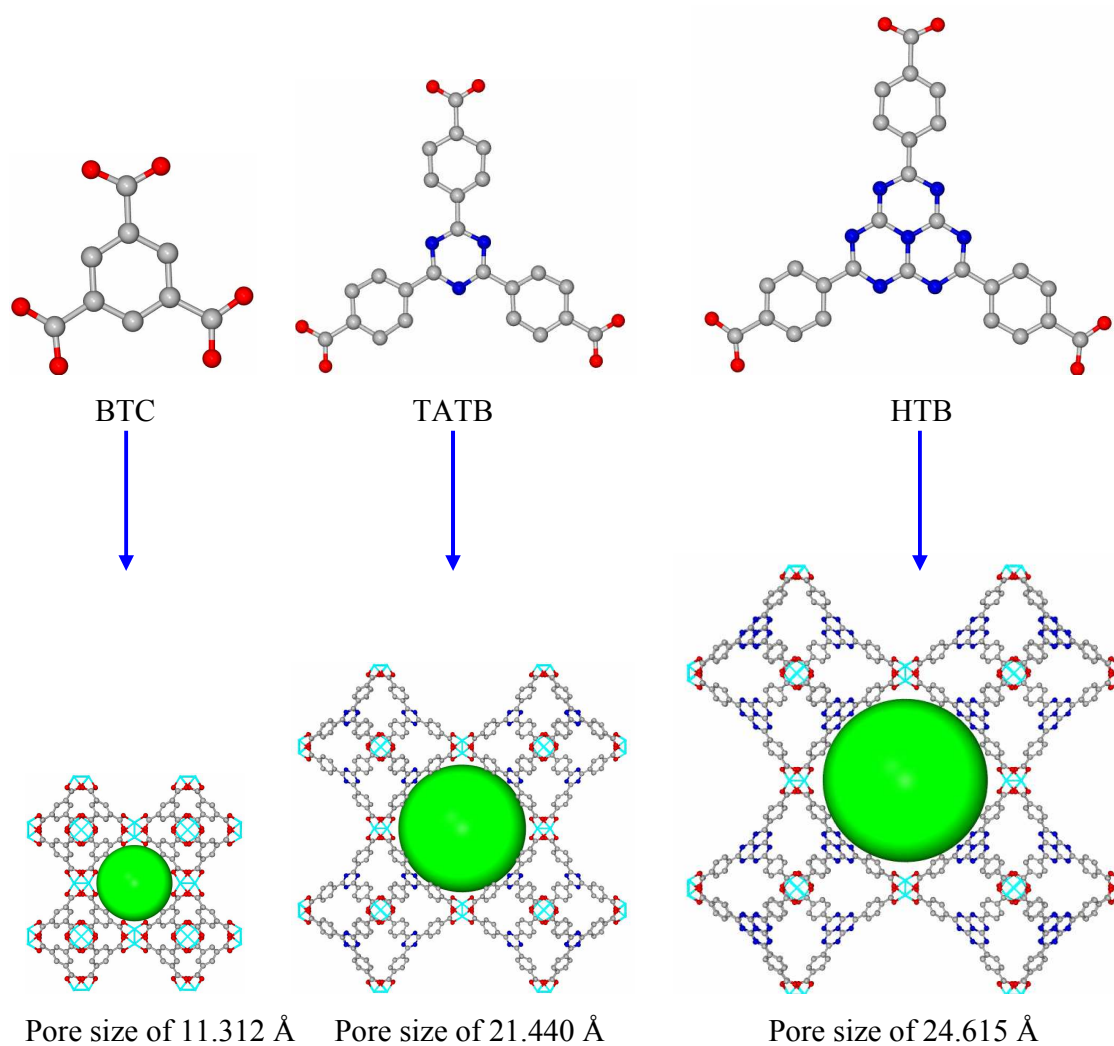


Figure 1.3 Expansion of pore sizes through extension of triangular coplanar carboxylate ligands.

Through the judicious selection of the SBUs and organic linkers, not only can a variety of topologies and structures be produced, but the pore sizes can be systematically tuned and the pore walls functionalized. The latter was well illustrated in the reticular syntheses of IRMOFs (isorecticular MOFs), which are built from the octahedral $Zn_4O(COO)_6$ SBU and a series of linear dicarboxylate linkers.¹² The controllability of pore sizes was also discerned in the construction of porous MOFs with twisted boracite net topology based on the square paddlewheel $Cu_2(COO)_4(H_2O)_2$ SBU (Figure 1.2a) and triangular coplanar carboxylate ligands (Figure 1.3). The extension from bezenetricarboxylate (BTC) (3.467 Å) to TATB (7.600 Å) and to *s*-heptazine tribenzoate (HTB) (8.915 Å) leads to proportional expansion of pore size from 11.312 Å in HKUST-1¹³ to 21.440 Å in PCN-6' and to 24.615 Å in Cu-HTB', respectively.¹⁴

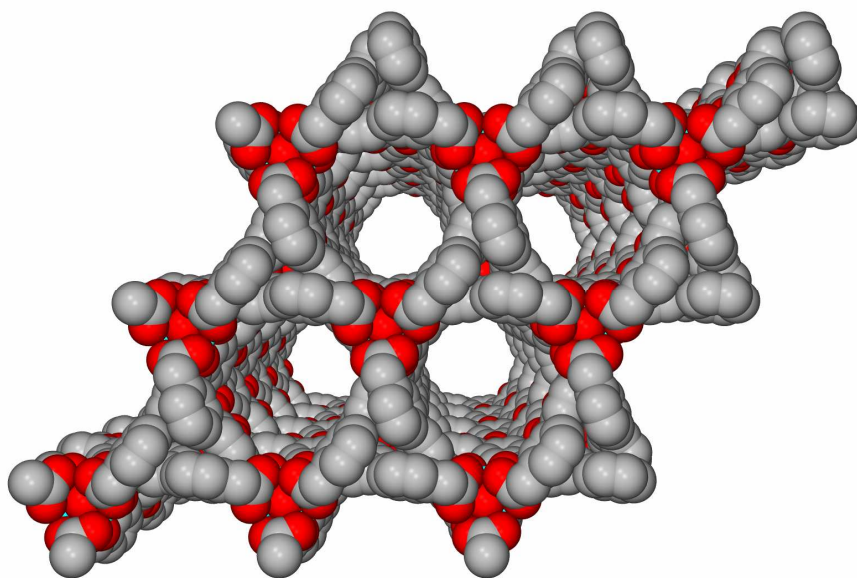


Figure 1.4 Nanotubular porous MOFs regulated by ADC ligand with trigonal prismatic $M_3(\mu_3-O)(COO)_6$ SBU ($M = Co^{2+}$, Mn^{2+} , Ni^{2+} , and Zn^{2+}).

In contrast to reticular synthesis,^{9,10} which allows the construction of porous MOFs with exactly the same connectivity based on the same metal cluster SBU but different ligands, “ligand-regulation” synthesis permits the formation of isostructural porous MOFs with the same ligand and similar SBUs but different metals. A typical example was demonstrated in the construction of porous MOFs based on the 9,10-

anthracene dicarboxylate (ADC) ligand (Figure 1.2e). The utilization of ADC ligand to react with divalent Co^{2+} , Mn^{2+} , Ni^{2+} , and Zn^{2+} ions resulted in four isostructural nanotubular porous MOFs (Figure 1.4) adopting the same trigonal prismatic $\text{M}_3(\mu_3\text{-O})(\text{COO})_6$ SBU (Figure 1.2c). This could be partially attributed to the similarities of those transition metal ions in coordination modes and oxidation states. However, it should be noted that the desired SBUs adopted in porous MOFs are not introduced directly but are formed *in situ* under specific synthetic conditions. The success of an SBU in the design of porous MOFs relies both on its rigidity and directionality of bonding. To this point, organic ligands play a critical role in directing the formation of the same specific SBU despite the use of different metal ions, and final structures can thus be regulated into isomorphous categories. Examples of this phenomenon are frequently encountered when bulky multidentate ligands are employed.

1.3 Synthetic Considerations of Porous MOFs¹⁵

Compared to the syntheses of inorganic zeolites which usually require the use of inorganic or organic templates (amines, quaternary ammoniums) in addition to the components of the skeleton and the solvent, the solvents utilized in the syntheses of porous MOFs can act as the templates themselves. The solvents normally have very weak interactions with the frameworks but can keep the frameworks intact and provide readily accessible porosity.

Even though thousands of porous MOFs have been reported so far, the majority of studies are still exploratory with the goal of their syntheses to obtain high quality single crystals. A variety of techniques including slow evaporation of a solution of the precursors, layering of solutions, or slow diffusion of one component solution into another through a membrane or an immobilizing gel, all of which were previously used to grow crystals of simple inorganic salts, have been employed to produce highly crystalline porous MOFs. These methods generally involved the slow introduction of the building blocks to reduce the rate of crystallite nucleation, a process which usually takes weeks or even months before the crystals form out.

A convenient solution to supplant these time-consuming methods is to use hydro/solvothermal techniques, which can greatly reduce the crystallization time to a few days or even several hours. The precursors are typically combined as dilute solutions in polar solvents such as water, alcohols, alkyl formamides (such as dimethyl formamide, diethyl formamide), or dimethyl sulfoxide (DMSO) and heated at mild temperatures (typically between 50 and 250 °C) in sealed vessels such as Teflon-lined stainless steel bombs, glass vials, or glass tubes under autogenous pressure. Mixed solvent systems are often used to tune the solution polarity and the kinetics of solvent-ligand exchange to improve crystal growth. In cases where deprotonation of the organic linker (such as a carboxylic acid) is needed, a small amount of organic bases (such as amines or pyridine) can be added to neutralize the solution, but the adroit selection of base is necessary to avoid competitive coordination with the organic linkers for the available metal sites. While in some cases where alkyl formamides are used as solvents, the addition of a few drops of acid is usually very useful to adjust the pH values of the reaction systems. Sometimes if high yield is desired over crystal quality, reaction times can be greatly reduced by increased concentration and agitation of the solution. This often results in the formation of microcrystalline, rather than amorphous, products.

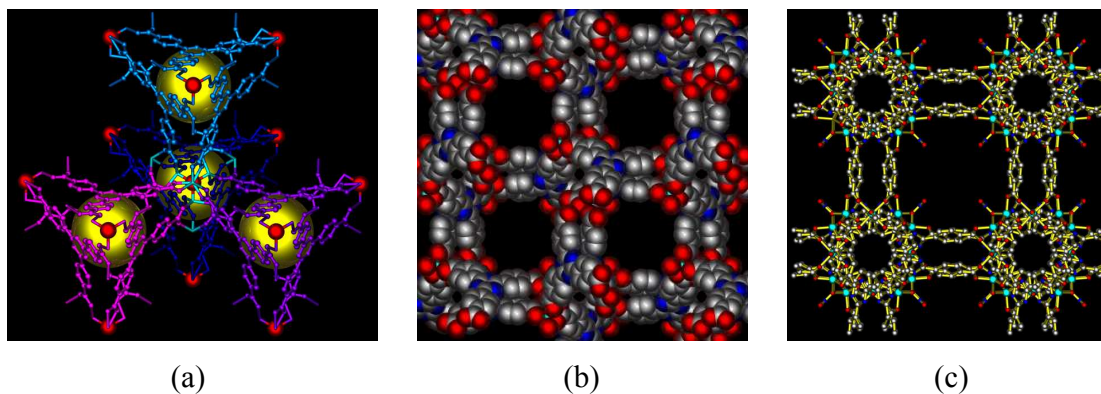


Figure 1.5 Different structures assembled from TATB ligand with the hour-glass $Zn_3(COO)_6$ SBU: (a) diamondoid structure with large tetrahedral cages; (b) (10, 3)-a structure with large chiral channels; (c) robust chiral porous MOF.

It should be born in mind that the porous MOF designer is always at the mercy of intermolecular forces that limit predictability, and great efforts must be made to identify and modify synthetic conditions that drive the building units to assemble in the intended fashion. It has often been observed that subtle changes in concentration, solvent polarity, pH, or temperature can lead to poorer quality crystals, lower yields, or even the formation of entirely new structures. A typical example lies in the assembly of TATB ligand (Figure 1.2f) with the hour-glass $Zn_3(COO)_6$ SBU (Figure 1.2b) at 120 °C, where the utilization of DMSO afforded a diamondoid structure with large tetrahedral cages (Figure 1.5a),¹⁶ while the employment of DMF led to a (10, 3)-a chiral porous MOF (Figure 1.5b),¹⁷ and the addition of several drops of HF_4 to DMF resulted in another new but more robust chiral porous MOF (Figure 1.5c).¹⁷ The richness of the possibilities of isolating new porous MOFs has necessitated the comprehensive investigation of influences from the pertinent chemical parameters of the syntheses such as concentration, solvent, pH, temperature, and ligand/metal salt ratio in order to discover new compounds and optimize the reaction conditions as well as identify the reaction trends. Fortunately, this can be accomplished using combinatorial high-throughput synthesis, which was used in screening for activity of drug molecules as well as in zeolites and polymers for applications in catalysis and phosphors.² The high-throughput method was recently well illustrated by Yaghi *et al.* in the syntheses of zeolitic imidazolate frameworks.¹⁸

Another efficient technique for the syntheses of porous MOFs is microwave method, which has been widely applied for the syntheses of nanoporous inorganic materials. This method can shorten the crystallization time to just several minutes as well as render the particle sizes of porous MOFs into nano-scale affording their potential applications in nanosciences. Microwave syntheses of porous MOFs were recently demonstrated for MOF-5¹⁹ and MIL-100/101.²⁰

1.4 Characterizations of Porous MOFs

The highly crystalline properties of porous MOFs facilitate the establishment of structure-property relationships which can in turn allow the identification of principles that govern the design and assembly of target frameworks. The properties of a porous

MOF are largely determined by the characteristics of the organic linker as well as the network connectivity of the building units, and thus the design and synthesis of organic ligand are essential to this end.

To elucidate the structure of a porous MOF, the most powerful tool is single-crystal X-ray diffraction. Normally, the utilization of molybdenum X-ray source can generate strong enough diffraction spots over the porous MOF crystal for structure determination. If the crystal gradually loses solvents when isolated from mother liquor, it requires freezing at low temperature or sealing with mother liquor in a capillary to obtain useful single-crystal X-ray data for structure determination. Sometimes, if the unit cell of the crystal is too big or the crystal is microcrystalline, a molybdenum X-ray source cannot generate strong enough diffraction spots, and a copper X-ray source or even synchrotron X-ray source must be used in its place for the crystal data collection.

Once the structure is elucidated, the pore size of the porous MOF can be determined simply by measuring the atom-to-atom distance across the pores or channels, and the pore volume can be estimated based on the accessible solvent volume calculated using PLATON.²¹

Nevertheless, one must be aware of the terminology used to describe porosity, which is often assumed in metal-organic frameworks. It is inappropriate to use the adjective *porous* solely by crystallographic analysis for frameworks whose framework integrity cannot be retained after the included solvent molecules are removed or exchanged. Instead, the term *open framework* can be conceded as an adequate description. However, the establishment of a MOF as porous requires investigations evidencing the reversible flow of guests in and out of the void volume.¹⁵

The best method to prove the *permanent porosity* of a porous MOF is gas sorption studies. Before gas sorption measurements, the porous MOF must be fully activated through solvent-exchange followed by evacuation or heating under dynamic vacuum to clear out the guest molecules residing in the pores or channels. Most often, nitrogen sorption at 77 K serves as the standard to quantify the surface area, pore volume, and pore size of the tested porous MOF, albeit argon sorption at 87 K and carbon dioxide sorption at 195 K are occasionally employed as well. Most porous MOFs exhibit typical type I sorption behavior of microporous materials, although recently there have also

appeared a few cases with type-IV behavior in some mesoporous MOFs. It is believed that the adsorption in a microporous MOF is pore-filling, and BET surface area should more accurately reflect its actual surface area than Langmuir surface areas as suggested by Snurr *et al.* in a recent theoretical study,²² although the latter is frequently used. The pore volume of a porous MOF can be calculated from the gas adsorption data using the Dubnin-Astakhov equation, and the pore size distribution can also be estimated fitting the gas sorption data with the Horvath-Kawazoe model. Conveniently, the surface area (both BET and Langmuir), pore volume and pore size distribution of the tested materials can now be automatically calculated by the software accompanied with sorption apparatus. The remarkable results obtained by gas sorption studies have led to the current excitement surrounding porous MOF research.

A complementary tool to gas sorption measurements to check the permanent porosity lies in powder X-ray diffraction (PXRD) analysis. The PXRD pattern of the sample after gas sorption studies is usually desired for referencing to the calculated pattern of the host structure to verify the framework integrity and phase purity of the activated sample. This method is also often correlated with thermogravimetric analysis (TGA), in which framework stability is indicated by negligible weight loss between the temperatures of guest loss and framework decomposition, to examine the thermal stability of a porous MOF.

1.5 Applications of Porous MOFs

The nanospace of porous materials is always of great interest for chemists, physicists, and material scientists to exert different functionalities for various applications. Particular attention has now been attracted to porous MOFs due to their amenability to design and the controllability of pore sizes as well as the functionalizability of pore walls, which promise great potential in a variety of important applications such as catalysis, gas adsorption/separation *etc.*^{2,4,8}

Catalysis Heterogeneous catalysis plays a crucial role in chemical industry, and is involved in over 90% of the chemical manufacturing processes currently in use. Porous MOFs have great potential in catalysis applications as was the case in microporous

zeolites and mesoporous materials, although only a small number of examples have been reported thus far.^{1,2}

The first study of catalysis in porous MOF was reported in 1994 by Fujita *et al.* on the cyanosilylation of aldehydes over $[\text{Cd}(\text{NO}_3)_2(4,4'\text{-bpy})_2]_n$, which indicated size-selective catalytic activation of small molecules over larger ones. Some other catalytic reactions such as the Diels-Alder reaction, hydrogenation, esterification, CO oxidation, *etc.*, have also been recently tested in porous MOFs.²³

The development of homochiral porous MOFs for chiral separation and asymmetric catalysis has attracted particular attention due to the lack of homochiral inorganic zeolites.³ The generation of homochirality in porous MOFs can be readily achieved by employing an enantiomerically pure organic ligand. The asymmetric catalysis in homochiral porous media was pioneered by Kim *et al.* on the transesterification over the homochiral porous MOF, POST-1, which was constructed from the chiral ligand (*4R,5R*)-2,2-dimethyl-5-[(4-pyridinylamino)carbonyl]-1,3-dioxolane-4-carboxylic acid or its enantiomer and trigonal prismatic $\text{Zn}_3(\mu_3\text{-O})(\text{COO})_6$ SBU.²⁴ Although the enantioselectivities were very modest, their work stands as the first demonstration of chiral catalytic selectivity for porous media and will likely be followed by materials with improved selectivity in the future.

Gas storage/separation This domain represents the most promising applications for porous MOFs. Compared to zeolites and activated carbon materials, porous MOFs exhibit exceptionally high surface areas and large pore volumes. Their nanospaces are ideal to store various strategic gases like H_2 , CH_4 , CO_2 , hydrocarbons *etc.*,² and interest is now focused on utilizing them for hydrogen²⁵ and methane storage²⁶ as well as carbon dioxide capture.²⁷

In addition, their tunable pore sizes and functional pore walls suggest a great potential for porous MOFs in gas separation, which originates from size exclusion molecular sieving effects or differences in the host-guest interaction for closely related sorbates.

The next three chapters will detail my investigations into porous MOFs for gas adsorption applications with hydrogen storage in section I, methane storage in section II, and selective gas adsorption in part III.

1.6 References:

- (1) Forster, P. M., Dissertation "Exploration of New Transition Metal Based Porous Materials". **2005**.
- (2) Férey, G., *Chem. Soc. Rev.* **2008**, 37, 191.
- (3) Davis, M. E., *Nature* **2002**, 417, 813.
- (4) Kitagawa, S.; Kitaura, R.; Noro, S.-i., *Angew. Chem., Int. Ed.* **2004**, 43, 2334.
- (5) IUPAC Manual of Symbols and Terminology, Appendix 2, Pt.1 Colloid and Surface Chemistry *Pure Appl. Chem.* **1972**, 31, 578.
- (6) Gregg, S. J.; Sing, K. S. W., *Adsorption, Surface Area, and Porosity*. Academic Press: London, New York, 1984.
- (7) James, S. L., *Chem. Soc. Rev.* **2003**, 32, 276.
- (8) Janiak, C., *Dalton Trans.* **2003**, 2781.
- (9) Eddaoudi, M.; Moler, D. B.; Li, H.; Chen, B.; Reineke, T. M.; O'Keeffe, M.; Yaghi, O. M., *Acc. Chem. Res.* **2001**, 34, 319.
- (10) Yaghi, O. M.; O'Keeffe, M.; Ockwig, N. W.; Chae, H. K.; Eddaoudi, M.; Kim, J., *Nature* **2003**, 423, 705.
- (11) Rowsell, J. L. C.; Yaghi, O. M., *Microporous Mesoporous Mater.* **2004**, 73, 3.
- (12) Eddaoudi, M.; Kim, J.; Rosi, N.; Vodak, D.; Wachter, J.; O'Keeffe, M.; Yaghi, O. M., *Science* **2002**, 295, 469.
- (13) Chui, S. S. Y.; Lo, S. M. F.; Charmant, J. P. H.; Orpen, A. G.; Williams, I. D., *Science* **1999**, 283, 1148.
- (14) Ma, S.; Sun, D.; Ambrogio, M. W.; Fillinger, J. A.; Parkin, S.; Zhou, H.-C., *J. Am. Chem. Soc.* **2007**, 129, 1858.
- (15) Rowsell, J., Dissertation "Hydrogen Storage in Metal-Organic Frameworks: An Investigation of Structure-Property Relationships". **2005**.
- (16) Sun, D.; Ma, S.; Ke, Y.; Petersen, T. M.; Zhou, H.-C., *Chem. Commun.* **2005**, 2663.
- (17) Sun, D.; Ke, Y.; Collins, D. J.; Lorigan, G. A.; Zhou, H.-C., *Inorg. Chem.* **2007**, 46, 2725.

- (18) Banerjee, R.; Phan, A.; Wang, B.; Knobler, C.; Furukawa, H.; O'Keeffe, M.; Yaghi, O. M., *Science* **2008**, 319, 939.
- (19) Ni, Z.; Masel, R. I., *J. Am. Chem. Soc.* **2006**, 128, 12394.
- (20) Jhung, J. H.; Lee, J.-H.; Forster, P. M.; Ferey, G.; Cheetham, A. K.; Chang, J.-S., *Chem.-Eur. J.* **2006**, 12, 7899-7905, S7899/1.
- (21) Spek, A. L. *PLATON, A Multipurpose Crystallographic Tool*; Utrecht University: Utrecht, The Netherlands, 2001.
- (22) Walton, K. S.; Snurr, R. Q., *J. Am. Chem. Soc.* **2007**, 129, 8552.
- (23) Fujita, M.; Kwon, Y. J.; Washizu, S.; Ogura, K., *J. Am. Chem. Soc.* **1994**, 116, 1151.
- (24) Seo, J. S.; Whang, D.; Lee, H.; Jun, S. I.; Oh, J.; Jeon, Y. J.; Kim, K., *Nature* **2000**, 404, 982.
- (25) Collins, D. J.; Zhou, H.-C., *J. Mater. Chem.* **2007**, 17, 3154.
- (26) Ma, S.; Sun, D.; Simmons, J. M.; Collier, C. D.; Yuan, D.; Zhou, H.-C., *J. Am. Chem. Soc.* **2008**, 130, 1012.
- (27) Millward, A. R.; Yaghi, O. M., *J. Am. Chem. Soc.* **2005**, 127, 17998.

Section I

Porous MOFs as Promising Candidates for Hydrogen Storage Application

Chapter 2

Introduction to Hydrogen Storage in Porous Metal-Organic Frameworks^a

Decreasing stockpiles of fossil fuels and the increasing threat of global warming have prompted the global community to search for alternative energy carriers to supplement those currently used, namely to replace the use of petroleum-based gasoline and diesel fuel in road vehicles such as automobiles, buses, and trucks. Among various alternatives, hydrogen stands at the forefront: hydrogen is ubiquitous (one dihydrogen molecule can be obtained from each molecule of water), oxidation of hydrogen in an engine or fuel cell releases only water as a byproduct (and thus generates no greenhouse gases), and hydrogen has a relatively high energy capacity.

2.1 Hydrogen Storage Targets and Current Storage Methods

In 2003, the US government launched the Hydrogen Fuel Initiative for developing clean, hydrogen-powered automobiles to replace those currently powered by fossil fuels. The success of commercialization of hydrogen fuel-cell powered vehicles, however, largely relies on the development of a safe, efficient, and economic on-board hydrogen storage system. Based on the concept that today's vehicles will be powered by future higher efficiency hydrogen fuel-cell power sources, the U.S. Department of Energy (DOE) has set a number of targets for the hydrogen storage system (including container and necessary components): 6.0 wt% or 45 kg/m³ by the year 2010, and 9.0 wt% or 81 kg/m³ by the year 2015 at near-ambient (-50~80 °C) and applicable pressures (less than 100 bar). Additionally, the kinetics of hydrogen release and recharging must meet the requirements for practical applications. In other words, the hydrogen adsorption and desorption should be totally reversible and the recharging of hydrogen should be completed within minutes.¹⁻³

Several methods are being explored for on-board hydrogen storage. Although compressed hydrogen gas and cryogenically stored liquid hydrogen are currently utilized

^a This chapter was adapted from the finished review manuscript "Design and Construction of Metal-Organic Frameworks for Hydrogen Storage and Selective Gas Adsorption" Submitted as an invited chapter to the book *Design and Construction of Coordination Polymers*; M. Hong, Ed.; Wiley: New York, 2008.

in the demonstration fuel-cell powered vehicles, the high pressure (>700 bar) of the compressed hydrogen gas and the large amount of energy input for the cryogenic storage of liquid hydrogen preclude their commercialization into daily use.⁴

Metal hydrides and chemical hydrides have also been actively studied as hydrogen carriers in the past decades; however, the irreversibility of hydrogen sorption and poor kinetics of hydrogen recharging necessitate continued investigation to improve the uptake/release kinetics and retention of cycling capacity.^{5,6}

Compared with chemical means for hydrogen storage, physisorption of hydrogen using porous materials has the advantages of fast charge-recharge process as well as an appreciable amount of hydrogen molecules held in the pores. In the past decade, activated carbons,⁷ nanotubes,⁸ and inorganic zeolites⁹ have been widely investigated as potential candidates for hydrogen storage. However, the weak interactions (through van der Waals forces) between hydrogen molecules and the frameworks yield very limited hydrogen uptake even at low temperatures under high pressures despite their high surface areas.

2.2 Hydrogen Storage in Porous MOFs

Porous MOFs have been recently deemed as one of the most promising candidates to approach the US DOE targets for on-board hydrogen storage, due to their high specific surface areas, tunable pore sizes, functionalizable pore walls and well-defined hydrogen binding sites.¹⁰

In 2003, Yaghi *et al.* reported the first measurements of hydrogen adsorption on a MOF, albeit the exceptionally high uptake value of 4.5 wt% at 77 K, 1 atm was later revised to 1.32 wt%¹¹. Since then, over 70 porous MOFs have been investigated for hydrogen adsorption.¹⁰

2.2.1 Low pressure cryo-temperature hydrogen adsorption studies

Although the US DOE targets for hydrogen storage are set at the condition of near ambient temperatures and high pressures, the uptake values of hydrogen at 77 K, 1 atm have been widely investigated and deemed as default standards to compare the hydrogen adsorption capacities of different MOF materials.¹⁰ These values are very useful and instructive at the early stage of exploration for hydrogen storage materials. Several

factors influencing the hydrogen uptake of porous MOFs at 77 K, 1 atm, such as specific surface area/pore volume, pore sizes, catenation etc. have been extensively studied.

Specific surface area/pore volume. Generally speaking, pore volume is proportional to specific surface area. Most porous MOFs have exhibited exceptionally high specific surface areas compared with carbon materials and inorganic zeolites. The high surface area records have been broken again and again in the past several years. For example, a porous MOF with specific surface area up to 4500 m²/g and pore volume of 1.61 cm³/g was reported for MOF-177 in 2004;¹² the surface area and pore volume values were then marked up to 5500 m²/g and 1.9 cm³/g respectively by MIL-101 in 2005.¹³

The parameters of surface area and pore volume influencing hydrogen uptake at 77 K and 1 atm have been intensively studied in MOFs. However, it has been found that MOFs with high specific surface areas (above 1000 m²/g) and large pore volumes (over 1.0 cm³/g) show no direct correlation between specific surface area/pore volume and hydrogen adsorption.¹⁰ For example, MOF-177 can only adsorb 1.25 wt% hydrogen at 77 K, 1 atm, despite its high surface area of 4500 m²/g and pore volume of 1.61 cm³/g; however, IRMOF-8, whose surface area (1466 m²/g) and pore volume (0.52 cm³/g) are less than one third of those of MOF-177, can uptake 1.5 wt% hydrogen under similar conditions.¹⁴ The lack of a linear correlation between hydrogen adsorption capacity and surface area/pore volume strongly indicates that low-pressure hydrogen adsorption is controlled by other factors, which will be discussed below.

Pore size. The low hydrogen adsorption capacities in porous MOFs with high surface areas and large pore volumes are presumably due to the weak interactions between hydrogen molecules and the frameworks resulting from large pore sizes and spatial free void spaces.¹⁰ Reduction in pore size is known to enhance the interaction energy as the attractive potential fields of opposite walls overlap.¹⁵ This has been extensively explored as a strategy to increase hydrogen-framework interactions thereby improving hydrogen uptake.^{16,17} Systematic investigation of pore sizes on hydrogen uptake was recently exemplified in a series of NbO type MOFs based on tetracarboxylate organic ligands and dicopper paddlewheel SBUs. Extension of biphenyl-3,3',5,5'-tetracarboxylate to terphenyl-3,3',5,5'-tetracarboxylate and quaterphenyl-3,3',5,5'-

tetracarboxylate leads to a proportional increase of pore sizes but a decrease of hydrogen uptake at 77 K, 1 atm.¹⁸

The ideal pore size for effective adsorption of hydrogen molecules in MOFs is comparable with the kinetic diameter of dihydrogen, which is 2.89 Å. This leads to optimal interaction between the dihydrogen molecule and the framework, thus maximizing the total van der Waals forces acting on dihydrogen.¹⁹

Catenation. Catenation, a frequent incidence in porous MOFs, is the intergrowth of two or more identical frameworks.²⁰ It is favored by the use of longer linkers, and deemed as an alternative strategy for reducing pore sizes in porous MOFs.^{10,16} The effects of catenation on hydrogen adsorption uptakes was illustrated by hydrogen adsorption studies on IRMOFs, which revealed that catenated IRMOF-9, IRMOF-11, and IRMOF-13 showed higher hydrogen adsorption capacities than non-catenated IRMOF-1.²¹ This effect is actually directly related to the reduction of pore diameter due to catenane formation.

Ligand functionalization. The functionalization of organic linkers not only plays a critical role in the construction of MOFs, but also plays an important role in further enhancement of hydrogen adsorption.^{10,21} Organic linkers with aromatic fragments, such as phenylene, naphthylene, and biphenylene, are widely used in the synthesis of MOFs to form a rigid three dimensional porous framework.^{14,21} Increasing the aromaticity of these organic ligands has been both theoretically predicted^{22,23} and experimentally proved to be an effective way to improve hydrogen adsorption capacity.¹⁴ A typical example is the synthesis of a series of IRMOFs, which have similar topology based on octahedral Zn₄O SBU. It was found that the hydrogen adsorption per formula unit at 77 K and 1 atm increased with an increasing number of aromatic rings in the organic linkers. The maximum adsorption increased from 4.2 molecules of H₂ per formula unit in IRMOF-18 (2,3,5,6-tetramethylphenylene-1,4-dicarboxylate) to 9.8 in IRMOF-13 (pyrene-2,7-dicarboxylate). Meanwhile, the gravimetric hydrogen capacity of IRMOF-13 (1.73 wt%) is almost double that of IRMOF-18 (0.89 wt%) formed by 2,3,5,6-tetramethylphenylene-1,4-dicarboxylate.^{31,38} These results indicate that the more aromatic the organic ligands are, the stronger the interactions between hydrogen and the MOFs.

In addition to increasing the aromaticity of the organic ligands, chemical modification of the organic linkers by introducing an electron-donating group (or groups) has been suggested, based on the *Ab initio* calculations, as another way to further enhance framework affinity for the dihydrogen molecule.²⁴ This was illustrated in the hydrogen adsorption studies of the IRMOF series. Adding one –Br, or one –NH₂ or four methyl groups to the central benzene ring of the linker in IRMOF-1 affords IRMOF-2, -3, and -18, respectively,¹⁴ while replacing the phenyl ring of bdc with a thieno-[3,2*b*]thiophene moiety affords IRMOF-20.²¹ The increased polarizability of the heteropolycyclic ligand essentially improves the hydrogen sorption on a molar basis in IRMOF-20 due to a stronger interaction of hydrogen with the organic linker, despite a reduction in the gravimetric capacity due to the heavier sulfur atom. Little enhancement, however, was found in IRMOF-2, IRMOF-3, IRMOF-18,²¹ although MP2 computational studies suggest that functionalizing phenylene ring with electron-donor groups, such as NH₂ or Me can improve hydrogen affinity by ~15%.²⁴ A similar lack of hydrogen adsorption enhancement was found in some pillared MOFs constructed by ligands with all phenyl H atoms replaced with either –F or –CH₃.²⁵ This may be attributed to the smaller pore sizes or blocking of some high-affinity binding sites by the larger ligand, thus canceling out the benefit derived from electronic enhancement of the ligand. It has also been proposed that N-heterocyclic ligands may have a higher hydrogen affinity than purely graphitic ligands, based on some studies of hydrogen adsorption in carbon, carbon nitride, and boron nitride nanotube structures.²⁶ This was illustrated in some porous MOFs constructed from triazine ligands developed in our lab.^{27,28}

The versatility of organic ligands has provided infinite space for the construction of MOFs with various topologies. Instead of just modifying the organic ligands to build MOFs with similar topology, utilizing flexible organic ligands having different stereoisomerism under external stimuli can result in porous MOFs with quite different topologies. This phenomenon is referred to as supramolecular isomerism. As structure determines property, supramolecular isomers are expected to exhibit different hydrogen adsorption capacities. Recently, we designed a tetra-carboxylate ligand, namely, the tetra-anion of N,N,N',N'-tetrakis(4-carboxyphenyl)-1,4-phenylenediamine (tcppda), which has three stereoisomers with a pair of enantiomers and a diastereomer.²⁹ The

diastereomer has a C_{2h} symmetry with three phenyl rings oriented as left and right handed propellers around the two N atoms and a plane of symmetry through the central phenyl ring, reflecting one N-centered propeller to the other. The pair of enantiomers possesses D_2 point group symmetry with the two N-centered propellers being either right handed ($^{\delta}D_2$) or inverted ($^{\lambda}D_2$). Under solvothermal conditions, the reaction between $\text{Cu}(\text{NO}_3)_2 \cdot 2.5\text{H}_2\text{O}$ and H_4TCPPDA in DMSO at 115 °C gave rise to a porous MOFs with NbO topology, wherein only the C_{2h} isomer of the tcppda ligand exists. While raising the temperature to 120 °C, another porous MOF with PtS topology was obtained, wherein only the D_2 tcppda isomer was found in a racemic combination with the ratio of $^{\delta}D_2$ and $^{\lambda}D_2$ 1:1 (Figure 2). The temperature-dependent supramolecular isomerism of the two MOFs can be attributed to the inter-conversion of the D_2 and C_{2h} isomers of tcppda from low temperature to high temperature. Nitrogen and hydrogen adsorption studies at 77 K revealed that both surface area and hydrogen uptake of the porous MOFs with PtS topology are $\sim 20\%$ higher than those of the NbO-typed porous MOF. These studies suggest that designing flexible organic linkers is a promising way to construct porous MOFs with high hydrogen uptake.

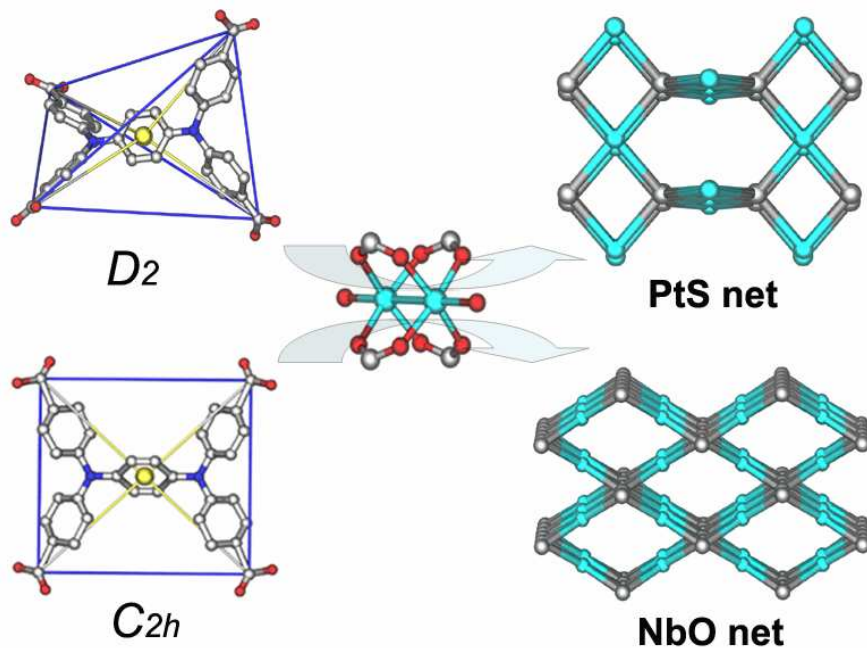


Figure 2.1 Different conformations of tcppda ligand lead to two porous MOFs with different topologies.

Unsaturated metal centers (UMCs). The impregnation of unsaturated metal centers (UMCs) into porous MOFs is very attractive for hydrogen adsorption. One of the advantages in porous MOFs when compared to carbon materials is that metal ions incorporated in porous MOFs have much higher hydrogen bonding energies than carbon.^{16,17} Recent neutron studies have revealed that hydrogen adsorption is much dependent on the nature of the metal cation or oxide of the SBUs in porous MOFs.^{11,30} Coordinatively unsaturated metal centers are usually very reactive and are known to play an important role in catalysis; consequently, their use in MOFs is a promising strategy to reach high hydrogen uptake due to their exceptional hydrogen affinity.¹⁷ An effective way to achieve coordinative unsaturation of the metal ions in the SBUs is to liberate the terminal bound labile solvent (aqua) ligands by evacuation at relative high temperatures (usually 100~200 °C), provided the porous framework integrity is retained during and after the process.

The contribution from such UMCs to hydrogen adsorption capacity is quite remarkable.³¹ This is well illustrated by the fact that MOF-505 has the exceptionally high hydrogen capacity of 2.47 wt% at 77 K and 1 atm after removal of axial aqua ligands from dicopper paddlewheel SBUs via thermal activation, generating the coordinatively unsaturated copper centers in MOF-505.³¹

2.2.2 Hydrogen saturation at cryo-temperatures and high pressure hydrogen adsorption studies at room temperature

Although extensive studies have been focused on hydrogen uptake at low temperatures and low pressure (usually 77 K, 1 atm), increasing attention is being drawn to high pressure hydrogen studies because of their direct application in practical on-board hydrogen storage. In addition to evaluating high-pressure gravimetric adsorption capacity in porous MOFs, volumetric adsorption capacity has also been widely assessed as it is another important criterion for on-board hydrogen storage.

Excess adsorption and absolute adsorption. In high pressure studies, two concepts namely, excess and the absolute adsorption, are frequently used to describe hydrogen adsorption in porous MOFs. In brief, the capacity of excess adsorption is the amount of adsorption gas interacting with the frameworks, while the capacity of absolute adsorption is the amount of gas both interacting with the frameworks and staying in pores

in the absence of gas-solid intermolecular forces. The majority of the reported experimental adsorption data in the literature are excess adsorption isotherms. The absolute adsorbed amount can be estimated for systems with known crystal structure. From the viewpoint of hydrogen storage, the total amount that a material can store or its absolute adsorption is most relevant for practical purposes.³²

Hydrogen saturation at 77 K. Hydrogen sorption behavior at saturation is a critical parameter for judging the practicality of porous MOF materials.³³ Hydrogen saturation is very hard to achieve at room temperature due to the rapid thermal motion of dihydrogen molecules. Current research is focusing on investigating hydrogen saturation uptake at 77 K. Existing studies revealed that hydrogen saturation uptake at 77 K scales up with surface area.^{10,33} As shown in Figure 3a, some of them can reach or even pass the 2010 US DOE gravimetric adsorption target of 6 wt%, albeit at 77K. The excess gravimetric uptake of MOF-177 is as high as 7.5 wt%, while the absolute gravimetric uptake is even much higher of 11.3 wt% at 77 K, 70 bar.³²

Most porous MOFs are very light. Generally speaking, the higher surface area, the lower the crystal density. In most cases, the low density trims down the volumetric hydrogen uptake of the MOF material despite its high gravimetric uptake. As indicated in Figure 3b, very few porous MOFs can reach the 2010 US DOE volumetric hydrogen uptake target. A typical example is MOF-177 which has an excess gravimetric uptake of 7.5 wt%, passing the 2010 US DOE gravimetric uptake goal of 6 wt%. Its low crystallographic density of 0.427 g/cm³, however, leads to the excess volumetric uptake of 32 g/L, which is far from the 2010 US DOE volumetric uptake goal of 45 g/L.³³ A compromise between the surface area and crystal density should be met in search of porous MOF material with both high gravimetric and volumetric hydrogen uptake. Nevertheless, in terms of absolute adsorption, there exist some MOF materials with both gravimetric and volumetric hydrogen uptake at 77 K exceeded the 2010 US DOE targets for hydrogen storage. The $\text{Mn}_3[(\text{Mn}_4\text{Cl})_3(\text{btt})_3(\text{CH}_3\text{OH})_{10}]_2$ (btt = 1,3,5-benzenetristetrazolate) reported by Long *et al.* exhibits high hydrogen adsorption capacity at 77 K under high pressure with the absolute gravimetric uptake of 6.9 wt% and volumetric uptake of 60 g/L.³⁴ The absolute gravimetric uptake and volumetric uptake in MOF-177 can reach 11 wt% and 48 g/L, respectively, both of which also exceed the

DOE goals albeit at 77 K.³² It seems very promising to store hydrogen in porous MOFs at 77 K, high pressure; however, the cost of the cryo-storage vessel precludes their practical on-board application, and porous MOFs with high hydrogen uptake near ambient temperature are badly needed.

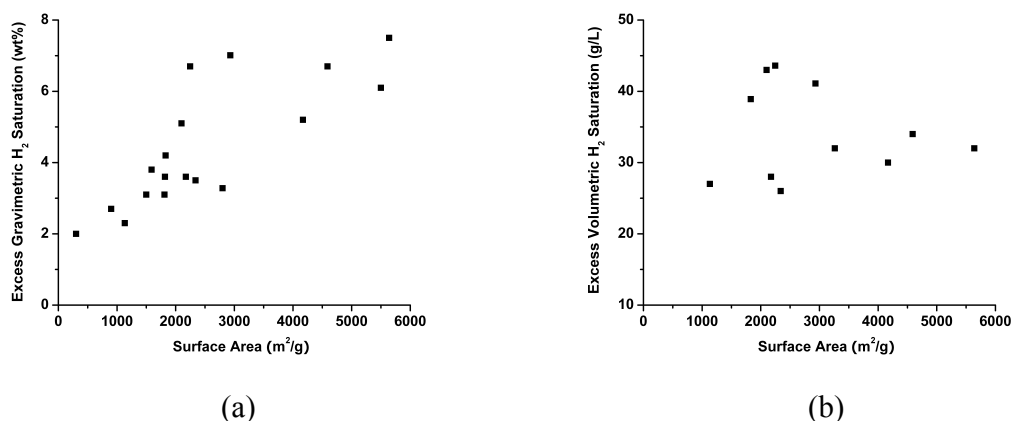


Figure 2.2 Correlation between surface area and hydrogen saturation at 77 K: (a) excess gravimetric, (b) excess volumetric.

High pressure hydrogen adsorption at room temperature. Room temperature hydrogen adsorption studies under high pressure have been being carried out for porous MOF materials. Unfortunately, these materials have very low hydrogen uptake at room temperature of less than 1.5 wt%.¹⁰ In this situation, high surface area is insufficient to achieve high-capacity ambient-temperature storage, albeit it can lead to high hydrogen saturation at 77 K. Instead, small pore size is more favorable for ambient-temperature hydrogen adsorption due to the enhanced interaction energy.^{10,15} This is well illustrated in [Cu(hfipbb)(H₂hfipbb)_{0.5}], a microporous MOF which contains small pores of two types: small ($\sim 3.5 \times 3.5$ Å) and large (5.1×5.1 Å). At room temperature and 48 atm, it can adsorb ~ 1 wt% of hydrogen, which is more than three times that of MOF-5 (0.28 wt%, 60 atm), which contains pore size of $\sim 7.7 \times 7.7$ Å and has a high surface area of 2300 m²/g.³⁵

An effective way to reduce pore size is by utilizing interpenetration (or catenation), which has been proposed as a strategy to improve hydrogen uptake. A typical example of this method is Zn₄O(L¹)₃ (L¹ = 6,6'-dichloro-2,2'-diethoxy-1,1'-binaphthyl-4,4'-dibenzoate), which is four-fold interpenetrated with open channels of less

than 5 Å, and a BET surface area of only 502 m² g⁻¹; this material adsorbs 1.12 wt% of hydrogen at room temperature and 48 bar, which is among the highest of reported MOF materials.³⁶

The exposition of UMCs has been known as the most promising way to improve hydrogen affinity and been widely explored for room temperature hydrogen adsorption studies. The ability of UMCs to adsorb significant amounts of hydrogen is well demonstrated by Long *et al.* in the porous MOF, Mn₃[(Mn₄Cl)₃(btt)₃(CH₃OH)₁₀]₂. Upon thermal activation, this MOF can adsorb hydrogen 1.4 wt% at 298 K and 90 bar. This high uptake capacity can be ascribed to exposed Mn²⁺ sites within the framework that interact strongly with H₂ molecules.³⁴

Despite the increasing number of investigations of hydrogen adsorption in porous MOFs, the near ambient temperature hydrogen uptakes of those materials reported so far fall short of the 2010 US DOE targets. Exploration of porous MOFs with high hydrogen uptake for on-board storage applications still has a long way to go.

2.2.3 Hydrogen adsorption enthalpy

The major barrier limiting hydrogen uptake at ambient temperature is the weak interaction between hydrogen molecules and the frameworks of porous MOFs. Thus it is necessary to improve the hydrogen binding energy (or hydrogen affinity) for high hydrogen adsorption at near ambient temperatures. Hydrogen binding energy or hydrogen affinity can be quantitatively estimated by measuring the isosteric heats of adsorption of hydrogen or the hydrogen adsorption enthalpy, ΔH_{ads} . The most frequently used method to determine the hydrogen adsorption enthalpy, ΔH_{ads} , is by applying the Clausius-Clapeyron equation to adsorption data collected at two different temperatures (typically 77 K and 87 K).³⁷ Enhancing the hydrogen adsorption enthalpy will increase the temperatures at which porous MOFs can uptake large amounts of hydrogen; this is essential in order to develop a storage system that meets the 2010 US DOE goals at near-ambient temperatures.

Recently, an optimal enthalpy of 15 kJ/mol has been theoretically proposed for ambient temperature, high pressure hydrogen adsorption.³⁸ Various strategies to be described below have been explored to increase the hydrogen adsorption enthalpy to approach this value.

Utilizing small pores sizes comparable to the kinetic diameter of dihydrogen molecules can maximize the hydrogen-framework interaction energy and is a good method to enhance hydrogen adsorption enthalpy. An example of this was found in a microporous magnesium MOF; this material contains very small pores of ~ 3.5 Å and exhibits high hydrogen adsorption enthalpy of 9.5 kJ/mol.³⁹ Catenation, an effective way to confine the pore size, has also been explored as a strategy to increase hydrogen adsorption enthalpy. Isotheric heat of adsorption studies on IRMOFs showed that the catenated IRMOF-11 surpasses other non-catenated IRMOFs in the adsorption enthalpy with a value of up to 9.1 kJ/mol at low hydrogen coverage.²¹ Our recent studies on catenation isomers revealed an average enhancement of hydrogen adsorption enthalpy of ~ 2 kJ/mol in the catenated PCN-6 over the non-catenated PCN-6'.²⁸

The introduction of UMCs into porous MOFs is considered as the most attractive strategy to increase hydrogen adsorption enthalpy. Evidence for this assumption was obtained from the isotheric heats of adsorption studies. The exposition of coordinately unsaturated Cu^{2+} centers after removal of the terminal aqua ligands in HKUST-1, leads to a ~ 2 kJ/mol increase in adsorption enthalpy when compared to MOF-5 under low-loading conditions.²¹ The same phenomenon was demonstrated in the porous MOFs $\text{Mn}_3[(\text{Mn}_4\text{Cl})_3(\text{btt})_3(\text{CH}_3\text{OH})_{10}]_2$ and $\text{NaNi}(\text{sip})_2$, both of which exhibit exceptionally high adsorption enthalpies of 10.1 kJ/mol at low hydrogen coverage after exposition the UMCs by removing the coordinated labile solvent ligands using thermal activation.^{34,40}

Exchanging positively charged guest molecules in anionic frameworks with metal cations is yet as another way to achieve coordinative unsaturation. The study of cation-exchange on hydrogen adsorption enthalpy and capacity was recently performed in an anionic porous MOF $\text{Mn}_3[(\text{Mn}_4\text{Cl})_3(\text{btt})_3(\text{CH}_3\text{OH})_{10}]_2$. The findings revealed that the Mn^{2+} -, Fe^{2+} -, and Co^{2+} - exchanged frameworks yielded the strongest H_2 binding among the cations assessed, particularly in the case of Co^{2+} whose framework exhibited an exceptionally high hydrogen adsorption enthalpy of 10.5 kJ/mol at zero coverage.⁴¹

The introduction of naked lithium cations into porous MOF was illustrated by a chemical reduction strategy. The lithium cations reside in the porous framework to balance the negative charge of the reduced ligands. Hydrogen adsorption studies

demonstrated that the inclusion of the lithium cations not only enhanced the hydrogen adsorption enthalpy significantly but also almost doubled the hydrogen uptake.⁴²

2.2.4 Tools to investigate the interactions between hydrogen molecules and frameworks

The investigation of the detailed interactions between hydrogen molecules and the framework is of great significance for future development of new porous MOF materials with high hydrogen adsorption capacities.

It is well known that neutron based studies are the most powerful tools for hydrogen research due to the fact that hydrogen has the largest neutron cross section.⁶⁴ One of the most useful methods for understanding hydrogen uptake in porous MOFs is inelastic neutron scattering (INS), which is extremely sensitive to the chemical environment of adsorbed H₂ and can provide important information about the centers that hydrogen occupies and the order in which they are filled.⁴³ This technique has become invaluable to understanding the hydrogen adsorption characteristics of a variety of nanoporous substrates including zeolites⁴⁴ and carbon nanostructures⁴⁵ and has been recently employed to investigate hydrogen adsorption in porous MOF materials.^{11,30,40,46,47}

INS studies on isoreticular MOFs revealed two types of hydrogen binding centers: Zn₄O inorganic clusters and organic fragments. The Zn₄O inorganic clusters are the primary H₂ adsorption sites and are first occupied at low hydrogen loadings. The Zn metal centers have much higher hydrogen binding energy than the organic linker, although it plays an important role in increasing hydrogen uptake further.³⁰

INS investigation of hydrogen adsorbed in HKUST-1 identified some specific hydrogen binding sites, with the first and strongest ones located around the coordinatively unsaturated Cu²⁺ sites.⁴⁸ The strong association between hydrogen molecules and coordinatively unsaturated metal centers was also revealed by a combination of temperature-programmed desorption and INS studies on H₂-loaded NaNi(sip)₂ (sip = 5-sulfoisophthalate).⁴⁰

The complementary tools to INS for the location of discrete hydrogen binding sites are single-crystal neutron diffraction and neutron powder diffraction, which have been recently utilized for hydrogen adsorption in porous MOFs.^{34,49-53} Single-crystal

neutron diffraction of MOF-5 revealed two hydrogen-binding sites, one higher-energy site over the center of the $Zn_4(\mu_4-O)(CO_2)_8$ SBU and a second site over the face of a ZnO_4 tetrahedron.⁴⁹ This is consistent with neutron powder diffraction studies on MOF-5, which also identified two additional sites at increased loading: one above the oxygen ions of the carboxylate group and the other over the phenyl ring of the ligand.⁵¹ Generally, these agree with an INS experiment performed on the same material, all revealing that the first hydrogen occupation sites are located around the inorganic $Zn_4(\mu_4-O)$ cluster.³⁰

Neutron powder diffraction of D_2 -loaded HKUST-1 identified six distinct D_2 sites within the nanopore structure. The first, highest-energy site is located at the coordinatively unsaturated axial sites of the dinuclear Cu center, and the remaining sites are located near the benzene ring and carboxylate moieties of the ligand, which are occupied progressively from the smallest to largest pores. The short Cu- H_2 distance of 2.39 Å indicates significant interaction with the d^9 coordinatively unsaturated Cu(II) center.⁵⁰ Similar association of H_2 molecules with UMCs was also observed via neutron powder diffraction studies of the porous MOF $Mn_3[(Mn_4Cl)_3(btt)_3(CH_3OH)_{10}]_2$. The 2.27 Å H_2 - Mn^{2+} distance represents the first H_2 -metal binding ever observed in porous MOFs (Figure 6) and also accounts for the high hydrogen adsorption enthalpy of the compound.³⁴

As enumerated above, the primary hydrogen adsorption sites in most MOFs are metal-based. However, neutron powder diffraction studies on the zeolite imidazolate frameworks (ZIFs), a subfamily of MOF revealed that the strongest adsorption sites are directly associated with the imidazolate organic linkers, instead of the triangular faces of the ZnN_4 tetrahedra. This finding suggests that modification of the organic linker rather than metal types in ZIFs is more important to optimize these materials for higher hydrogen adsorption capacity.⁵²

2.2.5 Hydrogen spillover

One of the most perspective methods for enhancing hydrogen absorption capacity is provided by secondary hydrogen spillover. It consists of the dissociative chemisorption of hydrogen on a metal catalyst with the subsequent migration of atomic hydrogen to the surface of a carrier contacting the metal (primary hydrogen receptor) and then to the second carrier (secondary receptor).⁵⁴ This technique has been recently

applied by Li and Yang in porous MOFs.^{55,56} Mechanically mixing 5% Pt on activated carbon with the MOF followed by melting and subsequent carbonizing of the sucrose resulted in the hydrogen adsorption capacity of MOF-5 and IRMOF-8 to increase up to 3% and 4% respectively, at 298 K and 10 MPa. The enhancement is as much as 8 times greater than their normal adsorption capacities under the same conditions. Meanwhile, the hydrogen adsorption enthalpy was increased to 20-23 kJ/mol, which is within the proposed work zone enthalpy range of 15-25 kJ/mol. The secondary hydrogen spillover technique is particularly exciting and shows great potential to achieve the 2010 US DOE targets for hydrogen storage.

2.3 Summary

As a class of porous materials, MOFs are still attracting increasing research interest and hold exceptional promise for on-board hydrogen storage application. These highly-crystalline materials with high surface areas, tunable pore sizes and functionalizable pore walls are ideal candidates for further exploration. Although ΔH_{ads} for hydrogen in reported porous MOFs ranges from 6–12 kJ/mol currently, it is conceivable that these values will increase even further, bringing them into the 15–25 kJ mol⁻¹ working zone range as more compounds are carefully designed and modified. Applying secondary hydrogen spillover to these new porous MOFs as well as existing ones will likely yield results that approach and hopefully meet the on-board hydrogen storage targets in the near future.

2.4 References

- (1) DOE Office of Energy Efficiency and Renewable Energy Hydrogen, Fuel Cells & Infrastructure Technologies Program Multi-Year Research, Development and Demonstration Plan, available at: <http://www.eere.energy.gov/hydrogenandfuelcells/mypp>.
- (2) FY 2006 Annual Progress Report for the DOE Hydrogen Program, November 2006, available at: http://www.hydrogen.energy.gov/annual_progress.html.

- (3) S. Satyapal et al., FY 2006 DOE Hydrogen Program Annual Merit Review and Peer Evaluation Meeting Proceedings, Plenary Session, available at: http://www.hydrogen.energy.gov/annual_review06_plenary.html.
- (4) Wolf, J. *MRS Bull.* **2002**, 27, 685
- (5) Sandrock, G. *J. Alloys Compd.* **1999**, 293–295, 877.
- (6) Bogdanovic', B.; Schwickardi, M. *J. Alloys Compd.* **1997**, 253–254, 1.
- (7) Hynek, S.; Fuller, W.; Bentley, J. *Int. J. Hydrogen Energy* **1997**, 22, 601.
- (8) Zrttel, A.; Sudan, P.; Mauron, P.; Kiyobayashi, T.; Emmenegger, C.; Schlapbach, L. *Int. J. Hydrogen Energy* **2001**, 27, 203.
- (9) Nijkamp, M. G.; Raaymakers, J. E. M. J.; van Dillen, A. J.; de Jong, K. P. *Appl. Phys. A* **2001**, 72, 619.
- (10) Collins, D. J.; Zhou, H.-C. *J. Mater. Chem.* **2007**, 17, 3154.
- (11) Rosi, N. L.; Eckert, J.; Eddaoudi, M.; Vodak, D. T.; Kim, J.; O'Keefe, M.; Yaghi, O. M. *Science* **2003**, 300, 1127.
- (12) Chae, H. K.; Siberio-Pérez, D. Y.; Kim, J.; Go, Y. B.; Eddaoudi, M.; Matzger, A. J.; O'Keefe, M.; Yaghi, O. M. *Nature* **2004**, 427, 523.
- (13) Férey, G.; Mellot-Draznieks, C.; Serre, C.; Millange, F.; Dutour, J.; Surblé, S.; Margiolaki, I. *Science* **2005**, 309, 2040.
- (14) Rowsell, J. L. C.; Millward, A. R.; Park, K. S.; Yaghi, O. M. *J. Am. Chem. Soc.* **2004**, 126, 5666.
- (15) Everett, D. H.; Powl, J. C. *J. Chem. Soc. Faraday Trans. 1* **1976**, 72, 619.
- (16) Rowsell, J. L. C.; Yaghi, O. M. *Angew. Chem. Int. Ed.* **2005**, 44, 4670.
- (17) Isacva, V. I.; Kustov, L. M. *Russ. J. Gen. Chem.* **2007**, 50, 56.
- (18) Lin, X.; Jia, J.; Zhao, X. K.; Thomas, M.; Blake, A. J.; Walker, G. S.; Champness, N. R.; Hubberstey, P.; Schröder, M.; *Angew. Chem. Int. Ed.* **2006**, 45, 7358.
- (19) Chapman, K. W.; Chupas, P. J.; Maxey, E. R.; Richardson, J. W. *Chem. Commun.* **2006**, 4013.
- (20) Batten, S. R.; Robson, R. *Angew. Chem. Int. Ed.* **1998**, 37, 1460.
- (21) Rowsell, J. L. C.; Yaghi, O. M. *J. Am. Chem. Soc.* **2006**, 128, 1304.
- (22) Han, S. S.; Goddard, W. A. III *J. Am. Chem. Soc.*, **2007**, 129, 8422.

- (23) Han, S. S.; Deng, W.-Q.; Goddard, W. A. III *Angew. Chem. Int. Ed.* **2007**, *46*, 6289.
- (24) Hrbner, O.; GIUss, A.; Fichtner, M.; Klopper, W.; *J. Phys. Chem. A* **2004**, *108*, 3019.
- (25) Chun, H. D. Dybtsev, N.; Kim, H.; Kim, K. *Chem. Eur. J.* **2005**, *11*, 3521.
- (26) Bai, X. D.; Zhong, D.; Zhang, G. Y.; Ma, X. C.; Liu, S.; Wang, E. G. *Appl. Phys. Lett.* **2001**, *79*, 1552.
- (27) Sun, D.; Ma, S.; Ke, Y.; Collins, D. J.; Zhou, H.-C. *J. Am. Chem. Soc.* **2006**, *128*, 3896.
- (28) Ma, S. Sun, D.; Ambrogio, M. W.; Fillinger, J. A.; Parkin, S.; Zhou, H.-C. *J. Am. Chem. Soc.* **2007**, *129*, 1858.
- (29) Sun, D.; Ke, Y.; Mattox, T. M.; Ooro, B. A.; Zhou, H.-C. *Chem. Commun.* **2005**, 5447.
- (30) Rowsell, J. L. C.; Eckert, J.; Yaghi, O. M. *J. Am. Chem. Soc.* **2005**, *127*, 14904.
- (31) Chen, B.; Ockwig, N. W.; Millward, A. R.; Contreras, D. S.; Yaghi, O. M. *Angew. Chem. Int. Ed.* **2005**, *44*, 4745.
- (32) Furukawa, H.; Miller, M. A.; Yaghi, O. M.; *J. Mater. Chem.* **2007**, *17*, 3197.
- (33) Wong-Foy, A. G.; Matzger, A. J.; Yaghi, O. M. *J. Am. Chem. Soc.* **2006**, *128*, 3494.
- (34) Dincă, M.; Dailly, A.; Liu, Y.; Brown, C. M.; Neumann, D. A.; Long, J. R. *J. Am. Chem. Soc.* **2006**, *128*, 16876.
- (35) Pan, L.; Sander, M. B.; Huang, X.; Li, J.; Jr. Smith, M. R.; Bittner, E. W.; Bockrath, B. C.; Johnson, J. K. *J. Am. Chem. Soc.* **2004**, *126*, 1308.
- (36) Kesanli, B.; Cui, Y.; Smith, M. R.; Bittner, E. W.; Bockrath, B. C.; Lin, W. *Angew. Chem. Int. Ed.* **2005**, *44*, 72.
- (37) Rouquerol, J.; Rouquerol, F.; Sing, K. *Adsorption by Powders and Porous Solids*, Academic Press, London, 1998.
- (38) Bhatia, S. K.; Myers, A. L. *Langmuir* **2006**, *22*, 1688.
- (39) Dincă, M.; Long, J. R. *J. Am. Chem. Soc.* **2005**, *127*, 9376.
- (40) Forster, P. M.; Eckert, J.; Heiken, B. D.; Parise, J. B.; Yoon, J. W.; Jung, S. H.; Chang, J. S.; Cheetham, A. K. *J. Am. Chem. Soc.* **2006**, *128*, 16846.

- (41) Dincă, M.; Long, J. R. *J. Am. Chem. Soc.* **2007**, *129*, 11172.
- (42) Mulfort, K. L.; Hupp, J. T. *J. Am. Chem. Soc.* **2007**, *129*, 9604.
- (43) Eckert, J.; Kubas, G. J. *J. Phys. Chem.* **1993**, *97*, 2378.
- (44) Silvera, I. F. *Rev. Mod. Phys.* **1980**, *52*, 393.
- (45) Forster, P. M.; Eckert, J.; Chang, J.-S.; Park, S. E.; Férey, G.; Cheetham, A. K. *J. Am. Chem. Soc.* **2003**, *125*, 1309.
- (46) Schimmel, H. G.; Kearley, G. J.; Nijkamp, M. G.; Visser, C. T.; de Jong, K. P.; Mulder, F. M.; *Chem.-Eur. J.* **2003**, *9*, 4764.
- (47) Liu, Y.; Eubank, J. F.; Cairns, A. J.; Eckert, J.; Kravtsov, V. C.; Luebke, R.; Eddaoudi, M. *Angew. Chem. Int. Ed.* **2007**, *46*, 3278.
- (48) Liu, Y.; Brown, C. M.; Neumann, D. A.; Peterson, V. K.; Kepert, C. J. *J. Alloys Compd.* **2007**, *446-447*, 385.
- (49) Spencer, E. C.; Howard, J. A. K.; McIntyre, G. J.; Rowsell J. L. C.; Yaghi, O. M. *Chem. Commun.* **2006**, 278.
- (50) Peterson, V. K.; Liu, Y.; Brown C. M.; Kepert, C. J. *J. Am. Chem. Soc.* **2006**, *128*, 15578.
- (51) Yildirim, T.; Hartman, M. R. *Phys. Rev. Lett.* **2005**, *95*, 215504/1.
- (52) Wu, H.; Zhou, W.; Yildirim, T. *J. Am. Chem. Soc.* **2007**, *129*, 5314.
- (53) Dincă, M.; Han, W. S.; Liu, Y.; Dailly, A.; Brown, C. M.; Long, J. R. *Angew. Chem. Int. Ed.* **2007**, *46*, 1419.
- (54) Conner, W. C.; Falconer, J. L. *Chem. Rev.* **1995**, *95*, 759.
- (55) Li, Y.; Yang, R. T. *J. Am. Chem. Soc.* **2006**, *128*, 726.
- (56) Li, Y.; Yang, R. T. *J. Am. Chem. Soc.* **2006**, *128*, 8136.

Chapter 3

A Metal-Organic Framework with Entatic Metal Centers Exhibiting High Gas Adsorption Affinity^b

3.1 Introduction

The lack of an effective, economic, and safe on-board vehicular gas (hydrogen or methane) storage method is one of the major technical barriers preventing fuel-cell driven automobiles to compete with traditional ones.¹ Recently, the gas-storage properties of metal-organic frameworks (MOFs) have been actively explored.² In the area of hydrogen storage, suggested strategies to increase hydrogen uptake include using pore sizes comparable to gas molecules³ and introducing coordinatively unsaturated metal centers.⁴ Both strategies boil down to the enhancement of gas-affinity of the material. Recent inelastic neutron scattering studies suggest that high-affinity H₂ binding sites are metal-based.⁵ These recent findings prompted us to search for new ways to increase the gas affinity of metal centers in MOFs.

In metalloproteins such as hemoglobin, reversible O₂ binding is achieved by utilizing an iron active center (Figure 1a), where a porphyrin ligand and a histidine residue force the iron center into a square pyramidal geometry, generating an open coordination site for gas binding. Similarly, in Vitamin B₁₂ (VB₁₂), the central cobalt is surrounded by a corrin and a proximal ligand, and the distal position is open for substrate binding.⁶ Herein we report a MOF with a novel secondary building unit (SBU, Figure 1b), containing four hemoglobin/VB₁₂-like cobalt centers bundled through sharing a μ_4 -oxo bridge, producing four metal centers at an entatic state for gas binding. This MOF exhibits exceptional gas-adsorption affinity for a number of gases.

In bioinorganic chemistry, an entatic state is a state in which an unusual geometry is *imposed* by the protein polypeptides on a metal center whose reactivity in electron transfer, substrate binding, or catalysis is enhanced.⁷ Similarly, due to the specific

^b This section was reprinted with permission from: Ma, S.; Zhou, H.-C. *J. Am. Chem. Soc.* **2006**, *128*, 11734-11735. Copyright 2006, American Chemical Society.

geometric requirements of the ligands and SBUs in a MOF, the metal centers can be forced into an entatic state to enhance their affinity toward gases.

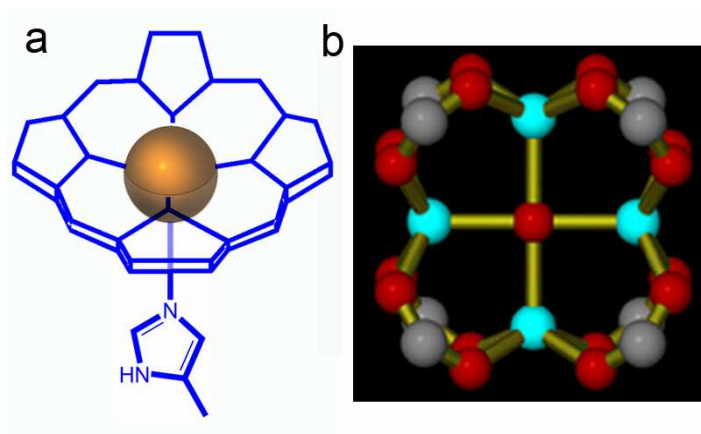


Figure 3.1 (a) Schematic drawing of the active center of hemoglobin. The gold sphere represents an Fe atom. (b) The $\text{Co}_4(\mu_4\text{-O})(\text{carboxylate})_4$ SBU found in PCN-9. Color scheme: C, gray; Co, aqua; and O, red.

Entatic metal centers (EMCs) represent a biomimetic approach to coordinatively unsaturated metal centers (UMCs).⁸ The latter are frequently obtained by removal of one or more ligands from a metal center to achieve coordinative unsaturation; the ligand removal required to achieve UMCs may collapse the entire network.⁹ Conversely, most of the EMCs are ready for substrate binding without the need for ligand removal.

In this chapter a MOF with EMCs, $\text{H}_2[\text{Co}_4\text{O}(\text{TATB})_{8/3}]$, designated PCN-9 (Porous Coordination Network) for convenience will be addressed. TATB (4,4',4''-s-triazine-2,4,6-triyl-tribenzoate) is a ligand developed in this laboratory for its planar conformation, potential ability to bind additional metal atoms, and high thermal stability of resulting MOFs.^{4b,10}

3.2 Experimental Details

Synthesis of PCN-9: A mixture of H_3TATB ligand (0.01 g, 2.26×10^{-5} mol), $\text{Co}(\text{NO}_3)_2 \cdot 6\text{H}_2\text{O}$ (0.025 g, 8.6×10^{-5} mol) in 1.2 mL dimethylsulfoxide (DMSO) was sealed in a Pyrex glass tube (ID 8mm/OD 10 mm) and heated to 135 °C at a rate of 1 °C / min. After staying at 135 °C for 72 hours, it was cooled to 35 °C at a rate of 0.1 °C / min.

The resulting violet crystals were washed with DMSO twice to give pure PCN-9 ($\text{Co}_4\text{O}(\text{TATB})_{8/3} \cdot 2\text{H}_3\text{O}^+ \cdot 5\text{H}_2\text{O} \cdot 8\text{DMSO}$, yield: 55%). The reaction was amplified to gram quantity using multiple tubes. Elemental analysis for PCN-9 calculated: C 44.20%, H 4.45%, N 5.15%; found: C 44.19%, H 4.51%, N 5.16%.

X-ray Structure determination: Single crystal X-ray determination was performed on a Bruker Smart Apex diffractometer using Mo-K α radiation ($\lambda = 0.71073$ Å). The data was collected on a crystal with approximate dimensions of 0.38 x 0.36 x 0.32 mm at 20 °C. A total of 1321 frames were collected using ω -scans with 0.3° and a counting time of 60 seconds per frame. The raw data was processed using SAINT to yield the .HKL file. The structure was solved by direct method and refined by full-matrix least-squares on F^2 with anisotropic displacement using SHELX-97. Non-hydrogen atoms of the metal and the ligands were refined with anisotropic displacement parameters. The hydrogen atoms on the carbon were calculated in ideal position with isotropic displacement parameters set to $1.2 \times U_{\text{eq}}$ of the attached atom. Absorption corrections were applied using SADABS after the formula of the compound is determined approximately. The solvent molecules in the structure were highly disordered. Efforts to locate and refine the solvent peaks were in vain. The SQUEEZE routine was used to remove the scattering from the highly disordered solvent molecules. The structure was then refined again using the new .HKL file generated by SQUEEZE.

Gas Adsorption Measurements: Gas adsorption measurements were measured with a Beckman Coulter SA 3100 surface area and pore size analyzer. A sample was soaked with methanol for 24 hours, and the extract was discarded. Fresh methanol was subsequently added, and the crystals were allowed to soak for another 24 hours to remove DMSO and H₂O solvates. The sample was then treated with dichloromethane similarly to remove methanol solvates. After the removal of dichloromethane by decanting, the sample was dried under dynamic vacuum ($< 10^{-3}$ torr) at room temperature (25 °C) overnight. Before gas adsorption measurement, the sample was dried again by using the “outgas” function of the surface area analyzer for 1 hour at 60 °C. A sample of 100.0 mg was used for N₂ adsorption measurement, and was maintained at 77K with liquid nitrogen. In the hydrogen storage measurement, high purity hydrogen (99.9995%) and an 80.0 mg sample were used. The regulator and pipe were flushed with hydrogen before connecting

to the analyzer. The internal lines of the instrument were flushed three times by utilizing the “flushing lines” function of the program to ensure the purity of H₂. The measurement was maintained at 77 K with liquid nitrogen. High purity O₂ (99.99%), CO (99.99%), and CH₄ (99.997%) were used for O₂, CO and CH₄ adsorption measurements, which were carried out following procedures similar to that of H₂ at 77 K. The temperature at 87K, 113 K, 143 K, 157 K, 175 K, 195 K were maintained with liquid argon bath, isopentane-liquid nitrogen bath, n-pentane-liquid nitrogen bath, ethyl alcohol-liquid nitrogen, methanol-liquid nitrogen, and acetone-dry ice bath respectively.

Analysis of Gas Adsorption Isotherms: The gas adsorption isotherms were fitted using the Langmuir-Freundlich equation. The Langmuir-Freundlich model gives a better fit over the entire measured pressure range, resulting in a more accurate prediction of the gas adsorption capacities of the compound at saturation. The enthalpies of gas adsorption onto the compound were calculated using a modified version of the Clausius-Clapeyron equation:

$$\ln\left(\frac{P_1}{P_2}\right) = \Delta H_{ads} \times \frac{T_2 - T_1}{R \times T_1 \times T_2} \quad \text{(I)} \quad \text{where: } P_i = \text{pressure for isotherm } i$$

$T_i =$ temperature for isotherm i

$$R = 8.3147 \text{ J}_K^{-1} \text{ mol}^{-1}$$

which can be used to calculate the enthalpy of adsorption of a gas as a function of the quantity of gas adsorbed. Pressure as a function of the amount of gas adsorbed was determined using the Langmuir-Freundlich fit for the isotherms:

$$\frac{Q}{Q_m} = \frac{B \times P^{(1/t)}}{1 + B \times P^{(1/t)}} \quad \text{(II) where: } Q = \text{moles adsorbed}$$

$Q_m =$ moles adsorbed at saturation

$P =$ pressure

B and $t =$ constants

Equation II rearranges to:

$$P = \left(\frac{Q/Q_m}{B - B \times Q/Q_m} \right)^t, \text{ which when substituted into equation I above gives:}$$

$$\Delta H_{abs} = \frac{R \times T_1 \times T_2}{T_2 - T_1} \times \ln \left(\frac{\left(\frac{Q/Q_m}{B_1 - B_1 \times Q/Q_{m1}} \right)^{t_1}}{\left(\frac{Q/Q_m}{B_2 - B_2 \times Q/Q_{m2}} \right)^{t_2}} \right)$$

In order to obtain more accurate value of the enthalpy of adsorption, gas adsorption measurements for a certain gas were carried out at three different temperatures. The enthalpy ΔH_{ads} is the average of three sets of the adsorption enthalpies calculated from the isotherms between every two different temperatures.

Table 3.1 Crystal data of PCN-9

Empirical formula	C ₆₄ Co ₄ H ₃₂ N ₈ O ₁₇
Formula weight	1420.70
Temperature	293(2) K
Wavelength	0.71073 Å
Crystal system, space group	Cubic, Im-3m
Unit cell dimensions	a = 25.4387(5) Å alpha = 90°; b = 25.4387(5) Å beta = 90°; c = 25.4387(5) Å gamma = 90°.
Volume	16462.1(6) Å ³
Z, Calculated density	6, 0.860 g/cm ³
Absorption coefficient	0.638 mm ⁻¹
F(000)	4296
Crystal size	0.38 x 0.36 x 0.32 mm
Theta range for data collection	1.13 to 25.04 deg.
Reflections collected / unique	47359 / 1442 [R(int) = 0.0775]
Completeness to theta = 25.04	99.5 %
Absorption correction	Empirical
Max. and min. transmission	0.815 and 0.742
Refinement method	Full-matrix least-squares on F ²
Goodness-of-fit on F ²	1.218
Final R indices [I > 2sigma(I)]	R1 = 0.103, wR2 = 0.307
R indices (all data)	R1 = 0.123, wR2 = 0.320

Table 3.2 Selected bond lengths (Å) and angles (deg) of PCN-9

Co(1)-O(1)#1	1.965(5)	Co(1)-O(1)	1.965(5)
Co(1)-O(1)#2	1.965(5)	Co(1)-O(1)#3	1.965(5)
Co(1)-O(2)	2.3513(18)	O(2)-Co(1)#4	2.3513(18)
O(2)-Co(1)#5	2.3513(18)	O(2)-Co(1)#6	2.3513(18)
O(1)-Co(1)-O(1)#1	86.1(5)	O(1)-Co(1)-O(1)#2	87.7(4)
O(1)#1-Co(1)-O(1)#2	153.2(6)	O(1)-Co(1)-O(1)#3	153.2(6)
O(1)#1-Co(1)-O(1)#3	87.7(4)	O(1)#2-Co(1)-O(1)#3	86.1(5)
O(1)-Co(1)-O(2)	103.4(3)	O(1)#1-Co(1)-O(2)	103.4(3)
O(1)#2-Co(1)-O(2)	103.4(3)	O(1)#3-Co(1)-O(103.4(3)
C(1)-O(1)-Co(1)	139.5(6)	Co(1)#4-O(2)-Co(1)#5	90.0
Co(1)#4-O(2)-Co(1)	90.0	Co(1)#5-O(2)-Co(1)	180.0
Co(1)#4-O(2)-Co(1)#6	180.0	Co(1)#5-O(2)-Co(1)#6	90.0
Co(1)-O(2)-Co(1)#6	90.0	Co(1)#5-O(2)-Co(1)#6	180.0

3.3 Results and Discussion

X-ray single-crystal analysis¹¹ revealed that PCN-9 crystallizes in the *Im-3m* space group. It adopts a square-planar $\text{Co}_4(\mu_4\text{-O})$ SBU, with a $\mu_4\text{-oxo}$ residing at the center of a square of four Co atoms. All four Co atoms in the SBU are five coordinate with square-pyramidal geometry. The $\text{Co}-\mu_4\text{-O}$ distance is 2.351(2) Å. If one of the five-coordinate Co atoms is compared to the active center in hemoglobin, the $\mu_4\text{-O}$ is analogous to the proximal ligand, and on the opposite side of the square-pyramidal base is the distal position of the Co, which is below the plane of the four O atoms in an entatic state, and ready to bind a substrate to achieve octahedral coordination. Although tetrahedral $\mu_4\text{-oxo}$ bridge is common,¹² square-planar $\mu_4\text{-oxo}$ bridge is rare. Only a few examples have been found in iron,^{13a} copper,^{13b} vanadium,^{13c} and niobium^{13d} compounds. The square-planar $\mu_4\text{-oxo}$ bridge found in PCN-9 is unique in a MOF. Every $\text{Co}_4(\mu_4\text{-O})$ SBU connects eight trigonal-planar TATB ligands and every TATB ligand connects three $\text{Co}_4(\mu_4\text{-O})$ SBUs to form a (8,3)-net. Alternatively, this (8,3)-net can also be described as a three-dimensional network formed by corner sharing of octahedral cages (Figure 2a);

the O_h -cage is defined by six $\text{Co}_4(\mu_4\text{-O})$ SBUs at the corners and eight TATB ligands on the faces. Overall, the structure of PCN-9 can be obtained by the interpenetration of two (8,3)-nets, the second being generated through translation along $[1\ 1\ 0]$.

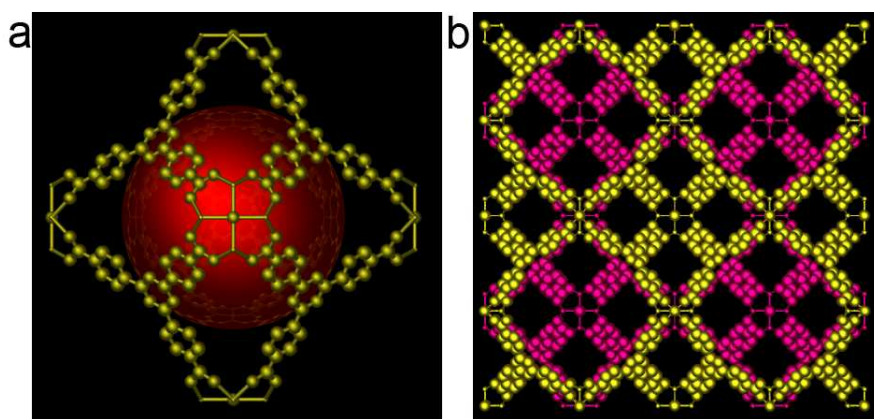


Figure 3.2 Crystal structures of PCN-9: (a) showing an octahedral cage; the red sphere represents void inside the cage. (b) View of the crystal structure of PCN-9 along the a -axis; the two interpenetrated networks are shown in gold and pink respectively. All atoms are shown in arbitrary scales.

The volume of the octahedral cage is 2740 \AA^3 . Each open window of the cage is $6.7 \times 6.7 \text{ \AA}$ (atom to atom distance), and possesses two EMCs with distal sites pointing toward the void. The solvent accessible volume of PCN-9 calculated using PLATON¹⁴ is 58.8%. The permanent porosity of PCN-9 is confirmed by its N_2 adsorption isotherm. After desolvation, PCN-9 exhibits a Langmuir surface area of $1355 \text{ m}^2/\text{g}$ and a pore volume of $0.51 \text{ cm}^3/\text{g}$.

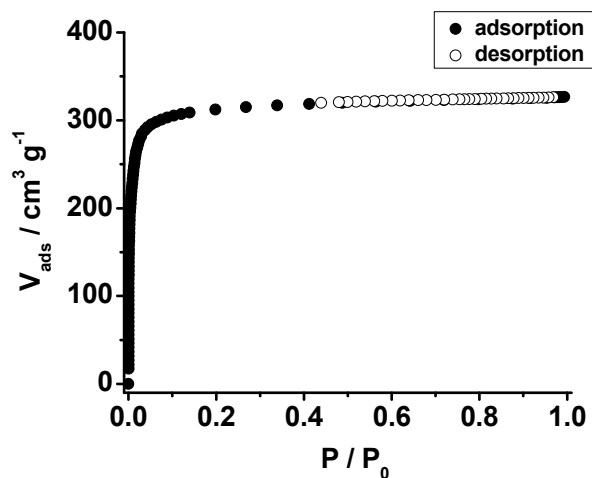


Figure 3.3 N₂ sorption isotherm of PCN-9.

To determine the gas affinity of PCN-9, adsorption isotherms were collected at various temperatures, and the data was fit using the Langmuir-Freundlich equation.¹⁵ Isothermic adsorption enthalpies as a function of the quantity of gas adsorbed were calculated using a variant of the Clausius-Clapeyron equation.^{16,18a,18b}

At low coverage, PCN-9 exhibits an O₂-adsorption enthalpy of 17.8 kJ/mol, comparable to that of Co exchanged zeolites (15.1-18.5 kJ/mol).¹⁷ Similarly, at low coverage, the CO-adsorption enthalpy of PCN-9 reaches 21.0 kJ/mol. These results represent the first measurement of O₂- or CO-adsorption enthalpy in MOFs.

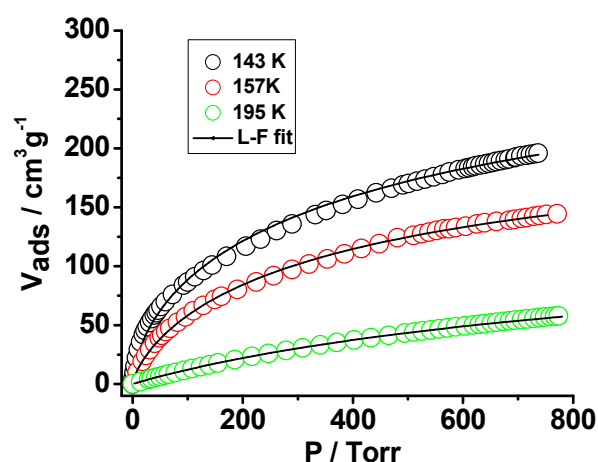


Figure 3.4 O₂ adsorption isotherms for PCN-9 at different temperatures: n-pentane-liquid nitrogen bath (black circles), ethyl alcohol-liquid nitrogen bath (red circles) and acetone-

dry ice bath (green circles). Solid lines correspond to Langmuir-Freundlich fits to the experimental data.

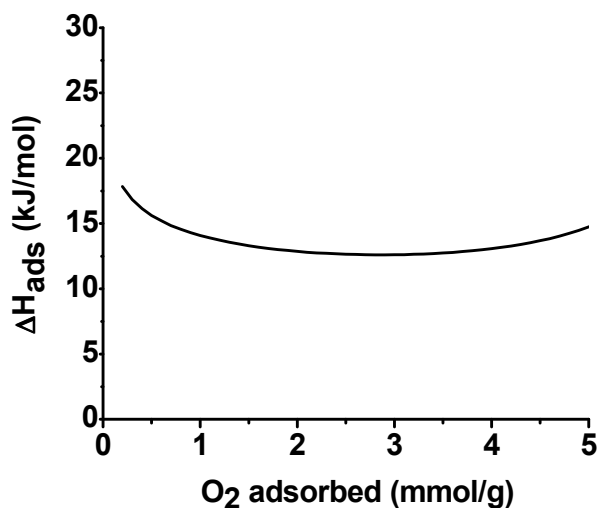


Figure 3.5 Enthalpy of adsorption of O₂ for PCN-9. The enthalpy ΔH_{ads} is the average of $\Delta H_{\text{ads}}(143\text{K}-157\text{K})$, $\Delta H_{\text{ads}}(143\text{K}-195\text{K})$, and $\Delta H_{\text{ads}}(157\text{K}-195\text{K})$, which represent the isosteric adsorption enthalpies calculated from the isotherms between 143 and 157K, between 143 and 195K, and between 157 and 195K.

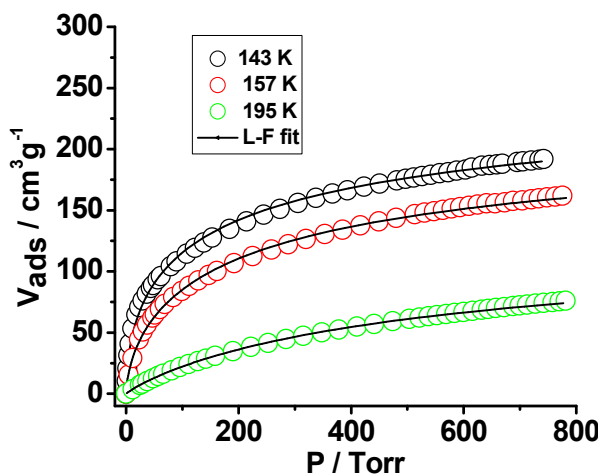


Figure 3.6 CO adsorption isotherms for PCN-9 at different temperatures: n-pentane-liquid nitrogen bath (black circles), ethyl alcohol-liquid nitrogen bath (red circles) and acetone-dry ice bath (green circles). Solid lines correspond to Langmuir-Freundlich fits to the experimental data.

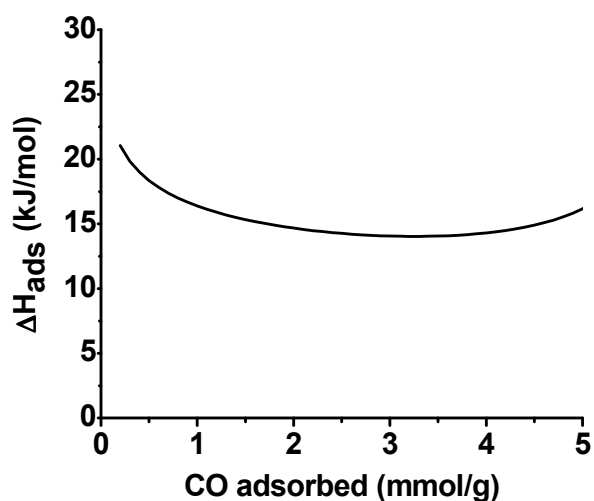


Figure 3.7 Enthalpy of adsorption of CO for PCN-9. The enthalpy ΔH_{ads} is the average of $\Delta H_{\text{ads}}(143\text{K}-157\text{K})$, $\Delta H_{\text{ads}}(143\text{K}-195\text{K})$, and $\Delta H_{\text{ads}}(157\text{K}-195\text{K})$, which represent the isosteric adsorption enthalpies calculated from the isotherms between 143K and 157K, between 143K and 195K, and between 157K and 195K.

H_2 adsorption isotherm at 77K indicates that PCN-9 has an uptake of 1.53 wt% at 760 Torr. Hydrogen adsorption isotherms at two other temperatures were collected and used to calculate the heat of adsorption. At low coverage, the heat of adsorption of PCN-9 for H_2 is 10.1 kJ/mol, which is higher than that of MOF-5 (5.2 kJ/mol), Prussian blue (7.4 kJ/mol), MOF-74 (8.3 kJ/mol), or HKUST-1 (6.6 kJ/mol), and is comparable to that of IRMOF-11 (9.1 kJ/mol) or a magnesium MOF (9.5 kJ/mol).¹⁸

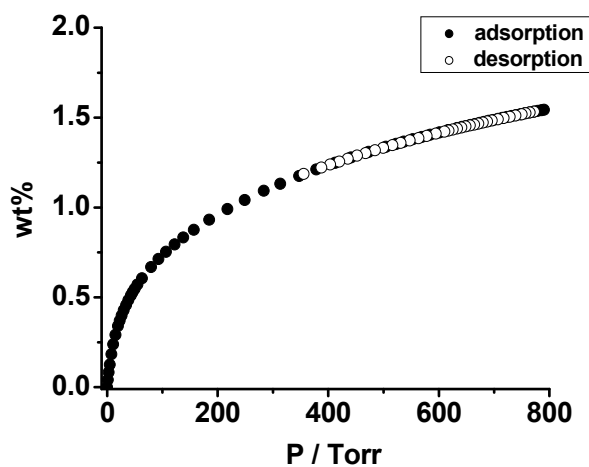


Figure 3.8 H₂ sorption isotherms of PCN-9: indicating that it has an uptake of **1.53wt%** at 77K, 760 Torr. A fit of Langmuir-Freundlich equation to the data gives a predicted saturation of **2.51wt%**.

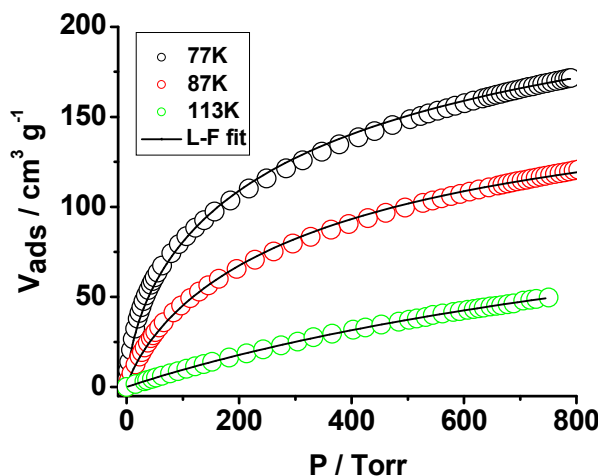


Figure 3.9 H₂ adsorption isotherms for PCN-9 at different temperatures: liquid nitrogen bath (black circles), liquid argon (red circles) and isopentane-liquid nitrogen bath (green circles). Solid lines correspond to Langmuir-Freundlich fits to the experimental data.

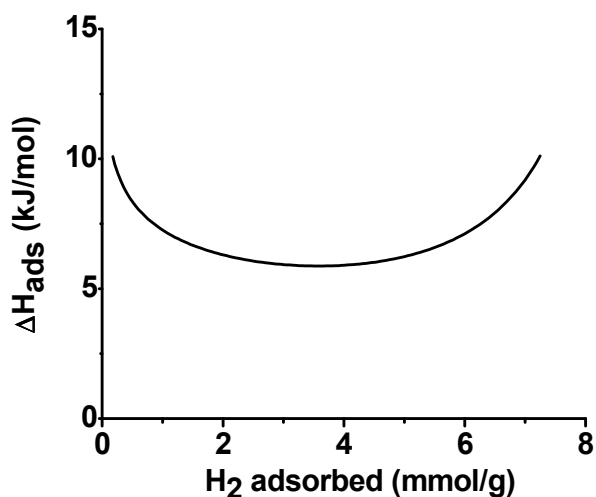


Figure 3.10 Enthalpy of adsorption of H₂ for PCN-9. The enthalpy ΔH_{ads} is calculated from the isotherms between 77 and 87K, which is commonly used for calculating the enthalpy ΔH_{ads} of H₂,⁵ deriving a value of 10.1 kJ/mol at low coverage.

In VB₁₂, the active center can bind a methyl or alkyl group.⁶ It is expected that PCN-9, with its SBUs structurally similar to the active center of VB₁₂, should have a high methane-affinity. The CH₄-isotherms of PCN-9 at three temperatures were collected, corresponding to an adsorption enthalpy of 23.3 kJ/mol at low coverage. To the best of our knowledge, this is by far the highest CH₄-adsorption enthalpy found among MOFs (IRMOF-6: 12.1 kJ/mol, MIL-53: 17 kJ/mol).¹⁹

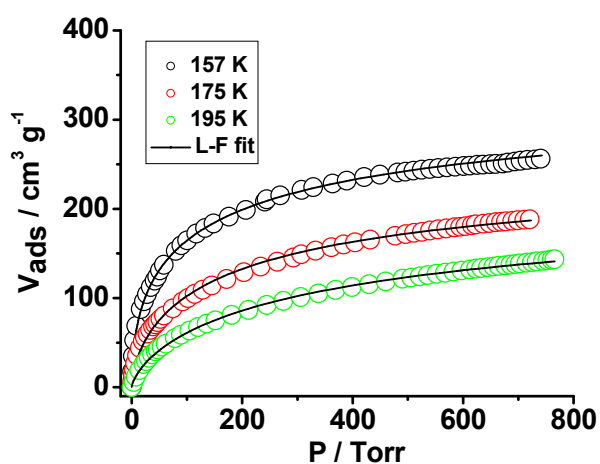


Figure 3.11 CH₄ adsorption isotherms for PCN-9 at different temperatures: ethyl alcohol-liquid nitrogen bath (black circles), methanol-liquid nitrogen bath (red circles) and acetone-dry ice bath (green circles). Solid lines correspond to Langmuir-Freundlich fits to the experimental data.

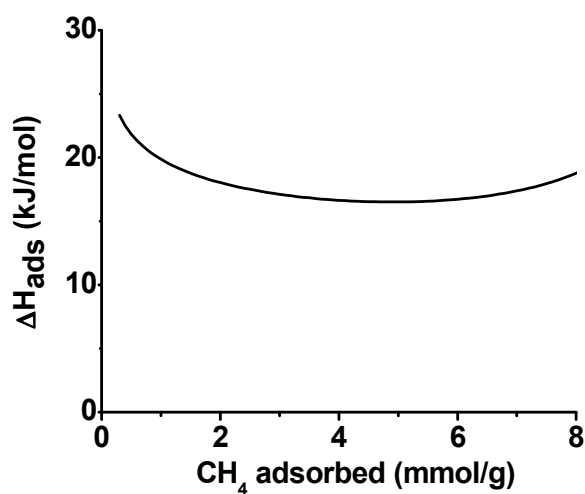


Figure 3.12 Enthalpy of adsorption of CH₄ for PCN-9. The enthalpy ΔH_{ads} is the average of $\Delta H_{\text{ads}}(143\text{K}-157\text{K})$, $\Delta H_{\text{ads}}(143\text{K}-195\text{K})$, and $\Delta H_{\text{ads}}(157\text{K}-195\text{K})$, which represent the isosteric adsorption enthalpies calculated from the isotherms between 157K and 175K, between 157K and 195K, and between 175K and 195K.

To further confirm that this remarkable enhancement of gas affinity is due to the EMCs, freshly prepared PCN-9 crystals (or a guest-free sample) were soaked in a dilute tetrabutylammonium cyanide solution in THF (1 mg/ml) for two days until the color of the crystals changed from violet to dark red. An IR spectra using this dark-red polycrystalline sample showed a sharp peak at 2105 cm⁻¹, a +50 cm⁻¹ shift of the C≡N stretch relative to that of free cyanide, consistent with the literature value for terminal cyanides bound to Co atoms.²⁰

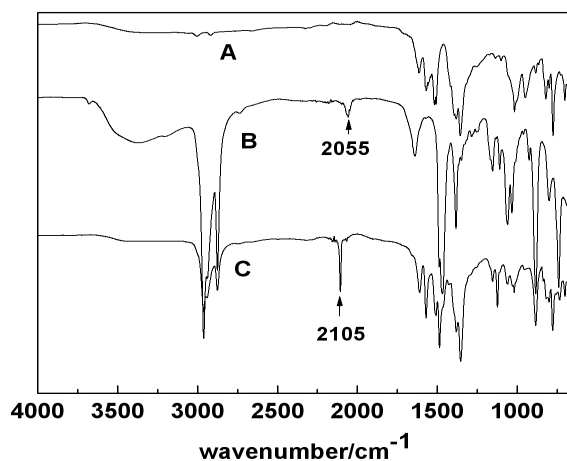


Figure 3.13 IR spectra of PCN-9: (A) Fresh PCN-9 crystals; (B) n-tetrabutylammonium cyanide; (C) PCN-9 crystals soaked in n-tetrabutyl ammonium cyanide/THF solution (1 mg/ml) (Washed with THF several times using ultrasonic before measurement in order to remove free CN⁻ ions on the surface).

Aware that the bulkiness of the counter-ion may prevent cyanide ions from permeating into the channels, we decided to use CO as an IR probe. A guest-free PCN-9 sample was kept under a CO atmosphere (3 bar) overnight. IR spectra of the sample showed a peak at 2044 cm⁻¹ (compared to 2143 cm⁻¹ for free CO),²¹ indicating terminal

CO binding to the EMCs. The same sample was then kept under dynamic vacuum for half an hour to remove CO guests. The 2044 cm^{-1} feature disappeared, demonstrating the reversibility of EMC binding, consistent with CO-adsorption measurements.

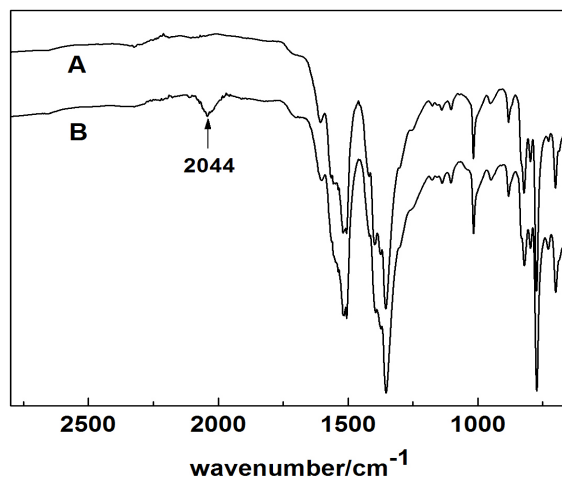


Figure 3.14 IR spectra of PCN-9 with CO attached: (A) PCN-9 after removal of solvent molecules. (B) Solvent-free PCN-9 after immersed in CO atmosphere (3 bar) overnight.

In summary, EMCs have been created based on the geometric requirements of a MOF. This approach is analogous to the formation of protein EMCs, which are enforced by surrounding polypeptides. The EMC-containing MOF possesses exceptionally high affinity to a number of commercially relevant gases. In particular, the H_2 and CH_4 adsorption enthalpies of PCN-9 are among the highest reported thus far. The biomimetic strategy presented here will be generally applicable in the search of new adsorptive materials to meet the requirements of on-board vehicular gas storage.

3.4 References

- (1) (a) G. Hoogers, editor, *Fuel Cell Technology Handbook*, CRC Press LLC, 2003. (b) L. Schlapbach, A. Züttel, *Nature* **2001**, *414*, 353. (c) “Hydrogen, Fuel Cells & Infrastructure Technologies Program: Multi-year Research, Development, and

- Demonstration Plan”, US Dept. of Energy, 2005, <http://www.eere.energy.gov/hydrogenandfuelcells/mypp/>.
- (2) (a) Rowsell, J. L. C.; Yaghi, O. M., *Angew. Chem. Int. Ed.* **2005**, *44*, 4670. (b) Wong-Foy, A. G.; Matzger, A. J.; Yaghi, O. M., *J. Am. Chem. Soc.* **2006**, *128*, 3494.
 - (3) Pan, L.; Sander, M. B.; Huang, X.; Li, J.; Smith, M. R., Jr.; Bittner, E. W.; Bockrath, B. C.; Johnson, J. K., *J. Am. Chem. Soc.* **2004**, *126*, 1308.
 - (4) (a) Chen, B. L.; Ockwig, N. W.; Millward, A. R.; Contreras, D. S.; Yaghi, O. M., *Angew. Chem. Int. Ed.* **2005**, *44*, 4745. (b) Sun, D.; Ma, S.; Ke, Y.; Collins, D. J.; Zhou, H.-C., *J. Am. Chem. Soc.* **2006**, *128*, 3896. (c) Yang, Q.; Zhong, C. *J. Phys. Chem.*, **2006**, *110*, 655.
 - (5) (a) Rosi, N. L.; Eckert, J.; Eddaoudi, M.; Vodak, D. T.; Kim, J.; O’Keeffe, M.; Yaghi, O. M., *Science* **2003**, *300*, 1127, (b) Rowsell, J. L. C.; Eckart, J. Yaghi, O. M., *J. Am. Chem. Soc.* **2005**, *127*, 14904.
 - (6) Lippard, S. J.; Berg, J. M., *Principles of Bioinorganic Chemistry*. University Science Books: Mill Valley, California, 1994.
 - (7) (a) Vallee, B. L.; Williams, R. J. P., *PNAS* **1968**, *59*, 498. (b) Darensbourg, M. Y.; Lyon, E. J.; Zhao, X.; Georgakaki, I. P., *PNAS* **2003**, *100*, 3683. (c) Williams, R. J. P., *Eur. J. Biochem.* **1995**, *234*, 363.
 - (8) (a) Kitaura, R.; Onoyama, G.; Sakamoto, H.; Matsuda, R.; Noro, S.; Kitagawa, S. *Angew. Chem. Int. Ed.* **2004**, *43*, 2684. (b) Chen, B.; Eddaoudi, M.; Reineke, T. M.; Kampf, J. W.; O’Keeffe, M.; Yaghi, O. M. *J. Am. Chem. Soc.* **2000**, *122*, 11559; (c) Kitagawa, S.; Noro, S.; Nakamura, T. *Chem. Commun.* **2006**, 701.
 - (9) Ke, Y.; Collins, D. J.; Sun, D.; Zhou, H.-C. *Inorg. Chem.* **2006**, *45*, 1897.
 - (10) Sun, D.; Ma, S.; Ke, Y.; Petersen, T. M.; Zhou, H. *Chem. Commun.* **2005**, 2663.
 - (11) X-ray crystal data for PCN-9: Co₄C₆₄H₃₂N₈O₁₇, fw = 1420.70, cubic, *Im-3m*, *a* = 25.4387(5) Å, *b* = 25.4387(5) Å, *c* = 25.4387(5) Å, *V* = 16462.1(6) Å³, *Z* = 6, *T* = 293 K, $\rho_{\text{calcd}} = 0.86 \text{ g/cm}^3$, $R_1 (I > 2\sigma(I)) = 0.103$, $wR_2 (\text{all data}) = 0.307$.
 - (12) Jaitner, P.; Ricker, C.; Wurst, K. *Chem. Commun.* **1997**, 1245.
 - (13) (a) Nair, V. S.; Hagen, K. S. *Inorg. Chem.* **1994**, *33*, 185. (b) Samuels, J. A.; Vaartstra B. A.; Huffman J. C.; Trojan, K. L.; Hatfield W. E.; Caulton, K. G. *J. Am. Chem. Soc.* **1990**, *122*, 9623. (c) Rambo, J. R.; Huffman, J. C.; Christou, G. *J. Am.*

- Chem. Soc.* **1989**, *111*, 8027. (d) Cotton, F. A.; Shang, M. *J. Am. Chem. Soc.* **1990**, *112*, 1584.
- (14) Spek, A. L. *PLATON, A Multipurpose Crystallographic Tool*; Utrecht University: Utrecht, The Netherlands, 2001.
- (15) Yang, R.T. *Gas adsorption by Adsorption Processes*; Butterworth: Boston, 1997.
- (16) Rouquerol, F.; Rouquerol, J.; Sing, K., *Adsorption by Powders and Solids: Principles, Methodology, and Applications*; Academic Press: London, 1999.
- (17) Sebastian, J.; Jasra, R. V. *Ind. Eng. Chem. Res.*, **2005**, *44*, 8014.
- (18) (a) Kaye, S. S.; Long, J. R. *J. Am. Chem. Soc.* **2005**, *127*, 6506. (b) Dinca, M.; Long, J. R., *J. Am. Chem. Soc.* **2005**, *127*, 9376. (c) Rowsell, J. L. C. and Yaghi, O. M., *J. Am. Chem. Soc.* **2006**, *128*, 1304.
- (19) (a) Düren, T.; Sarkisov, L.; Yaghi O. M.; Snurr, R. Q. *Langmuir*, **2004** *20*, 2683. (b) Bourrelly, S.; Llewellyn, P. L.; Serre, C.; Millange, F.; Loiseau, T.; Ferey, G. *J. Am. Chem. Soc.* **2005**; *127*, 13519.
- (20) Cotton, F. A. Wilkinson, G.; Murillo, C. A.; Bochmann, M. *Advanced Inorganic Chemistry*, 6th ed.; John & Wiley & Sons, Inc.: New York, 1999.
- (21) Elschenbroich, C., *Organometallics*, 3rd ed. in English; WILEY-VCH: Weinheim, Germany, 2005.

Chapter 4

Hydrogen Adsorption in Porous Metal-Organic Frameworks Based on an Anthracene Derivative^c

4.1 Introduction

Increasing research interest has recently been drawn to the exploration of porous metal-organic frameworks (MOFs)¹⁻¹⁷ as promising candidates to approach the US DOE targets for on-board hydrogen storage.¹⁸ Compared to other porous materials such as activated carbon, nanotubes, and zeolites,¹⁹⁻²³ porous MOFs possess the advantages of well-defined specific hydrogen binding sites²⁴⁻²⁸ and functionalizable pore walls¹² capable of increasing hydrogen interaction energies.

Recent inelastic neutron scattering (INS)²⁷ and neutron powder diffraction^{25,26} studies revealed inorganic metal clusters as the preferable hydrogen binding sites with successive binding sites located over the phenyl rings of the organic linkers. Although the primary hydrogen binding sites are metal-based, the functionalization of organic linkers plays an important role in further enhancing hydrogen adsorption.³⁰ Through theoretical calculations, Sagara *et al.* suggested that it is possible to bind two H₂ molecules on each side of the 2,6-naphthalenedicarboxylate linker in IRMOF-8 and proposed that additional aromatic rings in the frameworks could potentially serve as hydrogen adsorption sites and improve the hydrogen binding energy.³¹ Increasing the aromaticity of the organic linkers has been both theoretically^{31,32} predicted and experimentally proved^{30,33} to be an effective way to improve hydrogen adsorption capacity.

Taking those above into consideration, we designed a ligand, 5,5'-(9,10-anthracenediyl)di-isophthalate (H₄adip) (Figure 1a) and expect the central anthracene to serve as additional hydrogen binding sites thus increasing the hydrogen uptake. Under solvothermal conditions, reactions of H₄adip with Cu(NO₃)₂ and FeCl₂ gave rise to two porous MOFs designated as PCN-14 and PCN-15, respectively (PCN represents porous

^c This chapter was adapted from the finished manuscript "Hydrogen Adsorption in Porous Metal-Organic Frameworks Based on an Anthracene Derivative" to be submitted to *Chemistry, Eur. J.*

coordination network). In this chapter, their syntheses, structural descriptions and hydrogen adsorption properties will be discussed.

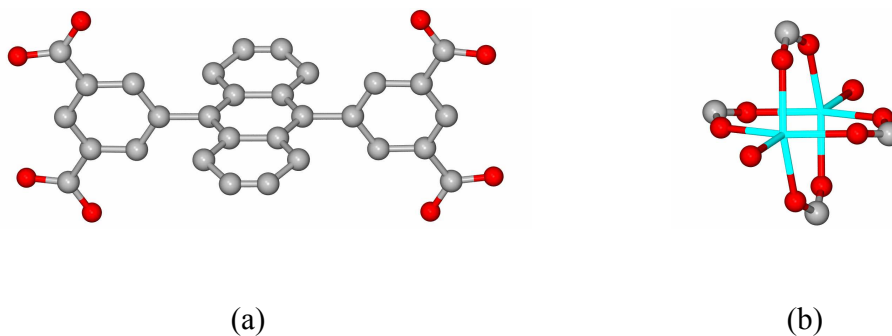


Figure 4.1 (a) H₄adip ligand; (b) M₂(COO)₄(H₂O)₂ (M = Cu, Fe) paddlewheel SBU.

Color scheme: C, grey; O, red; M, turquoise.

4.2 Experimental Details

Synthesis of PCN-14 and PCN-15: PCN-14 was prepared according to the procedures described in our previous work.³⁴ PCN-15 was synthesized by heating a sealed Pyrex tube with a mixture of H₄adip ligand (0.005 g, 1.4×10^{-5} mol) and FeCl₂ (0.02 g, 1.6×10^{-5} in 1.5 mL DMSO (dimethyl sulfoxide) at 120°C for 3 days followed by cooling to room temperature at a rate of 0.1 °C/min. The resulting orange block crystals were washed with DMSO in glove box under nitrogen atmosphere (yield: 75% based on **2**) and have a formula of Fe₆(H₂O)₆(adip)₃Cl·9DMSO·12H₂O, which was derived from crystallographic data and elemental analysis (calcd: C, 44.64; H, 4.58. Found: C, 44.55; H, 4.62.)

Single-crystal X-ray crystallography: Single crystal X-ray data of PCN-15 were collected on a Bruker Smart Apex diffractometer equipped with an Oxford Cryostream low temperature device and a fine-focus sealed-tube X-ray source (Mo-K_α radiation, $\lambda = 0.71073$ Å, graphite monochromated) operating at 45 kV and 35 mA. Frames were collected with 0.3° intervals in φ and ω for 60 s per frame such that a hemisphere of data was collected. Raw data collection and refinement were done using SMART. Data reduction was performed using SAINT+ and corrected for Lorentz and polarization effects.³⁵ The structure was solved by direct methods and refined by full-matrix least-squares on F^2 with anisotropic displacement using SHELX-97.³⁶ Non-hydrogen atoms

were refined with anisotropic displacement parameters during the final cycles. Hydrogen atoms on carbon were calculated in ideal positions with isotropic displacement parameters set to $1.2 \times U_{\text{eq}}$ of the attached atom. Absorption corrections were applied using SADABS after the formula of the compound is determined approximately.³⁵ Solvent molecules in the structure were highly disordered and were impossible to refine using conventional discrete-atom models. To resolve these issues, the contribution of solvent electron density was removed by the SQUEEZE routine in PLATON.³⁷ CCDC-682384 (PCN-15) contains the supplementary crystallographic data, which can be obtained free of charge at www.ccdc.cam.ac.uk/conts/retrieving.html (or from the Cambridge Crystallographic Data Center, 12, Union Road, Cambridge CB21EZ, UK; fax: (+44) 1223-336-033; or deposit@ccdc.cam.ac.uk).

Low-pressure Gas Sorption Measurements: The low-pressure nitrogen adsorption measurements were performed at 77 K and 0 - 760 torr on a Beckman Coulter SA 3100 surface area and pore size analyzer. An as-isolated sample of PCN-14 was immersed in methanol for 24 hours, and the extract was decanted. Fresh methanol was subsequently added, and the crystals were allowed to stay for an additional 24 hours to remove the non-volatile solvates (DMF and H₂O). The sample was collected by decanting and treated with dichloromethane similarly to remove methanol solvates. After the removal of dichloromethane by decanting, the sample was dried under a dynamic vacuum ($< 10^{-3}$ torr) at room temperature (25 °C) overnight. Before the measurement, the sample was dried again by using the “outgas” function of the surface area analyzer for 4 hour at 120 °C. High purity nitrogen (99.999%) was used for the measurement. A sample of 100 mg was used for N₂ (99.999%) adsorption measurement and was maintained at 77K with liquid nitrogen. In the hydrogen adsorption measurement, high purity hydrogen (99.9995%) was used. The regulator and pipe were flushed with hydrogen before connecting to the analyzer. The internal lines of the instrument were flushed three times by utilizing the “flushing lines” function of the program to ensure the purity of H₂. A sample of 100 mg was used for the measurement, and the temperature was also maintained at 77 K with liquid nitrogen.

High-pressure Hydrogen Sorption Measurements: High pressure hydrogen sorption isotherm measurements on PCN-14 were performed using a home-built fully

computer-controlled Sievert apparatus at NIST. The methane used for the high pressure measurements is scientific/research grade with the purity of 99.9995%. The detailed specification of the Sievert apparatus and the data analysis can be found in a recently published work.³⁸ Briefly, the Sievert system is equipped with four high-precision gauges (0.1%) and a closed-cycle cryostat, enabling methane-adsorption measurements over a wide pressure (0 - 50 bar) and temperature (77 - 87 K) range. In all measurements, about 200 mg solvent-exchanged sample was used, which was activated under vacuum (less than 10^{-4} torr) in two stages: first heating at room temperature overnight, and then at 120 °C for at least 4 h. Once activated, the samples were transferred to He-glove box and never exposed to air.

4.3 Results and Discussion

Crystal structure description: Single crystal X-ray analysis revealed that both PCN-14 and PCN-15 adopt the $M_2(\text{COO})_4(\text{H}_2\text{O})_2$ ($M = \text{Cu}, \text{Fe}$) paddlewheel as their secondary building unit (SBU) (Figure 1b), but with PCN-14 crystallizing in the space group $R-3c$, while PCN-15 crystallizes in the space group $R-3m$ (Table 1). The Cu-Cu distance is 2.654 Å, and the Cu-aqua distance is 2.122 Å for the paddlewheel SBU found in PCN-14, while the distance of Fe-Fe is 3.094 Å and that of the Fe-aqua is 2.288 Å for the paddlewheel SBU in PCN-15. The distances of Cu and oxygen of the carboxylate groups of the adip ligand ranges from 1.940 Å to 1.960 Å in PCN-14, while those of Fe and oxygen of the carboxylate groups of the adip ligand ranges from 2.049 Å to 2.059 Å in PCN-15.

The structure detail of PCN-14 was described in our previous work,³⁴ and it consists of nanoscopic cages with volume of 1150 Å³ for each cage (Figure 2a). In contrast, PCN-15 contains no cage, having only one-dimensional hexagonal channels along the (0 0 1) direction with a size of 13.636 Å (Figure 2b). Chlorine anions are observed residing throughout the center of the hexagonal channels indicating a mixture of +2 and +3 oxidation states for Fe in PCN-15 (Figure S1). Calculated using PLATON/SOLV,³⁷ the solvent accessible volume of PCN-14 is 63.5% and that of PCN-15 is 47.9%.

Table 4.1 Crystal data^[a] and structure refinement of PCN-14 and PCN-15.

	PCN-14	PCN-15
formula	C ₂₇₀ H ₁₆₂ Cu ₁₈ O ₉₀	C ₉₀ H ₅₄ ClFe ₆ O ₃₀
FW	5989.9	1985.88
crystal	Rhombohedral	Rhombohedral
space	<i>R</i> -3 <i>c</i>	<i>R</i> -3 <i>m</i>
<i>a</i> , Å	18.4530(4)	27.1117(9)
<i>b</i> , Å	18.4530(4)	27.1117(9)
<i>c</i> , Å	76.976(4)	16.5413(1)
α, deg	90.00	90.00
β, deg	90.00	90.00
γ, deg	120.00	120.00
<i>V</i> , Å ³	22699.7 (1)	10529.6 (1)
<i>Z</i>	2	3
<i>d</i> _{cacl.} g	0.871	0.940
GOF	1.071	1.636
<i>R</i> ₁ , <i>wR</i> ₂ ^[b]	0.0518, 0.1591	0.1088, 0.3462

[a] Obtained with graphite-monochromated *Mo Kα* ($\lambda = 0.71073$ Å) radiation ,

[b] $R_1 = \sum ||F_o| - |F_c|| / \sum |F_o|$ and $wR_2 = \{[\sum w(F_o^2 - F_c^2)^2] / [\sum w(F_o^2)^2]\}^{1/2}$

Although PCN-14 and PCN-15 are constructed from the same ligand and the same SBU, their structures are quite different and they crystallize in different space groups. Those differences can be attributed to different dihedral angles between the anthracene and the phenyl rings of the adip ligand in PCN-14 and PCN-15. In PCN-14, the dihedral angle is 70.4° (Figure S2a) which facilitates the enclosure of cages resulting from reduced repulsion from the anthracene rings as well as lowers the crystal symmetry to *R*-3*c*. This is different from those previously reported MOFs which are also based on tetracarboxylate ligands and dicopper paddlewheel SBUs, which all crystallize in *R*-3*m*.^{10,39,40} However, in PCN-15, the dihedral angle is near 90° (88.7°) (Figure S2b) and it renders the adip ligand with mirror plane symmetry thus leading to the crystal symmetry of *R*-3*m* the same as the previous reported MOFs with ideal NbO type structure. The near 90° dihedral angle between the anthracene and the phenyl rings of the adip ligand results in large repulsions between the anthracene rings of adjacent adip ligands thus forcing the formation of only one-dimensional channels instead of cages in PCN-15.

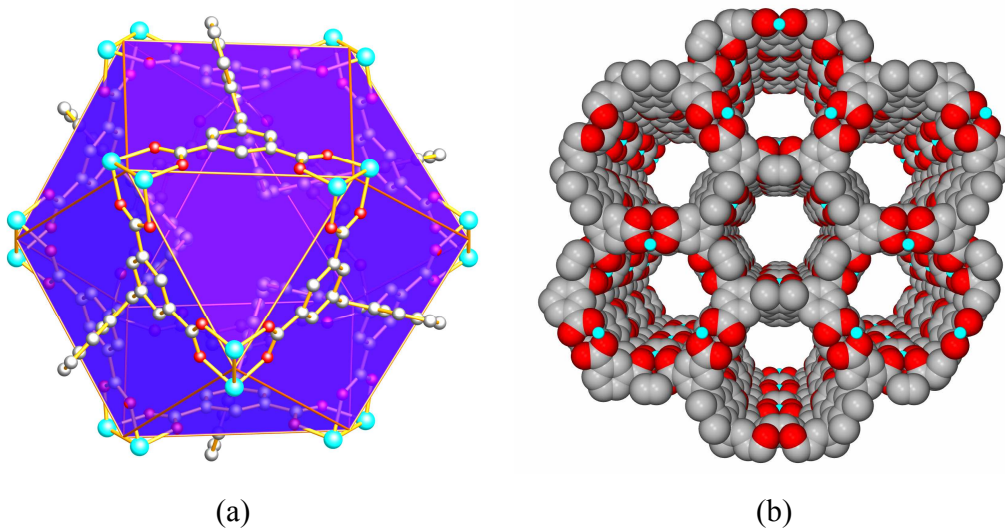


Figure 4.2 (a) nanoscopic cage in PCN-14; (b) one-dimensional hexagonal channels of PCN-15 viewing from (0 0 1) direction.

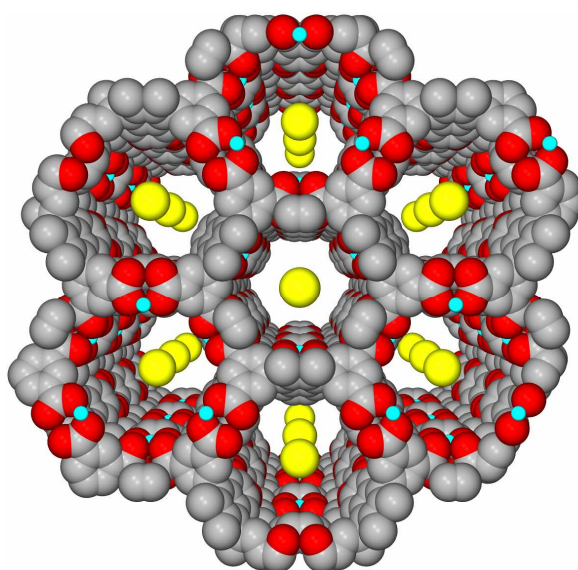


Figure 4.3 Chlorine anions residing in the one-dimensional hexagonal channels of PCN-15 viewing from (0 0 1) direction.

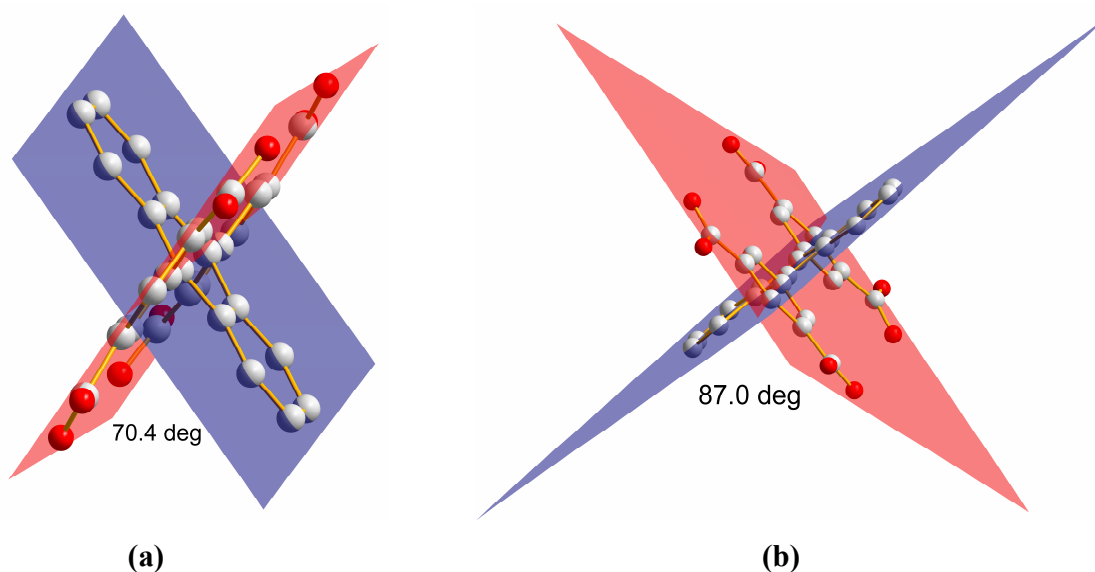


Figure 4.4 Dihedral angles between the anthracene plane and the phenyl ring plane of the adip ligand: (a) in PCN-14; (b) in PCN-15.

N₂ sorption analysis: N₂ sorption isotherms at 77 K were measured to check the permanent porosities and surface areas of PCN-14 and PCN-15. Before the sorption measurements, a sample of PCN-14 was fully activated by the procedure described before while a sample of PCN-15 was activated by solvent-exchanging the freshly prepared sample with THF in a glove box followed by evacuation under dynamic vacuum at 50 °C overnight. As shown in Figure 3, PCN-14 exhibits typical Type-I sorption behavior without any hysteresis confirming its permanent porosity. Calculated from the N₂ adsorption data, the estimated BET surface area of PCN-14 is 1753 m²/g. Unfortunately, N₂ sorption isotherms of the PCN-15 sample activated at 50 °C or even 150 °C revealed that it could adsorb very limited amount of N₂ (Figure S3), indicating the framework collapse after solvent exchange.

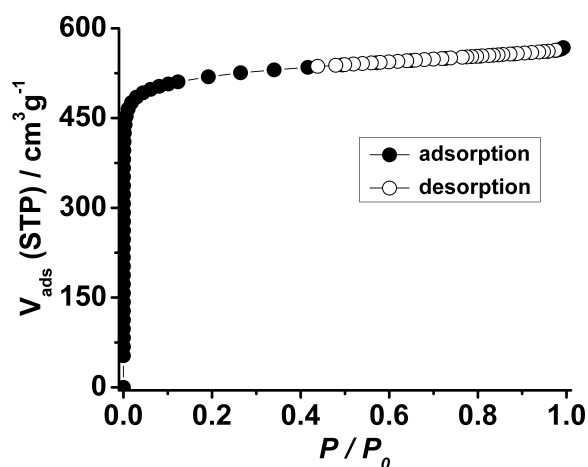


Figure 4.5 N₂ sorption isotherms of PCN-14 at 77 K.

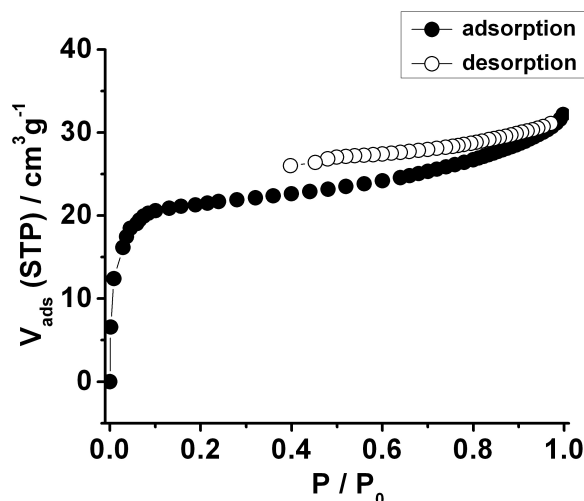


Figure 4.6 N₂ sorption isotherms of PCN-15 at 77 K.

Hydrogen sorption studies: The highly porosity of PCN-14 in addition to its nanoscopic cages, which are suitable for gas storage, prompted us to evaluate its hydrogen adsorption performances. Low-pressure hydrogen sorption isotherms of the fully activated PCN-14 sample at 77 K revealed reversible hydrogen adsorption in PCN-14, as shown Figure 4.7. At 77 K and 760 Torr, the gravimetric hydrogen uptake capacity of PCN-14 can reach 2.70 wt%, which is among the highest of reported MOFs under similar conditions.^{10,30,39-41}

Noticing that the hydrogen uptake of PCN-14 is not saturated even at 800 Torr, we decided to investigate its hydrogen sorption behaviors under high pressure. As shown in Figure 4, the excess gravimetric hydrogen uptake of PCN-14 reaches saturation at 50 bar with a value of 4.42 wt%, corresponding to a volumetric value of 36.6 g/L calculated using the crystal density of dehydrated PCN-14 (0.829 g/cm^3).

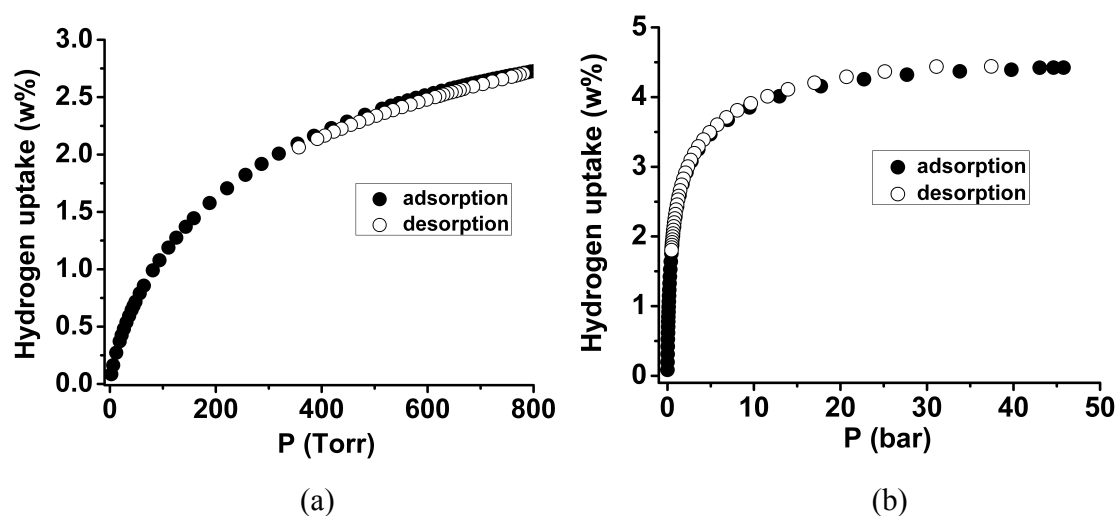
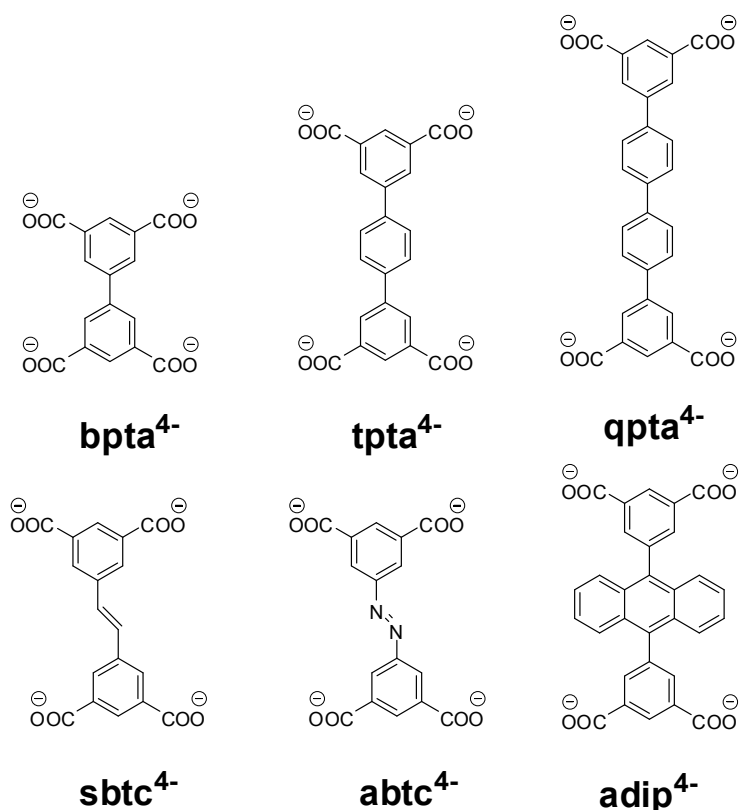


Figure 4.7 (a) Low-pressure H₂ sorption isotherms of PCN-14 at 77 K; (b) High-pressure H₂ sorption isotherms of PCN-14 at 77 K.

The impressive hydrogen adsorption performances of PCN-14 necessitate its comparison with other reported NbO typed porous MOFs constructed from tetracarboxylate ligands (Scheme 1) and dicopper paddlewheel SBU to figure out how ligand functionalization affects hydrogen uptake capacities of them. For hydrogen adsorption at 77 K, 760 Torr, it can be seen from Table 2 that increasing the aromaticity by elongating the bpta ligand with one or two phenyl rings leads to a steady decrease of hydrogen uptake in Cu-tpta and Cu-qpta.¹⁰ This can be attributed to the reduced energy well overlaps resulting from the enlarged pore sizes.^{30,42} Our previous attempts to enhance hydrogen uptake by grafting double-bond functionalities in PCN-10 and PCN-11 resulted in the same relationship according to size, indicating negligible contribution from unsaturated π -bonds.⁴⁰ However, expanding the aromatic conjugation by adding two

fused rings greatly favors the hydrogen adsorption in PCN-14, which exhibits the highest hydrogen uptake of 2.7 wt% among the six NbO typed porous MOFs. This is also consistent with recent theoretical calculations that an increase in the number of fused rings would boost hydrogen uptake in porous MOFs.^{31,32}



Scheme 4.1 Tetracarboxylate ligands employed for the construction of NbO type MOFs: bpta = biphenyl-3,3',5,5'-tetracarboxylate; tpta = terphenyl-3,3',5,5'-tetracarboxylate; qpta = quaterphenyl-3,3',5,5'-tetracarboxylate; sbtc = *trans*-stilbene-3,3',5,5'-tetracarboxylate; abtc = azobenzene-3,3',5,5'-tetracarboxylate; adip = 5,5'-(9,10-anthracenediyl)diisophthalate.

Nevertheless, the high pressure hydrogen uptakes scale up with surface areas as observed in other types of porous MOFs.⁵ The extension of the bpta ligand by adding phenyl rings or double bonds leads to an increase in surface areas with almost proportional augments of hydrogen adsorption capacities at saturation particularly for C-tpta and Cu-qpta. The relatively low surface area of PCN-14 can be ascribed to the

bulkiness of the anthracene rings which block partial pores thus resulting in only moderate hydrogen uptake of 4.42 wt% at saturation.

It has been theoretically calculated that fused aromatic rings can potentially serve as hydrogen adsorption sites and improve the hydrogen binding energy.^{31,32} The strength of interactions between the framework and hydrogen can be reflected by isosteric heats of adsorption Q_{st} . The isosteric heats of adsorption of hydrogen for PCN-14 were calculated utilizing the Clausius-Clapeyron equation,⁴³

$$Q_{st} = -R \cdot d(\ln P) / d(1/T)$$

using isotherms measured at 77, 80, and 87 K (Figure 4.8). As shown in Figure 4.9, the Q_{st} of PCN-14 is 8.6 kJ/mol at low coverage, which is higher than those of PCN-10 (6.9 kJ/mol), PCN-11 (7.0 kJ/mol),⁴⁰ and Cu-BTC (6.8 kJ/mol).³⁰ The relatively high Q_{st} of PCN-14 compared to porous MOFs based on dicopper paddlewheel SBU can be presumably attributed to the increased aromaticity of the anthracene rings when considering similar contribution from coordinatively unsaturated copper sites. This also supports the theoretical predictions that adding more fused aromatic rings to the ligand can lead to higher affinity of hydrogen.^{31,32}

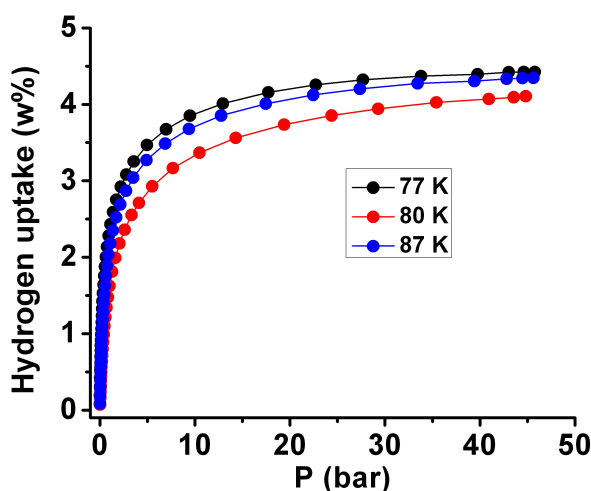


Figure 4.8 H₂ adsorption isotherms of PCN-14 at 77, 80, and 87 K.

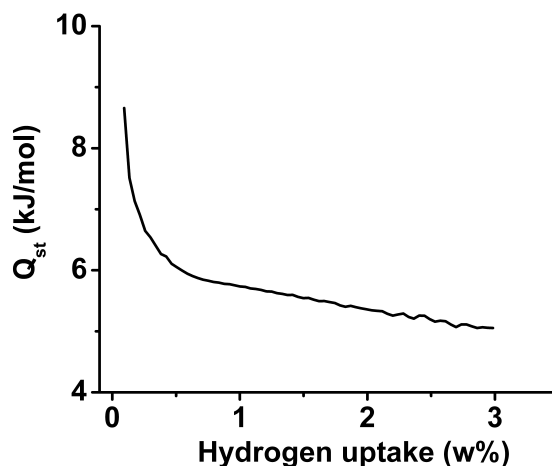


Figure 4.9 Isosteric heats of adsorption of H₂ for PCN-14.

In summary, two porous MOFs, PCN-14 and PCN-15 based on an anthracene derivative tetracarboxylate ligand and dimetal paddlewheel SBUs have been constructed and structurally described. Despite being built from the same ligand and the same type of SBUs, PCN-14 consists of nanoscopic cages while PCN-15 only contains one-dimensional channels along (0 0 1) direction. Their structural differences can be attributed to different dihedral angles between the anthracene and the phenyl rings of the adip ligands. N₂ sorption analysis revealed that PCN-14 retains its permanent porosity and has a BET surface area of 1753 m²/g, while PCN-15 can hardly maintain its structure integrity after activation. H₂ sorption studies indicated that the aromaticity of anthracene grants PCN-14 high hydrogen uptake capacities of 2.70 wt% at 77 K, 760 Torr, and 4.42 wt% at 77 K, 50 bar. The contribution from the aromaticity of the anthracene rings to framework-hydrogen interaction was reflected by the high heats of adsorption of 8.6 kJ/mol at low coverage, supporting the theoretical predictions that functionalizing the ligand with more fused aromatic rings favors hydrogen uptake in porous MOFs.

Table 4.2 Physical characteristics and hydrogen adsorption properties of NbO typed porous MOFs based on tetracarboxylate ligands and dicopper paddlewheel SBU.

	BET surface area (m ² /g)	Solvent accessible volume ^[a] (%)	Calculated crystal density (g/cm ³)	H ₂ uptake at 77 K, 760 Torr (wt%)	Gravimetric H ₂ saturation uptake at 77 K (wt%)	Volumetric H ₂ saturation uptake at 77 K (g/L)
PCN-14 (adip)	1753	63.5	0.829	2.70	4.42	36.6
MOF-505 (bpta) ¹⁰	1670	63.3	0.927	2.59	4.20	38.9
Cu-tpta ¹⁰	2247	70.4	0.886	2.52	6.70	43.6
Cu-qpta ¹⁰	2932	75.5	0.587	2.24	7.01	41.1
PCN-10 (abtc) ⁴⁰	1407	71.2	0.825	2.34	4.20	34.7
PCN-11 (sbtc) ⁴⁰	1779	71.9	0.805	2.55	5.04	40.6

[a] Calculated using PLA TON/SOLV.³⁵

4.4 References

- (1) Ma, S.; Sun, D.; Ambrogio, M. W.; Fillinger, J. A.; Parkin, S.; Zhou, H.-C., *J. Am. Chem. Soc.* **2007**, *129*, 1858.
- (2) Isaeva, V. I.; Kustov, L. M., *Russ. J. Gen. Chem.* **2007**, *77*, 721.
- (3) Hirscher, M.; Panella, B., *Scr. Mater.* **2007**, *56*, 809.
- (4) Furukawa, H.; Miller, M. A.; Yaghi, O. M., *J. Mater. Chem.* **2007**, *17*, 3197.
- (5) Collins, D. J.; Zhou, H.-C., *J. Mater. Chem.* **2007**, *17*, 3154.
- (6) Wong-Foy, A. G.; Matzger, A. J.; Yaghi, O. M., *J. Am. Chem. Soc.* **2006**, *128*, 3494.
- (7) Sun, D.; Ma, S.; Ke, Y.; Collins, D. J.; Zhou, H.-C., *J. Am. Chem. Soc.* **2006**, *128*, 3896.
- (8) Panella, B.; Hirscher, M.; Pütter, H.; Müller, U., *Adv. Funct. Mater.* **2006**, *16*, 520.
- (9) Ma, S.; Zhou, H.-C., *J. Am. Chem. Soc.* **2006**, *128*, 11734.
- (10) Lin, X.; Jia, J.; Zhao, X.; Thomas, K. M.; Blake, A. J.; Walker, G. S.; Champness, N. R.; Hubberstey, P.; Schröder, M., *Angew. Chem. Int. Ed.* **2006**, *45*, 7358.
- (11) Latroche, M.; Surblé, S.; Serre, C.; Mellot-Draznieks, C.; Llewellyn, P. L.; Lee, J.-H.; Chang, J.-S.; Jung, S. H.; Férey, G., *Angew. Chem. Int. Ed.* **2006**, *45*, 8227.
- (12) Forster, P. M.; Eckert, J.; Heiken, B. D.; Parise, J. B.; Yoon, J. W.; Jung, S. H.; Chang, J. S.; Cheetham, A. K., *J. Am. Chem. Soc.* **2006**, *128*, 16846.
- (13) Dincă, M.; Dailly, A.; Liu, Y.; Brown, C. M.; Neumann, D. A.; Long, J. R., *J. Am. Chem. Soc.* **2006**, *128*, 16876.
- (14) Chen, B.; Ma, S.; Zapata, F.; Lobkovsky, E. B.; Yang, J., *Inorg. Chem.* **2006**, *45*, 5718.
- (15) Kesanli, B.; Cui, Y.; Smith, M. R.; Bittner, E. W.; Bockrath, B. C.; Lin, W., *Angew. Chem. Int. Ed.* **2005**, *44*, 72.
- (16) Chen, B.; Ockwig, N. W.; Fronczek, F. R.; Contreras, D. S.; Yaghi, O. M., *Inorg. Chem.* **2005**, *44*, 181.
- (17) Pan, L.; Sander, M. B.; Huang, X.; Li, J.; Smith, M.; Bittner, E.; Bockrath, B.; Johnson, J. K., *J. Am. Chem. Soc.* **2004**, *126*, 1308.

- (18) DOE Office of Energy Efficiency and Renewable Energy Hydrogen, Fuel Cells & Infrastructure Technologies Program Multi-Year Research, Development and Demonstration Plan, available at: <http://www.eere.energy.gov/hydrogenandfuelcells/mypp>. . In.
- (19) Züttel, A.; Wenger, P.; Sudan, P.; Mauron, P.; Orimo, S.-i., *Mater. Sci. Eng., B* **2004**, *108*, 9.
- (20) Jung, J. H.; Han, W. S.; Rim, J. A.; Lee, S. J.; Cho, S. J.; Kim, S. Y.; Kang, J. K.; Shinkai, S., *Chem. Lett.* **2006**, *35*, 32.
- (21) Weck, P. F.; Kim, E.; Balakrishnan, N.; Cheng, H.; Yakobson, B. I., *Chem. Phys. Lett.* **2007**, *439*, 354.
- (22) Thomas, K. M., *Catal. Today* **2007**, *120*, 389.
- (23) Lachance, P.; Bénard, P., *Int. J. Green Energy* **2007**, *4*, 377.
- (24) Spencer, E. C.; Howard, J. A. K.; McIntyre, G. J.; Rowsell, J. L. C.; Yaghi, O. M., *Chem. Comm.* **2006**, 278.
- (25) Peterson, V. K.; Liu, Y.; Brown, C. M.; Kepert, C. J., *J. Am. Chem. Soc.* **2006**, *128*, 15578.
- (26) Yildirim, T.; Hartman, M. R., *Phys. Rev. Lett.* **2005**, *95*, 215504.
- (27) Rowsell, J. L. C.; Eckert, J.; Yaghi, O. M., *J. Am. Chem. Soc.* **2005**, *127*, 14904.
- (28) Rowsell, J. L. C.; Spencer, E. C.; Eckert, J.; Howard, J. A. K.; Yaghi, O. M., *Science* **2005**, *309*, 1350.
- (29) Eddaoudi, M.; Kim, J.; Rosi, N.; Vodak, D.; Wachter, J.; O'Keeffe, M.; Yaghi, O. M., *Science* **2002**, *295*, 469.
- (30) Rowsell, J. L. C.; Yaghi, O. M., *J. Am. Chem. Soc.* **2006**, *128*, 1304.
- (31) Sagara, T.; Klassen, J.; Ortony, J.; Ganz, E., *J. Chem. Phys.* **2005**, *123*, 014701.
- (32) Han, S. S.; Deng, W.-Q.; Goddard, W. A., *Angew. Chem. Int. Ed.* **2007**, *46*, 6289.
- (33) Rowsell, J. L. C.; Millward, A. R.; Park, K. S.; Yaghi, O. M., *J. Am. Chem. Soc.* **2004**, *126*, 5666.
- (34) Ma, S.; Sun, D.; Simmons, J. M.; Collier, C. D.; Yuan, D.; Zhou, H.-C., *J. Am. Chem. Soc.* **2008**, *130*, 1012.
- (35) SAINT+, version 6.22; Bruker Analytical X-Ray Systems, Inc.: Madison, WI, 2001.

- (36) Sheldrick, G. M. SHELX-97; Bruker Analytical X-Ray Systems, Inc.: Madison, WI, 1997.
- (37) Spek, A. L., *J. Appl. Crystallogr.* **2003**, *36*, 7.
- (38) Zhou, W.; Wu, H.; Hartman, M. R.; Yildirim, T., *J. Phys. Chem. C* **2007**, *111*, 16131.
- (39) Chen, B.; Ockwig, N. W.; Millward, A. R.; Contreras, D. S.; Yaghi, O. M., *Angew. Chem., Int. Ed.* **2005**, *44*, 4745.
- (40) Wang, X.-S.; Ma, S.; Rauch, K.; Simmons, J. M.; Yuan, D.; Wang, X.; Yildirim, T.; Cole, W. C.; López, J. J.; De Meijere, A.; Zhou, H.-C., *Chem. Mater.* **2008**, in press.
- (41) Wang, X.-S.; Ma, S.; Forster, P. M.; Yuan, D.; Yoon, J. W.; Hwang, Y. K.; Chang, J.-S.; Eckert, J.; Murphy, B. J.; Parise, J. B.; Zhou, H.-C., **2007**, submitted to JACS.
- (42) Rowsell, J. L. C.; Yaghi, O. M., *Angew. Chem., Int. Ed.* **2005**, *44*, 4670.
- (43) Rouquerol, J.; Rouquerol, F.; Sing, K., *Adsorption By Powders and Porous Solids*. Academic Press: London, 1998.

Chapter 5

Framework-Catenation Isomerism in Metal-Organic Frameworks and Its Impact on Hydrogen Uptake^d

5.1 Introduction

Recent studies have focused on metal-organic frameworks (MOFs) with high hydrogen uptake¹ in order to reach the 2010 DOE targets for on-board vehicular hydrogen storage.² Strategies such as using pore sizes comparable to hydrogen molecules³ and introducing coordinatively unsaturated metal centers (UMCs) have been explored.^{3b, c, 4} Recently, we have reported a biomimetic approach to UMCs utilizing entatic metal centers (EMCs).⁵ We have also demonstrated in both PCN-6^{3c} (porous coordination networks) and PCN-9⁵ that interpenetration is an important factor contributing to their respective hydrogen uptake. However, interpenetration (or framework catenation) as an *independent* criterion has never been resolved from other factors. Normally in a given metal-ligand combination, *either* an interpenetrated network *or* a non-interpenetrated network is favored, not both. Conceptually, an interpenetrated MOF and its non-interpenetrated counterpart can be viewed as a supramolecular pair of stereoisomers. In reality, however, such *framework-catenation isomerism* has never been deliberately explored prior to the work in this chapter. To study the precise role of catenation in hydrogen uptake, using oxalate as a template, the non-interpenetrated counterpart of PCN-6 (PCN-6') have been successfully made here.

5.2 Experimental Details

Synthesis of PCN-6': A mixture of H₃TATB ligand (0.01 g, 2.26×10^{-5} mol), Cu(NO₃)₂·2.5H₂O (0.025 g, 1.07×10^{-4} mol) and oxalic acid (2mg,) in 1.5 mL dimethylacetamide (DMA) was sealed in a Pyrex glass tube (8mm/10 mm) and heated to 75 °C (1 °C / min). After 48 hours at 75 °C, the glass tube was cooled to 35 °C (0.1°C / min). The resultant octahedral turquoise crystals were washed with DMA twice to give

^d This chapter was reprinted with permission from: Ma, S.; Ambrogio, M.; Fillinger, J. A.; Parkin, S.; Zhou, H.-C. *J. Am. Chem. Soc.* **2007**, *129*, 1858-1859. Copyright 2007, American Chemical Society.

pure PCN-6' ($\text{Cu}_6(\text{H}_2\text{O})_6(\text{TATB})_4\cdot\text{DMA}\cdot 12\text{H}_2\text{O}$). Elemental analysis for PCN-6' calculated: C 47.22%, H 3.69%, N 7.16%; found: C 47.39%, H 3.61%, N 6.94%. Replacement of DMA by DMF (dimethylformamide) or DEF (diethylformamide), Also gave PCN-6' under similar reaction conditions.

Synthesis of PCN-6: PCN-6 was originally synthesized using the method described in ref. 10b. It can also be obtained by the following method: a mixture of H_3TATB (0.01 g, 2.26×10^{-5} mol) and $\text{Cu}(\text{NO}_3)_2\cdot 2.5\text{H}_2\text{O}$ (0.025 g, 1.07×10^{-4} mol) in 1.5 mL DMA (or DMF, or DEF) was sealed in a Pyrex glass tube (8mm/10 mm) and heated to 75 °C (1 °C / min), kept at that temperature for 48 hours, and cooled to room temperature at a constant rate of 0.1°C/min.

Synthesis of MOF-HTB': A mixture of HTB ligand (0.01 g, 2.26×10^{-5} mol), $\text{Cu}(\text{NO}_3)_2\cdot 2.5\text{H}_2\text{O}$ (0.025 g, 1.07×10^{-4} mol) and oxalic acid (2mg,) in 1.5 mL dimethylacetamide (DMA) was sealed in a Pyrex glass tube (8mm/10 mm) and heated to 75 °C (1 °C / min). After 48 hours at 75 °C, the glass tube was cooled to 35 °C (0.1°C / min). The resultant octahedral yellow green crystals were washed with DMA twice to give pure **MOF-HTB'** ($\text{Cu}_3(\text{H}_2\text{O})_3(\text{HTB})_2\cdot\text{DMA}\cdot 2\text{H}_2\text{O}$). Elemental analysis for PCN-7 calculated: C 48.76%, H 3.03%, N 14.7%; found: C 47.99%, H 3.02%, N 14.38%. Replacement of DMA with DMF (dimethylformamide) or DEF (diethylformamide), also gave **MOF-HTB'** under similar reaction conditions.

Synthesis of MOF-HTB: A mixture of HTB ligand (0.01 g, 2.26×10^{-5} mol), $\text{Cu}(\text{NO}_3)_2\cdot 2.5\text{H}_2\text{O}$ (0.025 g, 1.07×10^{-4} mol) in 1.5 mL dimethylacetamide (DMA) was sealed in a Pyrex glass tube (8mm/10 mm) and heated to 75 °C (1 °C / min). After 48 hours at 75 °C, the glass tube was cooled to 35 °C (0.1°C / min). The resultant block-shaped yellow green crystals were washed with DMA twice to give pure compound **MOF-HTB** ($\text{Cu}_3(\text{H}_2\text{O})_3(\text{HTB})_2\cdot 2\text{DMA}\cdot 6\text{H}_2\text{O}$). Elemental analysis for PCN-8 calculated: C 46.9%, H 3.81%, N 14.11%; found: C 45.84%, H 3.72%, N 13.78%. Replacement of DMA with DMF (dimethylformamide) or DEF (diethylformamide), also gave **MOF-HTB** under similar reaction conditions. PCN-8 can be synthesized by placing 1.5 mL dimethylsulfoxide (DMSO) solution of HTB ligand (0.01 g, 2.26×10^{-5} mol) and $\text{Cu}(\text{NO}_3)_2\cdot 2.5\text{H}_2\text{O}$ (0.025 g, 1.07×10^{-4} mol) in a sealed Pyrex glass tube (8mm/10 mm) at 120 °C for 20 hours.

X-ray Structure determinations: Single crystal X-ray determination of PCN-6 was performed on a Bruker Smart Apex diffractometer using Mo-K α radiation ($\lambda = 0.71073 \text{ \AA}$). The structures of PCN-6', MOF-HTB and MOF-HTB' were determined using a specially configured diffractometer based on the Bruker-Nonius X8 Proteum using focused Cu-K α radiation ($\lambda = 1.54178 \text{ \AA}$). Raw data for all structures were processed using SAINT and absorption corrections were applied using SADABS. The structures were solved by direct method and refined by full-matrix least-squares on F^2 with anisotropic displacement parameters for non-H atoms using SHELX-97. The hydrogen atoms on the carbon were placed in calculated position with isotropic displacement parameters set to $1.2 \times U_{eq}$ of the attached atom. Solvent molecules in the structure were highly disordered and were impossible to refine using conventional discrete-atom models. To resolve these issues, the contribution of solvent electron density were removed by the SQUEEZE routine in PLATON.

Gas Adsorption Measurements: Gas sorption measurements were measured with a Beckman Coulter SA 3100 surface area and pore size analyzer. The samples of PCN-6' and PCN-6 were soaked with methanol for 24 hours, and the extract was discarded. Fresh methanol was subsequently added, and the crystals were allowed to soak for another 24 hours to remove DMA and H₂O solvates. The sample was then treated with dichloromethane in a similar manner to remove methanol solvates. After the removal of dichloromethane by decanting, the sample was dried under dynamic vacuum ($< 10^{-3}$ torr) at room temperature (25 °C) overnight. Before the measurement, the sample was dried again by using the "outgas" function of the surface area analyzer for 2 hour at 150 °C. A sample of 100.0 mg was used for N₂ adsorption measurements, and was maintained at 77K with liquid nitrogen. In the hydrogen storage measurement, high purity hydrogen (99.9995%) and an 80.0 mg sample were used. The regulator and pipe were flushed with hydrogen before connecting to the analyzer. The internal lines of the instrument were flushed three times by utilizing the "flushing lines" function of the program to ensure the purity of H₂. The temperature was maintained at 77 K with liquid nitrogen throughout all measurements.

Table 5.1 Crystal data^a for PCN-6, PCN-6', MOF-HTB and MOF-HTB'.

	PCN-6'	PCN-6	MOF-HTB'	MOF-HTB
chemical formula	C ₃₂ H ₁₆ Cu ₂ N ₄ O ₁₀	C ₄₈ H ₃₀ Cu ₃ N ₆ O ₁₅	C ₉ H ₄ Cu _{0.5} N _{2.33} O _{2.5}	C ₁₀₈ H ₄₈ Cu ₆ N ₂₈ O ₃₀
fw, g mol ⁻¹	743.59	1121.4	216.58	866.33
space group	<i>Fm-3m</i>	<i>R-3m</i>	<i>Fm-3m</i>	<i>R-3m</i>
<i>T</i> , K	250(2)	293(2)	295(2)	258(2)
<i>a</i> , Å	46.636(5)	32.9680(1)	52.993(6)	37.291(2)
<i>b</i> , Å	46.636(5)	32.9680(1)	52.993(6)	37.291(2)
<i>c</i> , Å	46.636(5)	80.783(5)	52.993(6)	92.159(3)
α , deg	90	90	90	90
β , deg	90	90	90	90
γ , deg	90	120	90	120
<i>V</i> , Å ³	101432(20)	76039(6)	148815(30)	110988(9)
<i>Z</i>	24	24	96	12
ρ_{calc} , g cm ⁻³	0.292	0.588	0.232	0.467
μ , mm ⁻¹	0.415	0.528	0.304	0.611
<i>R</i> ₁ ^b , <i>wR</i> ₂ ^c , %	6.5, 16.05	5.3, 14.15	4.17, 9.71	10.8, 32.72
GOF (<i>F</i> ²)	1.153	0.877	0.951	1.637

^a Obtained with graphite-monochromated Mo K α ($\lambda = 0.71073$ Å) radiation.

^b $R_1 = \Sigma||F_o| - |F_c|| / \Sigma|F_o|$.

^c $wR_2 = \{\Sigma[w(F_o^2 - F_c^2)^2] / \Sigma[w(F_o^2)^2]\}^{1/2}$; $w = 1 / [\sigma^2(F_o^2) + (aP)^2 + bP]$, $P = [\max(F_o^2 \text{ or } 0) + 2(F_c^2)] / 3$

5.3 Results and Discussion

Single-crystal X-ray⁶ diffraction studies reveal that PCN-6' crystallizes in cubic space group $Fm-3m$. It is isostructural with HKUST-1,⁷ mesoMOF-1,⁸ and with a single net of the interpenetrated PCN-6.^{3c} In PCN-6', dicopper tetracarboxylate paddlewheel SBUs (secondary building units) are linked by TATB bridges. Each SBU connects four TATB ligands, and each TATB binds three SBUs to form a Td -octahedron (Figure 5.1b), which has idealized Td symmetry with four ligands covering alternating triangular faces of the octahedron and an SBU occupying each vertex. Eight such Td -octahedra occupy the eight vertices of a cube to form a cuboctahedron through corner sharing with idealized Oh symmetry (Figure 5.1a).^{3c} The average diameter of the void inside the cuboctahedron is 30.32 Å. Every cuboctahedron connects eight Td -octahedra via face-sharing, and each Td -octahedron links four cuboctahedra to form a three-dimensional framework with a twisted boracite net topology (Figure 5.1c). Open square channels from all three orthogonal directions are identical in size and are 15.16×15.16 Å or 21.44×21.44 Å along the edges or diagonals respectively (atom to atom distance). Alternatively the structure can be described as four honeycomb nets connected by the SBUs at the center of the hexagonal-edges; the TATB ligands occupy the corners of each hexagon and each hexagon is in a chair conformation (Figure 5.1d).

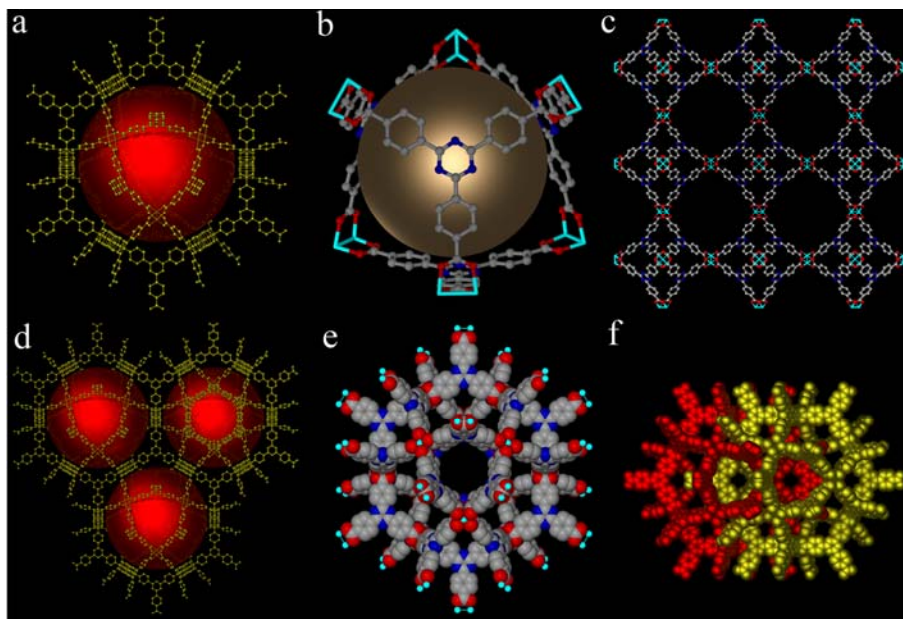


Figure 5.1 Structures of PCN-6 and PCN-6': (a) Cuboctahedral cage; (b) T_d -octahedral cage; (c) A view of the packing of PCN-6' from the [001] direction; (d) A view of the cuboctahedral net from the [111] direction of PCN-6'; (e) Space-filling model of the non-interpenetrated net in PCN-6'; (f) Two interpenetrated nets in PCN-6. The large spheres shown in a, b, and d represent void inside the cages.

The structure of PCN-6 (space group $R\bar{3}m$) can be reproduced by two identical interpenetrated nets of PCN-6', the second being generated by translation of the first by $c/5$ (c represents the c axis in PCN-6) along [1 1 1] direction of PCN-6'. PCN-6' and PCN-6 are thus catenation isomers (Figure 5.1e,f). To the best of our knowledge, this is among the first pair of such catenation isomers.^{3b}

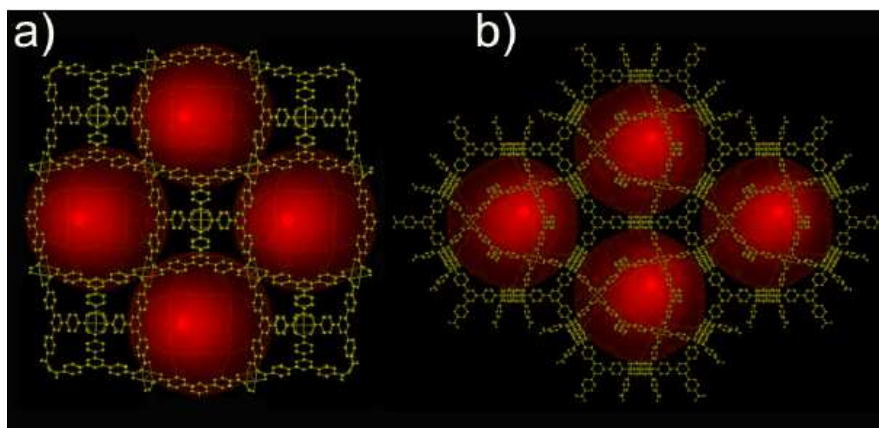


Figure 5.2 Nanocages in PCN-6: (a) A cuboctahedral net built from T_d -octahedral cages through corner-sharing. The view is from the [001] direction of PCN-6'; (b) A view of the cuboctahedral net from the [111] direction of PCN-6'. The chair conformation of three of the four honeycomb-nets can also be seen.

Variables in the synthetic procedures of PCN-6 and PCN-6' include temperature, solvent, and template addition. Controlled experiments were performed to confirm that template addition is the only factor determining the final topology. Without the addition of oxalic acid, the reaction between $\text{Cu}(\text{NO}_3)_2 \cdot 2.5\text{H}_2\text{O}$ and H_3TATB in DMA, dimethylformamide (DMF), or diethylformamide (DEF) at 75 °C or 120 °C (with DMSO as solvent) led to the formation of PCN-6. In contrast, with oxalic-acid addition the

same reaction in DMA, DMF, or DEF at 75 °C or 120°C (DMSO) gives PCN-6'. Thus, only template addition can account for the presence or absence of catenation.

To test the general pertinence of this finding, another large trigonal-planar ligand HTB (for *s*-heptazine tribenzoate)⁹ was employed to react with Cu(NO₃)₂·2.5H₂O under reaction conditions similar to those of PCN-6 and PCN-6'. As expected, an interpenetrated MOF isostructural with PCN-6 (MOF-HTB) was obtained without the addition of oxalic acid, while a non-interpenetrated MOF isostructural with PCN-6' (MOF-HTB') was formed in the presence of oxalic acid. The mechanistic details of this remarkable templating effect are still under investigation.

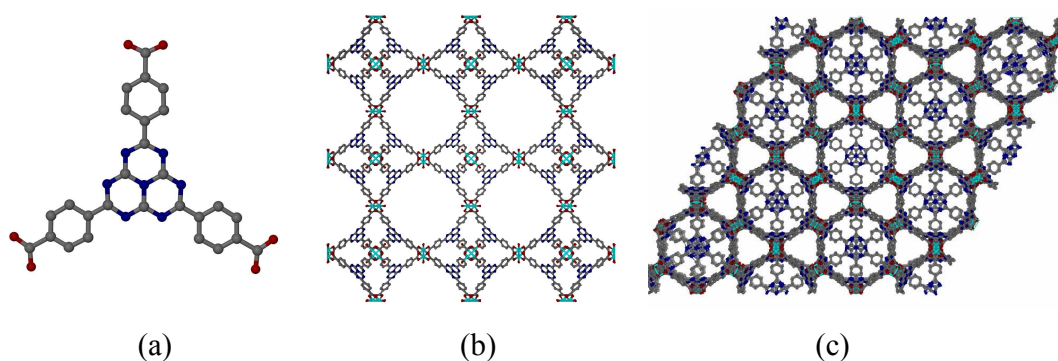


Figure 5.3 (a) HTB (*s*-heptazine tribenzoate) ligand; (b) MOF-HTB' viewing from (001) direction; (c) MOF-HTB viewing from (001) direction.

Both PCN-6' and PCN-6 exhibit permanent porosity, confirmed by gas sorption (Figure 5.4) and powder X-ray diffraction (PXRD) studies (Figure 5.5). In contrast, both HTB MOFs collapse upon guest solvent removal presumably owing to the instability of the larger open channels in the two HTB MOFs. The N₂ adsorption isotherm of PCN-6' (Figure 5.4a) indicates typical Type-I sorption behavior, with a Langmuir surface area of 2700 m²/g (pore volume 1.045 ml/g). This is lower than the Langmuir surface area of PCN-6 (3800 m²/g, pore volume 1.453 ml/g), although PCN-6' has a higher solvent-accessible volume (86%, calculated using PLATON¹⁰) than that of PCN-6 (74%). Thus, catenation has led to 41% increase in Langmuir surface area. This counter-intuitive increase can be attributed to that the new adsorption sites are formed by the catenation as well as the small pores formed as a result of catenation may strengthen the overall

interaction between gas molecules and the pore walls therefore increase the *apparent* surface area, as predicted by a recent theoretical simulation.¹¹ If open channels are blocked as a result of catenation, however, the overall surface area may drop significantly.

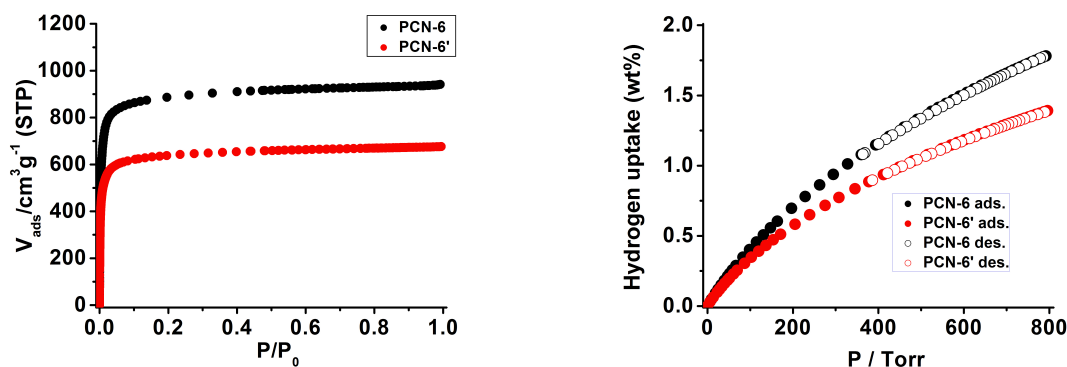


Figure 5.4 Gas sorption isotherms (77 K) of PCN-6' and PCN-6 activated at 50°C for N₂ (left) and H₂ (right).

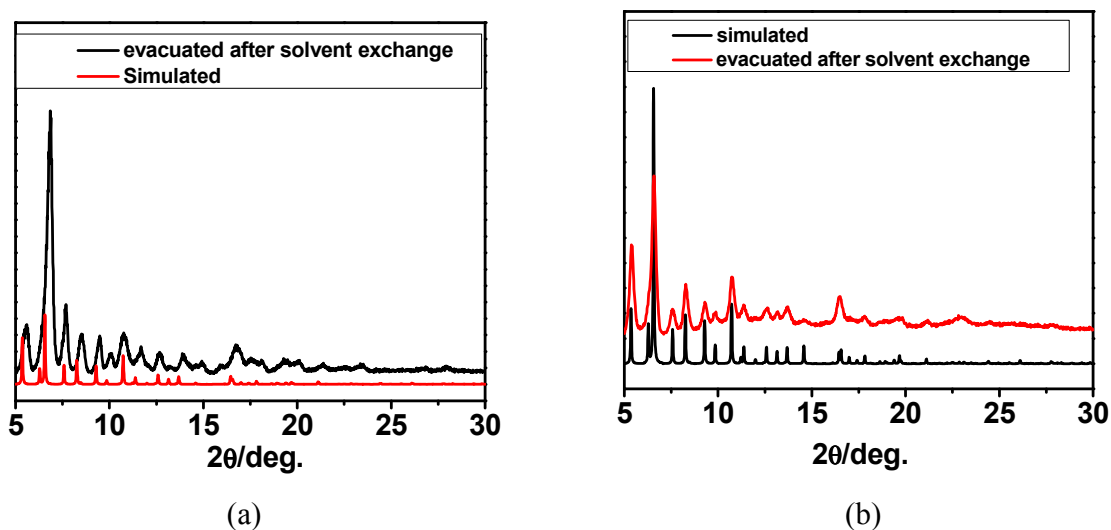


Figure 5.5 Powder X-ray diffraction patterns: (a) PCN-6'; (b) PCN-6.

It is important to study the independent contribution of catenation to hydrogen uptake. In the catenation isomer pair of PCN-6 and PCN-6', the contributions from interpenetration and UMCs must be separated. TGA studies on the two MOFs suggest that activation at 50 °C will remove only guest molecules. To expose the UMCs, the

samples must be heated at 150 °C to remove the axial aqua ligands on the Cu centers. A facile way to resolve the contributions by UMCs and catenation to hydrogen uptake is to measure the hydrogen adsorption isotherms of samples activated at the two temperatures.

Hydrogen adsorption studies revealed that PCN-6' activated at 50 °C can adsorb 1.35 wt % (volumetric uptake of 3.94 kg/m³, calculated density: 0.292 g/cm³) hydrogen at 760 torr and 77 K (Figure 5.4b), significantly lower than that of PCN-6 activated at the same temperature (1.74 wt %; volumetric uptake of 9.19 kg/m³, calculated density: 0.528 g/cm³). Hence, catenation has led to a 133% of enhancement in volumetric (29% in gravimetric) hydrogen uptake. Previously we have reported that after activation at 150 °C, PCN-6 can adsorb 1.9 wt % hydrogen (at 760 torr and 77 K), a 10% improvement over that of PCN-6 activated at 50 °C (Figure 5.6). Similarly, after activation at 150 °C, PCN-6' can adsorb 1.62 wt % hydrogen, a 20% increase from that of PCN-6' activated at 50 °C (Figure 5.6). These further improvements upon activation at 150 °C can only be attributed to UMCs. The smaller improvement of hydrogen uptake upon UMC activation in PCN-6 than that in PCN-6' suggests that most of the UMCs in PCN-6 are blocked as a result of catenation (observed from the crystal structure), while the UMCs in PCN-6' are open.

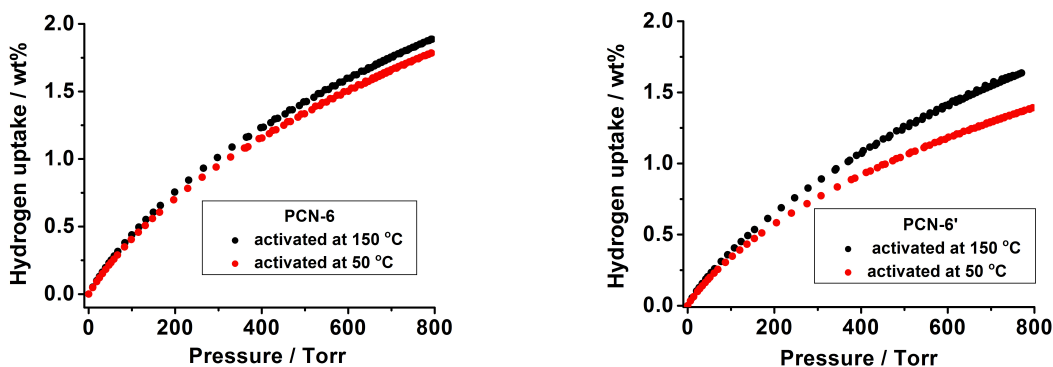


Figure 5.6 H₂ sorption isotherms of PCN-6' (left) and PCN-6 (right) activated at 50 °C and 150 °C.

In summary, using an unprecedented templating strategy, new catenation isomer-pairs can be synthesized predictably using copper paddlewheel SBUs and two trigonal-planar ligands (TATB and HTB) developed in our lab. Gas sorption studies on the isomer

pair using TATB have revealed that catenation leads to a 41% improvement of Langmuir surface area and a 133% increase in volumetric hydrogen uptake (29% increase in gravimetric). The resolution of the contributions from UMCs and catenation to the hydrogen uptake of a MOF is unprecedented.

5.4 References

- (22) (a) Rowsell, J. L. C.; Millward, A. R.; Park, K. S.; Yaghi, O. M., *J. Am. Chem. Soc.* **2004**, *126*, 5666; (b) Rowsell, J. L. C.; Eckart, J. Yaghi, O. M., *J. Am. Chem. Soc.* **2005**, *127*, 14904; (c) Kesanli, B.; Cui, Y.; Smith Milton, R.; Bittner Edward, W.; Bockrath Bradley, C.; Lin, W., *Angew. Chem. Int. Ed.* **2005**, *44*, 72; (d) Lee, J. Y.; Pan, L.; Kelly, S. P.; Jagiello, J.; Emge, T. J.; Li, J., *Adv. Mater.* **2005**, *17*, 2703; (e) Sun, D.; Ke, Y.; Mattox, T. M.; Betty, A. O.; Zhou, H. -C., *Chem. Commun.*, **2005**, 5447; (f) Panella, B.; Hirscher, M., *Adv. Mater.* **2005**, *17*, 538; (g) Rowsell, J. L. C.; Yaghi, O. M., *J. Am. Chem. Soc.* **2006**, *128*, 1304; (h) Wong-Foy, A. G.; Matzger, A. J.; Yaghi, O. M., *J. Am. Chem. Soc.* **2006**, *128*, 3494; (i) Chen, B.; Ma, S.; Zapata, F.; Lobkovsky, E. B.; Yang, J., *Inorg.Chem.* **2006**, *45*, 5718; (j) Dincă, M.; Yu, A. F.; Long, J. R., *J. Am. Chem. Soc.* **2006**, *128*, 8091; (k) Li, Y.; Yang, R. T., *J. Am. Chem. Soc.* **2006**, *128*, 726; (l) Li, Y.; Yang, R. T., *J. Am. Chem. Soc.* **2006**, *128*, 8136.
- (23) L. Schlapbach, A. Zuttel, *Nature* **2001**, *414*, 353. (c) “Hydrogen, Fuel Cells & Infrastructure Technologies Program: Multi-year Research, Development, and Demonstration Plan”, US Dept. of Energy, 2005, <http://www.eere.energy.gov/hydrogenandfuelcells/mypp/>.
- (24) (a) Pan, L.; Sander, M. B.; Huang, X.; Li, J.; Smith, M. R., Jr.; Bittner, E. W.; Bockrath, B. C.; Johnson, J. K., *J. Am. Chem. Soc.* **2004**, *126*, 1308; (b) Rowsell, J. L. C.; Yaghi, O. M., *Angew. Chem. Int. Ed.* **2005**, *44*, 4670; (c) Sun, D. ; Ma, S. ; Ke, Y. ; Collins, D. J.; Zhou, H. -C.; *J. Am. Chem. Soc.* **2006**, *128*, 3896.
- (25) (a) Chen, B. L.; Ockwig, N. W.; Millward, A. R.; Contreras, D. S.; Yaghi, O. M., *Angew. Chem. Int. Ed.* **2005**, *44*, 4745; (b) Dietzel, P. D. C.; Panella, B.; Hirscher, M.; Blom, R.; Fjellvag, H., *Chem. Commun.*, **2006**, 959; (c) Yang, Q.; Zhong, C. *J. Phys. Chem. B*, **2006**, *110*, 655.

- (26) Ma, S.; Zhou, H.-C. *J. Am. Chem. Soc.* **2006**, *128*, 11734.
- (27) X-ray crystal data for PCN-6': C₃₂H₁₆Cu₂N₄O₁₀, fw = 743.59, cubic, *Fm-3m*, *a* = 46.636(5) Å, *b* = 46.636(5) Å, *c* = 46.636(5) Å, *V* = 101432(20) Å³, *Z* = 24, *T* = 250 K, $\rho_{\text{calcd}} = 0.292 \text{ g/cm}^3$, $R_1 (I > 2\sigma(I)) = 0.0650$, $wR_2 (\text{all data}) = 0.1605$.
- (28) Chui, S. S.-Y.; Lo, S. M.-F.; Charmant, J. P. H.; Orpen, A. G.; Williams, I. D., *Science* **1999**, *283*, 1148.
- (29) Wang, X.-S.; Ma, S.; Sun, D.; Parkin, S.; Zhou, H.-C. *J. Am. Chem. Soc.* **2006**, *128*, 11734.
- (30) Ke, Y.; Collins, D. J.; Sun, D.; Zhou, H.-C. *Inorg. Chem.* **2006**, *45*, 1897.
- (31) Spek, A. L., *J. Appl. Crystallogr.* **2003**, *36*, 7.
- (11) Jung, D. H.; Kim, D.; Lee, T. B.; Choi, S. B.; Yoon, J. H.; Kim, J.; Choi, K.; Choi, S.-H. *J. Phys. Chem. B.* **2006**; *110*, 22987.

Chapter 6

Investigation of Hydrogen Binding in MOF Catenation Isomers by Inelastic Neutron Scattering and High Pressure Hydrogen Adsorption Properties of the Isomers[°]

6.1 Introduction

Safe and efficient on-board hydrogen storage has been recognized as a critical problem preventing the widespread use of hydrogen for mobile applications.¹ Among a variety of promising hydrogen storage candidates,² porous metal-organic frameworks (MOFs)³ currently stand at the forefront to approach the DOE targets¹ due to their high specific surface areas⁴ and well-defined hydrogen binding sites.⁵ Some of them reported thus far have reached or even surpassed the DOE target values for hydrogen storage albeit at cryonic temperatures (mostly at 77 K).⁶ In order to improve the hydrogen uptake of porous MOFs particularly at near ambient temperatures, various strategies such as increasing surface areas, using small pore sizes comparable to hydrogen molecules,⁷ introducing accessible coordinatively unsaturated metal centers (UMCs),^{6b,c,8} constructing cuboctahedral cages,⁹ and utilizing catenation¹⁰ have recently been widely explored.

Catenation, the intergrowth of two or more identical frameworks, has long been a topic of interest in the MOF research area.¹¹ It can be considered an alternative way to reduce pore sizes in porous MOFs and has been pursued as a viable approach for enhancing hydrogen uptake.¹² Some catenated porous MOFs were reported to adsorb ~1 wt% of hydrogen at room temperature and 48 bar.¹³

Recently, we developed a templating strategy to systematically control catenation and non-catenation in porous MOFs and quantitatively evaluate the contribution from catenation to the hydrogen uptake of a MOF material (Figure 6.1).¹⁴ Our studies revealed that catenation can lead to a 41% improvement of *apparent* surface area and a 29% increase in gravimetric hydrogen uptake at 77 K, 760 torr for the catenated PCN-6

[°] This chapter was adapted from the finished manuscript “Investigation of Hydrogen Binding in MOF Catenation Isomers by Inelastic Neutron Scattering and High Pressure Hydrogen Adsorption Properties of the Isomers” Submitted to *J. Am. Chem. Soc.* Unpublished work copyright 2008, American Chemical Society.

compared to the non-catenated PCN-6'. Similar results were also demonstrated by Long *et al.* in the ligand-directed catenation studies.¹⁵

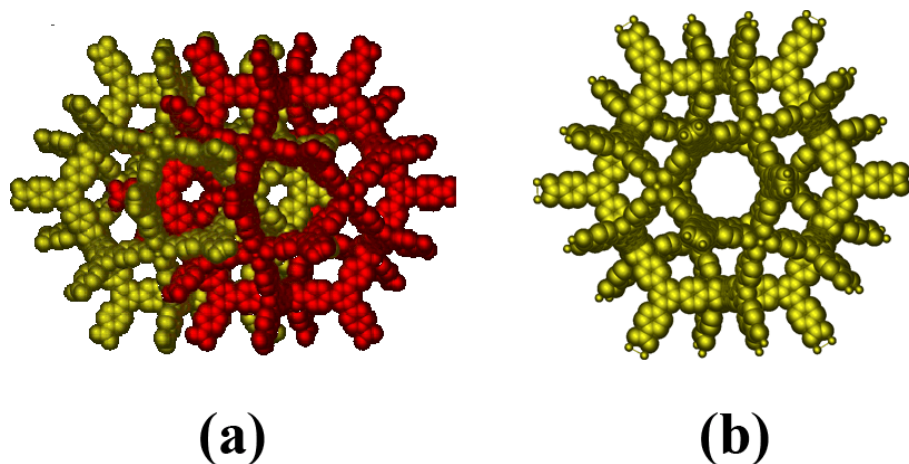


Figure 6.1. (a) Catenated PCN-6; (b) Non-catenated PCN-6'.

It has been well documented that hydrogen adsorption in porous MOFs is closely related to their structural features,¹² and it is therefore essential that the interactions between hydrogen molecules and these frameworks as well as the hydrogen binding sites be elucidated.^{3h} The most useful experimental method for obtaining a molecular level understanding of hydrogen adsorption in porous MOFs is inelastic neutron scattering (INS) spectroscopy of the hindered rotational transitions of the adsorbed hydrogen molecules.¹⁶ The lowest transition hindered rotor energy levels of the H₂ molecule is a rotational tunneling transition, which depends exponentially on the height of the barrier to rotation. It is for this reason that this technique is extremely sensitive to the chemical environment of adsorbed H₂ and can thereby provide detailed information about the various binding sites that the hydrogen molecules occupy and the approximate order in which these are filled.¹⁷ Because of the very large inelastic incoherent neutron scattering cross section for hydrogen, vibrational modes not involving hydrogen are not normally observed, which greatly simplifies the analysis of the observed spectra. This technique has become invaluable to understanding the hydrogen adsorption characteristics of a variety of nanoporous substrates including zeolites¹⁸ and carbon nanostructures,¹⁹ and has also been recently employed to investigate the details of hydrogen adsorption in porous MOFs.^{8c,20}

To clarify how catenation favors the hydrogen uptake, and to elucidate the different hydrogen adsorption mechanisms in the catenated and non-catenated frameworks, this chapter will discuss the INS investigation of hydrogen adsorption in the catenation isomers PCN-6 and PCN-6' together with the analysis of their heats of adsorption for hydrogen as well as high pressure hydrogen sorption studies.

6.2 Experimental Details

Sample Preparation: PCN-6 and PCN-6' were synthesized by the methods described previously.¹⁴ The prepared fresh samples were immersed first in methanol and then dichloromethane to exchange the included DMSO or DMF solvent molecules. After solvent-exchange, the samples were evacuated under dynamic vacuum at room temperature over night, followed by activation under dynamic vacuum at 150 °C for two hours. The crystalline phase purity of each activated sample was confirmed by comparing the powder X-ray diffraction patterns (Scintag X1 powder diffractometer system using CuK radiation with a variable divergent slit, solid-state detector, and a routine power of 1400 W (40 kV and 35 mA) with those calculated from single crystal data.

Inelastic Neutron Scattering Experiments: Inelastic neutron scattering spectra were collected on the QENS21 spectrometer at the Intense Pulsed Neutron Source at Argonne National Laboratory. The samples of PCN-6 and PCN-6' were dehydrated for two hours in a tube furnace set to 423 K. A quantity of 1.0 g of the materials were subsequently sealed inside an aluminum sample containers in a solvent free N₂ glove-box. The container was then mounted in a closed-cycle He refrigerator, connected to an external gas loading manifold, and placed into the QENS instrument. After the sample was degassed for 1 h, the sample was cooled to 15 K and a “blank” spectrum of the material was collected for approximately 12 h. Gas loadings were carried out in situ with the sample container at 70-150 K by monitoring the pressure drop from the calibrated volume of the manifold of the external gas handling system. Each of a total of three loadings delivered 4.2×10^{-2} mol of H₂ gas to the sample.

Low-Pressure Hydrogen Adsorption Measurements: The low-pressure hydrogen adsorption isotherms in the range of 0-800 torr were measured using a Beckman Coulter SA 3100 surface area and pore size analyzer. High purity hydrogen

(99.9995%) was used for H₂ adsorption measurements. The regulator and pipe were flushed with hydrogen before connecting to the analyzer. The internal lines of the instrument were flushed three times utilizing the “flushing lines” function of the program to ensure the purity of H₂. Before the measurement, the activated samples were again evacuated by heating at 150 °C under dynamic vacuum ($< 10^{-3}$ torr) for 2 hour by using the “outgas” function of the surface area analyzer. The evacuated sample tube containing degassed samples was covered with a rubber cap and then carefully transferred to an electronic analysis balance (accuracy of 0.0001 mg) and weighted to determine the mass of sample (typically 60-150 mg). The tube was then transferred back to the analysis port of the surface area analyzer and evacuated to a vacuum of less than 10^{-3} torr before the gas dose. For all the isotherms, the free space correction were performed using high-purity He gas (99.999%). The H₂ adsorption isotherms at 77K were measured in liquid nitrogen bath, and those at 87 K were measured in liquid argon bath.

High pressure gas adsorption measurements: The high pressure adsorption experiments were conducted using a volumetric sorption analyzer HPVA-100 (VTI Corporation, USA) equipped with a rotary vane pump (DUO 5 M, PFEIFFER), a turbomolecular drag pump (TMH 064/TMU 064, Pfeiffer), a PMP 4010 (Druck/GE, Max. 6 MPa) transducer, a Datel pressure meter, a JC Controls TC610 vacuum gauge and a Polyscience circulator. The sample holder consisted of a sample cell and tube equipped with diaphragm valve (6LV-DSBW4, Swagelok). The two assemblies were connected via filter gasket (SS-4-VCR-2-.5M, Swagelok) and the materials of construction were all 316 stainless steel. The volumetric technique consisted of dosing a known amount of gas into the cell containing the sample to be analyzed. When the sample reached equilibrium with the gas adsorbate, the initial and final equilibrium pressures were recorded. This data was then used to calculate the volume of gas adsorbed by the sample. This process was repeated at given pressure intervals until the maximum pre-selected pressure was reached. Each of the resulting equilibrium points (volume adsorbed and equilibrium pressure) were then plotted to provide an isotherm. Good reproducibility and accuracy were obtained by using separate transducers for dosing the sample and for monitoring the pressure in the sample cell. In a typical experiment, around 0.5 g of sample was transferred to the sample cell and outgassing was performed overnight at 423 K under

high vacuum (~ 0.001 Pa). After finishing the outgassing, the sample cell was recharged with He (99.999%) to measure the loading amounts of the dehydrated samples which were calculated from weight difference between blank sample cell and sample-loaded cell. Above activation was repeated again, and then gas sorption was performed. Ultra-high purity H₂ (99.999%) was obtained from Korea Gas Co. The sample cell was immersed in thermostated circulating bath at 303 K.

6.3 Results and Discussion

Analysis of Isothermic Heats of Adsorption: It is believed that the reduced pore size resulting from catenation increase the overlap of the attractive potential of opposite walls thus enhancing the heat of adsorption.^{3e,21} To estimate the heats of adsorption Q_{st} , for H₂ in PCN-6 and PCN-6', H₂ adsorption isotherms were measured at 77 and 87 K (Figure 6.3). The adsorption data were fitted using the Langmuir-Freundlich equation²² (utilizing the virial-type expression^{3e,6b} to fit the data could yield similar results but large ($\sim 15\%$) deviations), and the heats of adsorption were calculated using the Clausius-Clapeyron equation.²³

$$Q_{st} = -R \cdot d(\ln P) / d(1/T)$$

As shown in Figure 6.2, in the uptake range of 0.05-7 mmol/g, the Q_{st} of PCN-6 is 6.2-4.5 kJ/mol, while that of PCN-6' is 6.0-3.9 kJ/mol. At the low coverage of 0.05 mmol/g, PCN-6 has a hydrogen enthalpy of 6.2 kJ/mol, and PCN-6' has a value of 6.0 kJ/mol. These are comparable with the reported Q_{st} of Cu-BTC^{3e,24} and can be attributed to the interactions between dihydrogen molecules and open Cu sites as revealed by the recent neutron powder diffraction studies.^{5b} With the increase of H₂ coverage, Q_{st} of the two MOFs decreases steadily but declines more rapidly in PCN-6'. The larger Q_{st} of PCN-6 compared to that of PCN-6' at high H₂ coverage can be ascribed to the reduced pore size of PCN-6 due to catenation thereby enhancing the interaction energy between dihydrogen molecules and the framework walls.^{12, 21}

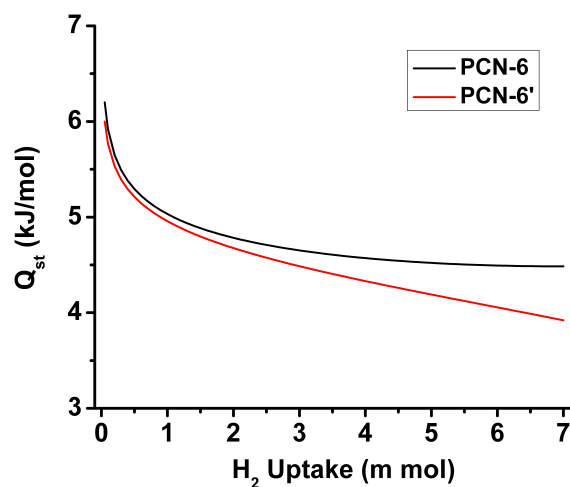


Figure 6.2 Isothermic heats of adsorption vs H_2 for PCN-6 and PCN-6'.

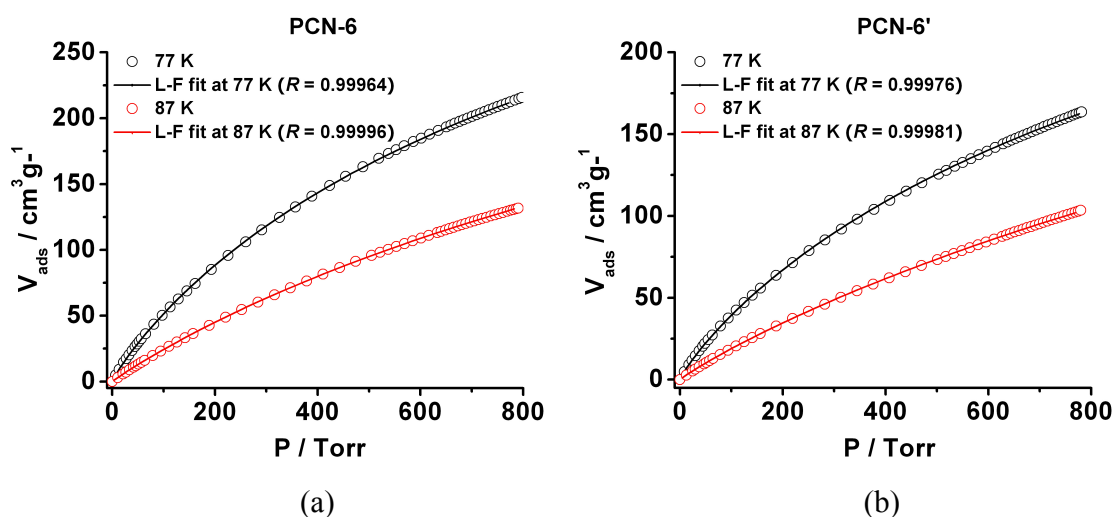


Figure 6.3 H_2 adsorption isotherms at 77 and 87 K fitted with Langmuir-Freundlich equation. (a) PCN-6; (b) PCN-6'.

Inelastic Neutron Scattering (INS) Studies. INS spectra were obtained from a sample of 1.0 g of PCN-6 and of PCN-6' on the QENS spectrometer at the Intense Pulsed Neutron Source of Argonne National Laboratory. Each sample was evacuated at temperatures up to 150 °C and transferred under He atmosphere into the sample holder for the neutron scattering experiments. Following the collection of a data set of the “blank” sample at 15 K, the sample was warmed to 77 K, and an amount of hydrogen corresponding to 0.5 molecules per Cu was adsorbed *in-situ*. Subsequent data sets with

two or three additional loadings (also at 77 K) of hydrogen were obtained at 15 K. The INS spectra for H₂ in PCN-6 and PCN-6', after the subtracting the “blank” run, are shown in Figure 6.4 and 6.5. The identifiable peaks in the INS spectra were assigned based on the same model previously used by us,^{20a} namely that of a hindered rotor with two angular degrees of freedom in a simple double-minimum potential.²⁵ In the absence of a barrier to rotation, the lowest transition is that between *para*- and *ortho* H₂, and it occurs at 14.7 meV (or 119 cm⁻¹, = 2B, where B is the rotational constant of the H₂ molecule). The interaction of the adsorbed hydrogen molecules with the host material gives rise to a barrier to rotation which in turn partially lifts the degeneracy of the $J = 1$ level. The lowest transition frequency for the hindered rotor (between the $J = 0$ and the $J = 1, m_J = 0$ states, which we subsequently refer to as the “0-1” transition) decreases approximately exponentially with increasing barrier height (rotational tunnel splitting) and is therefore extraordinarily sensitive to small differences in barrier height (see Table 1). All rotational energy levels are labeled sequentially for reasons of simplicity, *i.e.* 0, 1, 2, and not by quantum numbers.

Previous studies^{5b,20c,26} of porous MOFs containing the Cu paddlewheel SBU have shown that the preferred binding site for H₂ is the open Cu site, and this is also found to be the case in PCN-6/6'. The lowest loading used in the INS studies in both cases was 0.5 H₂ per Cu site with the assumption that only this site would be occupied. The INS spectra at this low loading indeed show mainly one prominent peak at about 8.8 meV in both compounds, which we can readily assign to H₂ adsorbed at the open Cu sites. We note, however, that the peak for H₂ in PCN-6 is somewhat broader than that in PCN-6'. This difference can be ascribed to the fact that in PCN-6 there are three inequivalent Cu-sites whereas all those sites in PCN-6' are identical. One may speculate that the catenation in PCN-6 may be at least in part give rise to slight differences in the coordination geometry about the three Cu sites, which in turn affect binding of H₂ as well as that of the water ligand initially present. A rough assessment of the differences in Cu-H₂ interaction strengths at these sites can be obtained by comparing the Cu-OH₂ distances found for the removable aquo ligands of the paddlewheel SBUs in the crystal structures. In PCN-6^{10a} there are three such Cu-O distances of 2.199, 2.110, 2.140 Å (average 2.150 Å) whereas the one such distance in PCN-6' is 2.173 Å.¹⁴ If we can assume that those for

Cu-(H₂) would be proportional to these, we might conclude that the average interaction with the Cu sites in PCN-6 is slightly greater than that in PCN-6'.

Table 6.1 Tentative assignments of bands in the INS spectra of PCN-6 and PCN-6' according to the model used in ref. 20.

PCN-6					
Transition Frequency (meV)*				Barrier Height (V₂/B)	
0-1		0-2		1-2	
(0.5)	(1)	(2+)	loading (H₂ per Cu)		
8.7		19.1		10.4	3.5
9.5sh		18.3		8.8	2.9
		10.3	17.7	7.4	2.45
11.3		16.7		5.4	1.8
	11.6	16.6		5.0	1.7
	12.9	15.7		2.8	0.9
		14.0	15.0	(1.0)	0.35
PCN-6'					
8.85		19.0		10.2	3.4
	9.6	18.3		8.8	2.9
	10.2	17.8		7.6	2.5
11.6		16.6		5.0	1.7
13.7		15.2		(1.5)	0.5
14.5		14.8		(0.3)	0.1

* 1 meV = 8.07 cm⁻¹

B = 7.35 meV = 0.71 kJ/mol

peak positions are approximate; some of the 1-2 transitions (in parentheses) were not observed most likely because of low population of the "1" level.

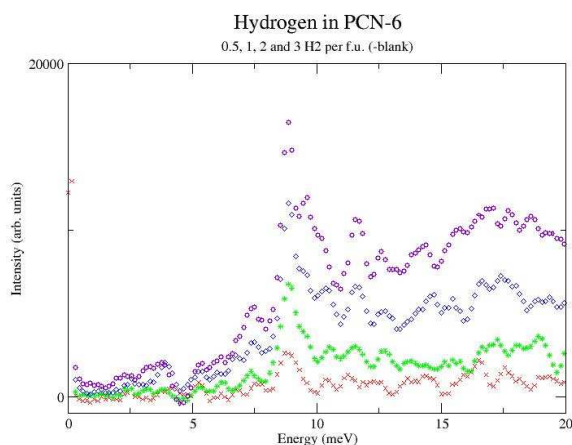


Figure 6.4 INS spectra (15 K) for H₂ adsorbed in PCN-6 at loadings of 0.5, 1, 2, and 3 molecules per Cu

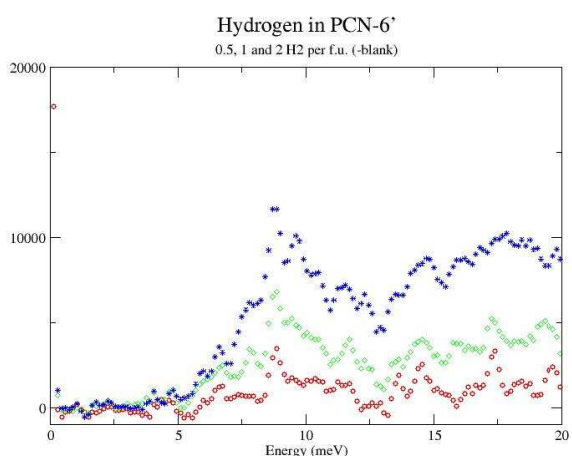


Figure 6.5 INS spectra (15 K) for H₂ adsorbed in PCN-6' at loadings of 0.5, 1, and 2 molecules per Cu site.

Close inspection of the band in the INS spectrum corresponding to the 0-1 transition in both systems does indeed reveal that the position of this peak is at slightly lower energy (8.7 meV) in PCN-6 (indicating stronger interaction with H₂) than in PCN-6' (8.85 meV). This observation is qualitatively in agreement with the relative Q_{st} values of 6.2 kJ/mol for PCN-6 vs. 6.0 kJ/mol for PCN-6' at low coverage. It must, however, be noted that the barrier to rotation for H₂ as determined from the INS experiment does not necessarily have a one-to-one correspondence with the binding energy.²⁷ Nonetheless previous studies^{20a} have shown that in general a larger barrier for rotation of H₂ at a

particular site is associated with a higher binding energy. The greater width of this peak for H₂ in PCN-6 may also reflect the presence of three different Cu sites, which slightly differ in binding energies for H₂. These observations are in qualitative accord with our previous report of a similar broad band with principal transition frequencies of 7.7 and 8.6 meV in PCN-12,²⁶ which has eight Cu-OH₂ distances ranging from 2.116 to 2.178 Å.

The general appearance of the INS spectra for both compounds is rather similar, which does of course reflect the identical chemical composition. Some important differences are evident, however, as a result of the framework catenation in PCN-6. The presence of interpenetrating frameworks in PCN-6 should make it possible for the adsorbed H₂ to interact with more atoms than in PCN-6' because of the proximity of the “second” framework, and hence result in some increase in binding energies. Inspection of the crystal structures of the two compounds shows that this effect is likely to be more pronounced for sites on or near the organic linkers than those on or near the open Cu sites.

The rotational transition energies associated with H₂ on the organic linkers tend to be in the region between 11 and 14.7 meV²⁰. The latter is the value of the 0-1 transition for the free rotor. All the INS intensities above that value originate from higher transitions. Comparison of the INS spectra in this energy range at higher loadings in PCN-6' show a strong peak growing in at about 14.5 meV, which is rather weak in PCN-6. Instead, the spectrum for PCN-6 shows that a peak at 11.6 meV develops at and increases with higher loadings. The transition at about 14.5 meV is well known from work on H₂ adsorbed on various carbons²⁸ as well as on organic links in MOFs,^{20a} and reflects the rather weak binding to those structures. The apparent shift to much lower energy (i.e. stronger interaction) demonstrates that the binding sites on the linkers in PCN-6 are strongly affected by the catenated structure, and this observation is indeed reflected by the higher values for Q_{st} for PCN-6 at higher loadings.

An interesting observation related to H₂ binding sites on part of the organic may be also made from the H₂ loading dependence of the strong peak at 4.5 meV which arises from the framework. This peak may be assigned to the torsion of the benzene carboxylate, and this motion has in fact been studied by NMR for benzene dicarboxylate in MOF-5.²⁹ It occurs at a similar energy in the INS of the MOF-5 framework.^{20a} This peak has been subtracted out in the spectra shown in Figure 3 and 4, but the difference

spectrum shows much more intensity in the region about 4.5 meV at higher H₂ loading for PCN-6 than PCN-6'. This increase results from H₂ molecules bound to sites on the benzene carboxylate and hence participating in the torsional motion along with the H's of the organic ligand.

The INS studies therefore clearly indicate that the much stronger interactions of adsorbed H₂-with the organic linker in the catenated material must result from a greater number of interacting atoms from the organic ligands especially at high hydrogen loadings. These results are also consistent with recent theoretical simulations suggesting that catenation favors hydrogen uptake by maximizing the *effective* hydrogen binding sites on the organic linkers.³⁰

High Pressure H₂ Sorption Studies: In order to check their hydrogen adsorption behaviors at elevated pressure, high pressure H₂ sorption isotherms were measured at 77 and 298 K. As shown in Figure 6.6, at 77 K and 50 bar, the excess H₂ uptake of PCN-6 can reach as high as 7.2 wt% without saturation. This value, to the best of our knowledge, is the highest among reported porous MOFs under similar conditions (MOF-177 (7.1 wt%, 50 bar; 7.5 wt%, 70 bar),^{6a,f} Table 6.3), and it is expected to increase further at higher pressure before the saturation is achieved. Calculated with its crystal density of 0.558 g/cm³ after removal of the axial aqua ligands of the paddlewheel, the excess volumetric H₂ uptake of PCN-6 is 40.2 g/L. At 298 K and 50 bar, PCN-6 can uptake 0.93 wt% hydrogen, which is among the highest for reported porous MOFs.^{3j,o,7,13} Noticing the almost linear relationship between the adsorbed hydrogen amount of PCN-6 and the pressure at 298 K, it can be estimated that PCN-6 can uptake ~1.8 wt% at 100 bar by extrapolating the hydrogen adsorption isotherm. As for PCN-6', its excess H₂ adsorption is 4.2 wt% at 50 bar without saturation, corresponding to an excess volumetric value of 11.8 g/L (0.280 g/cm³, calculated similarly). At 298 K and 50 bar, PCN-6' can adsorb 0.40 wt% hydrogen, which is less than one half of the amount PCN-6 can adsorb. Since PCN-6' is isostructural with Cu-BTC, high pressure H₂ sorption data were also collected for comparison. The excess hydrogen uptake of Cu-BTC is 3.6 wt% (Figure 6.7) of the saturation at 77 K, 20 bar and 0.3 wt% at 298 K, 50 bar, which are very close the results reported by other groups.^{3h} The higher hydrogen uptake of PCN-6' than that of Cu-BTC can be ascribed to the larger surface area of PCN-6' resulting from the expansion from

BTC ligand to TATB ligand, which has more phenyl rings thus providing more hydrogen binding sites.^{30c,31}

Nevertheless, the higher hydrogen adsorption capacity of PCN-6 compared to that of PCN-6' can be attributed to the reduced pore size (9.0 Å) as a result of catenation. Catenation can increase the overlap of the attractive potential of opposite walls thus enhancing the interaction between hydrogen molecules and the frameworks,²¹ and the boosted energy fields of the pore walls also increases the *effective* hydrogen binding sites.³⁰ As for PCN-6', although it has a larger solvent accessible volume, the long distances (21.4 Å) between the opposite pore walls leads to no overlap of the potential energy fields which results in a lot of unused void volume at the center of the pores as well as a decrease of the *effective* hydrogen binding sites. void volume at the center of the pores as well as a decrease of the *effective* hydrogen binding sites. The same conclusions have also been reached by the above INS studies and are reflected in the higher heats of adsorption for PCN-6 with the increase of hydrogen coverage as well.

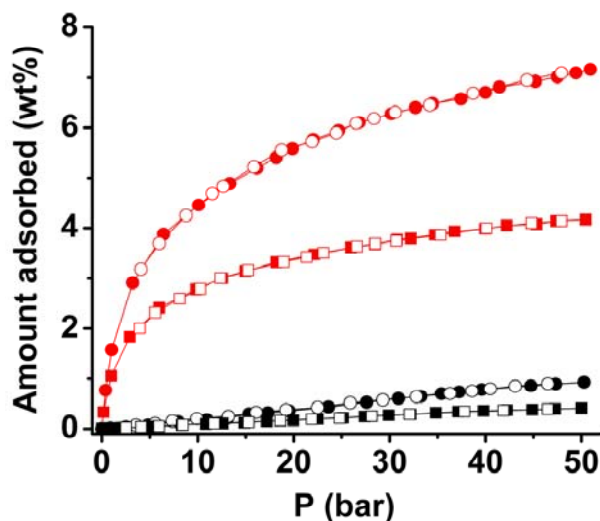


Figure 6.6 Excess hydrogen sorption isotherms of PCN-6 and PCN-6' at 77 K (red) and 298 K (black): circle, PCN-6; square, PCN-6'; solid symbol, adsorption; void symbol, desorption.

For practical applications, the total hydrogen uptake defined as the total amount of hydrogen stored in the bulk volume of the materials can usually provide a more informative quantity. The total H₂ gravimetric adsorption capacity of PCN-6, as shown in Figure 6.8 can reach 9.5 wt% at 77 K 50 bar, corresponding to a volumetric capacity of

53.0 g/L. These two values are again the record high among reported porous MOFs (Table 6.3). At 77 K, 50 bar, the total gravimetric hydrogen uptake of PCN-6' is 5.8 wt% corresponding to the volumetric value of 16.2 g/L. At 298 K, 50 bar, the total gravimetric hydrogen adsorption capacity of PCN-6 is 1.5 wt%, while that of PCN-6' is 0.81 wt%. The contribution of catenation to hydrogen uptake at room temperature is even more profound as indicated by more than doubled adsorbed hydrogen amount in PCN-6 compared to PCN-6'.

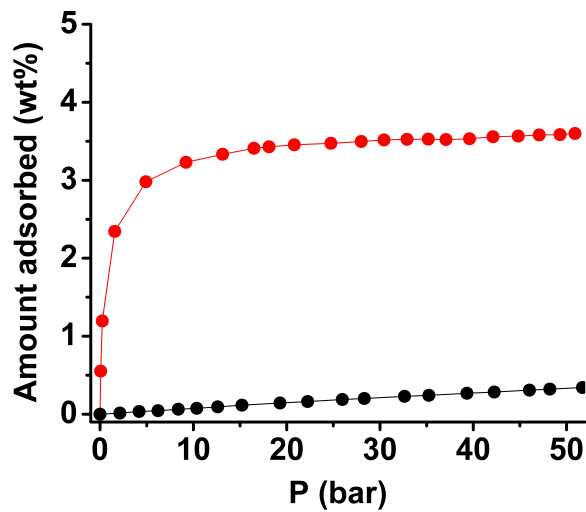


Figure 6.7 Excess hydrogen adsorption isotherms of HKUST-1 at 77 (red) and 298 K (black).

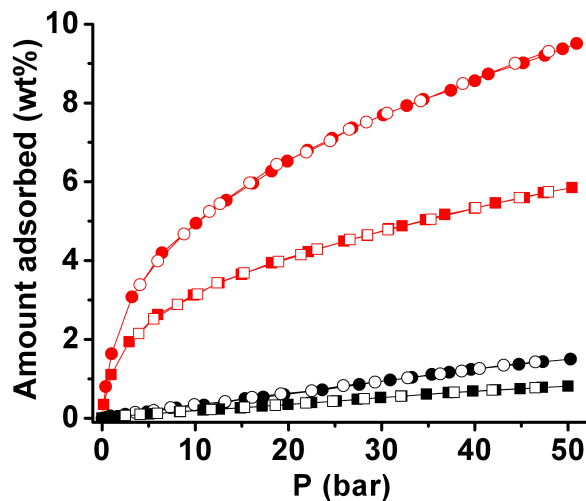


Figure 6.8 Total hydrogen sorption isotherms of PCN-6 and PCN-6' at 77 K (red) and 298 K (black): circle, PCN-6; square, PCN-6'; solid symbol, adsorption; void symbol, desorption.

Recent studies have demonstrated porous MOFs to be promising cryonic hydrogen storage media (77 K)⁶ for achieving the 2010 DOE hydrogen storage system targets values. However, an important criterion of on-board hydrogen storage under practical conditions even for cryonic hydrogen storage is the total amount of delivered H₂ known as usable (or deliverable) H₂, which can be defined as an absolute adsorbed amount of H₂ ranging from 1,5 bar to the storage pressure.^{6f} This requires the hydrogen adsorption isotherm to be fully reversible and most of the absorbed hydrogen releasable. As shown in Figures 6.6 and 6.8, hydrogen sorption isotherms of PCN-6 and PCN-6' are fully reversible with virtually no hysteresis. At 77 K, the total usable hydrogen of PCN-6 is ~7.5 wt% (or 41.9 g/L) and that of PCN-6' is 4.2 wt% (or 11.8 g/L).

In summary, isosteric heats of adsorption analysis indicated that catenated PCN-6 and non-catenated PCN-6' have similar hydrogen adsorption enthalpies at low coverage. However with increasing hydrogen uptake, PCN-6 exhibited steadily higher hydrogen adsorption enthalpies than PCN-6'. INS studies revealed that the first sites occupied by H₂ are the open Cu centers of the paddlewheel SBUs in both PCN-6 and PCN-6' but with PCN-6 having three specific H₂ binding Cu sites while PCN-6' possesses only one. At high hydrogen loadings, H₂ molecules interact with the organic linker more strongly in catenated PCN-6 than in non-catenated PCN-6'. The stronger H₂-organic linker interactions in catenated PCN-6 resulted in more *effective* hydrogen binding sites thus favoring hydrogen uptake under both low and high pressures when compared to non-catenated PCN-6'. High pressure hydrogen sorption studies demonstrate that catenation favors excess gravimetric hydrogen uptakes with 7.2 wt% at 77 K, 50 bar and 0.93 wt% at 298 K, 50 bar in catenated PCN-6 v.s. 4.2 wt% at 77 K, 50 bar and 0.40 wt% at 298 K, 50 bar in non-catenated PCN-6'. Moreover, PCN-6 exhibits a total gravimetric hydrogen uptake capacity of 9.5 wt% (corresponding to a total volumetric value of 53.0 g/L) at 77 K, 50 bar and 1.5 wt% 298 K, 50 bar as well as a deliverable hydrogen amount of ~7.5 wt% (or 41.9 g/L) at 77 K, promising its great potential as a cryonic hydrogen storage medium.

Table 6.2 Hydrogen adsorption data of PCN-6 and PCN-6'

	Heats of adsorption (coverage of 0.05-8 mmol)	Excess gravimetric uptake (77 K, 50 bar)	Excess volumetric uptake (77 K, 50 bar)	Total gravimetric uptake (77 K, 50 bar)	Total volumetric uptake (77 K, 50 bar)	Total usable adsorbed hydrogen (77 K, 1.5-50 bar)	Excess gravimetric uptake (298 K, 50 bar)	Total gravimetric uptake (298 K, 50 bar)
PCN-6	6.2-4.5 kJ/mol	7.2 wt%	40.2 g/L	9.5 wt%	53.0 g/L	7.5 wt% (or 41.9 g/L)	0.93 wt%	1.5 wt%
PCN-6'	6.0-3.9 kJ/mol	4.2 wt%	11.8 g/L	5.8 wt%	16.2 g/L	4.2 wt% (or 11.8 g/L)	0.40 wt%	0.81 wt%

Table 6.3 Hydrogen adsorption data of PCN-6 and some reported MOFs.

	Excess gravimetric uptake (wt%, 77 K)	Excess volumetric uptake (g/L, 77 K)	Total gravimetric uptake (wt%, 77 K)	Total volumetric uptake (g/L, 77 K)	Excess gravimetric uptake (wt%, 298 K)	Total gravimetric uptake (wt%, 298 K)
PCN-6	7.2 (50 bar)	42.3 (50 bar)	9.5 (50 bar)	53.0 (50 bar)	0.93 (50 bar)	1.5 (50 bar)
MOF-177 ^{6a,f}	7.5 (70 bar)	32.0 (70 bar)	11.0 (70 bar)	48.3 (70 bar)	0.68 (100 bar) ³²	
IRMOF-20 ^{6a}	6.7 (80 bar)	34.0 (80 bar)				
Mn-BTT ^{6c}	5.1 (35 bar)	44.3 (35 bar)	6.9 (90 bar)	60 (90 bar)	~0.8 (90bar)	1.4 (90 bar)
Cu-BTT	4.2 (30 bar)	38.0 (30 bar)	5.7 (90 bar)	53 (90 bar)	~0.4 (90 bar)	
MIL-101 ^{6c}	6.1 (60 bar)				0.43 (80 bar)	
MOF-5 ^{3h}	5.1 (60 bar)				0.28 (60 bar)	
MOF-5 ^{6g}	7.1 (40 bar)	46.9 (40 bar)	10.0 (100 bar)	66 (100 bar)		
Cu ₂ (tptc) ^{6d}	6.06 (20 bar)	43.6 (20 bar)				
Cu ₂ (qptc) ^{6d}	6.07 (20 bar)	41.1 (20 bar)				
UMCM-150 ^{3m}	5.7 (45 bar)	36.0 (45bar)				

6.4 References

1. (a) DOE Office of Energy Efficiency and Renewable Energy Hydrogen, Fuel Cells & Infrastructure Technologies Program Multi-Year Research, Development and Demonstration Plan, available at: <http://www.eere.energy.gov/hydrogenandfuelcells/mypp>; (b) FY 2006 Annual Progress Report for the DOE Hydrogen Program, November 2006, available at: http://www.hydrogen.energy.gov/annual_progress.html; (c) S. Satyapal et al., FY 2006 DOE Hydrogen Program Annual Merit Review and Peer Evaluation Meeting Proceedings, Plenary Session, available at: http://www.hydrogen.energy.gov/annual_review06_plenary.html.
2. (a) Sandrock, G. *J. Alloys Compd.* **1999**, 293–295, 877; (b) Bogdanovic', B.; Schwickardi, M. *J. Alloys Compd.* **1997**, 253–254, 1; (c) Hynek, S.; Fuller, W.; Bentley, J. *Int. J. Hydrogen Energy* **1997**, 22, 601; (d) Zuttel, A.; Sudan, P.; Maunon, P.; Kiyobayashi, T.; Emmenegger, C.; Schlapbach, L. *Int. J. Hydrogen Energy* **2001**, 27, 203; (e) Seayad, A.; Antonelli, D. M. *Adv Mater* **2004**, 16, 765.
3. (a) Rowsell, J. L. C.; Millward, A. R.; Park, K. S.; Yaghi, O. M. *J. Am. Chem. Soc.* **2004**, 126, 5666; (b) Sun, D.; Ke, Y.; Mattox, T. M.; Betty, A. O.; Zhou, H. -C. *Chem. Commun.*, **2005**, 5447; (c) Chun, H. D. Dybtsev, N.; Kim, H.; Kim, K. *Chem. Eur. J.* **2005**, 11, 3521; (d) Lee, J. ; Y.; Pan, L.; Kelly, S. &. P.; Jagiello, J.; Emge, T.; J.; Li, J. *Adv Mater* **2005**, 17, 2703; (e) Rowsell, J. L. C.; Yaghi, O. M. *J. Am. Chem. Soc.* **2006**, 128, 1304; (f) Li, Y.; Yang, R. T. *J. Am. Chem. Soc.* **2006**, 128, 726; (g) Li, Y.; Yang, R. T. *J. Am. Chem. Soc.* **2006**, 128, 8136; (h) Panella, B.; Hirscher, M. Putter, H.; Muller, U. *Adv. Funct. Mater.* **2006**, 16, 520; (i) Mulfort, K. L.; Hupp, J. T. *J. Am. Chem. Soc.* **2007**, 129, 9604; (j) Collins, D. J.; Zhou, H.-C. *J. Mater. Chem.*, **2007**, 17, 3154; (k) Farha, O. K.; Spokoyny, A. M.; Mulfort, K. L.; Hawthorne, M. F.; Mirkin, C. A.; Hupp, J. T. *J. Am. Chem. Soc.* **2007**, 129, 12680; (l) Ji, J.; Lin, X.; Wilso, C.; Blak, A. J.; Champnes, N. R.; Hubberste, P.; Walke, G.; Cusse, E. J.; Schröde, M. *Chem. Comm.* **2007**, 840; (m) Wong-Foy, A. G.; Lebel, O.; Matzger, A. J. *J. Am. Chem. Soc.* **2007**, 129, 15740; (n) Yang, C.; Wang, X.; Omary, M. A. *J. Am. Chem. Soc.* **2007**, 129, 15454; (o) Isaeva, V. I.; Kustov, L. M. *Russ. J. Gen. Chem.* **2007**, 77, 721.

4. (a) Chae, H. K.; Siberio-Pérez, D. Y.; Kim, J.; Go, Y. B.; Eddaoudi, M.; Matzger, A. J.; O’Keeffe, M.; Yaghi, O. M. *Nature* **2004**, *427*, 523; (b) Férey, G.; Mellot-Draznieks, C.; Serre, C.; Millange, F.; Dutour, J.; Surblé, S.; Margiolaki, I. *Science* **2005**, *309*, 2040.
5. (a) Spencer, E. C.; Howard, J. A. K.; McIntyre, G. J.; Rowsell J. L. C.; Yaghi, O. M. *Chem. Commun.* **2006**, 278; (b) Peterson, V. K.; Liu, Y.; Brown C. M.; Kepert, C. J. *J. Am. Chem. Soc.* **2006**, *128*, 15578; (c) Yildirim, T.; Hartman, M. R. *Phys. Rev. Lett.* **2005**, *95*, 215504/1; (d) Wu, H.; Zhou, W.; Yildirim, T. *J. Am. Chem. Soc.* **2007**, *129*, 5314.
6. (a) Wong-Foy, A. G.; Matzger, A. J.; Yaghi, O. M., *J. Am. Chem. Soc.* **2006**, *128*, 3494; (b) Dincă, M.; Dailly, A.; Liu, Y.; Brown, C. M.; Neumann, D. A.; Long, J. R. *J. Am. Chem. Soc.* **2006**, *128*, 16876; (c) Dincă, M.; Han, W. S.; Liu, Y.; Dailly, A.; Brown, C. M.; Long, J. R. *Angew. Chem. Int. Ed.* **2007**, *46*, 1419; (d) Lin, X.; Jia, J.; Zhao, X.; Thomas, K. M.; Blake, A. J.; Walker, G. S.; Champness, N. R.; Hubberstey, P.; Schroder M. *Angew. Chem., Int. Ed.*, **2006**, *45*, 7358; (e) Latroche, M.; Surble, S.; Serre, C.; Mellot-Draznieks, C.; Llewellyn, P. L.; Lee, J.-H.; Chang, J.-S.; Jung, S. H.; Férey, G. *Angew. Chem. Int. Ed.* **2006**, *45*, 8227; (f) Furukawa, H.; Miller, M. A.; Yaghi, O. M.; *J. Mater. Chem.* **2007**, *17*, 3197; (g) Kaye, S. S.; Dailly, A.; Yaghi, O. M.; Long, J. R. *J. Am. Chem. Soc.* **2007**, *129*, 14176.
7. Pan, L.; Sander, M. B.; Huang, X.; Li, J.; Smith, M. R., Jr.; Bittner, E. W.; Bockrath, B. C.; Johnson, J. K. *J. Am. Chem. Soc.* **2004**, *126*, 1308.
8. (a) Chen, B.; Ockwig, N. W.; Millward, A. R.; Contreras, D. S.; Yaghi, O. M., *Angew. Chem. Int. Ed.* **2005**, *44*, 4745; (b) Ma, S.; Zhou, H.–C. *J. Am. Chem. Soc.* **2006**, *128*, 11734; (c) Forster, P. M.; Eckert, J.; Heiken, B. D.; Parise, J. B.; Yoon, J. W.; Jung, S. H.; Chang, J.-S.; Cheetham, A. K. *J. Am. Chem. Soc.* **2006**, *128*, 16846.
9. (a) Nouar, F.; Eubank, J. F.; Bousquet, T.; Wojtas, L.; Zaworotko, M. J.; Eddaoudi, M. *J. Am. Chem. Soc.* **2008**, *130*, 1833; (b)
10. (a) Sun, D.; Ma, S.; Ke, Y.; Collins, D. J.; Zhou, H.–C. *J. Am. Chem. Soc.* **2006**, *128*, 3896; (b) Chen, B.; Ma, S.; Zapata, F.; Lobkovsky, E. B.; Yang, J. *Inorg. Chem.* **2006**, *45*, 5718.
11. Batten, S. R.; Robson, R. *Angew. Chem. Int. Ed.* **1998**, *37*, 1460.
12. Rowsell, J. L. C.; Yaghi, O. M. *Angew. Chem. Int. Ed.* **2005**, *44*, 4670.

13. Kesanli, B.; Cui, Y.; Smith, M. R.; Bittner, E. W.; Bockrath, B. C.; Lin, W. *Angew. Chem. Int. Ed.* **2005**, *44*, 72.
14. Ma, S. Sun, D.; Ambrogio, M. W.; Fillinger, J. A.; Parkin, S.; Zhou, H.-C. *J. Am. Chem. Soc.* **2007**, *129*, 1858.
15. Dinca, M.; Dailly, A.; Tsay, C.; Long, J. R. *Inorg. Chem.* **2008**, *47*, 11.
16. Eckert, J.; Kubas, G. J. *J. Phys. Chem.* **1993**, *97*, 2378-2384.
17. Silvera, I. F. *Rev. Mod. Phys.* **1980**, *52*, 393-452.
18. Forster, P. M.; Eckert, J.; Chang, J.-S.; Park, S. E.; Férey, G.; Cheetham, A. K. *J. Am. Chem. Soc.* **2003**, *125*, 1309.
19. Schimmel, H. G.; Kearley, G. J.; Nijkamp, M. G.; Visser, C. T.; de Jong, K. P.; Mulder, F. M. *Chem.-Eur. J.* **2003**, *9*, 4764.
20. (a) Rowsell, J. L. C.; Eckert, J. Yaghi, O. M. *J. Am. Chem. Soc.*, **2005**, *127*, 14904; (b) Liu, Y.; Eubank, J. F.; Cairns, A. J.; Eckert, J.; Kravtsov, V. C.; Luebke, R.; Eddaoudi, M. *Angew. Chem. Int. Ed.* **2007**, *46*, 3278; (c) Liu, Y.; Brown, C. M.; Neumann, D. A.; Peterson, V. K.; Kepert, C. J. *J. Alloys Compd.* **2007**, *446-447*, 385.
21. Everett, D. H.; Powl, J. C. *J. Chem. Soc. Faraday Trans. 1* **1976**, *72*, 619.
22. Yang, R.T. *Gas adsorption by Adsorption Processes*; Butterworth: Boston, 1997.
23. Roquerol, F.; Rouquerol, J.; Sing, K., *Adsorption by Powders and Solids: Principles, Methodology, and Applications*; Academic Press: London, 1999.
24. Lee, J. Y.; Li, J. Jagiello, J. *J. Solid State Chem.* **2005**, *178*, 2527.
25. Nicol, J. M.; Eckert, J.; Howard, J.; *J. Phys. Chem.* **1988**, *92*, 7117.
26. Wang, X.-S.; Ma, S.; Forster, P.M.; Yuan, D.; Yoon, J. W.; Hwang, Y. K.; Chang, J.-S.; Eckert, J.; López, J. J.; Murphy, B. J.; Parise, J. B.; Zhou, H.-C. submitted to *JACS*.
27. (a) Anderson, C.-R.; Coker, D. F.; Eckert, J.; Bug, A. L. R. *J. Chem. Phys.* **1999**, *111*, 7599; (b) Anderson, C.-R.; McKinnon, J. A.; Coker, D. F.; Eckert, J.; Bug, A. L. R. *J. Chem. Phys.* **2001**, *114*, 10137.
28. Schimmel, H. G.; Kearley, G. J.; Nijkamp, M. G.; Visser, C. T.; de Jong, K. P.; Mulder, F. M. *Chem. Eur. J.* **2003**, *9*, 4764.
29. Gould, S. L.; Tranchemontagne, D.; Yaghi, O. M.; Garcia-Garibay, M. A. *J. Am. Chem. Soc.* **2008**, *130*, 3246.

30. (a) Jung, D. H.; Kim, D.; Lee, T. B.; Choi, S. B.; Yoon, J. H.; Kim, J.; Choi, K.; Choi, S.-H. *J. Phys. Chem. B.* **2006**, *110*, 22987; (b) Dubbleldam, D.; Frost, H.; Walton, K. S.; Snurr, R. Q. *Fluid Phase Equilibria*, **2007**, *261*, 152; (c) Sagara, T.; Klassen, J.; Ortony, J.; Ganz, E., *J. Chem. Phys.* **2005**, *123*, 014701
31. (a) S. S. Han, W. A., III Goddard, *J. Am. Chem. Soc.*, 2007, **129**, 8422; (b) S. S. Han, W.-Q. Deng, W. A., III Goddard, *Angew. Chem. Int. Ed.*, **2007**, *46*, 6289.
32. Li, Y.; Yang, R. T. *Langmuir*, **2007**, *23*, 12937.

Section II

Methane Storage Application of Porous MOFs

Chapter 7

Introduction to Methane Storage in Porous Metal-Organic Frameworks^f

As with hydrogen, methane is considered an ideal energy gas for future applications. In terms of near-term practical utilization and innovations necessary for commercialization, methane appears to be a more promising alternative for mobile applications.

7.1 Methane Storage Goals

Methane is the primary component of natural gas; as such, an extensive system of collection, purification, and distribution infrastructure already exists, capable of delivering methane to the majority of homes and businesses in the US and many other countries worldwide. Deposits of methane-containing natural gas are more widespread globally than those of petroleum, and its refinement (purification) to an energy fuel is much simpler than that of crude petroleum oil to gasoline or diesel fuels. Methane is also produced by decomposition of organic waste and by bacteria in the guts of ruminants and termites. In fact, methane and natural gas are often considered waste products in crude oil collection and refining and other industrial processes and are often burned off in giant flares with no secondary energy capture. Finally, compressed natural gas (CNG) vehicles already exist and make up a small fraction of commercial and personal vehicle fleets in Argentina, Brazil, Pakistan, Italy, Iran, and the US. However, as in the case of hydrogen, current vehicles store the methane CNG in high-pressure (greater than 200 atm) tanks, which are heavy and potentially explosive. To address the needs for better methane-storage technology, the US Department of Energy has set targets for methane storage systems at 180 v(STP)/v (STP equivalent of methane per volume of adsorbent material storage system) under 35 bar and near ambient temperature, with the energy density of adsorbed natural gas comparable to that of current CNG technology.¹

^f This section was adapted from the co-authored review manuscript “Hydrogen and Methane Storage in MOFs” submitted as an invited chapter to the book *Metal-Organic Frameworks: Design and Application* L. MacGillivray Ed.; Wiley-VCH, 2009.

As in the case of hydrogen storage, a variety of porous materials have been extensively evaluated as methane storage materials, including activated carbon,² carbon nanotubes,³ and zeolites.⁴ However, with the exception of activated carbon,¹ none of these materials have been able to store quantities equal to the DOE targets, and a high-capacity adsorbent remains elusive; like the hydrogen molecule, the methane molecule is small and interacts only weakly with the pore walls of the adsorbent.

7.2 Methane Storage in Porous MOFs

MOFs are a relative newcomer to the field of methane adsorbants: while carbon materials have been extensively studied for methane storage since the early 1990s. The first reported measurement of methane uptake by a MOF was in 1999 by Kitagawa and coworkers.⁵ The methane uptake of this pyrazine-based MOF was low, comparable to several zeolites. A second MOF reported by Kitagawa and coworkers the next year represented a serious effort at rationally synthesizing a material that would have a higher uptake of methane; this material exceeded by nearly 100% the most absorptive zeolite, zeolite 5A.⁶ However, the field of methane storage on MOFs has not expanded as quickly as the hydrogen-storage field, perhaps due to the existence of a successful, albeit unattractive, storage system for methane, namely the CNG cylinder.

As in the case of hydrogen storage, a variety of factors influence the ability of the framework to adsorb methane, namely surface area and pore volume, pore size, and heat of adsorption (with contributions from both framework topology and chemical functionality).⁷ For example, the contribution of catenation / interpenetration was demonstrated by Kitagawa and coworkers by a series of azopyridine-based MOFs, with the highest of the series adsorbing ~ 60 v(STP)/v.⁸

The ability of IRMOF-6 to adsorb a higher amount of methane than the other members of the IRMOF series was attributed to both the accessible surface area and the functionality of the ligand: in IRMOF-6, the phenyl ring of the typical bdc ligand was modified to generate 1,2-cyclobutane-3,6-benzenedicarboxylate. The resulting MOF was found to adsorb 155 v(STP)/v methane at 298 K and 36 atm, considerably higher than any zeolite material or any other MOF at the time.⁹ Molecular simulations indicated that

further functionalization of the ligand by inclusion of an anthracene ring would increase methane uptake further, perhaps within reach of the DOE goal.⁷

7.3 References

- (1) Burchell, T.; Rogers, M., *SAE Tech. Pap. Ser.* **2000**, 2000-01-2205.
- (2) Quinn, D. F.; MacDonald, J. A., *Carbon* **1992**, 30, 1097.
- (3) Muris, M.; Dupont-Pavlovsky, N.; Bienfait, M.; Zeppenfeld, P., *Surf. Sci.* **2001**, 492, 67.
- (4) Dunn, J. A.; Rao, M.; Sircar, S.; Gorte, R. J.; Myers, A. L., *Langmuir* **1996**, 12, 5896.
- (5) Kondo, M.; Okubo, T.; Asami, A.; Noro, S.-i.; Yoshitomi, T.; Kitagawa, S.; Ishii, T.; Matsuzaka, H.; Seki, K., *Angew. Chem. Int. Ed.* **1999**, 38, 140.
- (6) Noro, S.-i.; Kitagawa, S.; Kondo, M.; Seki, K., *Angew. Chem., Int. Ed.* **2000**, 39, 2082.
- (7) Düren, T.; Sarkisov, L.; Yaghi, O. M.; Snurr, R. Q., *Langmuir* **2004**, 20, 2683.
- (8) Kondo, M.; Shimamura, M.; Noro, S.-i.; Minakoshi, S.; Asami, A.; Seki, K.; Kitagawa, S., *Chem. Mater.* **2000**, 12, 1288.
- (9) Eddaoudi, M.; Kim, J.; Rosi, N.; Vodak, D.; Wachter, J.; O'Keeffe, M.; Yaghi, O. M., *Science* **2002**, 295, 469.

Chapter 8

Metal-Organic Framework from an Anthracene Derivative Containing Nanoscopic Cages Exhibiting High Methane Uptake[§]

8.1 Introduction

Ongoing efforts have been made in the search for alternative fuels to supplement or replace widely used gasoline and diesel fuels in vehicular application. Among various alternative fuels, methane stands out when its profusion and availability are considered.¹ However, the lack of an effective, economic, and safe on-board storage system is one of the major technical barriers preventing methane-driven automobiles from competing with the traditional ones. To promote the vehicular application of methane, the U.S. Department of Energy (DOE) has set the target for methane storage at 180 v(STP)/v (Standard temperature and pressure equivalent volume of methane per volume of the adsorbent material) under 35 bar, near ambient temperature), with the energy density of adsorbed natural gas (ANG) being comparable to that of compressed natural gas (CNG) used in current practice.²

Several types of porous materials including single-walled carbon nanotubes,³ zeolites,⁴ and activated carbon⁵ have been extensively tested and evaluated as potential storage media for methane. However, the DOE targets for methane storage remain illusive despite significant progress in activated carbon materials.⁶

Emerging as a new type of porous materials, metal-organic frameworks (MOFs)⁷ have become a burgeoning field of research in the past decade due to their interesting structures and various potential applications.⁸ In particular, their exceptionally high surface areas,⁹ uniform but tunable pore sizes,¹⁰ and functionalizable pore walls¹¹ make MOFs suitable for methane storage and a number of other applications. Several porous MOFs have been screened for methane storage but none have reached the DOE target.^{10a,12} A recent computational study indicated that aromatic rings in MOFs can

[§] This chapter was reprinted with permission from: Ma, S.; Sun, D.; Simmons, J. M.; Collier, C. D.; Yuan, D.; Zhou, H.-C. *J. Am. Chem. Soc.* **2008**, *130*, 1012-1016. Copyright 2008, American Chemical Society.

improve the methane-binding energy, enhancing both the uptake and the heat of methane-adsorption.¹³

Recently, a theoretically proposed MOF (IRMOF-993) based on 9, 10-anthracene-dicarboxylate (adc) (scheme 8.1) was predicted to have a methane adsorption capacity of 181 v(STP)/v, surpassing the DOE target.¹³ However, experiments in our laboratory using 9, 10-anthracene-dicarboxylate have led to an ultramicroporous MOF (PCN-13, PCN stands for Porous Coordination Network) with very limited methane uptake (Figure 8.1). Instead, PCN-13 exhibits selective adsorption of hydrogen and oxygen over nitrogen and carbon monoxide because of the confined pore size (~ 3.5 Å).¹⁴ To enlarge the pore size and to continue our theme of building metal-organic frameworks containing nanoscopic coordination cages for gas storage,^{8f,g,h} we have adopted a new ligand, 5,5'-(9,10-anthracenediyl)di-isophthalate (adip, scheme 8.1). Under solvothermal reaction conditions, the reaction between H₄adip and Cu(NO₃)₂ gave rise to a porous MOF designated PCN-14. In this chapter, the synthesis and characterization of H₄adip and PCN-14 and the methane-adsorption studies of the MOF will be addressed.

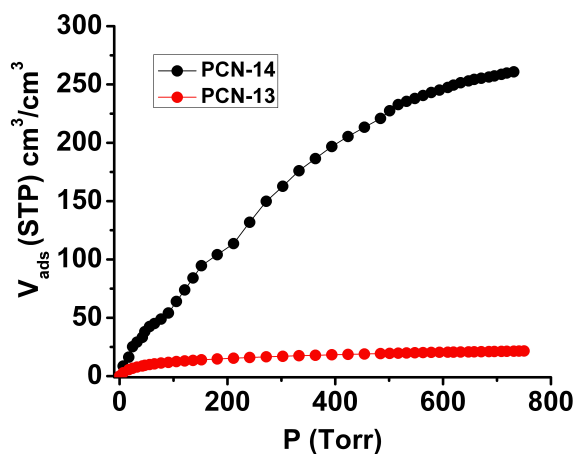
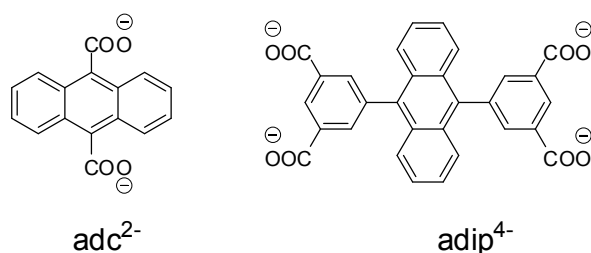


Figure 8.1 Methane adsorption isotherms for PCN-13 and PCN-14 at 195 K.



Scheme 8.1 The carboxylate linkers.

8.2 Experimental Details

General Information: Commercially available reagents were used as received without further purification. Elemental analyses (C, H, and N) were obtained by Canadian Microanalytical Service Ltd.¹⁵ TGA was performed under N₂ on a PerkinElmer TGA 7 and a Beckman Coulter SA3100 surface area analyzer was used to measure gas adsorption. NMR data were collected on a Bruker 300 MHz spectrometer. XRPD patterns were obtained on a Scintag X1 powder diffractometer system using CuK α radiation with a variable divergent slit, solid-state detector, and a routine power of 1400 W (40 kV, 35 mA). Powder samples were dispersed on low-background quartz XRD slides (Gem Depot, Inc., Pittsburgh, Pennsylvania) for analyses.

Synthesis of 5,5'-(9,10-anthracenediyl)bis(1,3-benzenedimethoxycarbonyl), 1: Anthracene 9,10-diboronic acid (0.5 g, 0.002 mol), dimethyl-5-bromo-isophthalate (1.7 g, 0.006 mol) and Pd(PPh₃)₄ (0.02 g) were mixed in a 500 mL flask. The flask was pumped under vacuum for 30 minutes and 80 mL degassed THF was added. After the addition of 15 mL degassed 2M Na₂CO₃ solution, the mixture was heated to reflux under nitrogen atmosphere for 40 hours. The resulting yellow mixture was diluted with water and extracted with CH₂Cl₂ three times. The mixed organic phase was dried with MgSO₄ and the solvent was removed to give a brown solid. The crude product was purified by column chromatography on silica gel with CHCl₃ as the eluent to give **1** as a yellow solid (0.6 g, 53 %). ¹H NMR (CDCl₃): δ = 8.9 (s, 2 H), 8.5 (s, 4 H), 7.6 (d, 4 H), 7.4 (m, 4 H), 4.0 (s, 12 H).

Synthesis of H4adip, 5,5'-(9,10-anthracenediyl)di-isophthalic acid, 2: Compound **1** (0.6 g, 0.001 mol) was suspended in 50 mL of THF, to which 10 mL of a 2 M KOH aqueous solution was added. The mixture was stirred at room temperature

overnight. THF was removed using a rotary evaporator and diluted hydrochloric acid was added to the remaining aqueous solution until it became acidic. The solid was collected by filtration, washed with water several times and dried to give **2** (0.4 g, 80%). ^1H NMR (CDCl_3): $\delta = 13.5$ (br, 4 H), 8.7 (s, 2 H), 8.2 (s, 4 H), 7.5 (m, 8 H).

Synthesis of PCN-14, $\text{Cu}_2(\text{H}_2\text{O})_2(\text{adip})\cdot 2\text{DMF}$: A mixture of **2** (0.005 g, 1.4×10^{-5} mol), $\text{Cu}(\text{NO}_3)_2 \cdot 2.5\text{H}_2\text{O}$ (0.02 g, 8.2×10^{-6} mol), and 2 drops of HBF_4 in 1.5 mL DMF was sealed in a Pyrex tube under vacuum and heated to 75°C at a rate of $1^\circ\text{C}/\text{min}$, kept at that temperature for 1 day, and cooled to room temperature at a rate of $0.1^\circ\text{C}/\text{min}$. The resulting green block crystals were washed with DMF (yield: 75% based on **2**), and has a formula of $\text{Cu}_2(\text{H}_2\text{O})_2(\text{adip})\cdot 2\text{DMF}$, which was derived from crystallographic data, elemental analysis (calcd: C, 49.94; H, 4.42; N, 3.24. Found: C, 51.03; H, 4.54; N, 3.15%), and TGA (Figure 8.2).

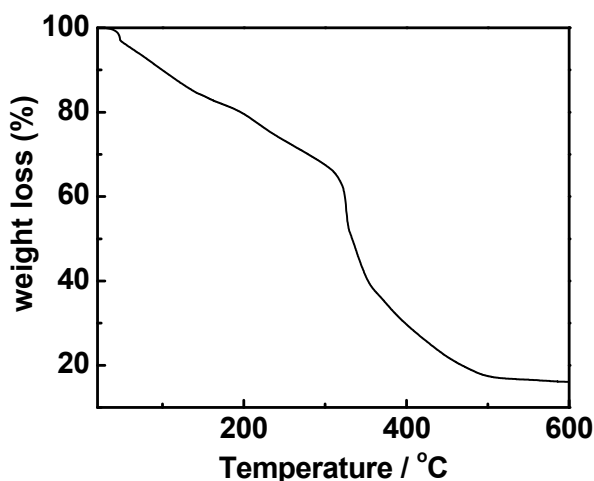


Figure 8.2 TGA plot of PCN-14.

X-ray Crystallography: Single crystal X-ray structure determination of PCN-14 was performed on a specially configured diffractometer based on the Bruker-Nonius X8 Proteum using focused $\text{Cu-K}\alpha$ radiation ($\lambda = 1.54178 \text{ \AA}$). Raw data for all structures were processed using SAINT and absorption corrections were applied using SADABS.¹⁶ The structures were solved by direct method and refined by full-matrix least-squares on F^2 with anisotropic displacement parameters for non-H atoms using SHELX-97.¹⁷ The hydrogen atoms on the carbon were placed in calculated position with isotropic

displacement parameters set to $1.2 \times U_{eq}$ of the attached atom. Solvent molecules in the structure were highly disordered and were impossible to refine using conventional discrete-atom models. To resolve these issues, the contribution of solvent electron density was removed by the SQUEEZE routine in PLATON.¹⁸

Low-pressure Nitrogen Sorption Measurements: The low-pressure nitrogen adsorption measurements were performed at 77 K and 0 - 760 torr on a Beckman Coulter SA 3100 surface area and pore size analyzer. An as-isolated sample of PCN-14 was immersed in methanol for 24 hours, and the extract was decanted. Fresh methanol was subsequently added, and the crystals were allowed to stay for an additional 24 hours to remove the non-volatile solvates (DMF and H₂O). The sample was collected by decanting and treated with dichloromethane similarly to remove methanol solvates. After the removal of dichloromethane by decanting, the sample was dried under a dynamic vacuum ($< 10^{-3}$ torr) at room temperature (25 °C) overnight. Before the measurement, the sample was dried again by using the “outgas” function of the surface area analyzer for 4 hour at 120 °C. High purity nitrogen (99.999%) was used for the measurement. The regulator and pipe were flushed with nitrogen before connecting to the analyzer. The internal lines of the instrument were flushed three times by utilizing the “flushing lines” function of the program to ensure the purity of N₂.

High-pressure Methane Sorption Measurements: High pressure methane sorption isotherm measurements on PCN-14 were performed using a home-built fully computer-controlled Sievert apparatus at NIST. The methane used for the high pressure measurements is scientific/research grade with the purity of 99.999%. The detailed specification of the Sievert apparatus and the data analysis can be found in a recently published work.¹⁹ Briefly, the Sievert system is equipped with four high-precision gauges (0.1%) and a closed-cycle cryostat, enabling methane-adsorption measurements over a wide pressure (0 - 50 bar) and temperature (125 - 290 K) range. In all measurements, about 200 mg solvent-exchanged sample was used, which was activated under vacuum (less than 10^{-4} torr) in two stages: first heating at room temperature overnight, and then at 120 °C for at least 4 h. Once activated, the samples were transferred to He-glove box and never exposed to air.

Excess Adsorption and Absolute Adsorption: Details of excess adsorption and absolute adsorption have been described in a recently published work¹⁹ as well as in some other published work.²⁰ In brief, the capacity of excess adsorption is the amount of adsorption gas interacting with the frameworks, while the capacity of absolute adsorption is the amount of gas both interacting with the frameworks and staying in pores in the absence of gas-solid intermolecular forces. For systems with known crystal structure, it is possible to directly measure the absolute adsorption in addition to excess adsorption.

8.3 Results and Discussion

Structural Descriptions of PCN-14: Single crystal X-ray diffraction²¹ revealed that PCN-14 crystallizes in the space group $R-3c$, different from those of previously reported $[\text{Cu}_2\text{L}(\text{H}_2\text{O})_2]$ MOFs (L = biphenyl-3,3',5,5'-tetracarboxylate, terphenyl-3,3'',5,5'''-tetracarboxylate, or quaterphenyl-3,3''',5,5''''-tetracarboxylate)²², which all crystallize in $R-3m$ space group. PCN-14 consists of a dicopper paddlewheel secondary building unit and the adip ligand. In the ligand, the four carboxylate groups and the two phenyl rings of the isophthalate motifs are almost in a plane, while the dihedral angle between the anthracene ring and the phenyl rings is 70.4° . Every 12 adip ligands connect 6 paddlewheel SBUs to form a squashed cuboctahedral cage (Figure 8.3a), if one connects the centers of the six paddlewheels and the six anthracenyl groups (broken lines in Figure 8.3a). The anthracenyl rings in the cage are in close contact (2.6 \AA between an H atom and the center of a phenyl ring from the adjacent anthracenyl group). The cuboctahedral cage has eight triangular windows and six square windows for gas molecules to access the interior surface. The cuboctahedral cage can also be viewed as four intersecting hexagons. The dimensions of the hexagons are 9.23 \AA along an edge and 18.45 between two opposite corners. Extending each hexagon in the cuboctahedral cage into two-dimensional honeycombs gives rise to a three-dimensional 4-connected net (Figure 8.4). The three-dimensional net can also be viewed as a framework consisting of cuboctahedral nanoscopic cages (Figure 8.5a). An alternative way of viewing the cage is to connect the centers of all isophthalate phenyl rings, forming a polygon with 18 vertices, 20 faces, and 30 edges. This polygon can be viewed as being formed by inserting an irregular hexagonal prism in between the two halves of a cuboctahedron (Figure 8.3b).

The cage has 1150 \AA^3 of void and is approximately spherical providing efficient and accessible interior surface for gas storage.

PCN-14 is very porous (Figure 8.5b). The solvent accessible volume for the desolvated PCN-14 is 63.5%, calculated using the PLATON routine,¹⁸ comparable to those of other MOFs based on isophthalate derivatives.^{22a}

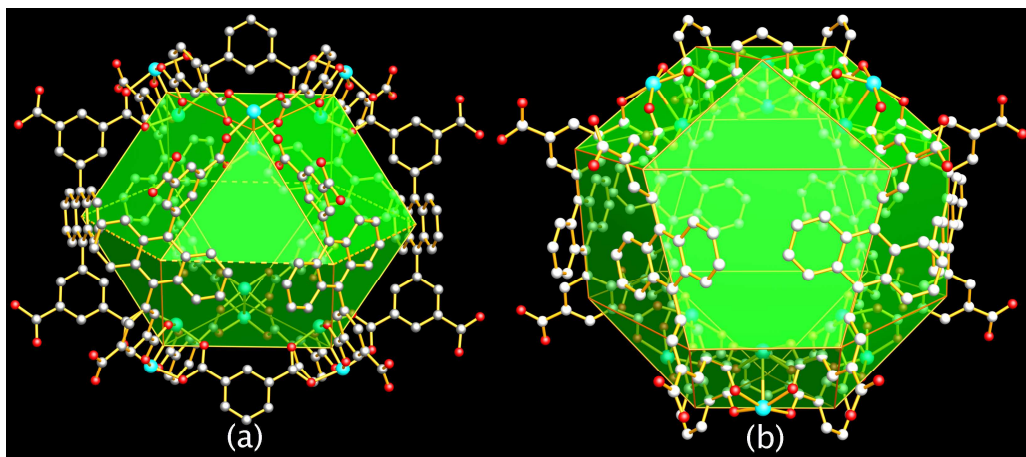


Figure 8.3 Nanoscopic cages in PCN-14: (a) The squashed cuboctahedral cage; (b) a nanoscopic cage with 18 vertices, 30 edges, and 20 faces. Color scheme: C, grey; Cu, turquoise; and O, red.

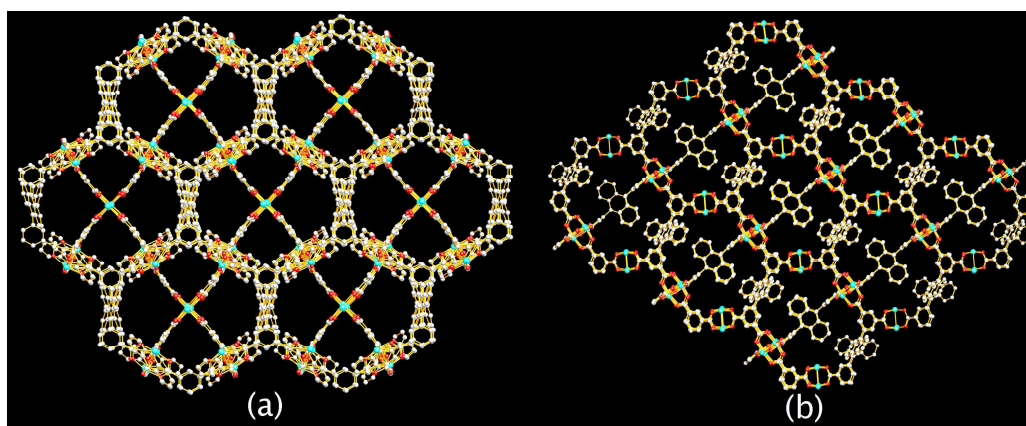


Figure 8.4 The 3D framework of PCN-14: viewed from (a) the $[2\ 1\ 1]$ and (b) the $[1\ 0\ 0]$ directions.

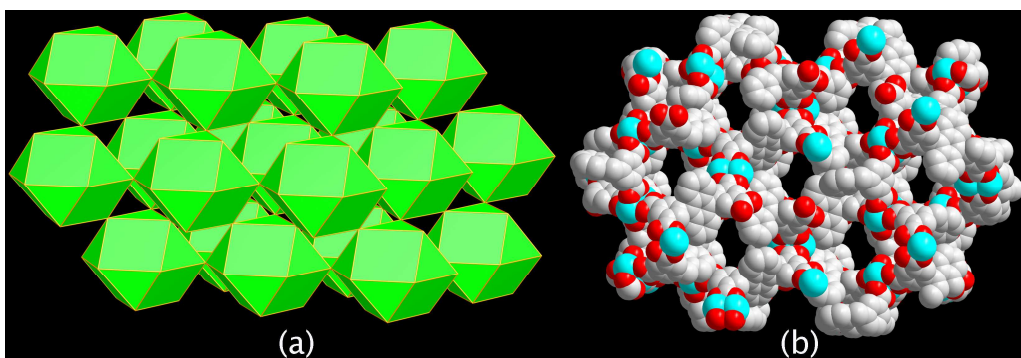


Figure 8.5 The 3D framework of PCN-14: viewed as (a) a cuboctahedral net (b) a space filling model on the $[1\ 0\ 3]$ plane.

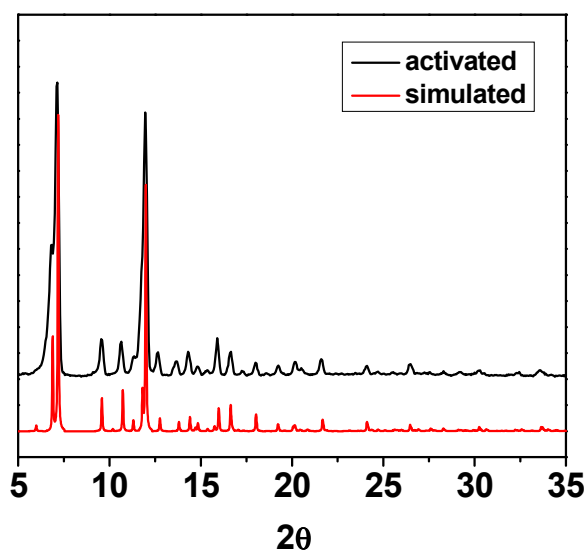


Figure 8.6 PXRD patterns of PCN-14.

Low-pressure Nitrogen Sorption: A PCN-14 sample was fully activated by the procedure described above in the experimental section. The integrity of the framework was confirmed by powder X-ray diffraction (PXRD) before the nitrogen sorption measurements (Figure 8.6). Nitrogen sorption isotherms of the fully activated PCN-14 sample (Figure 8.7) reveals typical Type-I sorption behavior, confirming the permanent porosity of the activated PCN-14. Calculated from the nitrogen adsorption data, the estimated BET surface area of PCN-14 is $1753\text{ m}^2/\text{g}$,²³ and the estimated pore volume is $0.87\text{ cm}^3/\text{g}$. These values are slightly higher than those of MOF-505, but lower than those

of the two other MOFs using isophthalate derivatives.²² Assuming monolayer coverage, PCN-14 has an estimated Langmuir surface area of 2176 m²/g.

High pressure methane sorption: High pressure methane sorption measurements were performed at various temperatures to investigate the methane uptake saturations. The methane uptake capacities were converted directly into v(STP)/v by using the crystallographic density of PCN-14 (0.871 g/cm³). As shown in Figure 8.8, the methane uptake saturations of both excess adsorption and absolute adsorption decrease with increasing temperatures. The saturation of excess methane adsorption in PCN-14 at 125 K can reach 434 v(STP)/v, which corresponds to an adsorbed methane density of 310 mg/ml. The density is 73.4% of that of liquid methane (422.6 mg/ml) at 113 K.²⁴ At 290 K and 35 bar, the excess adsorption capacity of methane in PCN-14 is 220 v(STP)/v, corresponding to an absolute adsorption capacity of 230 v(STP)/v. The excess methane adsorption value is 22% higher than the DOE target of 180 v(STP)/v for methane.² To the best of our knowledge, PCN-14 exhibits the highest methane uptake capacity among reported porous materials for methane adsorption.^{12,13}

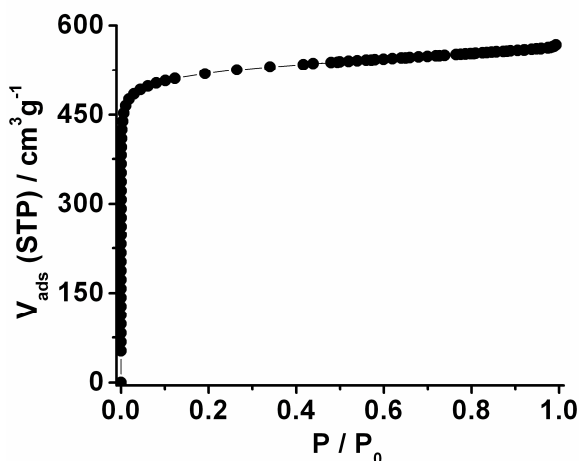


Figure 8.7 Nitrogen gas adsorption isotherm at 77 K of PCN-14.

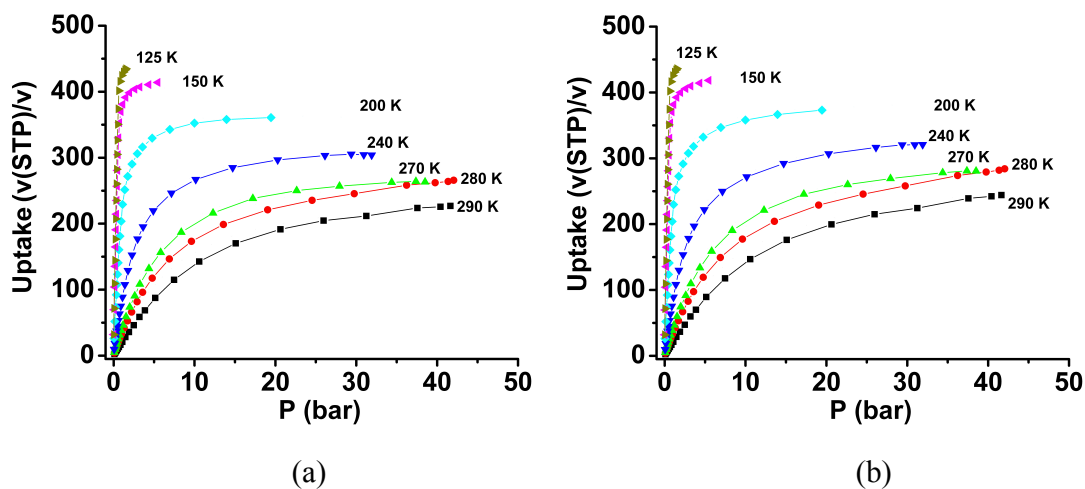


Figure 8.8 High pressure methane sorption isotherms at various temperatures: (a) excess adsorption; (b) absolute adsorption.

Analysis of Heat of Adsorption. The strength of interactions between the framework and methane can be reflected by isosteric heats of adsorption Q_{st} . The isosteric heats of adsorption of methane were calculated using the Clausius-Clapeyron equation,²⁵

$$Q_{st} = -R \cdot d(\ln P) / d(1/T)$$

using isotherms taken at 270, 280, and 290 K. As shown in Figure 8.9, the Q_{st} at initial stage is as high as 30 kJ/mol, revealing strong interactions between methane and the framework. The Q_{st} first slowly decreases and then increases gradually with the methane loading. This indicates that at high-concentration methane loading, the methane-methane interaction in addition to the methane-framework interaction becomes dominant as discovered in other MOFs systems.^{8e,19} The high Q_{st} of PCN-14 is unprecedented in MOFs,^{8e,12} and supports the predictions that adding more aromatic rings to the ligand and incorporating nanoscopic cages to the framework can lead to higher affinity of methane.¹³

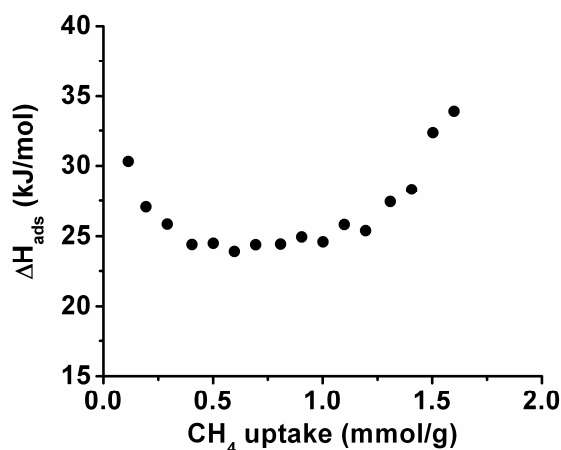


Figure 8.9 Isosteric heats of adsorption of methane for PCN-14.

In summary, a microporous MOF, PCN-14, based on a pre-designed anthracene derivative, 5,5'-(9,10-anthracenediyl)di-isophthalate, was synthesized and structurally characterized. It contains nanoscopic cages suitable for methane uptake. N₂ adsorption measurements of PCN-14 at 77 K reveal an estimated Langmuir surface area of 2176 m²/g and an estimated pore volume of 0.87 cm³/g. High pressure methane adsorption studies show that PCN-14 exhibits an absolute methane-adsorption capacity of 230 v/v (28% higher than the DOE target of 180 v/v at ambient temperatures) and heats of adsorption of methane of around 30 kJ/mol, both record highs among those reported for methane-storage materials.

8.4 References

- (1) U.S. Energy Policy Act of 1992 (EPAct).
- (2) Burchell, T; Rogers, M. *SAE Tech. Pap. Ser.* **2000**, 2000-01-2205.
- (3) Muris, M.; Dupont-Pavlovsky, N.; Bienfait, M.; Zeppenfeld, P. *Surf. Sci.* **2001**, *492*, 67.
- (4) Dunn, J. A.; Rao, M.; Sircar, S.; Gorte, R. J.; Myers, A. L. *Langmuir* **1996**, *12*, 5896.
- (5) Quinn, D. F.; MacDonald, J. A. F. *Carbon* **1992**, *29*, 1097.

- (6) (a) Wegrzyn, J.; Gurevich, M. *Appl. Energy*. **1996**, *55*, 71; (b) NSF press release (#07-011) http://www.nsf.gov/news/news_summ.jsp?cntn_id=108390.
- (7) (a) Eddaoudi, M.; Moler, D. B.; Li, H.; Chen, B.; Reineke, T. M.; O'Keeffe, M.; Yaghi, O. M. *Acc. Chem. Res.* **2001**, *34*, 319; (b) Janiak, C., *J. Chem. Soc., Dalton Trans.* **2003**, 2781; (c) Rowsell, J. L. C.; Yaghi, O. M. *Microporous Mesoporous Mater.* **2004**, *73*, 3; (d) Hill, R. J.; Long, D.-L.; Champness, N. R.; Hubberstey, P.; Schroder, M. *Acc. Chem. Res.* **2005**, *38*, 335; (e) Lin, W. B. *J. Solid State Chem.* **2005**, *178*, 2486; (f) Ockwig, N. W.; Delgado-Friedrichs, O.; O'Keeffe, M.; Yaghi, O. M. *Acc. Chem. Res.* **2005**, *38*, 176.
- (8) (a) Seo, J. S.; Whang, D.; Lee, H.; Jun, S. I.; Oh, J.; Jeon, Y. J.; Kim, K., *Nature* **2000**, *404*, 982; (b) Rowsell, J. L. C.; Yaghi, O. M., *Angew. Chem. Int. Ed.* **2005**, *44*, 4670; (c) Matsuda, R.; Kitaura, R.; Kitagawa, S.; Kubota, Y.; Belosludov, R. V. ; Kobayashi, T. C.; Sakamoto, H.; Chiba, T.; Takata, M.; Kawazoe, Y.; Mita, Y. *Nature* **2005**, *436*, 238; (d) Sun, D.; Ma, S.; Ke, Y.; Petersen, T. M.; Zhou, H.-C. *Chem. Commun.* **2005**, 2663; (e) Sun, D.; Ke, Y.; Mattox, T. M.; Ooro, B. A.; Zhou, H.-C. *Chem. Commun.*, **2005**, 5447; (f) Sun, D. ; Ma, S. ; Ke, Y. ; Collins, D. J.; Zhou, H. -C.; *J. Am. Chem. Soc.* **2006**, *128*, 3896; (g) Ma, S.; Zhou, H. -C.; *J. Am. Chem. Soc.* **2006**, *128*, 11734; (h) Ma, S; Sun, D.; Ambrogio, M. W.; Fillinger, J. A.; Parkin, S; Zhou, H.-C. *J. Am. Chem. Soc.* **2007**, *129*, 1858; (i) Sun, D.; Ke, Y.; Mattox, T. M.; Parkin, S.; Zhou, H.-C. *Inorg. Chem.*, **2006**, *45*, 7566; (j) Sun, D.; Collins, D. J.; Ke, Y.; Zuo, J.-L.; Zhou, H.-C. *Chem. Eur. J.*, **2006**, *12*, 3768; (k) Ma, S.; Wang, X.-S.; Manis, E. S.; Collier, C. D.; Zhou, H.-C. *Inorg. Chem.*, **2007**, *46*, 3432; (l) Ma, S.; Sun, D.; Wang, X.-S.; Zhou, H.-C. *Angew. Chem. Int. Ed.* **2007**, *46*, 2458; (m) Collins, D. J.; Zhou, H.-C. *J. Mater. Chem.*, **2007**, *17*, 3154; (n) Yu, C.; Ma, S.; Pechan, M. J.; Zhou, H.-C. *J. Appl. Phys.*, **2007**, *101*, 09E108; (o) Gu, J.-Z.; Lu, W.-G.; Zhou, H.-C.; Lu, T.-B. *Inorg. Chem.*, **2007**, *46*, 5835; (p) Sun, D.; Ke, Y.; Collins, D. J.; Lorigan, G. A.; Zhou, H.-C. *Inorg. Chem.*, **2007**, *46*, 2725.
- (9) (a) Chae, H. K.; Siberio-Perez, D. Y.; Kim, J.; Go, Y. B.; Eddaoudi, M.; Matzger, A. J.; O'Keeffe, M.; Yaghi, O. M. *Nature* **2004**, *427*, 523. (b) Ferey, G.; Mellot-Draznieks, C.; Serre, C.; Millange, F.; Dutour, J.; Surble, S.; Margiolaki, I. *Science* **2005**, *309*, 2040.

- (10) (a) Eddaoudi, Kim, J.; Rosi, N.; Vodak, D.; Wachter, J.; O'Keeffe, M.; Yaghi, O. M. *Science* **2002**, *295*, 469; (b) Chen, B.; Ma, S.; Zapata, F.; Lobkovsky, E. B.; Yang, J. *Inorg. Chem.*, **2006**, *45*, 5718; (c) Chen, B.; Ma, S.; Zapata, F.; Fronczek, F. R.; Lobkovsky, E. B.; Zhou, H.-C. *Inorg. Chem.*, **2007**, *46*, 1233.
- (11) (a) Kitagawa, S.; Kitaura, R.; Noro, S.-i. *Angew. Chem. Int. Ed.* **2004**, *43*, 2334; (b) Wang, X.-S.; Ma, S.; Sun, D.; Parkin, S.; Zhou, H.-C. *J. Am. Chem. Soc.* **2006**, *128*, 16474; (c) Bradshaw, D.; Claridge, J. B.; Cussen, E. J.; Prior, T. J.; Rosseinsky, M. J. *Acc. Chem. Res.* **2005**, *38*, 273.
- (12) (a) Noro, S.-i.; Kitagawa, S.; Kondo, M.; Seki, K. *Angew. Chem. Int. Ed.* **2000**, *39*, 1433; (b) Kondo, M.; Shimamura, M.; Noro, S.-i.; Minakoshi, S.; Asami, A.; Seki, K.; Kitagawa, S. *Chem. Mater.* **2000**, *12*, 1288; (c) Kesanli, B.; Cui, Y.; Smith Milton, R.; Bittner Edward, W.; Bockrath Bradley, C.; Lin, W., *Angew. Chem. Int. Ed.* **2005**, *44*, 72; (d) Bourrelly, S.; Llewellyn, P. L.; Serre, C.; Millange, F.; Loiseau, T.; Ferey, G. *J. Am. Chem. Soc.* **2005**, *127*, 13519.
- (13) Dueren, T.; Sarkisov, L.; Yaghi, O. M.; Snurr, R. Q. *Langmuir* **2004**, *20*, 2683.
- (14) Ma, S.; Wang, X.-S.; Collier, C. D.; Manis, E. S.; Zhou, H.-C. *Inorg. Chem.* **2007**, *46*, 8499.
- (15) Note: Certain commercial suppliers are identified in this paper to foster understanding. Such identification does not imply recommendation or endorsement by the National Institute of Standards and Technology, nor does it imply that the materials or equipment identified are necessarily the best available for the purpose.
- (16) *SAINT+*, version 6.22; Bruker Analytical X-Ray Systems, Inc.: Madison, WI, 2001.
- (17) Sheldrick, G. M. *SHELX-97*; Bruker Analytical X-Ray Systems, Inc.: Madison, WI, 1997.
- (18) Spek, A. L. *J. Appl. Crystallogr.* **2003**, *36*, 7.
- (19) Zhou, W.; Wu, H.; Hartman, M. R.; Yildirim, T. *J. Phys. Chem. C* **2007**, ASAP.
- (20) (a) Dincă, M.; Dailly, A.; Liu, Y.; Brown, C. M.; Neumann, D. A.; Long, J. R. *J. Am. Chem. Soc.* **2006**, *128*, 16876; (b) Furukawa, H.; Miller, M. A.; Yaghi, O. M. *J. Mater. Chem.* **2007**, *17*, 3197.

- (21) X-ray crystal data for PCN-14: $C_{270}H_{162}Cu_{18}O_{90}$, fw = 5989.9, Rhombohedral, $R\bar{3}c$, $a = 18.4530(4) \text{ \AA}$, $b = 18.4530(4) \text{ \AA}$, $c = 76.976(4) \text{ \AA}$, $V = 22699.7(1) \text{ \AA}^3$, $Z = 2$, $T = 90 \text{ K}$, $\rho_{\text{calcd}} = 0.871 \text{ g/cm}^3$, $R_1 (I > 2\sigma(I)) = 0.0518$, $wR_2 (\text{all data}) = 0.1591$, GOOF = 1.071.
- (22) (a) Chen, B. L.; Ockwig, N. W.; Millward, A. R.; Contreras, D. S.; Yaghi, O. M., *Angew. Chem. Int. Ed.* **2005**, *44*, 4745; (b) Lin, X.; Jia, J. H.; Zhao, X. B.; Thomas, K. M.; Blake, A. J.; Walker, G. S.; Champness, N. R.; Hubberstey, P. Schröder, M. *Angew. Chem. Int. Ed.* **2006**, *45*, 7358.
- (23) Walton, K. S.; Snurr, R. Q. *J. Am. Chem. Soc.* **2007**, *129*, 8552.
- (24) Lide, D. R. *Handbook of Chemistry and Physics*, 73rd ed.; CRC Press, Inc. 1992.
- (25) Roquerol, F.; Rouquerol, J.; Sing, K. Adsorption by Powders and Solids: Principles, Methodology, and Applications; Academic Press: London, 1999.

Section III

Microporous MOFs as Molecular Sieves for Selective Gas Adsorption Application

Chapter 9

Introduction to Selective Gas Adsorption in Porous Metal-Organic Frameworks^h

Gas separation and purification are important and energy-consuming in industry. A few of the commercially most important gas separation challenges are: N₂/O₂ separation, N₂/CH₄ separation for natural gas upgrading, and CO removal from H₂ for fuel cell applications¹. Although inorganic zeolites and porous carbon materials can be applied with some success, new adsorbents are still needed to optimize these separation processes to make them commercially more attractive. As a new type of zeolite analogues, porous MOFs feature amenability to design, tunable pore size, and functionalizability of the pore wall. These characteristics give them great potential in selective adsorption of gases.²⁻⁷

9.1 Molecular Sieving Effect in Porous Metal-Organic Frameworks

The molecular-sieving effect arises when molecules of appropriate size and shape are allowed entering the open channels of an adsorbent, while other molecules are excluded. It accounts for the underlying principle for most selective gas-adsorption processes in porous materials with uniform micropores.¹

It is essential to limit the pore size of an adsorbent for effective gas separation. To this point, apertures of porous MOFs can be rationally tuned to a certain size for selective adsorption of specific gas molecules.

Utilizing short bridging ligands is a good way to restrict pore sizes of porous MOFs for gas separation. This was exemplified by Kim *et al.* in the microporous manganese formate MOF. The short length of the formate leads to very small aperture size, which can discriminate H₂ from N₂, and CO₂ from CH₄.⁸ Recently, Long *et al.* confined the pore size of a microporous magnesium MOF to around 3.5 Å by using 2,6-naphthalenedicarboxylic acid. The magnesium MOF exhibited the capability of selective uptake of H₂ or O₂ over N₂ or CO.⁹ Similar molecular-sieving effect was also observed

^h This chapter was adapted from the finished review manuscript “Design and Construction of Metal-Organic Frameworks for Hydrogen Storage and Selective Gas-Adsorption” Submitted as an invited chapter to the book *Design and Construction of Coordination Polymers*; M. Hong, Ed.; Wiley: New York, 2008.

in a 2,4-pyridinedicarboxylate-based cobalt MOF (CUK-1), which could separate H₂ from N₂, O₂ from N₂ and Ar, and CO₂ from CH₄.¹⁰

Interpenetration is well known as an effective way to reduce pore size of MOFs, and has been recently employed to confine the pore size for selective adsorption of gas molecules. Chen *et al.* demonstrated that doubly interpenetrated primitive cubic nets based on bidentate pillar linkers and bicarboxylates could be rationally designed for selective gas adsorption. The microporous MOF Cu(FMA)(4,4'-Bpe)_{0.5} (FMA = fumarate; 4,4'-Bpe = trans-bis(4-pyridyl)ethylene) was constructed by the incorporation of the bicarboxylate FMA and bidentate pillar linker 4,4'-Bpe, and its pore size was tuned by double framework interpenetration to ~ 3.6 Å, which exhibits selective adsorption of H₂ over Ar, N₂ and CO.¹¹ By increasing the length of the bicarboxylates and bidentate pillar linkers, Chen *et al.* introduced triple interpenetration in the microporous MOF Zn(ADC) (4,4'-Bpe)_{0.5} (ADC = 4,4'-azobenzenedicarboxylate; 4,4'-Bpe = trans-bis(4-pyridyl)ethylene), which can distinguish H₂ from N₂ and CO.¹²

9.2 Porous Metal-Organic Frameworks for Kinetic Separation Application

Different from the molecular-sieving effect, kinetic separation is achieved by virtue of the differences in diffusion rates of different molecules. Kinetic separation is of great importance in industry applications, particularly chromatographic applications.¹

The separation of mixed C₈ alkylaromatic compounds (*p*-xylene, *o*-xylene, *m*-xylene, and ethylbenzene) is one of the most challenging separations in chemical industry due to the similarity of their boiling points.¹³ This separation is currently performed by cation-exchanged zeolites X and Y in industry;¹⁴ however, adsorbents with improved separation efficiency are still needed. Recently, Vos *et al.* for the first time investigated the adsorption and separation of a mixture of C₈ alkylaromatic compounds using three porous MOFs: HKUST-1, MIL-53, and MIL-47 in the liquid phase. Through chromatographic experiments, MIL-47 has the highest potential for real separations of C₈ alkylaromatic compounds among the three investigated MOFs. Compared with currently used zeolites, MIL-47 displays high uptake capacity and high selectivity, which are advantageous for its future practical application in industry.¹⁵

The separation of hexane isomers to boost octane ratings in gasoline represents a very important process in the petroleum industry.¹⁶ This is achieved using the high energy consuming method of cryogenic distillation, albeit some alternative novel materials and technologies are now under rapid development. By making use of the pore space to capture and discriminate hexane isomers, porous MOFs have the potential to separate hexane isomers. This was well illustrated by Chen *et al.* in the kinetic separation of hexane isomers by using the three dimensional microporous MOF, Zn(BDC)(Dabco)_{0.5}. The MOF Zn(BDC)(Dabco)_{0.5} contains three-dimensional intersecting pores of about 7.5 Å × 7.5 Å along axis [100] and pores of 3.8 Å × 4.7 Å along axes [010] and [001]. By making use of the narrow channels of 3.8 Å × 4.7 Å to exclusively take up linear nHEX while blocking branched hexane isomers, this MOF was successfully used in the kinetic separation of hexane isomers by fixed-bed adsorption. It exhibited extraordinary separation selectivity to separate branched hexane isomers from linear nHEX. This represented the first example of using microporous MOFs for the kinetic separation of hexane isomers, demonstrating great potential for applications in the very important industrial process of hexane-isomers separation.¹⁷

Another important process to boost octane ratings in gasoline is the separation of alkane isomers, which is currently practiced by some narrow pore zeolites.¹⁸ Chen *et al.* recently demonstrated the application of a microporous MOF (MOF-508) packed column in the GC separation of alkanes. MOF-508 contains 1D pores of 4.0 Å × 4.0 Å, which can selectively accommodate linear alkanes and discriminate branched alkanes. The subtle matching of the size and shape of the alkanes with the micropores of MOF-508 leads to different van der Waals interactions, thus resulting in selective GC separation of alkanes in the MOF-508 column.¹⁹

9.3 References

- (57) R. T. Yang, *Gas Adsorption by Adsorption Processes*; Butterworth: Boston, 1997..
- (58) Eddaoudi, M.; Moler, D. B.; Li, H.; Chen, B.; Reineke, T. M.; O'Keeffe, M.; Yaghi, O. M. *Acc. Chem. Res.* **2001**, *34*, 319.
- (59) James, S. L. *Chem. Soc. Rev.* **2003**, *32*, 276.

- (60) Yaghi, O. M.; O'Keeffe, M.; Ockwig, N. W.; Chae, H. K.; Eddaoudi, M.; Kim, J. *Nature* **2003**, *423*, 705.
- (61) Ockwig, N. W.; Delgado-Friedrichs, O.; O'Keeffe, M.; Yaghi, O. M. *Acc. Chem. Res.* **2005**, *38*, 176.
- (62) Kitagawa, S.; Kitaura, R.; Noro, S.-i. *Angew. Chem. Int. Ed.* **2004**, *43*, 2334.
- (63) Janiak, C. *J. Chem. Soc., Dalton Trans.* **2003**, 2781.
- (64) Dybtsev, D. N.; Chun, H.; Yoon, S. H.; Kim, D.; Kim, K. *J. Am. Chem. Soc.* **2004**, *126*, 32.
- (65) Dincă, M.; Long, J. R. *J. Am. Chem. Soc.* **2005**, *127*, 9376.
- (66) Humphrey, S. M.; Chang, J.-S.; Jhung, S. H.; Yoon, J. W.; Wood, P. T. *Angew. Chem., Int. Ed.* **2007**, *46*, 272.
- (67) Chen, B.; Ma, S.; Zapata, F.; Fronczek, F. R.; Lobkovsky, E. B.; Zhou, H.-C. *Inorg. Chem.* **2007**, *46*, 1233.
- (68) Chen, B.; Ma, S.; Hurtado, E. J.; Lobkovsky, E. B.; Zhou, H.-C. *Inorg. Chem.* **2007**, *46*, 8490.
- (69) Cottier, V.; Bellat, J.-P.; Simonot-Grange, M.-H. *J. Phys. Chem. B* **1997**, *101*, 4798.
- (70) Hulme, R.; Rosensweig, R.; Ruthven, D. *Ind. Eng. Chem. Res.* **1991**, *30*, 752.
- (71) Alaerts, L.; Kirschhock, C. E. A.; Maes, M.; van der Veen, M. A.; Finsy, V.; Depla, A.; Martens, J. A.; Baron, G. V.; Jacobs, P. A.; Denayer, J. F. M.; De Vos, D. E. *Angew. Chem. Int. Ed.* **2007**, *46*, 4293.
- (72) Sohn, S. W. Kerosene ISOSIV Process for Production of Normal Paraffins. In *Handbook of Petroleum Refining Processes*, 3rd ed.; Meyers, R. A., Ed.; McGraw-Hill: New York, 2004.
- (73) Barcia, P. S.; Zapata, F.; Silva, J. A. C.; Rodrigues, A. E.; Chen, B. *J. Phys. Chem. B.* **2007**, *111*, 6101.
- (74) Kulprathipanja, S.; Neuzil, R.W. US Patent 4 445 444, 1984, UOP; [Chem. Abs. 101, 75824].
- (75) Chen, B.; Liang, C.; Yang, J.; Contreras, D. S.; Clancy, Y. L.; Lobkovsky, E. B.; Yaghi, O. M.; Dai, S. *Angew. Chem. Int. Ed.* **2006**, *45*, 1390.

Chapter 10

Ultramicroporous Metal-Organic Framework Based on 9,10-Anthracenedicarboxylate for Selective Gas Adsorptionⁱ

10.1 Introduction

It is fundamental to tune pore sizes and control the pore-size distribution of microporous materials for gas separation and purification. Despite a recent report on a titanosilicate with tunable pore sizes,¹ it is generally difficult to tune pore sizes systematically in inorganic zeolites and zeo-type materials.

Emerging as a new zeolite analogue, microporous metal-organic frameworks (MOFs)² have attracted widespread research interests in the past decade due to their fascinating topologies³ and various potential applications⁴. Unlike traditional inorganic porous materials,⁵ microporous MOFs are amenable to design.⁶ They exhibit controllable pore sizes,⁷ high surface areas,⁸ and intriguing framework flexibility.^{2b,9} Strategies such as utilizing short struts (bridging ligands)¹⁰ or interpenetration¹¹ have been employed to restrict the pore sizes of microporous MOFs for gas separation.

Yaghi and coworkers employed “reticular synthesis”^{6a, b} strategy for the construction of isorecticular MOFs (IRMOFs).⁷ Based on the prototype IRMOF-1 (MOF-5) with $Zn_4O(COO)_6$ cluster as the secondary building unit (SBU), the pore sizes of the IRMOFs could be incrementally varied from 11.2 Å for IRMOF-1 to 19.1 Å for IRMOF-16 by increasing the length of the carboxylate linkers. In the field of gas separation, however, ultramicropores (with pore sizes smaller than 4 Å) are preferred. Our strategy for constructing such pores is to increase the bulkiness of the struts to restrict the pore sizes of the MOF. The sterically hindered ligands in MOF may also force unusual coordination geometry around the metal atoms, which are crucial for a number of applications.⁴

In this chapter, 9,10-anthracenedicarboxylate (adc, Figure 10.1a) is selected as the struts to assemble an ultramicroporous MOF, PCN-13 (PCN represents porous

ⁱ This chapter was reprinted with permission from: Ma, S.; Wang, X.-S.; Collier, C. D.; Manis, E. S.; Zhou, H. C. *Inorg. Chem.* **2007**, *46*, 8499-8501. Copyright 2007, American Chemical Society.

coordination network). Desolvated PCN-13 exhibits gas-adsorption selectivity of oxygen and hydrogen over nitrogen and carbon monoxide.

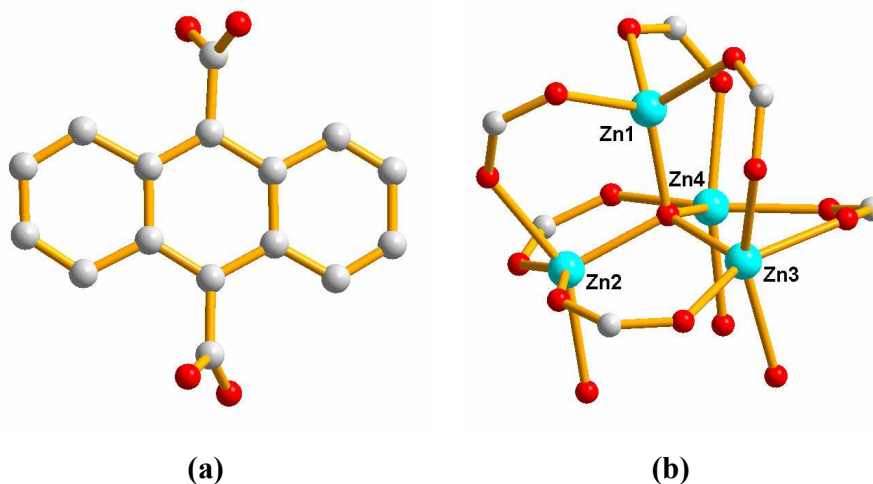


Figure 10.1 (a) The adc ligand; (b) the $Zn_4O(H_2O)_3(COO)_6$ SBU (carbon, grey; oxygen, red; zinc, turquoise).

10.2 Experimental Details

Synthesis of H₂adc ligand: The precursor to adc, 9,10-anthracenedicarboxylic acid (H₂adc), was synthesized by following a previously reported method.¹³ A stirred mixture of 9,10-dibromoanthracene (2.0 g, 5.96 mmol) in anhydrous diethyl ether (20 ml) was cooled in an ice bath, then n-butyllithium (9.76 ml of a 1.6 M solution in hexane, 15.6 mmol) was added dropwise from a syringe. The mixture was allowed to warm to room temperature and stirred for 30 min. After cooling again in ice, dry carbon dioxide (from evaporation of solid through a silica gel trap) was passed over mixture for 1 h. Water (10 ml) and diethyl ether (10 ml) were then added, the aqueous phase separated, washed with two more portions of diethyl ether (2 ml), acidified with 1 M sulfuric acid (pH 2.0), and the resulting yellow product filtered off and dried *in vacuo*.

Preparation of PCN-13: A mixture of H₂ADC (0.005g, 0.019 mmol) and Zn(NO₃)₂•6H₂O (0.02 g, 0.068 mmol) in 1.5 mL dimethylformamide (DMF) was placed in a sealed Pyrex tube, and heated to 120 °C (temperature increasing rate 1 °C/min) in a programmable oven. The tube was allowed to stay at the temperature for 24 hours and was allowed to cool to room temperature (temperature decreasing rate 0.2 °C/min). The light-

brown block crystals obtained were washed with DMF to give pure PCN-13 with the formula $\text{Zn}_4\text{O}(\text{H}_2\text{O})_3(\text{C}_{16}\text{H}_8\text{O}_4)_3 \cdot 2(\text{C}_3\text{H}_7\text{NO})$ (70% yield based on H_2ADC), which was determined based on an X-ray crystallographic study, elemental analysis, and thermogravimetric analysis (TGA) (Figure 10.2). Elemental analysis calcd (%): C 51.05, H 3.49, N 2.20; found: C 46.74, H 3.20, N 2.33.

Gas Sorption Measurements: Gas sorption measurements were performed with a Beckman Coulter SA 3100 surface area and pore size analyzer. A sample of PCN-13 was soaked with methanol for 24 hours, and the extract was discarded. Fresh methanol was subsequently added, and the crystals were soaked for another 24 hours to remove DMF and H_2O solvates. After the removal of methanol by decanting, the sample was dried under dynamic vacuum ($< 10^{-3}$ torr) at room temperature (25 °C) overnight. Before the measurement, the sample was dried again by using the “outgas” function of the surface area analyzer for 2 hour at 50 °C. A sample of 95.0 mg was used for N_2 (99.999%) adsorption measurement, and was maintained at 77K with liquid nitrogen. In the hydrogen adsorption measurement, high purity hydrogen (99.9995%) was used. The regulator and pipe were flushed with hydrogen before connecting to the analyzer. The internal lines of the instrument were flushed three times by utilizing the “flushing lines” function of the program to ensure the purity of H_2 . The measurement was maintained at 77 K with liquid nitrogen. Similar to the procedures used for H_2 measurement at 77 K, highly pure O_2 (99.99%), CO (99.99%), and CO_2 (99.99%) were used for their respective gas adsorption measurements. All the gases used for the measurements were purchased from Linde Gas LLC, Cincinnati, Ohio, USA. The temperatures at 195 K were maintained with an acetone-dry ice bath. To prevent condensation of CO and O_2 at 77 K, the pressure ranges were below 448 torr and 156 torr, respectively. For all adsorption isotherms, P_0 represents a relative saturation pressure given by the Beckman Coulter SA 3100 surface area and pore size analyzer during the measurements: at 77 K, P_0 was 757 torr for N_2 , 441 torr for CO , and 151 torr for O_2 . For hydrogen 757 torr was used as a relative standard.

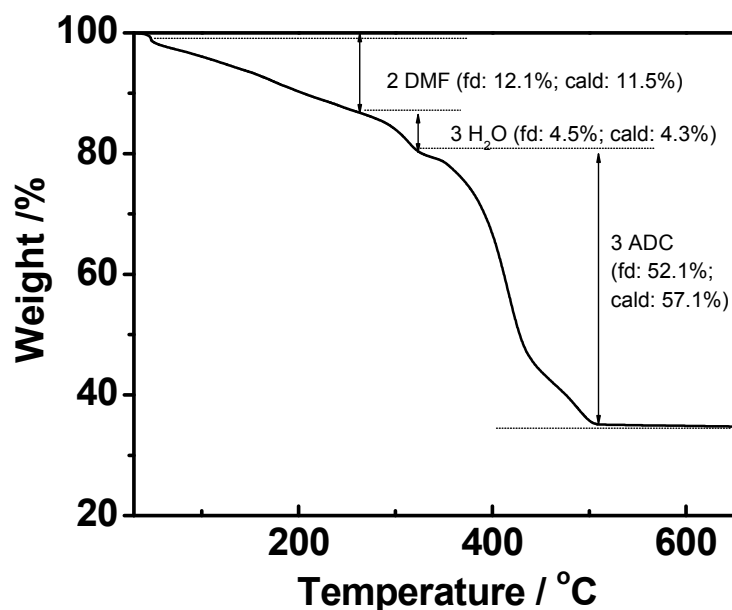


Figure 10.2. TGA for PCN-13.

10.3 Results and Discussions

A single-crystal X-ray crystallographic study¹⁴ revealed that PCN-13 crystallizes in cubic space group $I-43d$. It adopts a very unusual $Zn_4O(H_2O)_3(COO)_6$ cluster (or distorted $Zn_4O(COO)_6$ cluster, Figure 10.1b) as its SBU. In the regular $Zn_4O(COO)_6$ SBU of IRMOF series,⁷ all of the zinc atoms are equivalent and are 3.170 Å apart. However, as shown in Figure 1b, only Zn1 is four-coordinate with three carboxylate oxygen atoms from three different adc ligands and the μ_4 -O atom at the center of the cluster, whereas Zn2, Zn3, and Zn4, are five-coordinate with an additional aqua ligand on each Zn. Unlike the regular tetrahedral Zn_4O , the four zinc atoms form a trigonal pyramid. The basal Zn atoms (Zn2, Zn3 and Zn4) are in the same plane, 3.262 Å apart, and 3.127 Å from the apical Zn (Zn1). Zn1 and μ_4 -O reside on a C_3 axis imposed by crystallographic symmetry. The distances from μ_4 -O to Zn2, Zn3, Zn4 are equal (1.967 Å), which is slightly longer than that between μ_4 -O and Zn1 (1.928 Å). A careful search in the Cambridge Structural Database (CSD) showed that this is likely the only example that contains the $Zn_4O(H_2O)_3(COO)_6$ structural unit albeit the $Zn_4O(COO)_6$ structural motif is very common. Generally speaking, the Zn atoms in the $Zn_4O(COO)_6$ motif are coordinatively saturated. In PCN-13, however, this structural motif is distorted due to the bulkiness of

the anthracene rings; this distortion subsequently opens a coordination site on three of the four Zn atoms; on each open site an extra aqua ligand is accommodated. These aqua ligands will be critical for the gas-adsorption selectivity. Upon aqua ligand removal, the open site will be exposed for other applications.

Every distorted $\text{Zn}_4\text{O}(\text{COO})_6$ SBU connects with six adc ligands (Figure 10.3a) and every adc connects two distorted $\text{Zn}_4\text{O}(\text{COO})_6$ SBUs to form a three-dimensional framework (Figure 10.3b). Due to the bulkiness of the adc ligand, no π - π stacking is allowed in the framework and the structure is non-interpenetrated. The anthracene rings of the adc ligands and the aqua ligands on the Zn atoms block most of the pores, and only very small pores with size of $4.97 \times 4.97 \text{ \AA}$ (atom to atom distance, or $3.5 \times 3.5 \text{ \AA}$ excluding van der Waals radii¹⁵) can be found viewing from the $[1\ 0\ 0]$ direction (Figure 10.3b). This is even smaller than the pore size ($6.3 \times 6.3 \text{ \AA}$) of MOF-993, which is recently proposed theoretically,¹⁶ but should be ideal for gas separation.

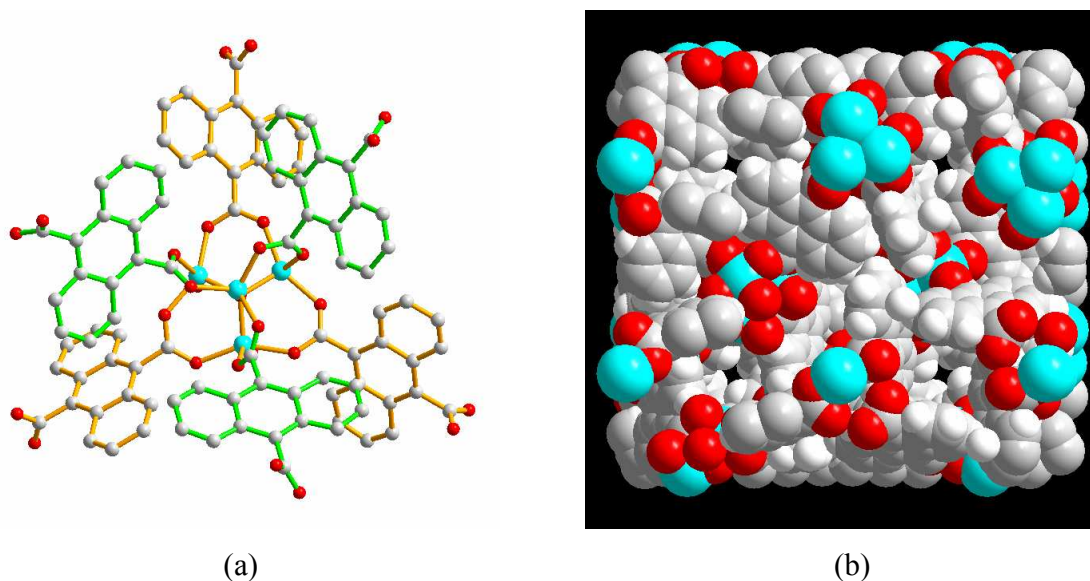


Figure 10.3. Structures of PCN-13: (a) Six adc ligands connecting with Distorted $\text{Zn}_4\text{O}(\text{COO})_6$ SBU; (b) Space-filling model from the $[1\ 0\ 0]$ direction showing ultramicropores.

Based on the pore size of PCN-13, an adsorption measurement using carbon dioxide (kinetic diameter: 3.3 \AA^{17}) instead of dinitrogen (kinetic diameter: 3.64 \AA) was carried out to verify porosity and to determine the surface area of PCN-13.

A freshly prepared sample of PCN-13 was soaked in methanol to remove DMF guest molecules, and then pumped under a dynamic vacuum at $25 \text{ }^\circ\text{C}$ overnight. This is followed by two-hour pumping on the Surface Area and Pore Size Analyzer at $50 \text{ }^\circ\text{C}$ to remove free solvates but not the aqua ligands before the gas adsorption measurements.

The carbon dioxide adsorption isotherm (Figure 10.4a) of a desolvated PCN-13 sample measured at 195 K reveals typical type-I behavior. Fitting the Brunauer-Emmett-Teller (BET) equation¹⁸ to the adsorption isotherm of carbon dioxide gives an estimated surface area of $150 \text{ m}^2/\text{g}$. Using the Dubinin-Radushkevich equation,¹⁹ the pore volume of PCN-13 is estimated to be $0.10 \text{ cm}^3/\text{g}$.

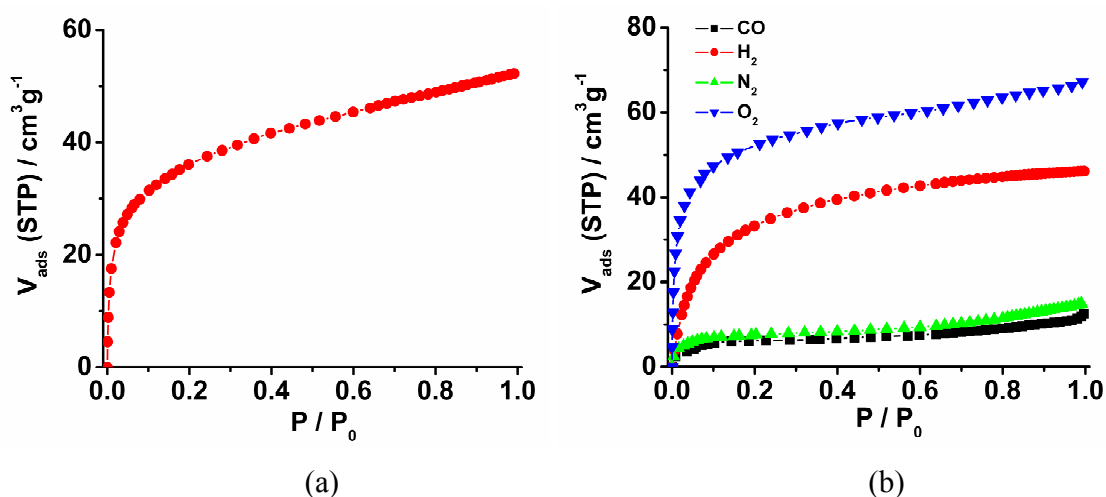


Figure 10.4. Gas adsorption isotherms of the desolvated PCN-13: (a) CO_2 at 195 K ; (b) H_2 , O_2 , N_2 , and CO at 77 K (for H_2 , P_0 represents a relative standard; refer to supporting information for details).

To check the selective adsorption properties of PCN-13, hydrogen, oxygen, nitrogen, and carbon monoxide adsorption studies were carried out at 77 K . As expected, PCN-13 can adsorb significant amount of H_2 ($46 \text{ cm}^3/\text{g}$) and O_2 ($67 \text{ cm}^3/\text{g}$), but very limited amount of N_2 and CO ($\sim 10 \text{ cm}^3/\text{g}$ for both) (Figure 10.4b). In view of the kinetic

diameters of 2.80 Å for H₂, 3.46 Å for O₂, 3.64 Å for N₂ and 3.76 Å for carbon monoxide,¹⁷ it can be inferred that the pore opening of PCN-13 should be between 3.46 and 3.64 Å in diameter. This is consistent with the crystallographically observed aperture size of (3.5 × 3.5 Å) for PCN-13. The ultramicropores permit only hydrogen and oxygen molecules to enter the channels. This selective adsorption of hydrogen and oxygen over nitrogen and carbon monoxide was reported very rarely in the literature.²⁰

The remarkable selectivity may originate from the restricted pore size in PCN-13. If the aqua ligands on the Zn atoms are removed (or “dehydrated”), the adsorption-selectivity should disappear. To test the hypothesis, a desolvated sample of PCN-13 was further heated up to 150 °C under a dynamic vacuum to remove the aqua ligands, which was then used for CO and N₂ gas adsorption measurements. Not surprisingly, the sample after aqua ligand removal takes up significant amount of CO and N₂, whereas the desolvated sample adsorbs very small amount of the two gases (Figure 10.5). After aqua ligand removal, the sample also takes up 35% more hydrogen (Figure 10.6), which can be attributed to the formation of coordinatively unsaturated Zn centers.²¹

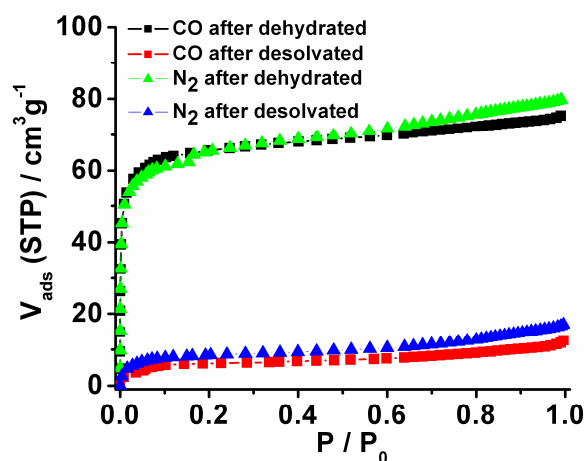


Figure 10.5. N₂ and CO adsorption isotherms at 77 K for desolvated and dehydrated (aqua ligands removed) PCN-13.

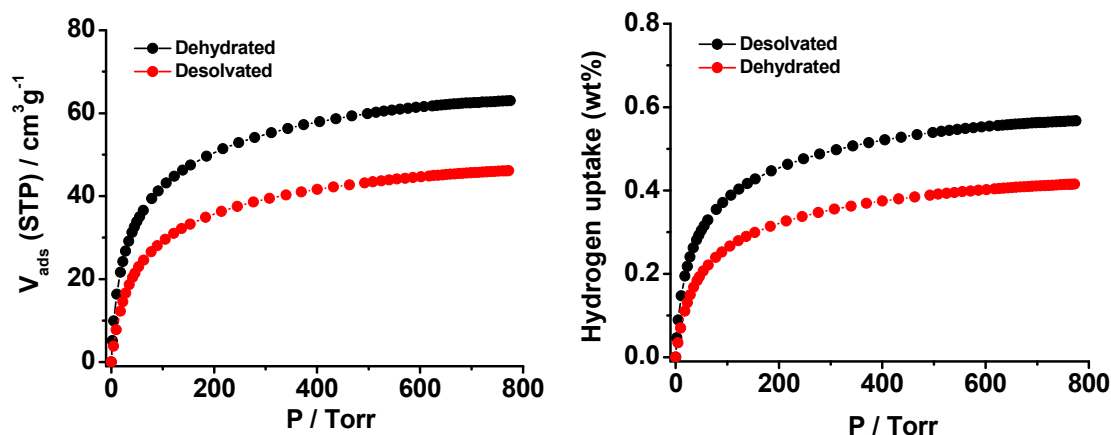


Figure 10.6. H₂ adsorption isotherms for desolvated and dehydrated PCN-13.

The selective adsorption behavior demonstrated by PCN-13 promises its utility in gas separation. For instance, it may have application potential for the separation of nitrogen and oxygen. Similarly, PCN-13 may play a role in the separation of hydrogen from carbon monoxide for fuel cell applications. In addition, it may be applied in hydrogen enrichment of the N₂/H₂ exhaust in ammonia synthesis.

In summary, an ultramicroporous MOF, PCN-13 has been successfully constructed based on a pre-designed anthracene derivative. It exhibits very rare gas-adsorption selectivity of O₂ over N₂, H₂ over CO, and H₂ over N₂. The strategy of using sterically hindered ligands for the rational design of ultramicroporous MOF for gas separation is unique, and may be of general use in the search of ultramicroporous MOFs for selective gas adsorption.

10.4 References

- (32) Kuznicki, S. M.; Bell, V. A.; Nair, S.; Hillhouse, H. W.; Jacubinas, R. M.; Braunbarth, C. M.; Toby, B. H.; Tsapatsis, M. *Nature* 2001, 412, 720.
- (33) (a) Yaghi, O. M.; Li, H.; Davis, C.; Richardson, D.; Groy, T. L. *Acc. Chem. Res.* 1998, 31, 474; (b) Janiak, C., *J. Chem. Soc., Dalton Trans.* 2003, 2781; (c) Kitagawa, S.; Kitaura, R.; Noro, S.-i., *Angew. Chem. Int. Ed.* 2004, 43, 2334; (d) Rowsell, J. L. C.; Yaghi, O. M. *Microporous Mesoporous Mater.* 2004, 73, 3; (e) Hill, R. J.; Long,

- D.-L.; Champness, N. R.; Hubberstey, P.; Schroeder, M. *Acc. Chem. Res.* 2005, 38, 335.
- (34) (a) Delgado-Friedrichs, O.; O'Keeffe, M.; Yaghi, O. M. *Acta Crystallogr., Sect. A: Found. Crystallogr.* 2003, 59, 515; (b) Ockwig, N. W.; Delgado-Friedrichs, O.; O'Keeffe, M.; Yaghi, O. M. *Acc. Chem. Res.* 2005, 38, 176; (c) Batten, S. R., *J. Solid State Chem.* 2005, 178, 2475; (d) Sun, D.; Ma, S.; Ke, Y.; Petersen, T. M.; Zhou, H.-C. *Chem. Commun.* 2005, 2663; (e) Ma, S.; Fillinger, J. A.; Ambrogio, M. W.; Zuo, J.-L.; Zhou, H.-C. *Inorg. Chem. Comm.* 2007, 10, 220.
- (35) (a) Seo, J. S.; Whang, D.; Lee, H.; Jun, S. I.; Oh, J.; Jeon, Y. J.; Kim, K., *Nature* 2000, 404, 982; (b) Zheng, Y.-Z.; Tong, M.-L.; Zhang, W.-X.; Chen, X.-M. *Angew. Chem. Int. Ed.* 2006, 45, 6310; (c) Rowsell, J. L. C.; Yaghi, O. M., *Angew. Chem. Int. Ed.* 2005, 44, 4670; (d) Matsuda, R.; Kitaura, R.; Kitagawa, S.; Kubota, Y.; Belosludov, R. V.; Kobayashi, T. C.; Sakamoto, H.; Chiba, T.; Takata, M.; Kawazoe, Y.; Mita, Y. *Nature* 2005, 436, 238; (e) Humphrey, S. M.; Chang, J.-S.; Jhung, S. H.; Yoon, J. W.; Wood, P. T. *Angew. Chem. Int. Ed.* 2006, 46, 272; (f) Sun, D.; Ma, S.; Ke, Y.; Collins, D. J.; Zhou, H.-C.; *J. Am. Chem. Soc.* 2006, 128, 3896; (g) Ma, S.; Zhou, H.-C.; *J. Am. Chem. Soc.* 2006, 128, 11734; (h) Ma, S.; Sun, D.; Ambrogio, M. W.; Fillinger, J. A.; Parkin, S.; Zhou, H.-C. *J. Am. Chem. Soc.* 2007, 129, 1858; (j) Ma, S.; Wang, X.-S.; Manis, E. S.; Collier, C. D.; Zhou, H.-C. *Inorg. Chem.*, 2007, 46, 3432; (k) Wang, X.-S.; Ma, S.; Sun, D.; Parkin, S.; Zhou, H.-C. *J. Am. Chem. Soc.*, 2006, 128, 16474; (l) Chen, B.; Ma, S.; Zapata, F.; Lobkovsky, E. B.; Yang, J. *Inorg. Chem.*, 2006, 45, 5178; (m) Halder, G. J.; Kepert, C. J.; Moubaraki, B.; Murray, K. S.; Cashion, J. D. *Science* 2002, 298, 1762; (n) Yu, C.; Ma, S.; Pechan, M. J.; Zhou, H.-C. *J. Appl. Phys.* 2007, 101, 09E108.
- (36) Davis, M. E. *Nature* 2002, 417, 813.
- (37) (a) Eddaoudi, M.; Moler, D. B.; Li, H.; Chen, B.; Reineke, T. M.; O'Keeffe, M.; Yaghi, O. M. *Acc. Chem. Res.* 2001, 34, 319. (b) Yaghi, O. M.; O'Keeffe, M.; Ockwig, N. W.; Chae, H. K.; Eddaoudi, M.; Kim, J. *Nature* 2003, 423, 705. (c) Férey, G.; Mellot-Draznieks, C.; Serre, C.; Millange, F. *Acc. Chem. Res.* 2005, 38, 217.
- (38) Eddaoudi, Kim, J.; Rosi, N.; Vodak, D.; Wachter, J.; O'Keeffe, M.; Yaghi, O. M. *Science* 2002, 295, 469.

- (39) (a) Chae, H. K.; Siberio-Pérez, D. Y.; Kim, J.; Go, Y. B.; Eddaoudi, M.; Matzger, A. J.; O'Keeffe, M.; Yaghi, O. M. *Nature* 2004, 427, 523. (b) Férey, G.; Mellot-Draznieks, C.; Serre, C.; Millange, F.; Dutour, J.; Surblé, S.; Margiolaki, I. *Science* 2005, 309, 2040.
- (40) (a) Uemura, K.; Matsuda, R.; Kitagawa, S. *J. Solid State Chem.* 2005, 178, 2420; (b) Bradshaw, D.; Claridge, J. B.; Cussen, E. J.; Prior, T. J.; Rosseinsky, M. J. *Acc. Chem. Res.* 2005, 38, 273; (c) Kitagawa, S.; Kazuhiro, U. *Chem. Soc. Rev.* 2005, 34, 109.
- (41) Dybtsev, D. N.; Chun, H.; Yoon, S. H.; Kim, D.; Kim, K. *J. Am. Chem. Soc.* 2004, 126, 32.
- (42) Chen, B.; Ma, S.; Zapata, F.; Fronczek, F. R.; Lobkovsky, E. B.; Zhou, H.-C. *Inorg. Chem.*, 2007, 46, 1233.
- (43) Ma, S.; Sun, D.; Wang, X.-S.; Zhou, H.-C. *Angew. Chem. Int. Ed.* 2007, 47, 2458.
- (44) Jones, S.; Atherton, J. C. C.; Elsegood, M. R. J.; Clegg, W. *Acta Crystallogr., Sect. C*, 2000, 56, 881.
- (45) X-ray crystal data for PCN-13: $C_{48}H_{30}O_{16}Zn_4$, fw = 1124.17, cubic, $I-43d$, $a = 28.790(1) \text{ \AA}$, $b = 28.790(1) \text{ \AA}$, $c = 28.790(1) \text{ \AA}$, $V = 23862(1) \text{ \AA}^3$, $Z = 16$, $T = 193 \text{ K}$, $\rho_{calcd} = 1.245 \text{ g/cm}^3$, $R_1 (I > 2\sigma(I)) = 0.0578$, wR_2 (all data) = 0.1482, GOF = 0.978.
- (46) Bondi, A. *J. Phys. Chem.* 1964, 68, 441.
- (47) Duren, T.; Sarkisov, L.; Yaghi, O. M.; Snurr, R. Q. *Langmuir*, 2004; 20, 2683.
- (48) Beck, D. W. *Zeolite Molecular Sieves*; Wiley & Sons: New York, 1974.
- (49) Brunauer, S.; Emmett, P. H.; Teller, E. *J. Am. Chem. Soc.* 1938, 60, 309.
- (50) Dubinin, M. M.; Radushkevich, L. V. *Dokl. Akad. Nauk USSR*, 1947, 55, 331.
- (51) Dincă, M.; Long, J. R. *J. Am. Chem. Soc.* 2005, 127, 9376.
- (52) Collins, D. J.; Zhou, H.-C. *J. Mater. Chem.*, 2007, 17, 3154.

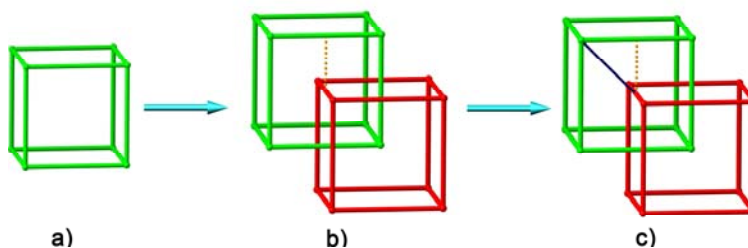
Chapter 11

A Coordinatively Linked, Doubly Interpenetrated, Yb Metal-Organic Framework Demonstrates High Thermal Stability and Uncommon Gas-Adsorption Selectivity^j

11.1 Introduction

Emerging as a new zeolite analogue, porous metal-organic frameworks (MOFs) have attracted considerable research interests in the past decade.¹ Compared to traditional zeolites,² MOFs possess high surface area, modifiable surface,³ and tuneable pore size.⁴ These characteristics have afforded MOFs enormous application potential in catalysis,⁵ gas storage,⁶ and adsorptive separation.⁷

One of the main concerns in porous MOFs is their limited thermal stability, which prevents them from competing with inorganic zeolites in practical applications.² Most porous MOFs can be heated up to 150-350 °C without losing their framework integrity.⁸ Interpenetration, which often arises from weak interactions, has been widely used to improve the thermal stability of porous MOFs.⁹ Interpenetrated porous MOFs stable up to 400 °C have been reported.¹⁰ Interpenetration increases the wall thickness and reduces the pore size of an MOF leading to enhanced thermal stability.⁹ If the two interpenetrated frameworks can be linked through coordination bonds, the thermal stability should be further boosted (Scheme 11.1). Herein we report such a coordinatively linked, doubly interpenetrated, Yb MOF with improved thermal stability (up to 500 °C) and uncommon gas-adsorption selectivity.



^j This chapter was reprinted from: Ma, S.; Wang, X.-S.; Yuan, D.; Zhou, H. C. *Angew Chem. Int. Ed.* **2008** DOI: 10.1002/anie.200800312 (Copyright 2008, Wiley-VCH Verlag GmbH & Co KG).

Scheme 11.1 a) A single net. b) Two doubly interpenetrated nets. c) Interpenetrated nets linked by coordination bonds.

Previously, we reported a Co porous MOF with doubly-interpenetrated, (8,3)-connected nets, PCN-9.¹¹ PCN-9 adopts a square-planar $\text{Co}_4(\mu_4\text{-O})$ SBU (secondary building unit), and each Co center is five coordinate with a coordinative site open toward the open channel. The interpenetration renders PCN-9 with thermal stability up to 400 °C. If the interpenetrated (8,3)-connected nets can be linked at the open metal sites through a bridging ligand, the thermal stability of the new MOF should be further enhanced.

Due to the proximity of the two nets, a short bridge should be adopted. We choose SO_4^{2-} as the bridging ligand because sulfate can chelate the two metal centers stabilizing the MOF further. In addition, sulfate can be generated slowly under solvothermal conditions when DMSO (dimethylsulfoxide) decomposes at elevated temperatures,¹² facilitating the formation of the coordinatively linked interpenetrated MOF.

However, initial attempts using sulfates to bridge the doubly-interpenetrated (8,3)-connected nets in PCN-9 failed. There are two possible reasons for such unsuccessful attempts: the limited coordination number (maximal six) of a cobalt center and the need of additional counter-ions to balance the overall charge. Using Ln^{3+} instead of Co^{2+} , the coordination number of the metal center can be increased¹³ and no additional counter-ions will be needed to balance the overall charge.

With the above considerations in mind, a ytterbium MOF with coordinatively linked, doubly interpenetrated, (8,3)-connected nets, PCN-17 (PCN: porous coordination network), has been made in this chapter. PCN-17 is stable up to 480 °C, and exhibits selective adsorption of H_2 and O_2 over N_2 and CO .

11.2 Experimental Details

Synthesis of PCN-17: A mixture of H_3TATB (0.01 g, 2.26×10^{-5} mol) and $\text{Yb}(\text{NO}_3)_3 \cdot 6\text{H}_2\text{O}$ (0.025 g, 5.47×10^{-5} mol) in 1.2 mL of DMSO (dimethylsulfoxide) with five drops of H_2O_2 (30%, aq.) was sealed in a Pyrex tube, heated to 145 °C (temperature increase rate, 2 °C / min), allowed to stay for 72 hours, and cooled to 35 °C (temperature decrease rate, 0.2 °C / min). The brown crystals obtained were washed with DMSO twice

to give pure PCN-17 with the following formula: $\text{Yb}_4(\mu_4\text{-H}_2\text{O})(\text{C}_{24}\text{H}_{12}\text{N}_3\text{O}_6)_{8/3}(\text{SO}_4)_2 \cdot 3\text{H}_2\text{O} \cdot 10\text{C}_2\text{H}_6\text{SO}$. Elemental analysis for PCN-17, calculated: C 34.71%, H 3.47%, N 3.85%; found: C 33.87%, H 3.41%, N 3.68%.

Single-crystal X-ray crystallographic studies of PCN-17: Single crystal X-ray data were collected on a Bruker Smart Apex diffractometer equipped with an Oxford Cryostream low temperature device and a fine-focus sealed-tube X-ray source (Mo- K_α radiation, $\lambda = 0.71073 \text{ \AA}$, graphite monochromated) operating at 45 kV and 35 mA. Frames were collected with 0.3° intervals in φ and ω for 30 s per frame such that a hemisphere of data was collected. Raw data collection and refinement were done using SMART. Data reduction was performed using SAINT+ and corrected for Lorentz and polarization effects.²⁴ The structure was solved by using the direct method and refined by full-matrix least-squares on F^2 with anisotropic displacement using SHELX-97.²⁵ Non-hydrogen atoms were refined with anisotropic displacement parameters during the final cycles. Hydrogen atoms on carbon were calculated in ideal positions with isotropic displacement parameters set to $1.2 \times U_{\text{eq}}$ of the attached atom. Absorption corrections were applied using SADABS after the formula of the compound is determined approximately.²⁴ Solvent molecules in the structure were highly disordered and were impossible to refine using conventional discrete-atom models. To resolve these issues, the contribution of solvent electron density was removed by the SQUEEZE routine in PLATON.²² In PCN-17, the Yb atoms are disordered and each Yb is refined as occupying two equally populated positions. Crystal data for PCN-17: $\text{C}_{72}\text{H}_{62}\text{N}_8\text{O}_{31}\text{S}_6\text{Yb}_4$, $M_r = 2419.82$; brown block, $0.25 \times 0.23 \times 0.20 \text{ mm}$, $T = 213(2) \text{ K}$, cubic, space group $Im\bar{3}m$, $a = 26.2253(2) \text{ \AA}$, $\alpha = 90.00^\circ$, $V = 18037(2) \text{ \AA}^3$, $Z = 6$, $d_{\text{calcd}} = 1.337 \text{ g/cm}^3$; R_1 ($I > 2\sigma(I)$) = 0.0969, wR_2 (all data) = 0.2685, GOF = 1.094, CCDC-669500 (PCN-17) contains the supplementary crystallographic data for this communication. These data can be obtained free of charge at www.ccdc.cam.ac.uk/conts/retrieving.html (or from the Cambridge Crystallographic Data Center, 12, Union Road, Cambridge CB21EZ, UK; fax: (+44) 1223-336-033; or deposit@ccdc.cam.ac.uk).

Gas Sorption Measurements: Gas sorption measurements were performed with a Beckman Coulter SA 3100 surface area and pore size analyzer. A fresh sample of PCN-17 was evacuated under a dynamic vacuum ($< 10^{-3}$ torr) at 250°C overnight to remove

guest molecules. Before the measurement, the sample was evacuated again by using the “outgas” function of the surface area analyzer for 2 hour at 250 °C. A sample of 100 mg was used for N₂ (99.999%) adsorption measurement, and was maintained at 77K with liquid nitrogen. In the hydrogen adsorption measurement, high purity hydrogen (99.9995%) was used. The regulator and pipe were flushed with hydrogen before connecting to the analyzer. The internal lines of the instrument were flushed three times by utilizing the “flushing lines” function of the program to ensure the purity of H₂. The measurement was maintained at 77 K with liquid nitrogen. Similar to the procedures used for H₂ measurement at 77 K, highly pure O₂ (99.99%), CO (99.99%), and CO₂ (99.99%) were used for their respective gas adsorption measurements. All the gases used for the measurements were purchased from Linde Gas LLC, Cincinnati, Ohio, USA. The temperature of 195 K was maintained with an acetone-dry ice bath. To prevent condensation of CO and O₂ at 77 K, the pressure ranges were below 448 torr and 156 torr, respectively. For all adsorption isotherms, P₀ represents a relative saturation pressure given by the Beckman Coulter SA 3100 surface area and pore size analyzer during the measurements: at 77 K, P₀ was 757 torr for N₂, 441 torr for CO, and 151 torr for O₂. For hydrogen 757 torr was used as a relative standard.

Powder X-ray diffraction (PXRD) studies: The heating of sample at desired temperatures under N₂ atmosphere was performed on a PerkinElmer TGA 7 Thermogravimetric Analyzer with N₂ flowing rate of 50.0 ml / min, and the PXRD patterns were obtained on a Scintag X1 powder diffractometer system using CuK radiation with a variable divergent slit, solid-state detector, and a routine power of 1400 W (40 kV, 35 mA).

11.3 Results and Discussions

X-ray structural analysis revealed that PCN-17 crystallizes in space group *Im-3m*. As expected, it adopts a square-planar Yb₄(μ₄-H₂O) SBU, with a μ₄-H₂O, probably disordered over two or more orientations, residing at the centre of a square of four Yb atoms (Figure 11.1a). The four Yb atoms in the SBU are in the same plane with each Yb coordinating seven O atoms (four from four carboxylate groups of four different TATBs, two from the bridging sulfate generated *in situ*,^[12] and one from the μ₄-H₂O). The Yb—

μ_4 -H₂O distance is 2.70 Å, indicating very weak Yb—H₂O bonding. It is reasonable to assign the μ_4 -center as a H₂O molecule instead of O atom when the overall charge balance and the weak Yb—H₂O interaction are considered. Because the coordination number of an aqua ligand is normally one or two, we suspect that the central H₂O is probably a statistical average of aqua ligands disordered over two or more orientations. This “ μ_4 -H₂O” bridged square-planar structural motif has also been observed previously in lanthanide complexes,¹⁴ but is unique in a lanthanide MOF. Every TATB ligand connects three Yb₄(μ_4 -H₂O) SBUs, every Yb₄(μ_4 -H₂O) SBU connects eight trigonal-planar TATB ligands and four sulfate ligands to form an infinite framework (Figure 11.2). PCN-17 can also be viewed as a MOF composed of an infinite SBU; each sulfate bridges two Yb₄(μ_4 -H₂O) clusters and each cluster connects four sulfates to form such an infinite SBU (Figure 11.3).

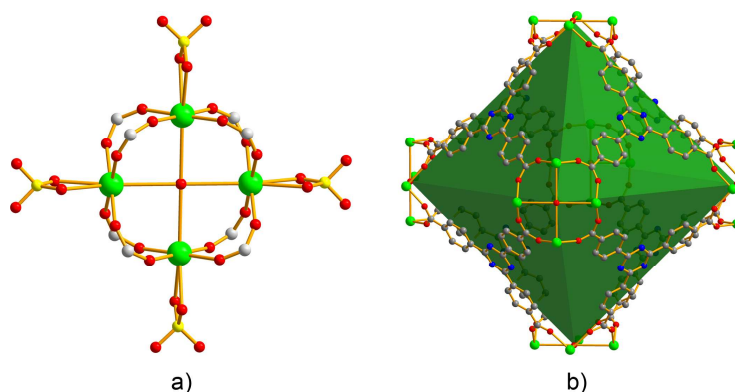


Figure 11.1 Structures of PCN-17 (Part I): a) a Yb₄(μ_4 -H₂O) SBU connecting four SO₄²⁻ in PCN-17. b) Octahedral cage in PCN-17. Color scheme: C, grey; N, blue; O, red; S, yellow; Yb, green (Hydrogen atoms are omitted for clarity).

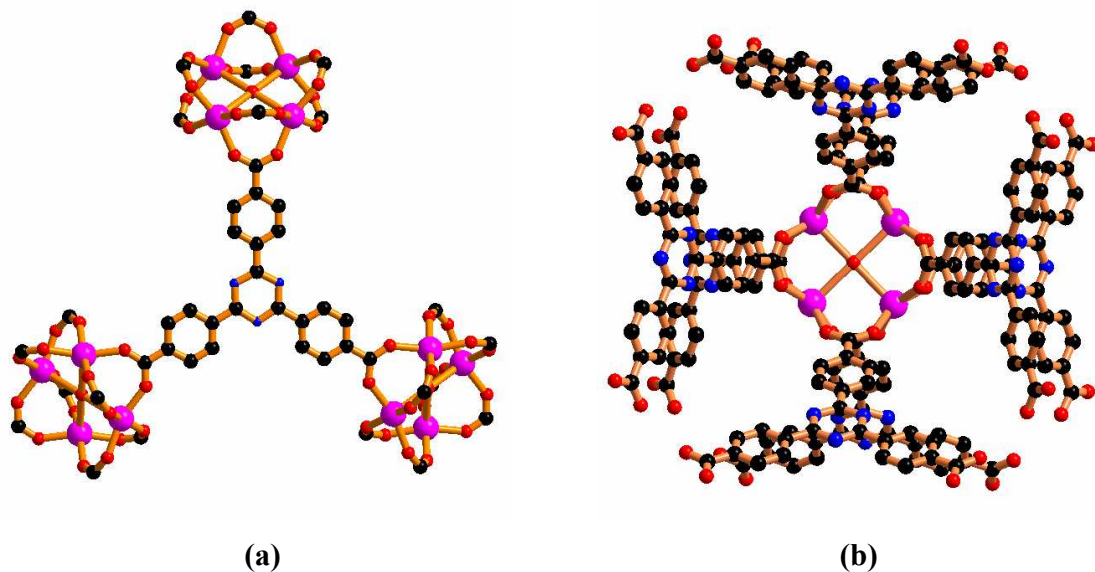


Figure 11.2 Structures of PCN-17 (Part II): (a) TATB Ligand connecting three $\text{Yb}_4(\mu_4\text{-H}_2\text{O})$ square-planar SBUs; (b) $\text{Yb}_4(\mu_4\text{-H}_2\text{O})$ SBU connecting eight trigonal-planar TATB ligands (pink: Yb; black: carbon; red: oxygen; yellow: sulphur; blue: nitrogen).

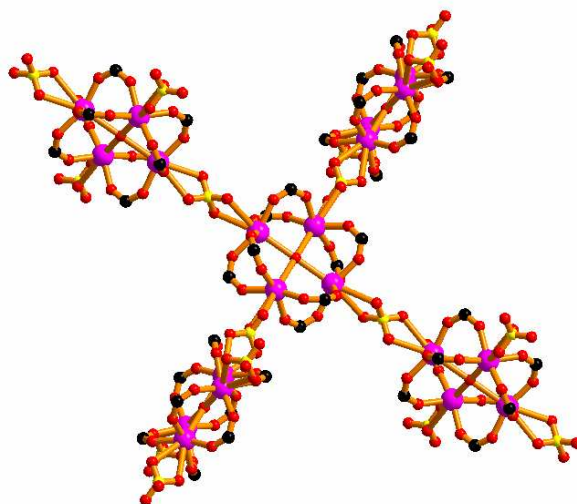


Figure 11.3 $\text{Yb}_4(\mu_4\text{-H}_2\text{O})$ SBU connecting with four sulfate ligands bridging four other $\text{Yb}_4(\mu_4\text{-H}_2\text{O})$ SBUs.

Alternatively, PCN-17 can be rationalized as directly linked, doubly interpenetrated, (8,3)-connected nets (Figure 11.4). There exist O_h -cages defined by six

$\text{Yb}_4(\mu_4\text{-H}_2\text{O})$ SBUs at the corners and eight TATB ligands on the faces in PCN-17 (Figure 11.1b); each octahedral cage shares corners with six others to form an (8,3)-connected net (Figure 11.4a). Two such (8,3)-connected nets are mutually interpenetrated giving rise to an isostructure of PCN-9 (Figure 11.4b).¹¹ Overall, the structure of PCN-17 can be obtained by sulfate-bridging (Figure 11.4c) of the two interpenetrated (8,3)-connected nets. The directly bridged interpenetration is very rare, and should lead to high thermal stability of PCN-17.

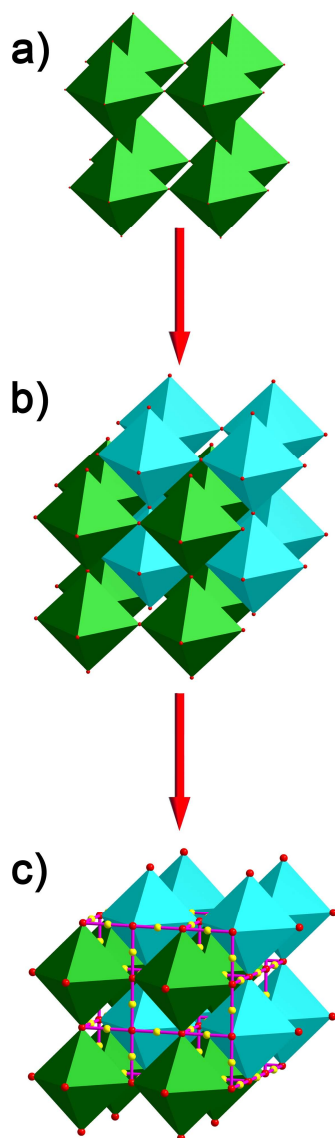


Figure 11.4 a) A single (8,3)-net. (b) Doubly-interpenetrated nets. c) Coordinatively linked interpenetration through sulfate bridges (yellow spheres represent sulfur and red spheres represent the square-planar SBU).

Thermal gravimetric analysis (TGA) (Fig. 11.5) indicates that PCN-17 is stable up to 500 °C. The first weight loss of 32.0% from 20 to 430 °C corresponds to the loss of ten DMSO, three H₂O guest solvent molecules and one μ_4 -H₂O molecule (calcd 29.4%), which is followed by a steady plateau up to 500 °C. The framework of PCN-17 starts to collapse with the loss of the TATB ligands (found 39.6%; calcd 40.2%) from 500 °C to

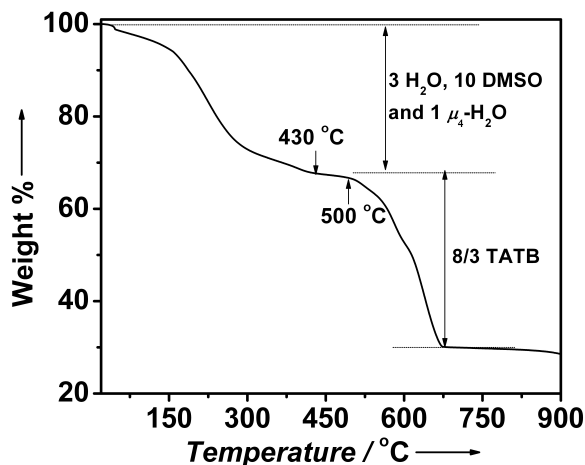


Figure 11.5 TGA plot of PCN-17.

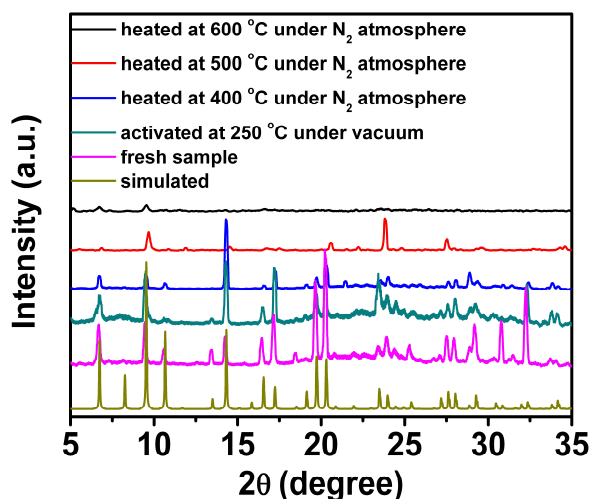


Figure 11.6 PXRD patterns of PCN-17.

700 °C. It should be noted that PCN-17 retains its framework integrity at very high temperature even after guest removal, as evidenced by the comparison of powder X-ray diffraction (PXRD) patterns collected at temperatures from 250 to 600 °C (Figure 11.6). The thermal stability of PCN-17 is among the highest reported in porous MOFs,¹⁵ albeit

some nonporous MOFs were reported to stable up to 600 °C.¹⁶ The unusual stability of PCN-17 can be attributed to the unique coordinatively linked interpenetration.

To check its permanent porosity, gas adsorption studies were carried out using activated PCN-17 samples. In our initial attempt to activate PCN-17, a freshly prepared sample was soaked in volatile solvents such as methanol and dichloromethane to remove the high-boiling-point H₂O and DMSO guest molecules using the method described previously.^{11,17} However, the solvent-exchanged sample took up neither N₂ nor H₂ even after thermal activation at 100 °C. A close look at the structure of PCN-17 reveals that the bridging sulfate ligands reduce the pore sizes of PCN-17 to ~3.5 Å (excluding van der Waals radii¹⁸), and these small pores preclude the entrance of methanol or dichloromethane for solvent exchange. Evacuating a fresh PCN-17 sample at 250 °C under a dynamic vacuum overnight proved efficient in guest removal. A N₂ adsorption isotherm measured at 77 K reveals that activated PCN-17 can hardly adsorb N₂ (kinetic diameter: 3.64 Å¹⁹) presumably due to its limited pore size of ~3.5 Å (Figure 11.7b). The CO₂ adsorption isotherm (Figure 11.7a) of the activated PCN-17 sample measured at 195 K reveals typical type-I behavior as expected for microporous materials. Fitting the Brunauer-Emmett-Teller (BET) equation²⁰ to the adsorption isotherm of CO₂ gives an estimated surface area of 820 m²/g. Using the Dubinin-Radushkevich equation,²¹ the pore volume of PCN-17 is estimated to be 0.34 cm³/g, consistent with its solvent accessible volume of 36.3% calculated from PLATON.²²

Aware of the small pore size of ~3.5 Å of activated PCN-17, we decided to check its selective gas adsorption properties. In addition to the N₂ adsorption measurement, H₂, O₂, and CO adsorption studies were also carried out at 77 K. As expected, PCN-17 can adsorb a large amount of O₂ (210 cm³/g) and a moderate amount of H₂ (105 cm³/g) with typical type-I behaviors, but very limited amount of N₂ and CO (~20 cm³/g for both) (Figure 11.7b). In view of the kinetic diameters of 2.89 Å for H₂, 3.46 Å for O₂, 3.64 Å for N₂ and 3.76 Å for CO,¹⁹ it can be inferred that the pore opening of PCN-17 should be between 3.46 and 3.64 Å in diameter. This is consistent with the crystallographically observed aperture size of (~3.5 Å) for PCN-17. The small pores allow only H₂ and O₂ molecules to enter the channels inside PCN-17. The adsorption selectivity of H₂ and O₂ over N₂ and CO shown by PCN-17 is very rare.²³

The gas-adsorption selectivity demonstrated by PCN-17 may have application potential in the following: the separation of nitrogen and oxygen, the separation of hydrogen from carbon monoxide in fuel cell applications, and hydrogen enrichment of the N₂/H₂ exhaust in ammonia synthesis.

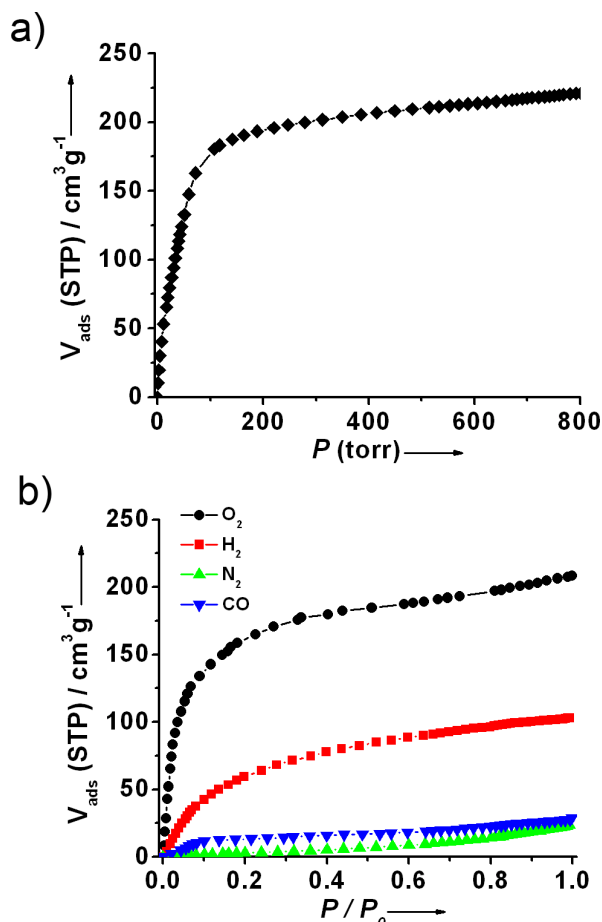


Figure 11.7 Gas adsorption isotherms of the activated PCN-17: a) CO₂ at 195 K; (b) H₂, O₂, N₂, and CO at 77 K (for H₂, P_0 represents a relative standard; refer to Experimental Section for details).

In order to further check its framework integrity at high temperature, hydrogen adsorption isotherm was measured for PCN-17 after heated at 500 °C. However, the adsorbed hydrogen amount was just about half of that of the activated PCN-17 (Figure 11.8), indicating partial framework decomposition. This accounts for the alteration of the PXRD patterns of thermally activated samples at high temperatures. Significantly, the adsorbed hydrogen amount of PCN-17 after thermal activation at 480 °C is comparable to

that of the activated PCN-17 at lower temperatures (Figure 11.8), indicating its framework integrity at 480 °C.

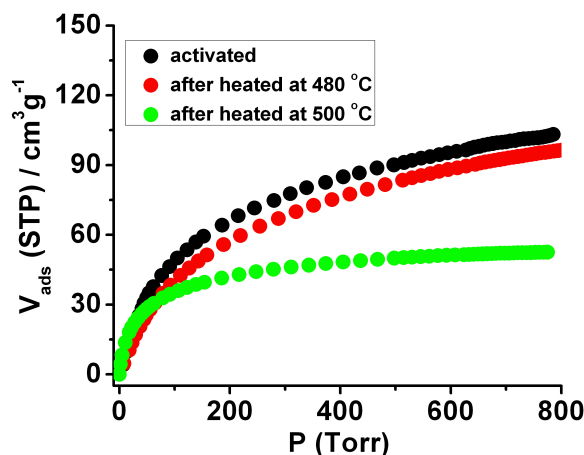


Figure 11.8 H₂ adsorption isotherms of PCN-17 treated at different conditions.

In summary, a three-dimensional microporous ytterbium metal-organic framework, PCN-17, based on a novel square-planar Yb₄(μ₄-H₂O) SBU, has been made and structurally characterized. PCN-17 contains a unique coordinatively linked interpenetration and possesses exceptionally high thermal stability of up to 500 °C while maintaining permanent porosity. The sulfate bridging ligands reduce the pore size of PCN-17 to ~3.5 Å, leading to selective adsorption of O₂ over N₂, H₂ over CO, and H₂ over N₂. The strategy of using bridging ligands to coordinatively link interpenetration to enhance thermal stability of porous MOFs is unique, and it also paves a new way to constrict the pore sizes of porous MOFs for selective gas adsorption applications.

11.4 Reference

- (1) (a) Yaghi, O. M.; Li, H.; Davis, C.; Richardson, D.; Groy, T. L. *Acc. Chem. Res.* **1998**, *31*, 474; (b) James, L. *Chem. Soc. Rev.* **2003**, *32*, 276; (c) Janiak, C. *J. Chem. Soc., Dalton Trans.* **2003**, 2781; (d) Kitagawa, S.; Kitaura, R.; Noro, S. *Angew. Chem. Int. Ed.* **2004**, *43*, 2334; (e) Mueller, U.; Schubert, M.; Teich, F.; Puetter, H.; Schierle-Arndt, K.; Pastre, J. *J. Mater. Chem.* **2006**, *16*, 626.

- (2) (a) Cheetham, A. K.; Férey, G.; Loiseau, T. *Angew. Chem. Int. Ed.* **1999**, *38*, 3268; (b) Davis, M. E.; *Nature*, **2002**, *417*, 813; (c) Auerbach, S. M.; K. Carrado, A.; Dutta, P. K. *Handbook of Zeolite Science and Technology*, Marcel Dekker, New York, **2003**.
- (3) (a) Eddaoudi, M.; Moler, D. B.; Li, H.; Chen, B.; Reineke, T. M.; O'Keeffe, M.; Yaghi, O. M. *Acc. Chem. Res.* **2001**, *34*, 319; (b) Ockwig, N. W.; Delgado-Friedrichs, O.; O'Keeffe, M.; Yaghi, O. M. *Acc. Chem. Res.* **2005**, *38*, 176.
- [4] (a) Eddaoudi, M.; Kim, J.; Rosi, N.; Vodak, D.; Wachter, J.; O'Keeffe, M.; Yaghi, O. M. *Science* **2002**, *295*, 469; (b) Kepert, C. J. *Chem Comm.* **2006**, 695.
- (5) (a) Seo, J. S.; Whang, D.; Lee, H.; Jun, S. I.; Oh, J.; Jeon, Y. J.; Kim, K. *Nature* **2000**, *404*, 982; (b) Hu, A.; Ngo, H. L.; Lin, W. *J. Am. Chem. Soc.* **2003**, *125*, 11490.
- (6) (a) Chen, B.; Ockwig, N. W.; Millward, A. R.; Contreras, D. S.; Yaghi, O. M. *Angew. Chem. Int. Ed.* **2005**, *44*, 4745; (b) Millward, A. R.; Yaghi, O. M. *J. Am. Chem. Soc.* **2005**, *127*, 17998; (c) Collins, D. J.; Zhou, H.-C. *J. Mater. Chem.* **2007**, *17*, 3154; (d) Sun, D.; Ke, Y.; Collins, D. J.; Lorigan, G. A.; Zhou, H.-C. *Inorg. Chem.*, **2007**, *46*, 2725; (e) Ma, S.; Wang, X.-S.; Collier, C. D.; Manis, E. S.; Zhou, H.-C. *Inorg. Chem.* **2007**, *46*, 3432; (f) Ma, S.; Sun, D.; Ambrogio, M. W.; Fillinger, J. A.; Parkin, S.; Zhou, H.-C. *J. Am. Chem. Soc.* **2007**, *129*, 1858.
- (7) (a) Dybtsev, D. N.; Chun, H.; Yoon, S. H.; Kim, D.; Kim, K. *J. Am. Chem. Soc.* **2004**, *126*, 32; (b) Matsuda, R.; Kitaura, R.; Kitagawa, S.; Kubota, Y.; Belosludov, R. V.; Kobayashi, T. C.; Sakamoto, H.; Chiba, T.; Takata, M.; Kawazoe, Y.; Mita, Y. *Nature* **2005**, *436*, 238; (c) Chen, B.; Liang, C.; Yang, J.; Contreras, D. S.; Clancy, Y. L.; Lobkovsky, E. B.; Yaghi, O. M.; Dai, S. *Angew. Chem. Int. Ed.* **2006**, *45*, 1390; (d) Chen, B.; Ma, S.; Zapata, F.; Fronczek, F. R.; Lobkovsky, E. B.; Zhou, H.-C. *Inorg. Chem.* **2007**, *46*, 1233; (e) Chen, B.; Ma, S.; Hurtado, E. J.; Lobkovsky, E. B.; Zhou, H.-C. *Inorg. Chem.* **2007**, *46*, 8490; (f) Chen, B.; Ma, S.; Hurtado, E. J.; Lobkovsky, E. B.; Liang, C.; Zhu, H.; Dai, S. *Inorg. Chem.* **2007**, *46*, 8705; (g) Barcia, P. S.; Zapata, F.; Silva, J. A. C.; Rodrigues, A. E.; Chen, B. *J. Phys. Chem. B.* **2007**, *111*, 6101; (h) Ma, S.; Sun, D.; Wang, X.-S.; Zhou, H.-C. *Angew. Chem. Int. Ed.* **2007**, *46*, 2458.
- (8) (a) Rowsell, J. L.; Yaghi, O. M. *Angew. Chem. Int. Ed.* **2005**, *44*, 4670; (b) Isacva, V. I.; Kustov, L. M. *Russ. J. Gen. Chem.* **2007**, *50*, 56-72.

- (9) (a) Batten, S. R.; Robson, R. *Angew. Chem. Int. Ed.* **1998**, *37*, 1460; (b) Rowsell, J. L. C.; Yaghi, O. M. *J. Am. Chem. Soc.* **2006**, *128*, 1304; (c) Dinca, M.; Dailly, A.; Tsay, C.; Long, J. R. *Inorg. Chem.* **2008**, *47*, 11.
- (10) (a) Yang, S. Y.; Long, L. S.; Jiang, Y. B.; Huang, R. B.; Zheng, L. S. *Chem. Mater.* **2002**, *14*, 3229; (b) Sun, D.; Ma, S.; Ke, Y.; Petersen, T. M.; Zhou, H.-C. *Chem. Commun.*, **2005**, 2663.
- (11) Ma, S.; Zhou, H.-C. *J. Am. Chem. Soc.* **2006**, *128*, 11734.
- (12) Pandey, S. K.; Kumar, P. *Eur. J. Org. Chem.* **2007**, *2*, 369.
- (13) Kido, J.; Okamoto, Y. *Chem. Rev.* **2002**, *102*, 2357; Marques, N.; Sella, A.; Takats, J. *Chem. Rev.* **2002**, *102*, 2137.
- (14) Deacon, G. B.; Forsyth, C. M.; Harika, R.; Junk, P. C.; Ziller, J. W.; Evans, W. J. *J. Mater. Chem.* **2004**, *14*, 3144.
- (15) Park, K. S.; Ni, Z.; Côté, A. P.; Choi, J. Y.; Huang, R.; Uribe-Romo, F. J.; Chae, H. K.; O'Keeffe, M.; Yaghi, O. M. *Proc. Nat. Acad. Sci. U.S.A.* **2006**, *103*, 10186.
- (16) de Lill, D. T.; Cahill, C. L. *Chem. Comm.* **2006**, 4946.
- (17) (a) Sun, D.; Ma, S.; Ke, Y.; Collins, D. J.; Zhou, H.-C. *J. Am. Chem. Soc.* **2006**, *128*, 3896; (b) Wang, X.-S.; Ma, S.; Sun, D.; Parkin, S.; Zhou, H.-C. *J. Am. Chem. Soc.* **2006**, *128*, 16474; (c) Ma, S.; Sun, D.; Simmons, J. M.; Collier, C. D.; Yuan, D.; Zhou, H.-C. *J. Am. Chem. Soc.* **2008**, *130*, 1012.
- (18) Bondi, A. *J. Phys. Chem.* **1964**, *68*, 441.
- (19) Beck, D. W. *Zeolite Molecular Sieves*; Wiley & Sons: New York, **1974**.
- (20) Brunauer, S.; Emmett, P. Teller, H.; E. *J. Am. Chem. Soc.* **1938**, *60*, 309.
- (21) Dubinin, M. M.; Radushkevich, L. V. *Dokl. Akad. Nauk USSR*, **1947**, *55*, 327.
- (22) Spek, A. L. *J. Appl. Crystallogr.* **2003**, *36*, 7.
- (23) (a) Dinca, M.; Long, J. R. *J. Am. Chem. Soc.* **2005**, *127*, 9376; (b) Humphrey, S. M.; Chang, J.-S.; Jhung, S. H.; Yoon, J. W.; Wood, P. T. *Angew. Chem., Int. Ed.* **2007**, *46*, 272; (c) Ma, S.; Wang, X.-S.; Collier, C. D.; Manis, E. S.; Zhou, H.-C. *Inorg. Chem.*, **2007**, *46*, 8499.
- (24) SAINT+, version 6.22; Bruker Analytical X-Ray Systems, Inc.: Madison, WI, 2001.

(25) G. M. Sheldrick, *SHELX-97*; Bruker Analytical X-Ray Systems, Inc.: Madison, WI, 1997.

Chapter 12

A Mesh-Adjustable Molecular Sieve for General Use in Gas Separation^k

12.1 Introduction

Gas separation using molecular sieves (MSs) can be a green, energy-conserving alternative to traditional separation processes such as distillation and absorption.¹ Using zeolites MSs,²⁻⁴ an accurate one-on-one match between the mesh size and the separation need is essential. However, when the size disparity of the two gases to be separated is small, a MS with the optimum mesh size is not always readily available. A mismatch inevitably leads to an inefficient separation. Recently, titanosilicate was shown to possess superior flexibility over traditional zeolites; a few MSs with discrete mesh sizes were made based on the degree of dehydration of this material at various temperatures.⁵ Nevertheless, a MS with *more than one* mesh size has never been made in the past. Herein we show the design, synthesis, and application of a novel Mesh-Adjustable Molecular Sieve (designated MAMS-1 for convenience) that possesses *infinite* number of mesh sizes. MAMS-1 is based on Metal-Organic Frameworks (MOFs), which are known for their dynamic porous properties.⁶ However, the concept of a MAMS never appeared in the literature prior to the present work. MAMS-1 represents an unprecedented MOF-based MS whose mesh can be adjusted *continuously*. In addition, the mesh range of MSAM-1 falls between 2.9 and 5.0 Å, covering the size range of almost all commercially important gas separations. When temperature is precisely controlled, any mesh size within this range can be accurately attained. Gas separations such as those of N₂/O₂ and N₂/CH₄, which are normally difficult to achieve, are readily attainable by using MAMS-1. In principle, by precise temperature control, any two gases with a size difference can be separated by a MAMS, an omnipotent MS for gas separation.

MOFs have attracted a great deal of attention due to their fascinating structures^{6a,7} and potential applications in catalysis,⁸ separation,⁹ and gas storage.¹⁰ In particular, flexible MOFs⁶ have caught enormous attention lately. Numerous studies have indicated

^k This section was reprinted with permission from: Ma, S.; Sun, D.; Wang, X.-S.; Zhou, H.-C. *Angew. Chem., Inter. Ed.* **2007**, 46, 5628-5631 (Copyright 2007, Wiley-VCH Verlag GmbH & Co KG)

that the key to constructing a flexible MOF lies in the utilization of weak interactions such as hydrogen bonding, π - π stacking, and hydrophobic interaction, in addition to strong covalent and coordinative bonding.⁶ Flexible MOFs based on hydrogen bonding have been widely studied,^{6b,c} but those originating from π - π stacking and hydrophobic interaction¹¹ have rarely been explored.

To make a MAMS, two factors must be taken into account: the material must have permanent porosity to hold gas molecules, and the pores must be flexible. The former usually requires strong bonds while the latter implies weak interactions in the framework. These two seemingly irreconcilable prerequisites for a MAMS can be met simultaneously by using a graphitic structure, where in each layer atoms are connected covalently, but the layers are held together by weak interactions. One approach to such a graphitic MOF is to apply an amphiphilic ligand that consists of hydrophobic and hydrophilic ends, similar to a surfactant,¹² but with the hydrophilic end functionalized. The functional group at the hydrophilic end of the ligand will bind metal ions/clusters and the structure will propagate into a 2D layer. Two layers of ligands will sandwich a metal ion/cluster layer giving rise to a tri-layer, and these tri-layers will pack through van der Waals interaction.

The ligand adopted for the aforementioned purposes is 5-*tert*-butyl-1, 3-benzenedicarboxylate (BBDC), which was previously used in this laboratory to build a micelle-like cuboctahedral cage to adjust the solubility of a 24-molybdenum cluster.¹³ Recently, it was also used in a zinc microporous MOF.^{9f}

To our delight, a solvothermal reaction between H₂BBDC and Ni(NO₃)₂ in H₂O/ethylene glycol using a Teflon-lined autoclave afforded such a graphitic structure, Ni₈(μ ₃-OH)₄(5-BBDC)₆ (designated MAMS-1 for convenience). Desolvated MAMS-1 demonstrates temperature-induced molecular-gating effects in which the size of the gates can be tuned continuously from 2.9 to 5.0 Å for the first time. Commercially relevant gas separations, such as those of H₂/N₂, H₂/CO, N₂/O₂, N₂/CH₄, CH₄/C₂H₄, and C₂H₄/C₃H₆, can be achieved by MAMS-1. In principle, by precise temperature control, any mesh size within this range can be achieved. In fact, all pairs of gases stated above have been separated by using MAMS-1.

12.2 Experimental Details

Synthesis of MAMS-1: 5-tert-butyl-1,3-benzenedicarboxylic acid, H₂BBDC, (0.075 g, 0.34 m mol) and Ni(NO₃)₂·6H₂O (0.15 g, 0.51 m mol) in 7.5 ml H₂O/ethylene glycol (volume ratio 4:1) were placed in a 20 ml Teflon container and sealed in an autoclave. The autoclave was heated to 210 °C (heating rate 2 °C/min) in a programmable oven at which it stayed for 24 hours before being cooled to room temperature (cooling rate 0.5 °C/min). The light green needle-like crystals obtained were washed with distilled water and methanol to give pure MAMS-1 with the formula Ni₈(μ₃-OH)₄(C₁₂H₁₂O₄)₆(H₂O)₈·8H₂O (55% yield based on H₂BBDC). Elemental analysis calcd (%): C 40.28, H 5.07, O 32.79; found: C 40.69, H 5.07, O 33.05. IR (cm⁻¹): 3305 (w, br), 2960 (m), 1620 (m), 1571 (m), 1419 (m), 1347 (vs), 1275 (m), 1098 (m), 1033 (s), 865 (s), 785 (m).

X-ray Structure determination: Single crystal X-ray determination was performed on a Bruker Smart Apex diffractometer using Mo-Kα radiation ($\lambda = 0.71073$ Å). The data was collected on a crystal with dimensions of 0.23 mm x 0.08 mm x 0.08 mm at -60 °C. A total of 1321 frames of data were collected using ω -scans with an increment of 0.3° and a counting time of 60 seconds per frame. The raw data was processed using SAINT to yield the HKL file. Absorption corrections were applied using SADABS. Direct methods were used to solve the structure, which was refined by full-matrix least-squares on F² with anisotropic displacement parameters using SHELX-97. Non-hydrogen atoms were refined with anisotropic displacement parameters. The hydrogen atoms on carbon and oxygen atoms were calculated in ideal positions with isotropic displacement parameters set to $1.2 \times U_{eq}$ of the attached atom.

Thermogravimetric Analysis: Thermogravimetric analysis (TGA) of MAMS-1 (9.8 mg) was performed with Perkin-Elmer TGA 7 Thermogravimetric Analyzer under 50.0 ml / min flow of N₂. The first weight loss of 6.72 % (calcd: 6.71%) from 50 °C to 120 °C corresponds to the loss of eight free H₂O molecules, followed by the weight loss of 6.42% (calcd: 6.71%) corresponding to eight coordinated H₂O molecules from 120 °C to 250 °C. Beyond 400 °C, the framework decomposes completely.

Gas Adsorption Measurements: Gas adsorption measurements were measured with a Beckman Coulter SA 3100 surface area and pore size analyzer. The sample was

held under dynamic vacuum ($< 10^{-3}$ torr) at 200 °C overnight to remove the free and coordinated water molecules. Before the measurement, the sample was evacuated again by using the “outgas” function of the surface area analyzer for 1 hour at 200 °C. A sample of 40.0 mg was used for N₂ (99.999%) adsorption measurement, and was maintained at 77K with liquid nitrogen. In the hydrogen adsorption measurement, high purity hydrogen (99.9995%) and a 40.0 mg sample were used. The regulator and pipe were flushed with hydrogen before connecting to the analyzer. The internal lines of the instrument were flushed three times by utilizing the “flushing lines” function of the program to ensure the purity of H₂. The measurement was maintained at 77 K with liquid nitrogen. Similar to the procedures used for H₂ measurement at 77 K, highly pure O₂ (99.99%), CO (99.99%), CH₄ (99.997%), C₂H₄ (99.5%), C₃H₆ (99.5%), *iso*-C₄H₁₀ (99.5%), SF₆ (99.8%) and CO₂ (99.99%) were used for their respective gas adsorption measurements. All the gases used for the measurements were purchased from Linde Gas LLC, Cincinnati, Ohio, USA. The temperatures at 87 K, 113 K, 143 K, 175K, 195 K and 231 K were maintained with a liquid argon bath, isopentane-liquid nitrogen bath, n-pentane-liquid nitrogen bath, methanol-liquid nitrogen bath, acetone-dry ice bath, and acetonitrile-dry ice bath, respectively. To prevent condensation of CO and O₂ at 77 K, the pressure ranges were below 448 torr and 156 torr, respectively; to prevent condensation of O₂ at 87 K, the pressure range was below 466 torr; to prevent condensation of C₂H₄ at 143 K, the pressure range was below 120 torr; to prevent condensation of C₃H₆ at 195 K, the pressure range was below 110 torr; to prevent condensation of *iso*-C₄H₁₀ at 241 K, the pressure range was below 210 torr. For all adsorption isotherms, P₀ represents a relative saturation pressure given by the Beckman Coulter SA 3100 surface area and pore size analyzer during the measurements: at 77 K, P₀ was 757 torr for H₂ and N₂, 441 torr for CO, and 151 torr for O₂; at 87 K, P₀ was 757 torr for CO and N₂ and 465 torr for O₂; at 113 K, P₀ was 757 torr for CO, CH₄, and N₂; at 143 K, P₀ was 757 torr for CH₄ and 118 torr for C₂H₄; at 175 K, P₀ was 757 torr for C₂H₄; at 195 K, P₀ was 757 torr for C₂H₄ and CO₂ and 108 torr for C₃H₆; at 241 K, P₀ was 757 torr for C₃H₆ and 205 torr for *iso*-C₄H₁₀; at 298 K, P₀ was 757 torr for *iso*-C₄H₁₀ and SF₆.

Table 12.1 Crystal data of MAMS-1

Empirical formula	C ₃₆ H ₅₂ Ni ₄ O ₂₁
Formula weight	1055.62
Temperature	213(2) K
Wavelength	0.71073 Å
Crystal system, space group	Monoclinic, P2(1)/c
Unit cell dimensions	a = 10.9685 (2) Å alpha = 90.00°; b = 11.308 (2) Å beta = 96.781(3)°; c = 38.405 (7) Å gamma = 90.00°.
Volume	4730.1(14) Å ³
Z, Calculated density	4, 1.482 g/cm ³
Absorption coefficient	1.641 mm ⁻¹
F(000)	2192
Crystal size	0.23 × 0.08 × 0.08 mm
Theta range for data collection	1.87 to 23.33°
Reflections collected / unique	16860 / 6818 [R(int) = 0.0668]
Completeness to theta = 18.91	99.2 %
Absorption correction	Empirical
Max. and min. transmission	1.000 and 0.648
Refinement method	Full-matrix least-squares on F ²
Data / restraints / parameters	6818 / 18 / 581
Goodness-of-fit on F ²	1.021
Final R indices [I>2sigma(I)]	R _I = 0.0609, wR ₂ = 0.1456
R indices (all data)	R _I = 0.0928, wR ₂ = 0.1624

12.3 Results and Discussion

Single crystal X-ray analysis¹⁴ revealed that MAMS-1 contains an octa-nickel [Ni₈(μ₃-OH)₄] cluster as one of the two secondary building units (SBUs) (Figure 12.1a), the other being the BBDC ligand. The eight octahedral Ni atoms are divided into four pairs by a two-fold axis through the center of the cluster. Ni1 binds five carboxylate O atoms from four BBDC ligands and one μ₃-OH. Ni2 is coordinated by three carboxylate

O atoms and three μ_3 -OH groups. Ni3 is bound to four carboxylate O atoms, one μ_3 -OH, and an aqua ligand. Ni4 connects two carboxylate O atoms, one μ_3 -OH, and three aqua ligands.

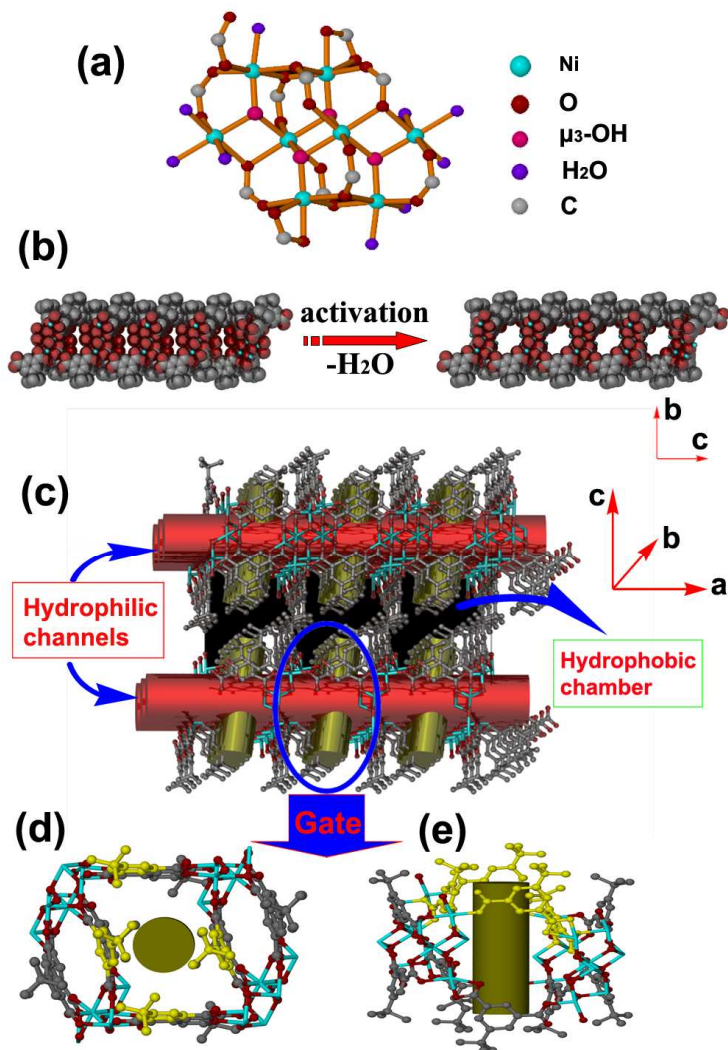


Figure 12.1 Crystal structure of MAMS-1: (a) Structure of the octa-nickel cluster; (b) Structures of solvated and desolvated tri-layers. The desolvated tri-layer displays hydrophilic channels along the *a* axis; (c) Two tri-layers pack along the *c* axis forming hydrophobic chambers; (d) Top and (e) Side views of BBDC pairs.

Every octa-nickel cluster connects twelve BBDC ligands, and every BBDC ligand binds two octa-nickel clusters to afford a tri-layer, with a hydrophilic cluster layer sandwiched by two hydrophobic BBDC layers (Figure 12.1b). There are 1-D channels along the *a* axis in the middle layer, in which guest water solvates reside. The tri-layers, with their exposed hydrophobic exteriors, pack along the *c* axis through van der Waals forces (Figure 12.1c), generating hydrophobic chambers between adjacent tri-layers.

Freshly isolated MAMS-1 is not active for adsorption, confirmed by gas adsorption studies with CO₂ and H₂ (Figure 12.2, 12.3). MAMS-1 must be activated at an elevated temperature (Figure 12.1b) as the crystal structure suggests. A thermogravimetric analysis of MAMS-1 reveals a loss of eight guest water molecules from 50 to 120°C, and the release of eight bound aqua ligands per formula unit when heated to 250°C (Figure 12.4).

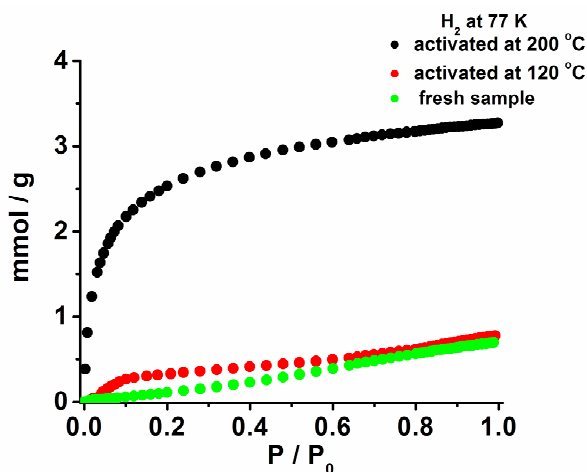


Figure 12.2 H₂ adsorption isotherms of MAMS-1 at 77K.

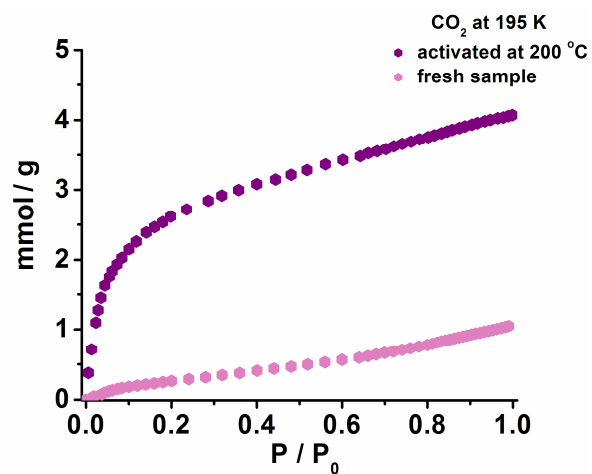


Figure 12.3 CO₂ adsorption isotherms of MAMS-1.

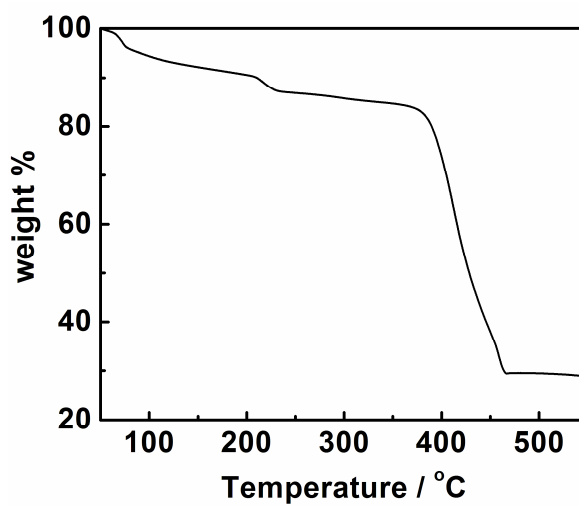


Figure 12.4 TGA plot of MAMS-1.

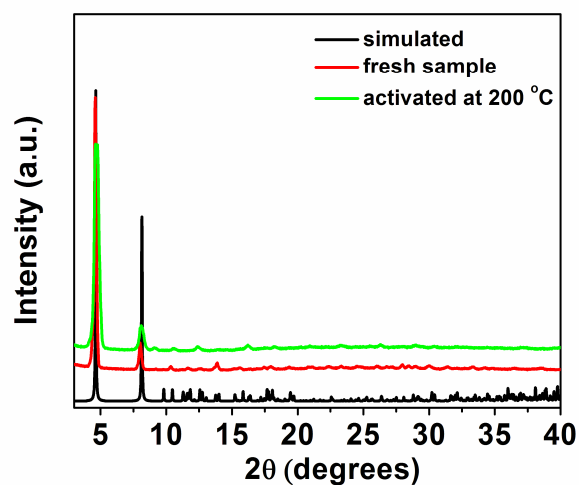


Figure 12.5 X-ray powder diffraction patterns for fresh sample and the sample activated at 200 °C.

Gas adsorption studies at 77K indicated that the sample evacuated at 120°C cannot take up N₂ or H₂ (Figure 12.3, 12.6). After activation under a dynamic vacuum at 200°C, MAMS-1 exhibits highly selective uptake of H₂ over CO, N₂, or O₂ (Figure 12.7a). Such selectivity in MOFs has been reported previously in only two cases,^{9c, e} but not with adjustable meshes.

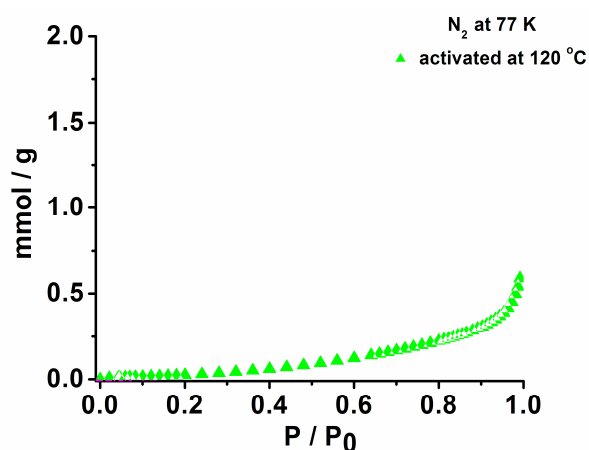


Figure 12.6 N₂ adsorption isotherm at 77 K of MAMS-1 activated at 120 °C.

A close examination of the crystal structure reveals that the hydrophilic channels (8.0 Å, atom to atom distance; 5.0 Å considering van der Waals radii¹⁵) are large enough

to accommodate O₂, N₂, or CO molecules, implying that the molecular gating effect has a different origin. In addition, the small pore volume of the hydrophilic channel is not large enough to account for the high observed H₂ uptake.

The crystal structure of MAMS-1 also shows that a hydrophobic chamber is accessible only through its hydrophobic/hydrophilic interface, on which two BBDCs point toward each other forming a gate based on van der Waals attraction between the two BBDCs (Figure 12.1d, 12.1e). When such gates are open, the hydrophilic channels and hydrophobic chambers are all connected giving rise to a 3D gas container with space continuity (Figure 12.1c), accounting for the high H₂ uptake of MAMS-1 at 77 K.

Most likely, the molecular sieving effect comes from the BBDC gates. In view of the kinetic diameters of 2.89 Å for H₂, 3.46 Å for O₂, 3.64 Å for N₂, and 3.76 Å for CO¹⁶, it can be inferred that the gate opening of MAMS-1 is around 3.0 Å to 3.4 Å. At 77 K, MAMS-1 excludes CO, N₂, and O₂ but allows H₂ to enter the hydrophobic chambers.

If this is indeed the case, the gates should open wider at higher temperatures, because the thermal vibration of the two BBDC groups can readily overcome the weak van der Waals interaction between them. The larger the amplitude of vibration, the wider the gate will open. When the temperature is raised to liquid argon temperature (87 K, Figure 12.7b), gas adsorption studies reveal that only a small amount of CO or N₂ is adsorbed by MAMS-1. However, MAMS-1 can take up significant amount of O₂. The adsorption isotherm of O₂ shows type-I behavior. Dioxygen (3.46 Å) can be selectively adsorbed from a mixture with N₂ (3.64 Å) and CO (3.76 Å), which implies that at 87 K the gate opens to around 3.5 Å. With the minute size disparity between O₂ and N₂ ($\Delta\sigma$: 0.18 Å) in mind, one has to be optimistic about the application potential of MAMS-1. However, an improved version of MAMS-1 should be capable of separating O₂ and N₂ at higher temperatures and will have enormous commercial impacts. The next question to ask: can MAMS-1 selectively adsorb N₂ from a mixture with CO and CH₄? This would also address an important application in industrial ammonia synthesis.

As expected, at 113 K, MAMS-1 can take up a moderate amount of N₂ but relatively low quantities of CO and CH₄ (3.8 Å) (Figure 12.7c). This is also consistent with the idea that the gating effect is due to the pair of BBDCs, and the gate opens wider under increased temperatures. This also implies that at 113 K, the gate opens to about 3.7

Å, wide enough to allow N₂ (3.64 Å) to enter the chambers, but molecules with larger kinetic diameters such as CO (3.76 Å) and CH₄ (3.8 Å) will stay in the hydrophilic channels. The resolution for size discrimination is now 0.12 Å. In fact, it can be inferred from all the adsorption data obtained thus far that if temperatures can be tuned continuously and precisely, any two molecules with a size difference can be separated by MAMS-1.

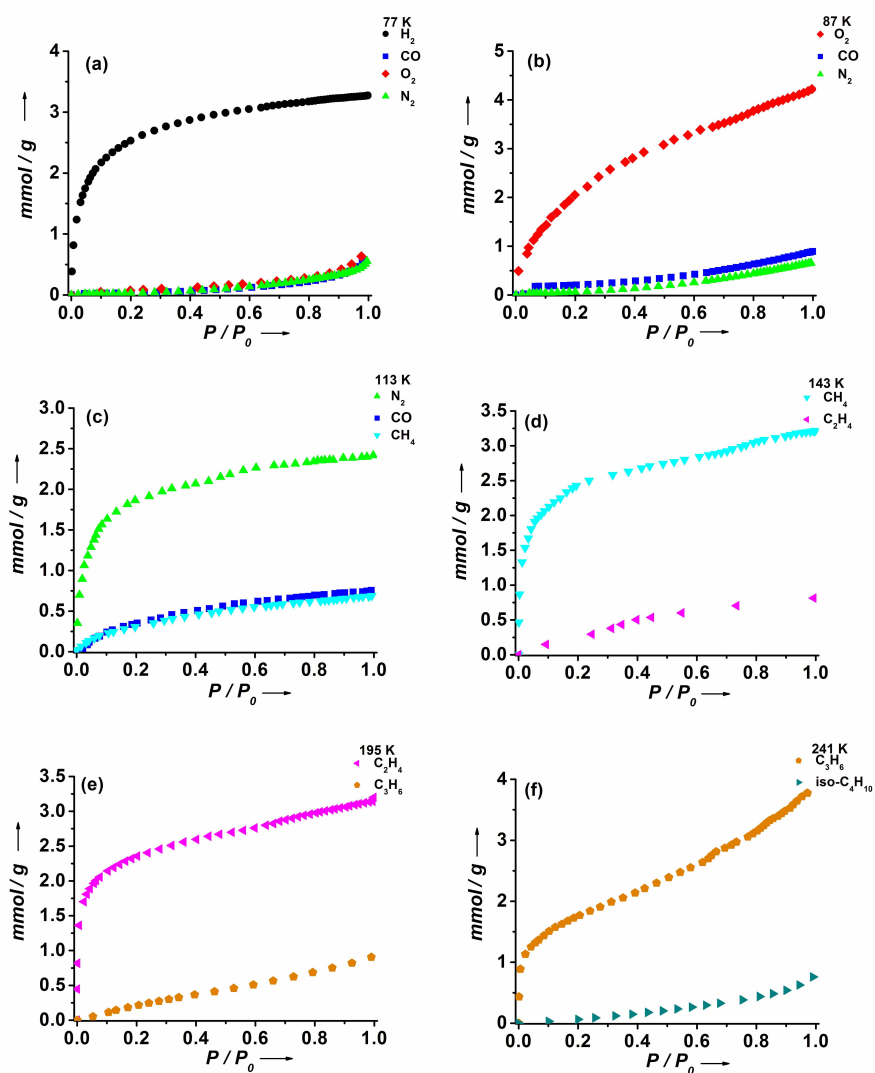


Figure 12.7 Gas adsorption isotherms at different temperatures: (a) 77 K, (b) 87 K, (c) 113 K, (d) 143 K, (e) 195 K, and (f) 241 K.

With these considerations in mind, we decided to explore the possibility of using MAMS-1 in separations important to petroleum refinery and petrochemical industry. Not surprisingly, MAMS-1 can distinguish methane from ethylene at 143 K, ethylene from propylene at 195 K, and propylene from iso-butane at 241 K (Figure 12.7d, 12.7e, 12.7f). Based on our data, it is certainly possible to design a temperature-swing apparatus based on MAMS-1 to perform *fractional adsorption* to separate a multi-component mixture into pure fractions just as in a distillation or absorption tower.

The mechanistic details of these unprecedented temperature-controlled gas-selective adsorption phenomena can be deduced from the crystal structure and adsorption data of MAMS-1 (Figure 12.8). The following are the major findings on MSAM-1:

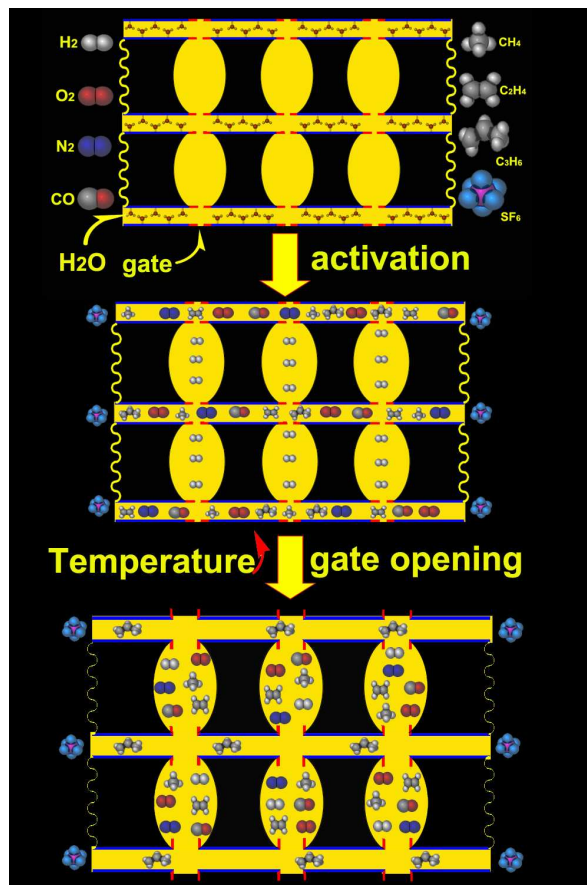


Figure 12.8 A schematic representation of the mechanism of the gating effect in MAMS-

1.

1. The temperature-dependent molecular-gating effect does not arise from simple thermal expansion of the framework. This assessment is supported by the temperature independence of cell parameters of MAMS-1 (Figure 12.9).

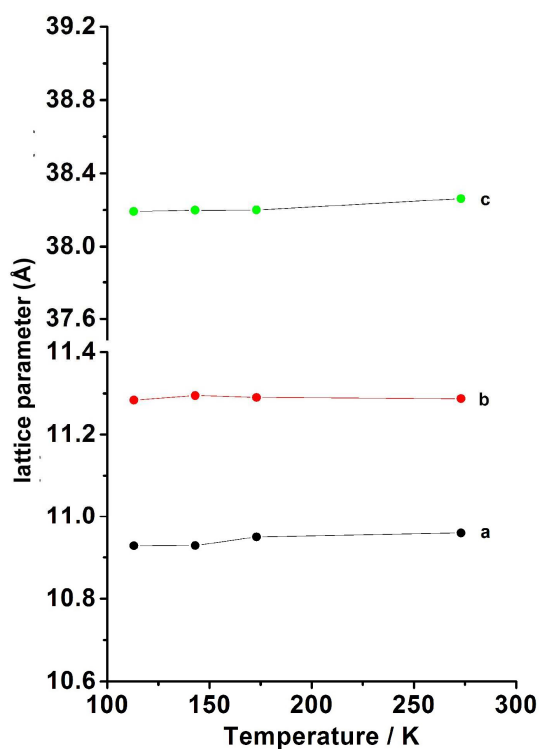


Figure 12.9 Cell parameters of MAMS-1 measured at different temperatures.

2. The hydrophobic chambers are not accessible when the hydrophilic channels are closed, which not only can be inferred from the crystal structure, but is also consistent with gas adsorption data. An inactivated sample had very low uptake of either H₂ or CO₂. A partially activated sample was inactive for gas uptake. The water guests and bound water ligands must be removed completely for MAMS-1 to be active for gas adsorption.

3. The hydrophilic channels alone are not responsible for the gas uptake. In fact, they account for only a very minor part of the adsorption. As the gas adsorption data at 77 K suggests, only H₂ can enter the hydrophobic chambers, showing a significant uptake.

At 77 K, other gas molecules stay in the hydrophilic channels and the uptake of these gases is very low, as shown by adsorption studies.

4. Gas molecules must go through the hydrophilic channel to access the hydrophobic chambers. As previously mentioned, activation of the hydrophilic channels is a prerequisite for gas adsorption on MAMS-1. Further evidence for the hydrophilic channels being the only passage to the gas storage chambers is provided by the observation that when the kinetic diameter of the gas molecule (for example, SF₆, 5.5 Å) exceeded the size of the hydrophilic channels (5.0 Å considering van der Waals radii), no meaningful uptake was observed in an adsorption study (Figure 12.10). The upper limit of the channel is also consistent with an adsorption study on iso-butane (5.0 Å), which is allowed to enter MAMS-1 at room temperature (Figure 12.10).

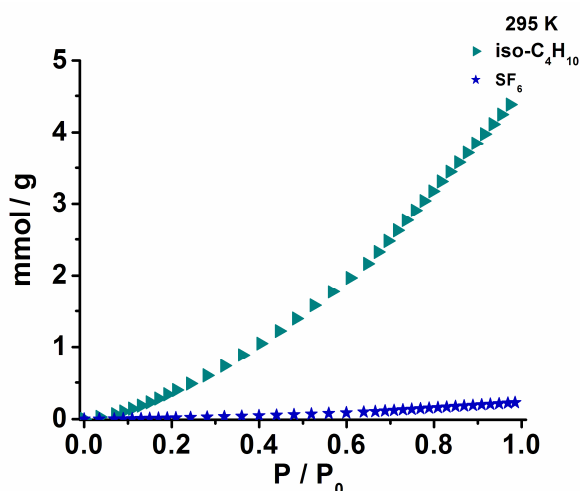


Figure 12.10 iso-C₄H₁₀ and SF₆ adsorption isotherms of MAMS-1 at 298 K.

5. Through the interface between the hydrophobic and hydrophilic channels, gas molecules enter the hydrophobic gas storage chambers, which account for the majority of gas uptake. The interface is controlled by a pair of BBDCs acting as a gate. The opening of this gate is controlled by the amplitude of thermal vibration. A drawing of temperature versus size of the molecule allowed to enter the gate is given in Figure 12.11. The data point at 77 K gives an under-estimation of the gate opening because a gas molecule with a size between 2.89 Å (H₂) and 3.40 Å (Ar) is not available for gas adsorption studies.

Ignoring the point at 77 K, the gate opening D , and temperature T , can be related by a linear equation, $D = 0.0076 T + 2.76$, with a correlation coefficient of 0.996 (Figure 12.11). This equation can be used to predict if a gas molecule will be allowed to enter the gate at a certain temperature. It can also be used to find the best temperature for the separation of a mixture.

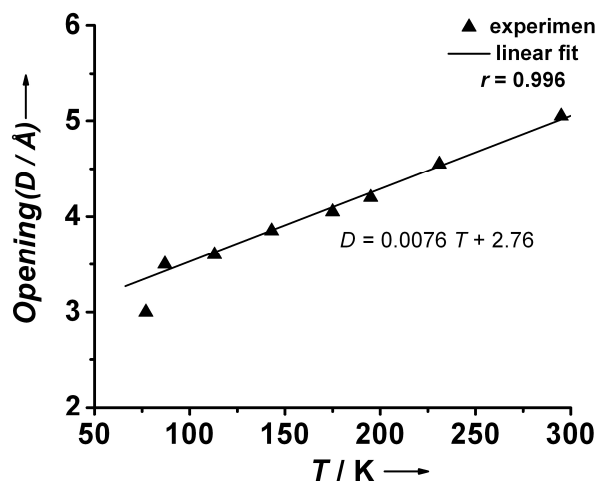


Figure 12.11 Temperature-dependent gate opening of MAMS-1.

In summary, by using an amphiphilic ligand, BBDC, in a solvothermal reaction with $\text{Ni}(\text{NO}_3)_2$, a graphitic MOF structure, MAMS-1, generated by packing of tri-layers through van der Waals interactions, was obtained. In each tri-layer, a hydrophilic octanickel cluster layer is sandwiched by two hydrophobic BBDC layers. Packing of the tri-layers generates hydrophobic gas storage chambers, which are not accessible without activation. There exist channels in the hydrophilic layer that can be desolvated at 200 °C under a dynamic vacuum, which activates MAMS-1 for gas storage. Gas molecules enter the hydrophobic gas storage chambers through the hydrophilic channels, and gates in the hydrophobic/hydrophilic interface. A gate is formed by a pair of BBDC groups held in close proximity via van der Waals interaction, which is readily weakened by thermal vibration. As temperature increases, the gates of MAMS-1 open linearly, giving rise to an unprecedented molecular sieve with an adjustable mesh that can separate any two gases with kinetic diameters in the range of 2.9 to 5.0 Å, corresponding to the size limits of most commercially relevant gases. In addition, a linear relationship between mesh size

and temperature, $D = D_0 + aT$ (D - mesh size at temperature T K, D_0 -mesh size at 0 K, and a -constant), has also been discovered. Mechanistic studies of the molecular gating effect of MAMS-1 suggest that D_0 can be tuned by ligand design, implying the possibility of a MAMS that will be omnipotent in gas separation even at ambient temperatures.

4.5.4 References

- (1) (a) Jasra, R. V.; Choudary, N. V.; Bhat, S. G. T. *Sep. Sci. Technol.* **1991**, *26*, 885; (b) Ko, D.; Siriwardane, R.; Biegler, L. T. *Ind. Eng. Chem. Res.* **2003**, *42*, 339.
- (2) Davis, M. E. *Nature*, **2002**, *417*, 813.
- (3) Auerbach, S. M.; Carrado, K. A.; Dutta, P. K. *Handbook of Zeolite Science and Technology*, Marcel Dekker, New York, **2003**.
- (4) Cheetham, A. K.; Férey, G.; Loiseau, T. *Angew. Chem. Int. Ed.* **1999**, *38*, 3268.
- (5) Kuznicki, S. M.; Bell, V. A.; Nair, S.; Hillhouse, H. W.; Jacubinas, R. M.; Braunbarth, C. M.; Toby, B. H.; Tsapatsis, M. *Nature*, **2001**, *412*, 720.
- (6) (a) Kitagawa, S.; Kitaura, R.; Noro, S. *Angew. Chem. Int. Ed.* **2004**, *43*, 2334; (b) Kitagawa, S.; Kazuhiro, U. *Chem. Soc. Rev.* **2005**, *34*, 109 and refs therein; (c) Kazuhiro, U.; Matsuda, R.; Kitagawa, S. *J. Solid State Chem.* **2005**, *178*, 2420.
- (7) (a) Rowsell, J. L. C.; M. Yaghi, O. *Microporous & Mesoporous Maters.* **2004**, *73*, 3; (b) Ockwig, N. W.; Delgado-Friedrichs, O.; O'Keeffe, M.; Yaghi, O. M. *Acc. Chem. Res.* **2005**, *176*; (c) Batten, S. R. *J. Solid State Chem.* **2005**, *178*, 2475; (d) Rosseinsky, M. J. *Microporous & Mesoporous Maters.* **2004**, *73*, 15; (e) Yaghi, O. M.; O'Keeffe, M.; Ockwig, N. W.; Chae, H. K.; Eddaoudi, M.; Kim, J. *Nature* **2003**, *423*, 705.
- (8) (a) Seo, J. S.; Whang, D.; Lee, H.; Jun, S. I.; Oh, J.; Young, J.; Kim, K. *Nature* **2000**, *404*, 982; (b) Zou, R.; Sakurai, H.; Xu, Q. *Angew. Chem. Int. Ed.* **2006**, *45*, 2542; (c) Dybtsev, D. N.; Nuzhdin, A. L.; Chun, H.; Bryliakov, K. P.; Konstantin, P.; Talsi, E. P.; Fedin, V. P.; Kim, K. *Angew. Chem. Int. Ed.* **2006**, *45*, 916.
- (9) (a) Matsuda, R.; Kitaura, R.; Kitagawa, S.; Kubota, Y.; Belosludov, R. V.; Kobayashi, T. C.; Sakamoto, H.; Chiba, T.; Takata, M.; Kawazoe, Y.; Mita, Y. *Nature* **2005**, *436*, 238; (b) Dinca, M.; Long, J. R. *J. Am. Chem. Soc.* **2005**, *127*, 9376; (c) Pan, L.; Adams, K. M.; Hernandez, H. E.; Wang, X.; Zheng, C.; Hattori, Y.; Kaneko, K. *J. Am.*

Chem. Soc. **2003**, *125*, 3062; (d) Dybtsev, D. N.; Chun, H.; Yoon, S. H.; Kim, D.; Kim, K. *J. Am. Chem. Soc.* **2004**, *126*, 32; (e) Pan, L.; Parker, B.; Huang, X.; Olson, D. H.; Lee, J. Y.; Li, J. *J. Am. Chem. Soc.* **2006**, *128*, 4180; (f) Chen, B.; Liang, C.; Yang, J.; Contreras, D. S.; Clancy, Y. L.; Lobkovsky, E. B.; Yaghi, O. M.; Dai, S. *Angew. Chem. Int. Ed.* **2006**, *45*, 1390; (g) Pan, L.; Olson, D. H.; Ciemnomolonski, L. R.; Heddy, R.; Huang, X.; Li, J. *Angew. Chem. Int. Ed.* **2006**, *45*, 616; (h) Chen, B.; Ma, S.; Zapata, F.; Fronczek, F. R.; Lobkovsky, E. B.; Zhou, H.-C. *Inorg. Chem.* **2007**, *46*, 1233.

(10) (a) Rowsell, J. L.; Yaghi, O. M. *Angew. Chem. Int. Ed.* **2005**, *44*, 4670; (b) Chen, B.; Ockwig, N. W.; Millward, A. R.; Contreras, D. S.; Yaghi, O. M. *Angew. Chem. Int. Ed.* **2005**, *44*, 4745; (c) Sun, D.; Ma, S.; Ke, Y.; Collins, D. J.; Zhou, H.-C. *J. Am. Chem. Soc.* **2006**, *128*, 3896; (d) Rowsell, J. L. C.; Yaghi, O. M. *J. Am. Chem. Soc.* **2006**, *128*, 1304; (e) Eddaoudi, M.; Kim, J.; Rosi, N.; Vodak, D.; Wachter, J.; O’Keeffe, M.; Yaghi, O. M. *Science* **2002**, *295*, 469; (f) Millward, A. R.; Yaghi, O. M. *J. Am. Chem. Soc.* **2005**, *127*, 17998; (g) Ma, S.; Zhou, H.-C. *J. Am. Chem. Soc.* **2006**, *128*, 11734.

(11) Sozzani, P.; Bracco, S.; Comotti, A.; Feretti, L.; Simonutti, R. *Angew. Chem. Int. Ed.* **2005**, *44*, 1816.

(12) Huo, Q.; Margolese, D. I.; Ciesla, U.; Feng, P.; Gier, T. E.; Sieger, P.; Leon, R.; P. Petroff, M.; Schüth, F.; Stucky, G. D. *Nature*, **1994**, *368*, 317.

(13) Ke, Y.; Collins, D. J.; Zhou, H.-C. *Inorg. Chem.* **2005**, *44*, 4154.

(14) Crystal structure determination of compound MAMS-1: $C_{36}H_{52}Ni_4O_{21}$, $M_r = 1055.62$; green block, $0.23 \times 0.08 \times 0.08$ mm, $T = 213(2)$ K, $\lambda(Mo_{K\alpha}) = 0.71073$ Å, monoclinic, space group $P2(1)/c$, $a = 10.9685(2)$ Å, $b = 11.308(2)$ Å, $c = 38.405(7)$ Å, $\beta = 96.781(3)^\circ$, $V = 4730.1(14)$ Å³, $Z = 4$, $d_{calcd} = 1.482$ g/cm³; $R_1 (I > 2\sigma(I)) = 0.0609$, wR_2 (all data) = 0.1456, GOF = 1.021, CCDC-617998 (MAMS-1) contains the supplementary crystallographic data for this communication. These data can be obtained free of charge at www.ccdc.cam.ac.uk/conts/retrieving.html (or from the Cambridge Crystallographic Data Center, 12, Union Road, Cambridge CB21EZ, UK; fax: (+44) 1223-336-033; or deposit@ccdc.cam.ac.uk).

(15) Bondi, A. *J. Phys. Chem.* **1964**, *68*, 441.

(16) Beck, D. W. *Zeolite Molecular Sieves*; Wiley & Sons: New York, **1974**.

Chapter 13

The Discovery and Gas Adsorption Studies of Mesh-Adjustable Molecular Sieves¹

13.1 Introduction

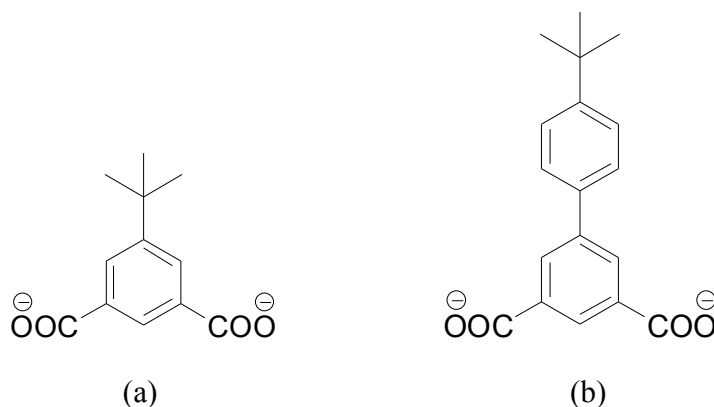
Molecular sieves are materials containing uniform pores that can selectively adsorb molecules based on their size. They have been widely used in shape/size selective catalysis and separation.¹ Conventionally, molecular sieves are made of inorganic zeolites. Due to the rigidity of the bonds in such materials, a molecular sieve is made with a fixed mesh size. This is advantageous when the mesh size precisely fits the separation needs. However, when the size disparity of the two gases is very small, a molecular sieve with the precise mesh size is not always readily available. In such cases, mesh-adjustable molecular sieves (MAMSs) that can always meet the separation needs are highly desirable. In order to make a MAMS, two factors—permanent porosity and flexibility of the pores, must be taken into account. Although a titanosilicate zeolite was reported to possess discrete mesh sizes based on the degree of dehydration of this material at various temperatures,² these two would seem irreconcilable for inorganic zeolites due to their robust frameworks.

As a new type of zeolitic analogues, porous metal-organic frameworks (MOFs)³ have in the past decade become a burgeoning research field due to their potential applications in gas storage,⁴ catalysis,⁵ magnetism,⁶ and gas separation.⁷ In particular, the dynamic features⁸ of porous MOFs have distinguished them from traditional inorganic zeolites and afforded the possibility to construct frameworks with flexible pores.^{1b, 8}

In chapter 12, a MOF-based mesh-adjustable molecular sieve, MAMS-1, built from the amphiphilic ligand 5-*tert*-butyl-1, 3-benzenedicarboxylate (BBDC) was reported (Scheme 13.11a).⁹ The mesh range of MAMS-1 falls between 2.9 and 5.0 Å. When the temperature is precisely controlled, any mesh size within this range can be accurately attained. In addition, a linear relationship between mesh size and temperature, $D = D_0 +$

¹ This chapter was reprinted from the prepared manuscript “The Discovery and Gas Adsorption Studies of Mesh-Adjustable Molecular Sieves” Submitted to *J. Am. Chem. Soc.* Unpublished work copyright 2008, American Chemical Society.

αT (D - mesh size at temperature T K, D_0 -mesh size at 0 K, and α -constant), was discovered. Moreover, mechanistic studies of the molecular gating effect of MAMS-1, which is controlled by the *tert*-butyl groups of the BBDC ligand, suggest that D_0 and α could be tuned by ligand design. This implies the possibility of a MAMS that will be versatile in gas separation even at ambient temperatures. In order to prove the feasibility of the hypothesis and explore new MAMSs for gas separation, in this chapter a new ligand 4'-*tert*-butyl-biphenyl-3,5-dicarboxylate (BBPDC) is designed (Scheme 1b), which has one more phenyl ring than BBDC. As expected, solvothermal reactions of BBPDC with $\text{Zn}(\text{NO}_3)_2$, $\text{Co}(\text{NO}_3)_2$, and $\text{Cu}(\text{NO}_3)_2$ give rise to MAMS-2, MAMS-3, and MAMS-4 respectively. The three new MAMSs are isostructural, and all display a temperature-induced molecular sieving effect similar to that observed with MAMS-1.



Scheme 13.1 *tert*-butyl carboxylate ligands: (a) 5-*tert*-butyl-1,3-benzenedicarboxylate (BBDC); (b) 4'-*tert*-butyl-biphenyl-3,5-dicarboxylate (BBPDC).

13.2 Experimental Details

General information: Commercially available reagents were used as received without further purification. Elemental analyses (C, H, and N) were obtained by Canadian Microanalytical Service Ltd. TGA was performed under N_2 on a PerkinElmer TGA 7 and a Beckman Coulter SA3100 surface area analyzer was utilized for the gas adsorption measurements. NMR data was collected on a Bruker 300 MHz spectrometer.

Synthesis of 4'-*tert*-butyl-biphenyl-3,5-dicarboxylate (BBPDC): To a 500 mL Schlenk flask, dimethyl-5-bromo-isophthalate (2 g, 0.015 mol), 4-*tert*-Butyl-phenyl boronic acid (4 g, 0.015 mol), CsF (2.3 g) and $\text{Pd}(\text{PPh}_3)_4$ (0.2 g) were added. The flask

was connected to a Schlenk line while 300 mL 1,2-Dimethoxyethane was degassed and added through a canula. The flask was equipped with a water condenser and refluxed under the nitrogen for 48 hours. The solution was dried on rotary evaporator. 100 mL H₂O was added and then extracted with CHCl₃. The organic phase was dried with MgSO₄. After the solvent was removed, the crude product was purified by column chromatography (silica, CHCl₃) to give the pure product 4'-tert-butyl-biphenyl-3,5-dicarboxylate methyl ester (¹H NMR (CDCl₃): 1.4 (s, 9H), 3.9 (s, 3H), 7.3 (d, 2H), 7.5 (d, 2H), 8.4 (s, 2H), 8.6 (s, 1H)). 4'-tert-butyl-biphenyl-3,5-dicarboxylate methyl ester was dissolved in a 100 mL mixture of THF and MeOH (v/v = 1:1), to which 20 mL 2N NaOH aqueous solution was added. The mixture was stirred at room temperature overnight. The organic phase was removed. The aqueous phase was acidified with diluted hydrochloric acid to give white precipitate, which was filtered and washed with water several times (¹H NMR (DMSO): 1.4 (s, 9H), 7.5 (d, 2H), 7.6 (d, 2H), 8.3 (s, 2H), 8.4 (s, 1H)).

Synthesis of MAMS-2: A mixture of 20 mg Zn(NO₃)₂·6H₂O and 10 mg BBPDC ligand in 1.5 ml dimethylformamide (DMF) solvent was sealed in a Pyrex glass tube (ID 8mm/OD 10 mm) and heated to 120 °C at a rate of 1 °C / min. After staying at 120 °C for 24 hours, it was cooled to 35 °C at a rate of 0.1°C / min. The resulting colorless crystals were washed with DMF twice to give pure MAMS-2 (Zn₂(H₂O)₂(BBPDC)₂·3DMF, yield: 85% based on BBPDC ligand). The reaction was amplified to gram quantity using multiple tubes. Elemental analysis for MAMS-2 calculated: C 55.22%, H 5.87%, N 4.29%; found: C 55.65%, H 5.39%, N 3.98%.

Synthesis of MAMS-3: A mixture of 20 mg Co(NO₃)₂·6H₂O and 10 mg BBPDC ligand in 1.5 ml dimethylacetamide (DMA) solvent was sealed in a Pyrex glass tube (ID 8mm/OD 10 mm) and heated to 120 °C at a rate of 1 °C / min. After staying at 120 °C for 24 hours, it was cooled to 35 °C at a rate of 0.1°C / min. The resulting violet crystals were washed with DMA twice to give pure MAMS-3 (Co₂(H₂O)₂(BBPDC)₂·3DMA, yield: 80% based on BBPDC ligand). The reaction was amplified to gram quantity using multiple tubes. Elemental analysis for MAMS-3 calculated: C 57.20%, H 6.30%, N 4.17%; found: C 58.85%, H 6.16%, N 4.15%.

Synthesis of MAMS-4: A mixture of 20 mg Cu(NO₃)₂·2.5H₂O and 10 mg BBPDC ligand in 1.5 ml dimethylformamide (DMF) solvent with 3 drops HBF₄ (50%

aqueous solution) added was sealed in a Pyrex glass tube (ID 8mm/OD 10 mm) and heated to 75 °C at a rate of 0.1 °C / min. After staying at 75 °C for 24 hours, it was cooled to 35 °C at a rate of 0.1°C / min. The resulting turquoise crystals were washed with DMA twice to give pure MAMS-4 ($\text{Cu}_2(\text{H}_2\text{O})_2(\text{BBPDC})_2 \cdot 3\text{DMF}$) yield: 80% based on BBPDC ligand). The reaction was amplified to gram quantity using multiple tubes. Elemental analysis for MAMS-2 calculated: C 55.43%, H 5.89%, N 4.31; found: C 55.13%, H 5.54%, N 4.58.

Single-crystal X-ray crystallography: Single crystal X-ray data were collected on a Bruker Smart Apex diffractometer equipped with an Oxford Cryostream low temperature device and a fine-focus sealed-tube X-ray source (Mo- K_α radiation, $\lambda = 0.71073 \text{ \AA}$, graphite monochromated) operating at 45 kV and 35 mA. Frames were collected with 0.3° intervals in φ and ω for 30 s per frame such that a hemisphere of data was collected. Raw data collection and refinement were done using SMART. Data reduction was performed using SAINT+ and corrected for Lorentz and polarization effects.¹⁰ The structure was solved by direct methods and refined by full-matrix least-squares on F^2 with anisotropic displacement using SHELX-97.¹¹ Non-hydrogen atoms were refined with anisotropic displacement parameters during the final cycles. Hydrogen atoms on carbon were calculated in ideal positions with isotropic displacement parameters set to $1.2 \times U_{\text{eq}}$ of the attached atom. In all cases solvent molecules were highly disordered, and attempts to locate and refine the solvent peaks were unsuccessful; contributions to scattering due to these solvent molecules were removed using the SQUEEZE routine of PLATON and refined further using the data generated.¹²

Gas Adsorption Measurements: Gas adsorption measurements were performed using a Beckman Coulter SA 3100 surface area and pore size analyzer. The samples were held under a dynamic vacuum ($< 10^{-3}$ torr) at 300 °C for MAMS-2 and MAMS-3, or 170 °C for MAMS-4, for five hours to remove the free guest solvent molecules (DMF or DMA) and coordinated aqua ligands. Before the measurement, the sample was evacuated again by using the “outgas” function of the surface area analyzer for 1 hour at 300 °C for MAMS-2 and MAMS-3 or 170 °C for MAMS-4. A sample of about 100 mg was used for N_2 (99.999%) adsorption measurement, and was maintained at 77K with liquid nitrogen. In the hydrogen storage measurement, high purity hydrogen (99.9995%) and a

100 mg sample was used. The regulator and pipe were flushed with hydrogen before they were connected to the analyzer. The internal lines of the instrument were flushed three times by utilizing the “flushing lines” function of the program to ensure the purity of H₂. The measurement was maintained at 77 K with liquid nitrogen. Similar to the procedures used for H₂ measurement at 77 K, highly pure O₂ (99.99%), CO (99.99%), CH₄ (99.997%), C₂H₄ (99.5%), C₃H₆ (99.5%), *iso*-C₄H₁₀ (99.5%), SF₆ (99.8%) and CO₂ (99.99%) were used for their respective gas adsorption measurements. All the gases used for the measurements were purchased from Linde Gas LLC, Cincinnati, Ohio, USA. The temperatures at 87 K, 113 K, 143 K, 195 K and 231 K were maintained with a liquid argon bath, isopentane-liquid nitrogen bath, n-pentane-liquid nitrogen bath, acetone-dry ice bath, and acetonitrile-dry ice bath, respectively.^{13,14} To prevent condensation of CO and O₂ at 77 K, the pressure ranges were below 448 torr and 156 torr, respectively; to prevent condensation of O₂ at 87 K, the pressure range was below 466 torr; to prevent condensation of C₂H₄ at 143 K, the pressure range was below 120 torr; to prevent condensation of C₃H₆ at 195 K, the pressure range was below 110 torr; to prevent condensation of *iso*-C₄H₁₀ at 241 K, the pressure range was below 210 torr. For all adsorption isotherms, P₀ represents a relative standard (pressure of the saturation tube of the Beckman Coulter SA 3100 surface area analyzer during the measurement): at 77 K, P₀ was 757 torr for H₂ and N₂, 441 torr for CO, and 151 torr for O₂; at 87 K, P₀ was 757 torr for CO and N₂ and 465 torr for O₂; at 113 K, P₀ was 757 torr for CO, CH₄, and N₂; at 143 K, P₀ was 757 torr for CH₄ and 118 torr for C₂H₄; at 195 K, P₀ was 757 torr for C₂H₄ and CO₂ and 108 torr for C₃H₆; at 241 K, P₀ was 757 torr for C₃H₆ and 205 torr for *iso*-C₄H₁₀; at 295 K, P₀ was 757 torr for *iso*-C₄H₁₀ and SF₆.

Powder X-ray Diffraction (PXRD): X-ray powder diffraction (XRPD) was carried out on a Bruker Apex diffractometer equipped with an Oxford Cryostream low temperature device using Mo-K α radiation ($\lambda = 0.71073 \text{ \AA}$). The sample was filled in a 0.4 mm thin wall capillary. Diffraction frames with an exposure time of 300 s were taken at different temperatures and processed with the GADDS program to yield the diffraction pattern.

13.3 Results and Discussion

Crystal structure description: Single-crystal X-ray studies reveal that the three new MAMSs are isostructural, and all of them crystallize in the trigonal space group $P-3c1$ (Table 13.1). They adopt the well-known $M_2(\text{COO})_4$ paddle-wheel as their secondary building unit (SBU), where two aqua axial ligands can be removed at high activation temperature. This type of di-metal paddle-wheel SBUs happens to be very common for copper MOFs,^{4a,c,h,i} and has also been frequently reported for zinc MOFs.^{4f,7e,15} However, as for cobalt, MAMS-3 represents one of the few instances of MOFs possessing the cobalt paddle-wheel SBU.^{6c,16} The differing radii of the metal ions can partially ascribe for the bond distances between the M and the axial aqua ligands (Table 13.2). The M•••M distances of the SBUs varies from 2.647 to 2.951 Å. For all of the three MAMSs, the longer the M•••M distance, the shorter the M-aqua distance. Those bonding distances also suggest that the stronger M-M interaction is, the weaker M-aqua interaction is.

Table 13.1 Crystal data^a and structure refinements of MAMS-2, MAMS-3 and MAMS-4.

	MAMS-2	MAMS-3	MAMS-4
formula	$\text{C}_{18}\text{H}_{18}\text{ZnO}_5$	$\text{C}_{18}\text{H}_{18}\text{CoO}_5$	$\text{C}_{18}\text{H}_{18}\text{CuO}_5$
FW	379.69	373.25	377.86
crystal system	Trigonal	Trigonal	Trigonal
space group	$P-3c1$	$P-3c1$	$P-3c1$
crystal size. (mm)	0.16x0.12x0.10	0.18x0.15x0.10	0.15x0.13x0.10
a , Å	18.6069(6)	18.9328(1)	18.4472(4)
b , Å	18.6069(6)	18.9328(1)	18.4472(4)
c , Å	22.6226(1)	22.307(3)	22.5760(1)
α , deg	90.00	90.00	90.00
β , deg	90.00	90.00	90.00
γ , deg	120.00	120.00	120.00
V , Å ³	6783.0(5)	6924.7(1)	6653.3(4)
Z	12	12	12
d_{cacl} , g cm ⁻¹	1.115	1.074	1.132
GOF	1.06	1.459	1.093
R_I, wR_2 ^b	0.0746, 0.2043	0.0665, 0.203	0.0731, 0.2152

^a Obtained with graphite-monochromated $Mo K\alpha$ ($\lambda = 0.71073$ Å) radiation,

^b $R_I = \sum ||F_o| - |F_c|| / \sum |F_o|$ and $wR_2 = \{[\sum w(F_o^2 - F_c^2)^2] / [\sum w(F_o^2)^2]\}^{1/2}$

Table 13.2 Selected bonding distances in MAMS-2, MAMS-3, and MAMS-4.

	MAMS-2 (Zn)	MAMS-3 (Co)	MAMS-4 (Cu)
M-M bonding distances (Å)	2.951	2.876	2.647
M-aqua bonding distances (Å)	1.869	1.978	2.016

Each paddle-wheel SBU connects with four BBPDC ligands, while every BBPDC ligand connects with two paddle-wheel SBUs and expands into a two-dimensional layer with the hydrophilic paddle-wheel SBUs layer sandwiched by two hydrophobic BBPDC layers (Figure 13.1). In each layer, every three paddle-wheel SBUs are connected by three BBPDC ligands to form the triangular hydrophilic holes with the *tert*-butyl groups of every three BBPDC ligands pointing up and down alternately. Every six paddle-wheel SBUs connect with six BBPDC ligands, three of which point down and three of which point up, to form a hydrophobic cage with a volume of 1360 Å³ for MAMS-2, 1386 Å³ for MAMS-3, and 1341 Å³ for MAMS-4. Every hydrophobic cage with six-fold symmetry is encircled by six hydrophilic holes, and every hydrophilic hole is surrounded by three hydrophobic cages (Figure 13.2). In each hydrophobic cage, there are six windows with the opening size of 9.709 Å (atom to atom distance; ~6.6 Å when considering van der Waals radii¹⁷) for MAMS-2, 9.867 Å (atom to atom distance; ~6.8 Å when considering van der Waals radii¹⁷) for MAMS-3, and 9.600 Å (atom to atom distance; ~6.5 Å when considering van der Waals radii¹⁷) for MAMS-4 (Figure 13.3a).

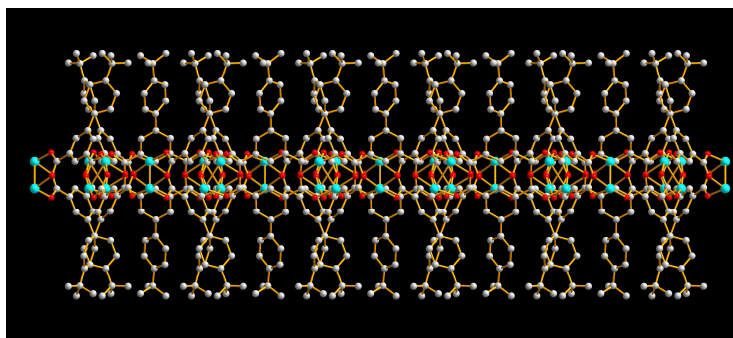


Figure 13.1 Two-dimensional trilayer sandwich structure.

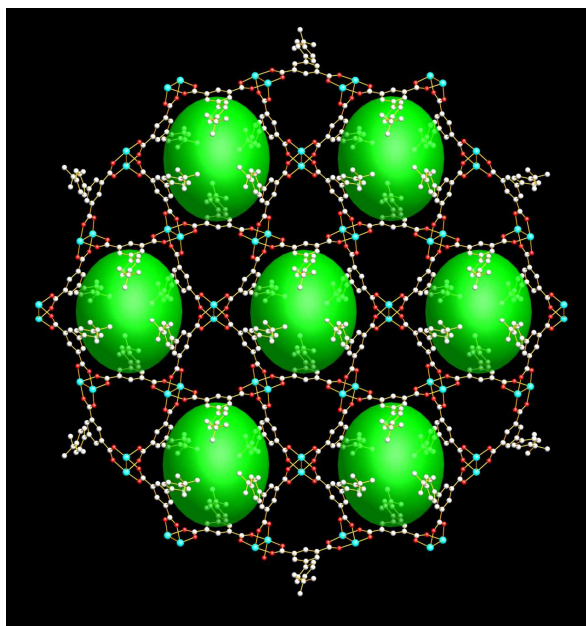


Figure 13.2 Hydrophilic holes and hydrophobic cages in a single layer.

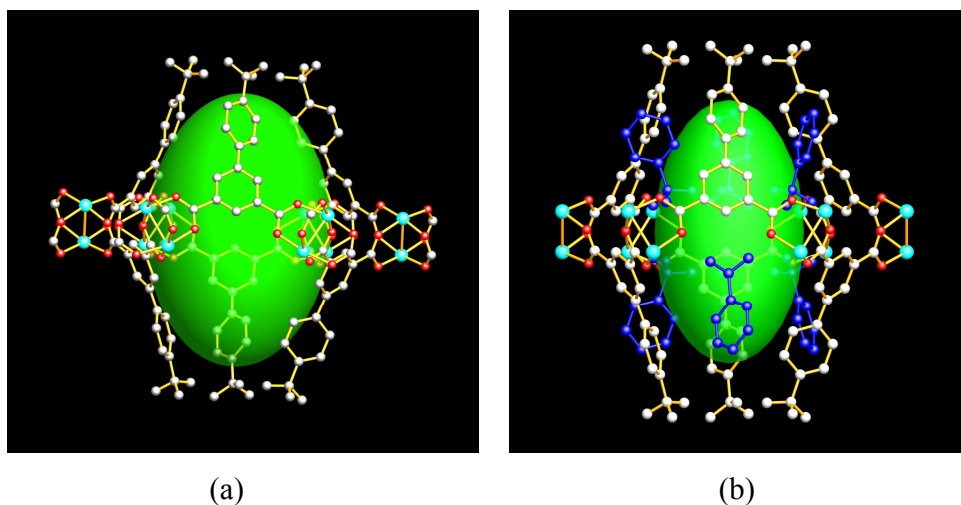


Figure 13.3 Hydrophobic cages in MAMS-2,3,4: (a) A hydrophobic cage with six open windows. (b) A hydrophobic cage with six *tert*-butyl groups of BBPDC ligands inserting in the windows.

Every layer connects with adjacent layers through the van der Waals interactions between *tert*-butyl groups (Figure 13.4) to form a graphitic structure. The triangular hydrophilic holes of each layer pack along *c* direction to form one-dimensional triangular

hydrophilic channel with an edge length of 7.822 Å for MAMS-2, 8.073 Å for MAMS-3, and 7.905 Å for MAMS-4 (metal atom to metal atom distances; ~ 4.9 Å for MAMS-2, ~ 4.8 Å for MAMS-3, and ~ 4.9 Å for MAMS-4 when considering van der Waals radii¹⁷) after removal of the aqua ligands. The hydrophobic cages of each layer pack along *c* direction with the *tert*-butyl groups from other layers inserting in the windows of the hydrophobic cages (Figure 13.3b). Viewing from *c* direction, it can be inferred that the hydrophobic cages should be the main storage space for gas molecules, while the hydrophilic channels should act as passages to let gas molecules pass into the cages through the *tert*-butyl groups. These groups might serve as gates at the intersections of the hydrophilic channels and hydrophobic cages (Figure 13.5).

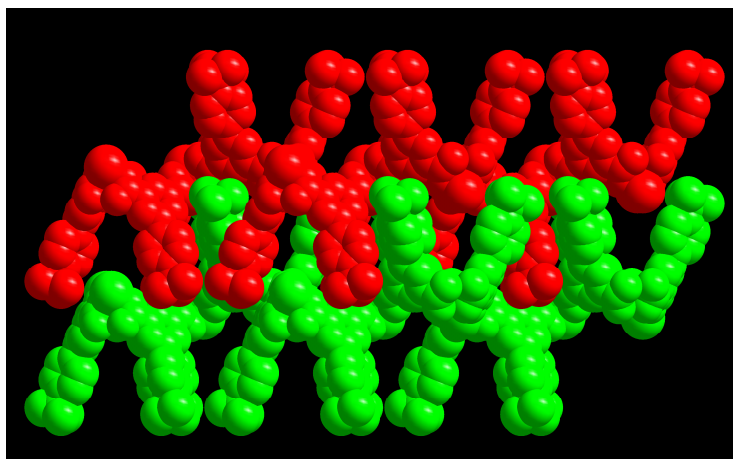


Figure 13.4 Two adjacent layers connect with each other through the van der Waals interactions.

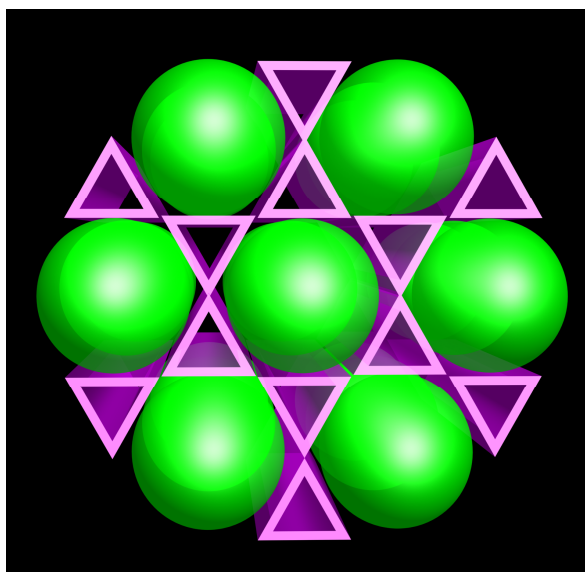


Figure 13.5 Hydrophilic channels and hydrophobic cages viewed along c direction.

Thermal Gravimetry Analysis (TGA): As shown in Figure 13.6, the first 24.6% (cald: 26.0) weight loss of MAMS-2 from about 300 °C to 420 °C corresponds to the loss of three DMF free guest molecules and two coordinated aqua ligands. Decomposition of the BBPDC ligands starts from around 430 °C and ends at 650 °C with an overall weight loss of 56.4% (cald: 57.2%). As for MAMS-3, the loss of three DMA free guest molecules and two coordinated aqua ligands also starts from around 300 °C and ends at about 420 °C (cald: 29.5%; found: 28.0%), which is followed by the decomposition of the BBPDC ligands with an overall weight loss of 55.0% (cald: 55.6%). Finally for MAMS-4, the loss of three DMF free guest molecules and two coordinated aqua ligands starts from about 150 °C and ends at about 350 °C (cald: 29.5%; found: 28.0%), which is closely followed by the decomposition of the BBPDC ligands with the weight loss of 54.0% (cald: 57.5%) ending at around 430 °C.

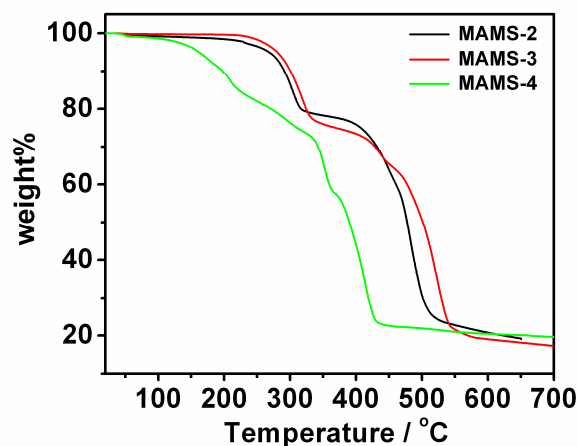


Figure 13.6 TGA plots of MAMSs.

Gas Adsorption Studies In order to investigate the temperature-induced molecular sieving effect of MAMS-2, the freshly isolated sample, which is not active for adsorption (Figure 13.7), was activated at 300 °C under a dynamic vacuum to remove the DMF guest molecules and coordinated aqua ligands based on TGA studies. Gas adsorption measurements were then carried out at different temperatures. As shown in Figure 13.8a, MAMS-2 exhibits highly selective uptake of H₂ over CO, N₂, or O₂ at 77 K. Such selectivity in MOFs has previously been reported in very few cases,^{7c,d,h} and was also observed in MAMS-1.⁹ We do not believe that this can be attributed to the size of the hydrophilic channels, which are around 4.9 Å (considering van der Waals radii) and are large enough to accommodate O₂, N₂, or CO molecules (kinetic diameters are 3.46, 3.64, 3.76 Å O₂, N₂, CO respectively).¹⁸ This implies that the molecular sieving effect has a different origin.

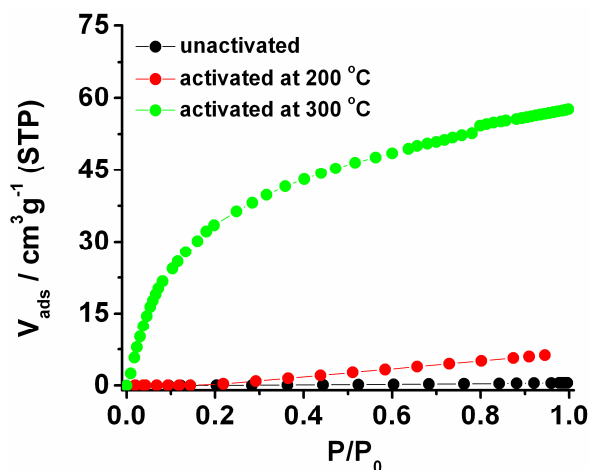


Figure 13.7 H₂ adsorption isotherms of MAMS-2 activated at different conditions.

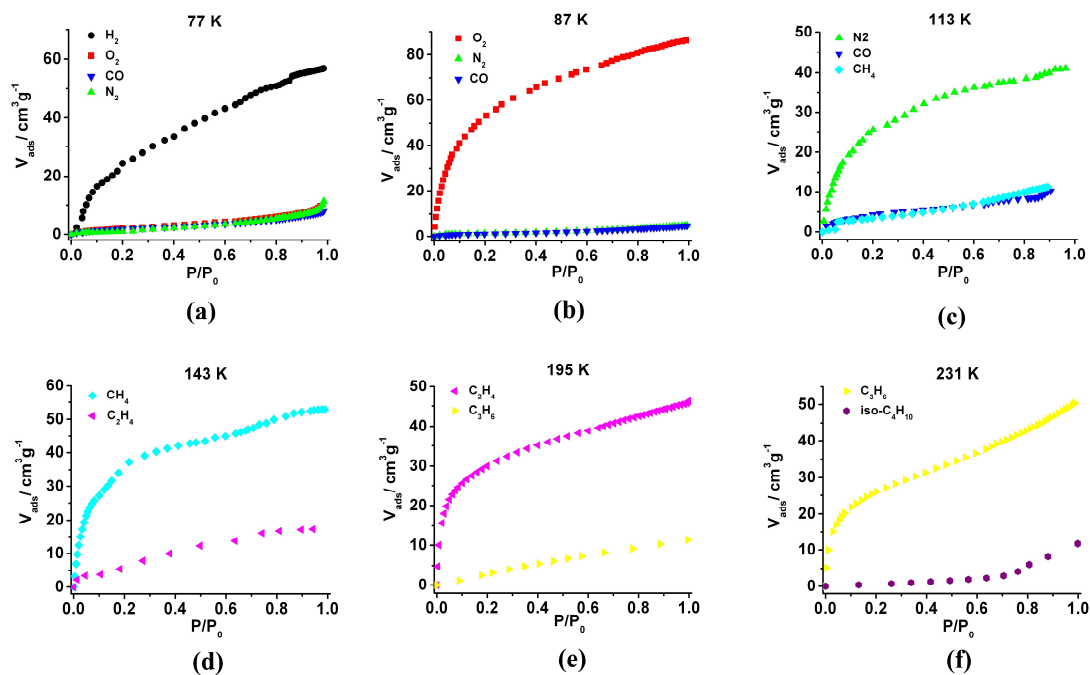


Figure 13.8 Gas adsorption isotherms of MAMS-2 at different temperatures.

The crystal structure of MAMS-2 shows that a hydrophobic cage is accessible by gas molecules only through its hydrophobic/hydrophilic interface, on which the *tert*-butyl groups of BBPDC ligands reside forming a gate based on van der Waals attractions

(Figure 13.3b). When such gates are open, the gas molecules in the hydrophilic channels can then enter the hydrophobic cages.

Most likely, the molecular sieving effect comes from the *tert*-butyl group gates. In view of the kinetic diameters of 2.89 Å for H₂, 3.46 Å for O₂, 3.64 Å for N₂, and 3.76 Å for CO,¹⁸ it can be inferred that the gate opening of MAMS-2 is around 3.0 Å to 3.4 Å. At 77 K, MAMS-2 excludes CO, N₂, and O₂ but allows H₂ to enter the hydrophobic cages.

If this is indeed the case, the gates should open wider at higher temperatures, because the increased thermal vibration and rotation frequency of the *tert*-butyl groups can result in more opportunities for the gas molecules to pass through, thus leading to the wider opening of the gate.

When the temperature is raised to liquid argon temperature (87 K, Figure 13.8b), gas adsorption studies reveal that only a small amount of CO or N₂ is adsorbed by MAMS-2. However, MAMS-2 can take up significant amount of O₂. The adsorption isotherm of O₂ shows type-I behavior. Dioxygen (3.46 Å) can be selectively adsorbed from a mixture with N₂ (3.64 Å) and CO (3.76 Å), which implies that at 87 K the gate opens to around 3.5 Å. With the minute size disparity between O₂ and N₂ ($\Delta\sigma$: 0.18 Å) in mind, one has to be optimistic about the application potential of MAMS-2. When the temperature is increased to 113 K, MAMS-2 can take up a moderate amount of N₂ but relatively low quantities of CO and CH₄ (3.8 Å) (Figure 13.8c). This is also consistent with the idea that the gating effect is due to *tert*-butyl groups of BBPDC ligands, and the gate opens wider under increased temperatures. This also implies that at 113 K, the gate opens to about 3.7 Å, wide enough to allow N₂ (3.64 Å) to enter the cages, but molecules with larger kinetic diameters such as CO (3.76 Å) and CH₄ (3.8 Å) will stay in the hydrophilic channels. The resolution for size discrimination is now 0.12 Å. In fact, it can be inferred from all the adsorption data obtained thus far that if temperatures can be tuned continuously and precisely, any two molecules with a size difference can be separated by MAMS-2, as seen in MAMS-1.

With these considerations in mind, we decided to explore the possibility of using MAMS-2 in separations important to petroleum refinery and petrochemical industry. Not

surprisingly, MAMS-2 can distinguish methane from ethylene at 143 K, ethylene from propylene at 195 K, and propylene from iso-butane at 231 K (Figure 13.8d, 13.8e, 13.8f).

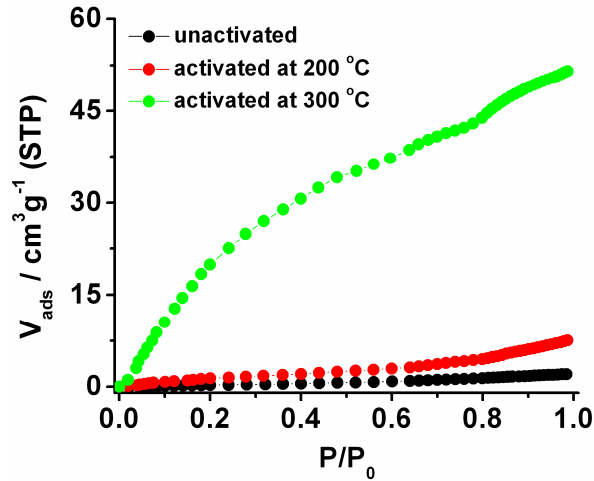


Figure 13.9 H₂ adsorption isotherms of MAMS-3 activated at different conditions.

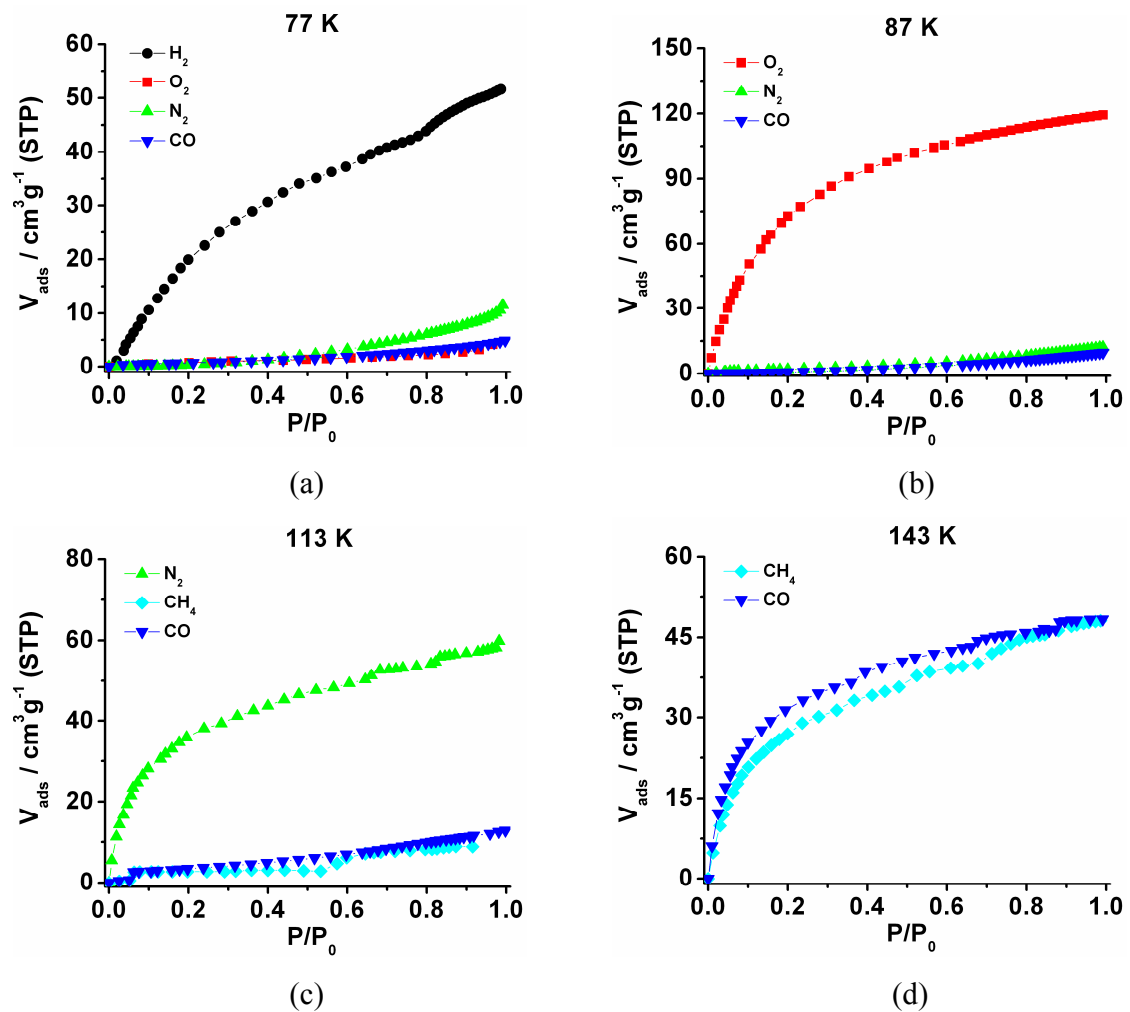


Figure 13.10 Gas adsorption isotherms of MAMS-3 at different temperatures: (a) H₂, O₂, N₂, and CO adsorption isotherms of MAMS-3 at 77 K; (b) O₂, N₂, and CO adsorption isotherms of MAMS-3 at 87 K; (c) N₂, CO and CH₄ adsorption isotherms of MAMS-3 at 113 K; (d) CO and CH₄ adsorption isotherms of MAMS-3 at 143 K.

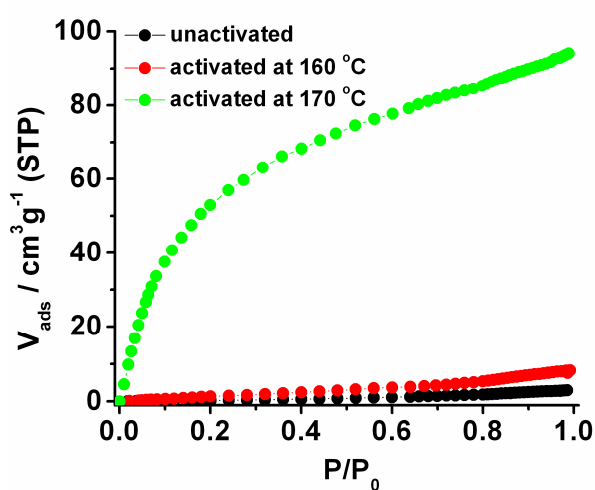


Figure 13.11 H₂ adsorption isotherms of MAMS-4 activated at different conditions.

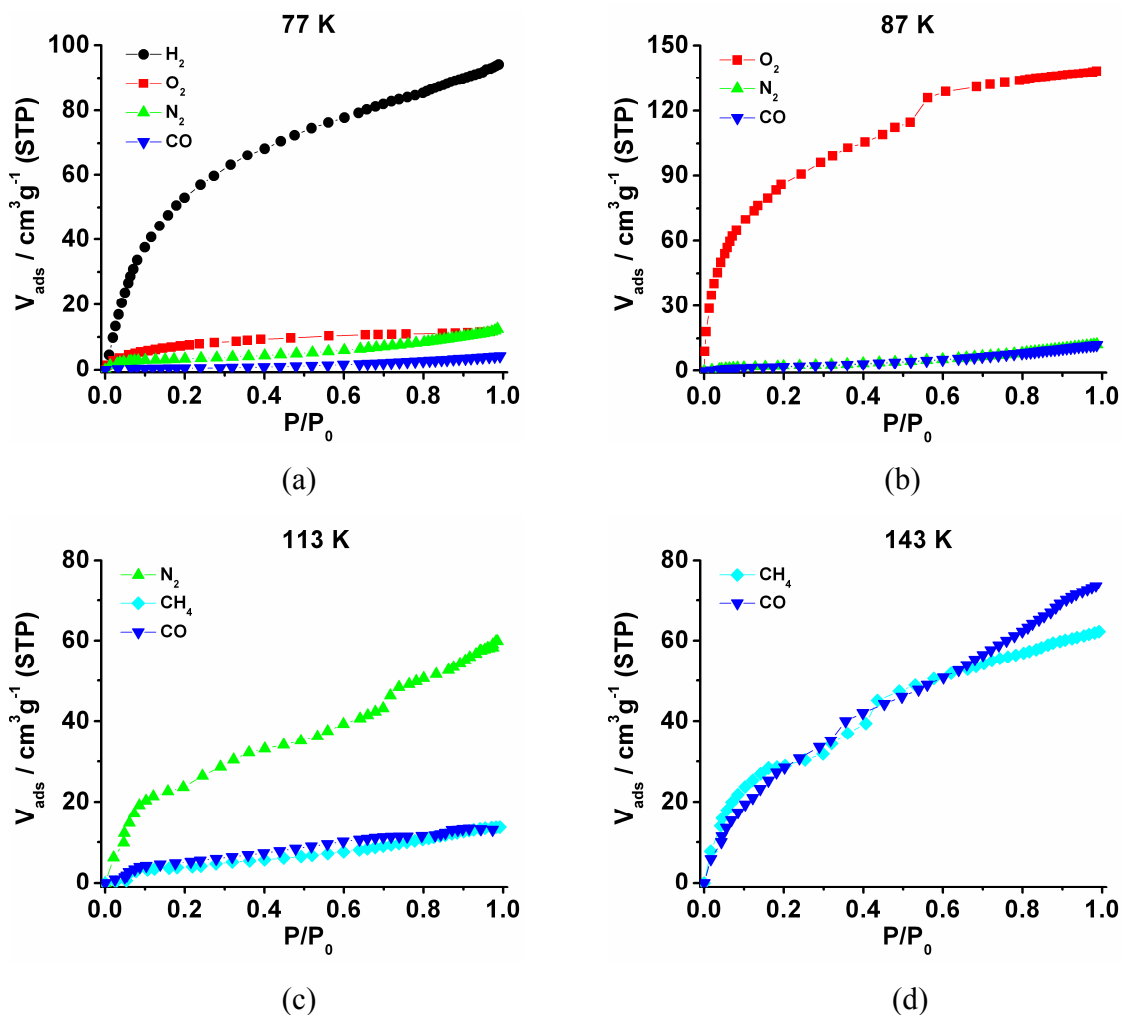


Figure 13.12 Gas adsorption isotherms of MAMS-4 at different temperatures: (a) H₂, O₂, N₂, and CO adsorption isotherms of MAMS-3 at 77 K; (b) O₂, N₂, and CO adsorption isotherms of MAMS-3 at 87 K; (c) N₂, CO and CH₄ adsorption isotherms of MAMS-3 at 113 K; (d) CO and CH₄ adsorption isotherms of MAMS-3 at 143 K.

Gas adsorption studies on activated MAMS-3 and activated MAM-4 reveal almost the same phenomena as discovered in MAMS-2 (Figure 13.9-Figure 13.12). These temperature-induced molecular-sieving effects of the three MAMSs are very similar to that of MAMS-1. However, unlike MAMS-1 where a significant amount of iso-butane can pass through the hydrophilic channels ($\sim 5.1 \text{ \AA}$) and then enter the storage room of hydrophobic chambers at room temperature,⁹ the relative smaller channels of the three new MAMSs ($\sim 4.9 \text{ \AA}$) preclude the entrance of iso-butane (kinetic diameter 5.0

Å)¹⁸ leading to very limited uptake. A drawing of temperature versus size of the molecule allowed to enter the gate is given in Figure 13.13. The gate opening D , and temperature T , can be related by a linear equation, $D = 0.0073 T + 2.83$, with a correlation coefficient of 0.996 (Figure 13.13). This is very close to the linear equation found in MAMS-1, $D = 0.0076 T + 2.76$. The equation can be used to predict if a gas molecule will be allowed to enter the gate at a certain temperature. It can also be used to find the best temperature for the separation of a mixture. The opening of the gates at 77 K is extrapolated to be 3.4 Å, which is consistent with the experimental observation that all gas molecules except hydrogen are blocked out.

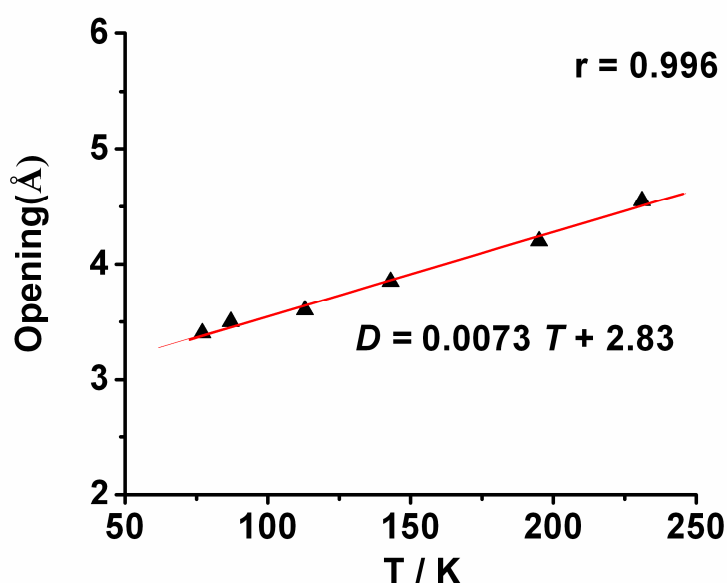


Figure 13.13 Temperature gate opening of MAMS-2. ▲: estimated values based on experimental data;
 — : linear fit.

Proposed Mechanism Studies The mechanistic details of these unprecedented temperature-controlled gas-selective adsorption phenomena can be deduced from the crystal structures and adsorption data of the new MAMSs.

These temperature-dependent molecular-gating effects do not arise from simple thermal expansion of the framework. As shown in Figure 13.14, the unit cell parameters

of the three new MAMSs remain almost constant while the temperature changes from 113 K to 273 K. This assessment is also supported by the temperature independence of powder X-ray diffraction (PXRD). Although MAMS-2 (Zn) lose crystallinity after activation, the PXRD patterns of activated MAMS-3 and MAMS-4 reveal their framework integrities and no peak shifts at different temperatures (Figure 13.15, 13.16).

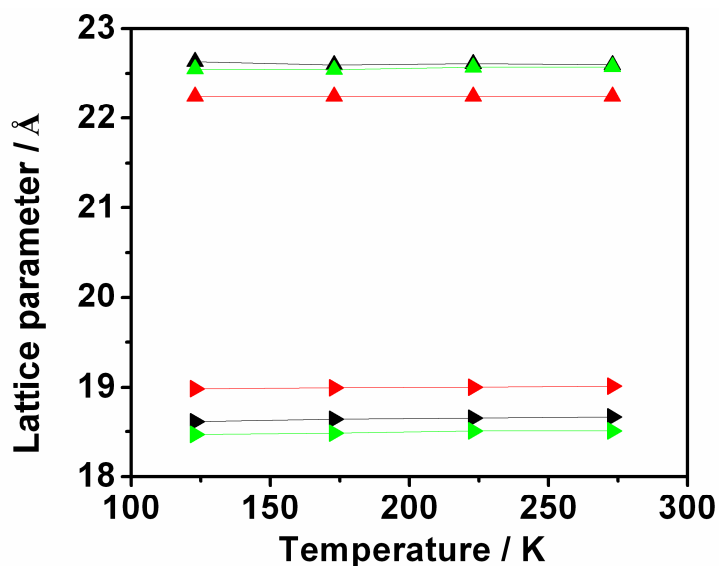


Figure 13.14 Crystal lattice parameters of MAMSs at different temperatures ► represents *a* or *b* axis; ▲ represents *c* axis; MAMS-2 (black); MAMS-3 (red); MAMS-4 (green).

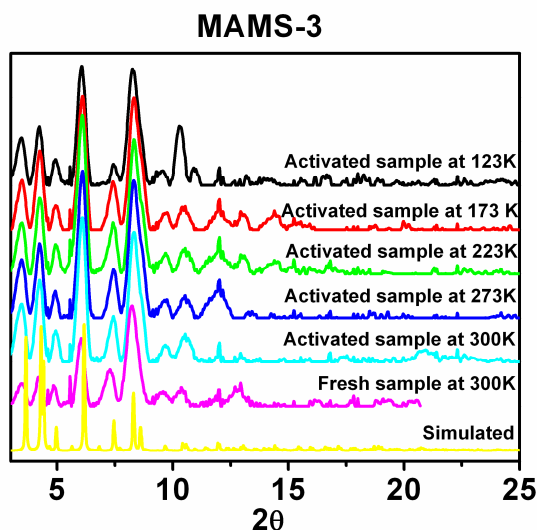


Figure 13.15 PXRD patterns of MAMS-3 at different temperatures.

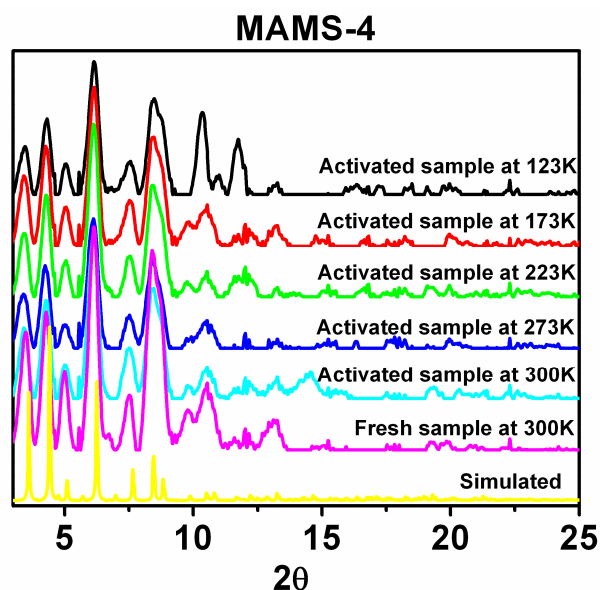


Figure 13.16 PXRD patterns of MAMS-4 at different temperatures.

The hydrophobic cages are not accessible when the hydrophilic channels are closed, which not only can be inferred from the crystal structure, but is also consistent with gas adsorption data. Inactivated sample had very low uptake of H_2 at 77K (Figure 13.7, 13.9, 13.11). A partially activated sample was inactive for gas uptake. The DMF (or DMA) guests and bound aqua ligands must be removed completely for MAMSs to be active for gas adsorption.

The hydrophilic channels alone are not responsible for the gas uptake. In fact, they account for only a very small part of the adsorption. As the gas adsorption data at 77 K suggests, only H_2 can enter the hydrophobic chambers, showing a significant uptake. At 77 K, other gas molecules stay in the hydrophilic channels and the uptake of these gases is very low, as shown by adsorption studies.

Gas molecules must go through the hydrophilic channel to access the hydrophobic cages. As previously mentioned, activation of the hydrophilic channels is a prerequisite for gas adsorption on MAMSs. Further evidence for the hydrophilic channels being the only passage to the gas storage chambers is provided by the observation that when the kinetic diameter of the gas molecule (for example, iso-butane, 5.0 Å and SF_6 , 5.5 Å) exceeded the size of the hydrophilic channels (~4.8-4.9 Å considering van der Waals

radii), no meaningful uptake was observed in an adsorption study (Figure 13.17, 13.18, 13.19) even at room temperature. The upper limit of the channel is also consistent with an adsorption study on propylene (4.5 Å), which is allowed to enter MAMS-2 at 231 K (Figure 13.8).

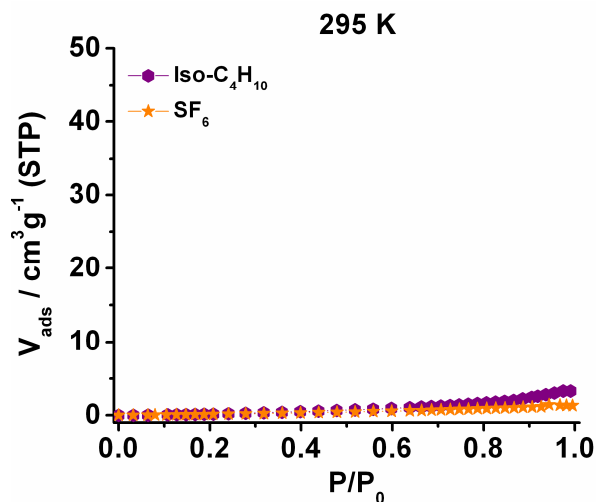


Figure 13.17 Iso-butane and SF_6 adsorption isotherms of MAMS-2 at 295 K.

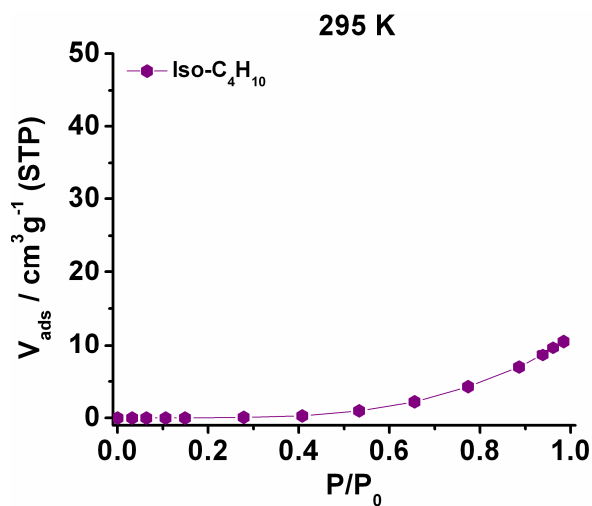


Figure 13.18 Iso-butane adsorption isotherm of MAMS-3 at 295 K.

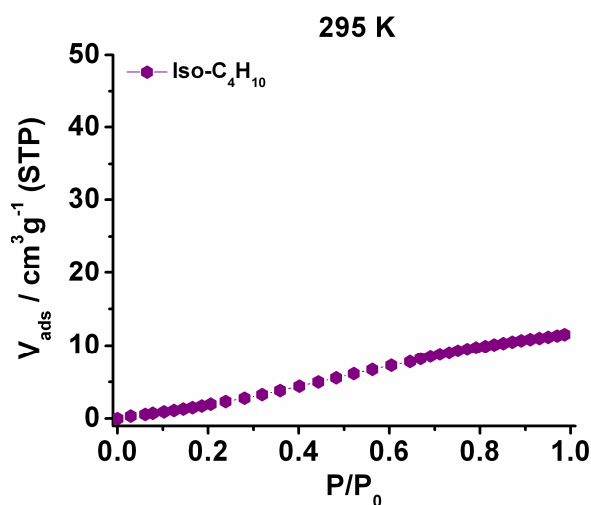


Figure 13.19 Iso-butane adsorption isotherm of MAMS-4 at 295 K.

Through the interface between the hydrophobic and hydrophilic channels, gas molecules enter the hydrophobic gas storage cages, which account for the majority of gas uptake. The interface is controlled by a *tert*-butyl group of a BBPDC ligand which inserts in each window of the cage acting as a gate. The opening of this gate is controlled by the amplitude (or frequency) of thermal vibration and rotation of the *tert*-butyl group. When the temperature is raised, the amplitude (or frequency) of thermal vibration and rotation of the *tert*-butyl group also increases leading to an enlargement of the apparent opening sizes (Figure 13.20). As shown in Figure 8, the gate opening D , and temperature T , have a linear relationship, $D = 0.0073 T + 2.83$, with a correlation coefficient of 0.996 (Figure 13.13) for the three new MAMSs. This is very close to the linear equation found in MAMS-1, $D = 0.0076 T + 2.76$. This means that, of the linear relationship between mesh size and temperature, $D = D_0 + \alpha T$ (D - mesh size at temperature T K, D_0 -mesh size at 0 K, and α -constant), D_0 and α are only related to the *tert*-butyl group. Changing the *tert*-butyl group to other functional groups such as a methyl or isopropyl group can lead to different values for D_0 and α .

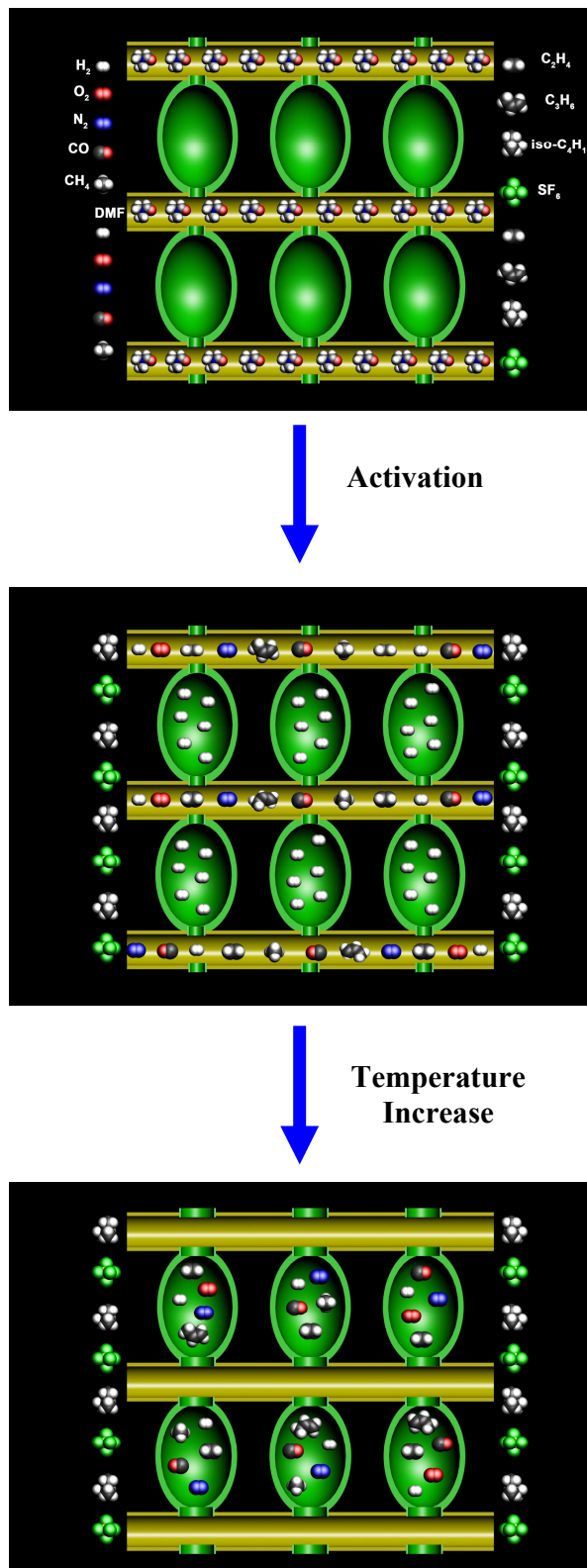


Figure 13.20 Schematic representation of the mechanism of the gate effects in MAMSs.

In summary, by designing a new amphiphilic ligand, BBPDC, and placing it in solvothermal reactions with $M(\text{NO}_3)_2$ ($M = \text{Zn}, \text{Co}, \text{Cu}$), three new graphitic MOF structures, MAMS-2, MAMS-3 and MAMS-4, generated by packing of tri-layers through van der Waals interactions, were obtained. In each tri-layer, the hydrophilic M-M paddlewheel cluster layer is sandwiched by two hydrophobic BBPDC layers; every three M-M paddlewheel clusters are connected to form triangular hydrophilic holes, and every six triangular hydrophilic holes are enclosed to form a hydrophobic cage which serves as the space for gas storage. Packing of the tri-layers generates one dimensional triangular hydrophilic channels, every six of which surround the hydrophobic cages, which are not accessible without activation. Gas molecules enter the hydrophobic gas storage cages through the hydrophilic channels, and gates in the hydrophobic/hydrophilic interface. The gates are formed by the BBPDC groups inserted in the windows of the hydrophobic cages via van der Waals interaction, which is readily weakened by thermal vibration. As temperature increases, the gates of the new MAMSs open linearly, giving rise to molecular sieves with adjustable meshes that can separate any two gases with kinetic diameters in the range of 2.9 to 4.6 Å, corresponding to the size limits of most commercially relevant gases. There exists a linear relationship between mesh size and temperature, $D = D_0 + \alpha T$ (D - mesh size at temperature T K, D_0 -mesh size at 0 K, and α -constant), D_0 and α are only related to the *tert*-butyl group. Changing the *tert*-butyl group to other functional groups such as methyl group or isopropyl group is expected to lead to different values for D_0 and α .

13.4 References

- (1) Davis, M. E. *Nature*, **2002**, *417*, 813.
- (2) Kuznicki, S. M.; Bell, V. A.; Nair, S.; Hillhouse, H. W.; Jacubinas, R. M.; Braunbarth, C. M.; Toby, B. H.; Tsapatsis, M. *Nature*, **2001**, *412*, 720.
- (3) (a) Yaghi, O. M.; Li, H.; Davis, C.; Richardson, D.; Groy, T. L. *Acc. Chem. Res.* **1998**, *31*, 474. (b) Kitagawa, S.; Kitaura, R.; Noro, S.-i., *Angew. Chem. Int. Ed.* **2004**, *43*, 2334; (c) Moulton, B.; Zaworotko, M. J., *Chem. Rev.* **2001**, *101*,

- 1629; (d) Ockwig, N. W.; Delgado-Friedrichs, O.; O'Keeffe, M.; Yaghi, O. M. *Acc. Chem. Res.* **2005**, *38*, 176.
- (4) (a) Chen, B.; Ockwig, N. W.; Millward, A. R.; Contreras, D. S.; Yaghi, O. M., *Angew. Chem. Int. Ed.* **2005**, *44*, 4745; (b) Kesanli, B.; Cui, Y.; Smith Milton, R.; Bittner Edward, W.; Bockrath Bradley, C.; Lin, W., *Angew. Chem. Int. Ed.* **2005**, *44*, 72; (c) Sun, D. ; Ma, S. ; Ke, Y. ; Collins, D. J.; Zhou, H. -C. *J. Am. Chem. Soc.* **2006**, *128*, 3896; (d) Ma, S.; Zhou, H. -C. *J. Am. Chem. Soc.* **2006**, *128*, 11734; (e) Dinca, M.; Dailly, A.; Liu, Y.; Brown, C. M.; Neumann, D. A.; Long, J. R. *J. Am. Chem. Soc.* **2006**, *128*, 16876; (f) Chen, B.; Ma, S.; Zapata, F.; Lobkovsky, E. B.; Yang, J. *Inorg. Chem.* **2006**, *45*, 5718; (g) Wang, X.-S.; Ma, S.; Sun, D.; Parkin, S.; Zhou, H.-C. *J. Am. Chem. Soc.* **2006**, *128*, 16474; (h) Ma, S; Sun, D.; Ambrogio, M. W.; Fillinger, J. A.; Parkin, S; Zhou, H.-C. *J. Am. Chem. Soc.* **2007**, *129*, 1858; (i) Ma, S.; Sun, D.; Simmons, J. M.; Collier, C. D.; Yuan, D.; Zhou, H.-C. *J. Am. Chem. Soc.* **2007**, *129*, in press.
- (5) (a) Seo, J. S.; Whang, D.; Lee, H.; Jun, S. I.; Oh, J.; Jeon, Y. J.; Kim, K., *Nature* **2000**, 404, 982; (b) Hu, A.; Ngo, H. L.; Lin, W. *J. Am. Chem. Soc.* **2003**, 125, 11490-11491; (c) Zou, R.; Sakurai, H.; Xu, Q. *Angew. Chem. Int. Ed.* **2006**, *45*, 2542.
- (6) (a) Halder, G. J.; Kepert, C. J.; Moubaraki, B.; Murray, K. S.; Cashion, J. D. *Science* **2002**, 298, 1762; (b) Janiak, C., *J. Chem. Soc., Dalton Trans.* **2003**, 2781; (c) Zheng, Y.-Z.; Tong, M.-L.; Zhang, W.-X.; Chen, X.-M. *Angew. Chem. Int. Ed.* **2006**, *45*, 6310; (d) Yu, C.; Ma, S.; Pechan, M. J.; Zhou, H.-C. *J. Appl. Phys.* **2007**, *101*, 09E108.
- (7) (a) Matsuda, R.; Kitaura, R.; Kitagawa, S.; Kubota, Y.; Belosludov, R. V. ; Kobayashi, T. C.; Sakamoto, H.; Chiba, T.; Takata, M.; Kawazoe, Y.; Mita, Y. *Nature* **2005**, *436*, 238; (b) Dinca, M.; Long, J. R. *J. Am. Chem. Soc.* **2005**, *127*, 9376; (c) Dybtsev, D. N.; Chun, H.; Yoon, S. H.; Kim, D.; Kim, K. *J. Am. Chem. Soc.* **2004**, *126*, 32; (d) Humphrey, S. M.; Chang, J.-S.; Jhung, S. H.; Yoon, J. W.; Wood, P. T. *Angew. Chem. Int. Ed.* **2006**, *46*, 272; (e) Chen, B.; Liang, C.; Yang, J.; Contreras, D. S.; Clancy, Y. L.; Lobkovsky, E. B.; Yaghi, O. M.; Dai, S. *Angew. Chem., Int. Ed.* **2006**, *45*, 1390; (f) Chen, B.; Ma, S.; Zapata, F.; Fronczek,

- F. R.; Lobkovsky, E. B.; Zhou, H.-C. *Inorg. Chem.*, **2007**, *46*, 1233; (g) Ma, S.; Wang, X.-S.; Manis, E. S.; Collier, C. D.; Zhou, H.-C. *Inorg. Chem.*, **2007**, *46*, 3432; (h) Ma, S.; Wang, X.-S.; Collier, C. D.; Manis, E. S.; Zhou, H.-C. *Inorg. Chem.*, **2007**, *46*, 8499; (i) Chen, B.; Ma, S.; Hurtado, E. J.; Lobkovsky, E. B.; Zhou, H.-C. *Inorg. Chem.*, **2007**, *46*, 8490.
- (8) (a) Uemura, K.; Matsuda, R.; Kitagawa, S. *J. Solid State Chem.* **2005**, *178*, 2420; (b) Bradshaw, D.; Claridge, J. B.; Cussen, E. J.; Prior, T. J.; Rosseinsky, M. *J. Acc. Chem. Res.* **2005**, *38*, 273; (c) Kitagawa, S.; Kazuhiro, U. *Chem. Soc. Rev.* **2005**, *34*, 109 and refs therein.
- (9) Ma, S.; Sun, D.; Wang, X.-S.; Zhou, H.-C. *Angew. Chem. Int. Ed.* **2007**, *46*, 2458.
- (10) *SAINT+*, version 6.22; Bruker Analytical X-Ray Systems, Inc.: Madison, WI, 2001.
- (11) Sheldrick, G. M. *SHELX-97*; Bruker Analytical X-Ray Systems, Inc.: Madison, WI, 1997.
- (12) Spek, A. L. *J. Appl. Crystallogr.* **2003**, *36*, 7.
- (13) R. E. Rondeau, *J. Chem. Eng. Data*, **1966**, *11*, 124.
- (14) A. M. Phipps, D. N. Hume, *J. Chem. Educ.*, **1968**, *45*, 664.
- (15) (a) Dybtsev, D. N.; Chun, H.; Kim, K. *Angew. Chem., Int. Ed.* **2004**, *43*, 5033; (b) Chun, H.; Dybtsev, D. N.; Kim, H.; Kim, K. *Chem.sEur. J.* **2005**, *11*, 3521; (c) Ma, B.-Q.; Mulfort, K. L.; Hupp, J. T. *Inorg. Chem.* **2005**, *44*, 4912.
- (16) (a) Choi, E.-Y.; Park, K.; Yang, C.-M.; Kim, H.; Son, J.-H.; Lee, S. W.; Lee, Y. H.; Min, D.; Kwon, Y.-U., *Chem. Eur. J.*, **2004**, *10*, 5535; (b) Chen, B.; Ma, S.; Hurtado, E. J.; Lobkovsky, E. B.; Liang, C.; Zhu, H.; Dai, S. *Inorg. Chem.*, **2007**, *46*, 8705.
- (17) Bondi, A. *J. Phys. Chem.* **1964**, *68*, 441.
- (18) Beck, D. W. *Zeolite Molecular Sieves*; Wiley & Sons: New York, 1974.

Chapter 14

Conclusions

14.1 Porous MOFs as Promising Hydrogen Storage Candidates

The exorbitant price of crude oil recently surpassed \$110 per barrel, almost tripled the price of ~\$40 per barrel in August 2003 when the graduate studies of the author commenced. Moreover, it remains unclear that how long the volatility in the fuel prices will continue. As fossil oil resource contributes to ~40% of global energy consumption and ~90% of the energy required by the transportation sector, it is essential to search for alternative energy carriers to replace the use of petroleum-based gasoline and diesel fuel in road vehicles. Hydrogen has long been touted as the “fuel of the future” and stands at the forefront among various alternatives due to its clean combustion and high energy capacity.¹

In 2003, the US government launched the Hydrogen Fuel Initiative for developing clean, hydrogen-powered automobiles to replace those currently powered by fossil fuels. The success of commercialization of hydrogen fuel-cell powered vehicles, however, largely relies on the development of a safe, efficient, and economic on-board hydrogen storage system. The U.S. Department of Energy (DOE) has set a number of targets for the hydrogen storage system based on standards adopted by today’s vehicles to ensure the acceptance of vehicles powered by higher efficiency hydrogen fuel-cell power sources.²

Porous MOFs, a new type of functional materials, hold great promise as on-board hydrogen storage media. Several strategies to improve dihydrogen adsorption were offered in this study. Employing a biomimetic approach, some cobalt centers in entatic states have been created in PCN-9. Those entatic cobalt centers lead to PCN-9 with a high hydrogen affinity of 10.1 kJ/mol, and their accessibility have been confirmed using carbon monoxide as a probe.

Functionalizing the organic ligand with more aromatic rings is theoretically predicted to increase hydrogen bind energy in porous MOFs.³ This has been well illustrated in hydrogen adsorption studies of PCN-14, which was constructed from an

anthracene derivative, adip. PCN-14 exhibits a high hydrogen uptake of 2.7 wt% at 77 K, 760 Torr, which can be attributed to the fused aromatic rings of the adip ligand

Catenation has long been considered an effective way to increase hydrogen uptake in porous MOFs.⁴ Its impact on hydrogen uptake has been quantitatively evaluated in the studies on catenated PCN-6 and non-catenated PCN-6', which can be controllably synthesized using a templating strategy. Catenation can lead to a 41% improvement of Langmuir surface area and 29% in gravimetric hydrogen uptake in the studied case. In addition, catenation also improves the excess gravimetric hydrogen uptakes with 7.2 wt% at 77 K, 50 bar and 0.93 wt% at 298 K, 50 bar in catenated PCN-6 vs. 4.2 wt% at 77 K, 50 bar and 0.40 wt% at 298 K, 50 bar in non-catenated PCN-6'. Moreover, PCN-6 exhibits a total gravimetric hydrogen uptake capacity of 9.5 wt% (corresponding to a total volumetric value of 53.0 g/L) at 77 K, 50 bar and 1.5 wt% at 298 K, 50 bar as well as a deliverable hydrogen amount of ~7.5 wt% (or 41.9 g/L) at 77 K, promising its great potential as a cryonic hydrogen storage medium.

The studies in this dissertation strongly suggest porous MOFs as promising hydrogen storage candidates to achieve the DOE target values at least at cryogenic temperatures (usually 77 K). However, their hydrogen storage performances are still poor at near ambient temperatures due to the low heats of adsorption for hydrogen. Although PCN-9 exhibits a relatively high hydrogen adsorption enthalpy of 10.1 kJ/mol, its low surface area limits its room temperature hydrogen uptake capacity to less than 1 wt% under high pressure. To improve hydrogen uptake in porous MOFs at room temperature, future work should focus on rational design of organic ligands and judicious selection of metal ion or metal clusters to construct porous MOFs to achieve both large surface area and high hydrogen adsorption enthalpy close to the 15–25 kJ mol⁻¹ working zone range.⁵

14.2 Methane Storage Applications of Porous MOFs

Compared to hydrogen, methane appears to be a more promising alternative for mobile applications in terms of near-term practical utilization and innovations necessary for commercialization.⁶

Stimulated by a theoretical simulation, the porous MOF, PCN-14, was constructed from a pre-designed anthracene derivative. It exhibits the highest methane

uptake capacity among currently reported materials with the value of 230 v/v, which is 28% higher than the US DOE target (180 v/v) for methane storage. This illustrates porous MOFs great potential for on-board methane storage application.

Since studies on methane storage in porous MOFs are far less numerous than those on hydrogen, future work should increase the pool of reported methane adsorption data to illustrate some of the fundamental structure-property relationships that are necessary for improved adsorption properties. In addition, the search for economical porous MOFs with even better methane storage performance should continue if these materials are to end up under the floorboards of a car.

14.3 Selective Gas Adsorption Applications of Porous MOFs

Gas separations represent important issues in industry, and currently they rely primarily on traditional inorganic zeolite materials.⁷ As a new type of zeolite analogues, porous MOFs have demonstrated great potential in separation applications due to their amendability of design and tunable pore sizes.

Increasing the bulkiness of the struts of the organic linker has been proved an effective way to restrict pore sizes for selective gas adsorption, as indicated in PCN-13 which can separate dihydrogen and dioxygen from dinitrogen and carbon monoxide.

A major concern in porous MOFs lies in their limited thermal stability, which prevents them from competing with inorganic zeolites in practical applications. The thermal stability can be greatly improved by introducing coordinatively linked interpenetration, as illustrated in PCN-17 which is stable up to 480 °C while maintaining permanent porosity. The coordinatively linked interpenetration also confines the pore size of PCN-17 for selective adsorption of dihydrogen and dioxygen over dinitrogen and carbon monoxide.

Compared to traditional inorganic zeolites whose pore sizes are normally fixed, the dynamic features of MOFs can produce materials with adjustable pore sizes. Based on an amphiphilic ligand BBDC, the first mesh-adjustable molecular sieve MAMS-1, whose pore sizes can be continuously tuned from 2.9 to 5.0 Å, has been constructed for various gas separation applications. The extension of BBDC ligand to the BBPDC ligand, when reacted with different metal ions under solvothermal conditions generates a series of new

MAMSs with similar molecular sieving effects to those observed in MAMS-1. For all of the MAMSs, there exists a linear relationship between mesh size and temperature, $D = D_0 + \alpha T$ (D - mesh size at temperature T K, D_0 -mesh size at 0 K, and α -constant), D_0 and α are only related to the *tert*-butyl group. Adjusting D_0 and α is expected to result in some new MAMSs which might be omnipotent for gas separation at near ambient temperatures. As a future work focus, the *tert*-butyl group can be replaced by other functional groups such as methyl group, isopropyl group etc.

14.4 Outlook

As a relatively new class of materials, porous MOFs will continue to attract interest and inquiry by both academia and industry. They exhibit considerable potential for the adsorptive storage of both hydrogen and methane in energy applications as well as gas separation and purification in industrial applications. The emerging ability to tune pore size and pore wall functionality allow researchers to focus on those factors which hold to the most promise, increasing both the volume available for storage and the affinity of the network for the stored gas. In particular, as alternative fuels such as hydrogen and methane continue to be developed in automotive and other applications, the needs for effective storage technologies will continue to increase, and porous MOFs are well-positioned to remain at the forefront of this research.⁸

14.5 References

- (1) Rowsell, J., Dissertation "Hydrogen Storage in Metal-Organic Frameworks: An Investigation of Structure-Property Relationships" **2005**.
- (2) DOE Office of Energy Efficiency and Renewable Energy Hydrogen, Fuel Cells & Infrastructure Technologies Program Multi-Year Research, Development and Demonstration Plan, available at: <http://www.eere.energy.gov/hydrogenandfuelcells/mypp>. . In.
- (3) Sagara, T.; Klassen, J.; Ortony, J.; Ganz, E., *J. Chem. Phys.* **2005**, *123*, 014701-014701-4.
- (4) Rowsell, J. L. C.; Yaghi, O. M., *Angew. Chem., Int. Ed.* **2005**, *44*, 4670-4679.

- (5) Bhatia, S. K.; Myers, A. L., *Langmuir* **2006**, *22*, 1688-1700.
- (6) Forster, P. M., Dissertation "Exploration of New Transition Metal Based Porous Materials" **2005**.
- (7) Davis, M. E., *Nature* **2002**, *417*, 813-821.
- (8) Collins, D. J.; Ma, S.; Zhou, H.-C., *Metal-Organic Frameworks: Design and Application* L. MacGillivray Ed.; . Wiley-VCH: Submitted, **2009**.

Vita

EDUCATION

Ph.D., Chemistry (May 2008), Miami University, Oxford, OH

Dissertation Title: “Gas Adsorption Applications of Porous Metal-Organic Frameworks.”

Advisor: Professor Hong-Cai Zhou

B.S., Applied Chemistry (July 2003), Jilin University, Changchun, China

Thesis Title: “Synthesis of Solid Superacid Nanoparticles with Solvent-free Method.” (Honored)

Advisor: Professor Feng-Shou Xiao

RESEARCH EXPERIENCE

Department of Chemistry & Biochemistry, Miami University, Oxford, OH

Graduate Research Assistant

August 2003–Present

- Design, synthesis and characterization of porous metal-organic frameworks (MOFs) for hydrogen storage, methane storage and gas separation applications.

State Key Laboratory of Inorganic Synthesis & Preparative Chemistry, Jilin University, Changchun, China

Undergraduate Research Assistant,

September 2001–July 2003

- Synthesis and characterization of solid superacid nanoparticles, microporous zeolite materials and silica and non-silica mesoporous materials.

FUNDED RESEARCH PROPOSAL

“Investigation of Hydrogen Adsorption in Porous Metal-Organic Frameworks with Heterometal Centers by Inelastic Neutron Scattering.” Funded by *Sigma Xi Grant-in-Aid of Research*, April 2007–April 2008.

PATENT

Zhou, H.-C.; Ma, S. “Mesh-Adjustable Molecular Sieve”, 2008, pending

HONORS AND AWARDS

- *Director’s Postdoctoral Fellowship* of Argonne National Laboratory 07/2008-07/2010
- *2007 Chinese Government Award for Outstanding Self-financed Students Abroad*, 04/2008
- *Young Investigator Award* from the ACS Division of Inorganic Chemistry, 2008
- *Dissertation Scholarship*, Miami University, 08/2007–05/2008
- *Graduate Student Achievement Award*, Miami University, 2006–2007
- *Marjorie Post Farrington Scholarship*, Miami University, 2007–2008
- *Sigma Xi Grant-in-Aid of Research Award*, Sigma Xi, the Scientific Research Society, 04/2007–04/2008
- *Student Initiative Fund Award*, Miami University, 06/2007–12/2007
- *Student Travel Award* from the ACS Division of Inorganic Chemistry, 03/2007
- *Graduate Student Summer Scholarship*, Miami University, 2004–2007
- *The Miami Co-Op Book Store Award*, Miami University, 04/2004
- *The William Hale Charch Scholarship*, Miami University, 2003–2004
- *Outstanding Undergraduate Scholarship*, Jilin University, 2000–2003

PUBLICATIONS

1. Ma, S.; Collier, C. D.; Zhou, H.-C. “Design and Construction of Metal-Organic Frameworks for Hydrogen Storage and Selective Gas Adsorption” Submitted as

- an invited chapter to the book *Design and Construction of Coordination Polymers*; M. Hong, Ed.; Wiley: New York, **2008**.
2. Wang, X.-S.; **Ma, S.**; Forster, P. M.; Yuan, D.; Yoon, J. W.; Hwang, Y. K.; Chang, J.-.; Eckert, J.; López, J. J.; Murphy, B. J.; Parise, J. B.; Zhou, H.-C. “Strengthening the Framework-H₂ Interaction by “Close-Packing” Alignment of Coordinatively Unsaturated Metal Centers in Metal-Organic Frameworks” (Submitted)
 3. Collins, D. J.; **Ma, S.**; Zhou, H.-C. “Hydrogen and Methane Storage in MOFs” submitted as an invited chapter to the book *Metal-Organic Frameworks: Design and Application* L. MacGillivray Ed.; Wiley-VCH, **2009**.
 4. Wang, X.-S.; **Ma, S.**; Rauch, K.; Simmons, J. M.; Yuan, D.; Wang, X.; Yildirim, T.; Cole, W. C.; López, J. J.; de Meijere, A.; Zhou, H.-C. “Metal-Organic Frameworks Based on Double-Bond-Coupled Di-Isophthalate Linkers Containing Nanoscopic Cages with High Hydrogen and Methane Uptakes.” *Chem. Mater.* **2008**. (in press)
 5. Zhou, H.-C.; **Ma, S.** “Mesh-Adjustable Molecular Sieve”, Patent, **2008**, pending
 6. **Ma, S.**; Wang, X.-S.; Yuan, D.; Zhou, H. C. “Coordinatively Linked, Doubly Interpenetrated, Yb Metal-Organic Framework Demonstrating High Thermal Stability and Uncommon Gas-Adsorption Selectivity” *Angew Chem. Int. Ed.* **2008**. (in press)
 7. Gung, B. W.; Zou, Y.; Xu, Z.; Amicangelo, J. C.; Irwin, D. G.; **Ma, S.**; Zhou, H.-C. “Quantitative Study of Interactions between Oxygen Lone Pair and Aromatic Rings: Substituent Effect and the Importance of Closeness of Contact.” *J. Org. Chem.* **2008**, *73*, 689-693.
 8. **Ma, S.**; Sun, D.; Simmons, J. M.; Collier, C. D.; Yuan, D.; Zhou, H.-C. “Metal-Organic Framework from an Anthracene Derivative Containing Nanoscopic Cages Exhibiting High Methane Uptake.” *J. Am. Chem. Soc.* **2008**, *130*, 1012-1016.
 9. Chen, B.; **Ma, S.**; Hurtado, E. J.; Lobkovsky, E. B.; Zhou, H.-C. “A Triply Interpenetrated Microporous Metal-Organic Framework for Selective Sorption of Gas Molecules.” *Inorg. Chem.* **2007**, *46*, 8490-8492.

10. Chen, B.; **Ma, S.**; Hurtado, E. J.; Lobkovsky, E. B.; Liang, C.; Zhu, H.; Dai, S. "Selective Gas Sorption within a Dynamic Metal-Organic Framework." *Inorg. Chem.* **2007**, *46*, 8705-8909.
11. **Ma, S.**; Wang, X.-S.; Collier, C. D.; Manis, E. S.; Zhou, H.-C. "Ultramicroporous Metal-Organic Framework Based on 9,10-Anthracenedicarboxylate for Selective Gas Adsorption." *Inorg. Chem.* **2007**, *46*, 8499-8501.
12. Yu, C.; **Ma, S.**; Pechan, M. J.; Zhou, H.-C. "Magnetic properties of a non-interpenetrating chiral porous Cobalt Metal-Organic Framework (MOF)." *J. Appl. Phys.* **2007**, *101*, 09E108.
13. **Ma, S.**; Wang, X.-S.; Manis, E. S.; Collier, C. D.; Zhou, H.-C. "A Metal-Organic Framework Based on a Trinickel Secondary Building Unit Exhibiting Gas-Adsorption Hysteresis." *Inorg. Chem.* **2007**, *46*, 3432-3434.
14. **Ma, S.**; Sun, D.; Wang, X.-S.; Zhou, H.-C. "A Mesh-Adjustable Molecular Sieve for General Use in Gas Separation." *Angew Chem. Int. Ed.* **2007**, *46*, 2458-2462.
15. **Ma, S.**; Sun, D.; Ambrogio, M.; Fillinger, J. A.; Parkin, S.; Zhou, H.-C. "Framework-Catenation Isomerism in MOFs and Its Impact on Hydrogen Uptake." *J. Am. Chem. Soc.* **2007**, *129*, 1858-1859.
16. Chen, B.; **Ma, S.**; Zapata, F.; Fronczek, F. R.; Lobkovsky, E. B.; Zhou, H.-C. "Rationally Designed Micropores within a Metal-Organic Framework for Selective Sorption of Gas Molecules." *Inorg. Chem.* **2007**, *46*, 1233-1236.
17. **Ma, S.**; Fillinger, J. A.; Ambrogio, M. W.; Zuo, J.-L.; Zhou, H.-C. "Synthesis and Characterizations of a Magnesium Metal-Organic Framework with the (10, 3)-a Net Topology." *Inorg. Chem. Comm.* **2007**, *10*, 220-222.
18. Wang, X.-S.; **Ma, S.**; Sun, D.; Parkin, S.; Zhou, H.-C. "A Mesoporous Metal-Organic Framework with Permanent Porosity." *J. Am. Chem. Soc.* **2006**, *128*, 16474-16475.
19. **Ma, S.**; Zhou, H.-C. "A metal-organic framework with entatic centers exhibiting high gas adsorption affinity." *J. Am. Chem. Soc.* **2006**, *128*, 11734-11735.
20. Sun, D.; **Ma, S.**; Ke, Y.; Collins, D. J.; Zhou, H.-C. "An Interweaving MOF with High Hydrogen Uptake." *J. Am. Chem. Soc.* **2006**, *128*, 3896-3897.

21. Chen, B.; **Ma, S.**; Zapata, F.; Lobkovsky, E. B.; Yang, J.; “Hydrogen Adsorption in an Interpenetrated Dynamic Metal-Organic Framework.” *Inorg. Chem.* **2006**, *45*, 5718-5720.
22. Sun, D.; **Ma, S.**; Ke, Y.; Petersen, T. M.; Zhou, H.-C. “Synthesis, characterization, and photoluminescence of isostructural Mn, Co, and Zn MOFs having a diamondoid structure with large tetrahedral cages and high thermal stability.” *Chem. Comm.* **2005**, *21*, 2663-2664.
23. Sun, Y.; **Ma, S.**; Du, Y.; Yuan, L.; Wang, S.; Yang, J.; Deng, F.; Xiao, F.-S. “Solvent-Free Preparation of Nanosized Sulfated Zirconia with Bronsted Acidic Sites from a Simple Calcination.” *J. Phys. Chem. B* **2005**, *109*, 2567-2572.
24. Sun, Y.; Yuan, L.; **Ma, S.**; Han, Y.; Zhao, L.; Wang, W.; Chen, C.-L.; Xiao, F.-S. “Improved catalytic activity and stability of mesostructured sulfated zirconia by Al promoter.” *Appl. Catal., A*, **2004**, *268*, 17-24.
25. Sun, Y.; Han, Y.; Yuan, L.; **Ma, S.**; Jiang, D.; Xiao, F.-S. “Microporosity in Ordered Mesoporous Aluminosilicates Characterized by Catalytic Probing Reactions.” *J. Phys. Chem. B* **2003**, *107*, 1853-1857.
26. **Ma, S.**; Eckert, J.; Forster, P. M.; Yoon, J. W.; Hwang, Y.K.; Chang, J.-S.; Collier, C. D.; Zhou, H.-C. “Investigation of Hydrogen Binding in MOF Catenation Isomers by Inelastic Neutron Scattering and High Pressure Hydrogen Adsorption Properties of the isomers.” (Submitted to *J. Am. Chem. Soc.*)
27. **Ma, S.**; Sun, D.; Yuan, D.; Wang, X.-S.; Collier, C. D.; Manis, E. S.; Zhou, H. C. “The Discovery and Gas Adsorption Studies of Mesh-Adjustable Molecular Sieves.” (Submitted to *J. Am. Chem. Soc.*)
28. **Ma, S.**; Simmons, J. M.; Sun, D.; Yuan, D.; Collier, C. D.; Zhou, H.-C. “Hydrogen Adsorption in Porous Metal-Organic Frameworks Based on an Anthracene Derivative.” (Submitted to *Chemistry, Eur. J.*)
29. **Ma, S.**; Yuan, D.; Collier, C. D.; Manis, E. S.; Zhou, H.-C. “Gas Adsorption Studies of Porous Metal-Organic Frameworks with Entatic Metal Centers,” (To be submitted)
30. **Ma, S.**; Wang, X.-S.; Yuan, D.; Manis, E. S.; Collier, C. D.; Zhou, H. C. “Microporous Lanthanide Metal-Organic Frameworks Containing Coordinatively

Linked Interpenetration: Syntheses, Thermal Stability Analysis, Gas Sorption Studies and Photoluminescence Investigation.” (To be submitted)

PRESENTATIONS

1. “Microporous metal-organic frameworks with high methane uptake.” The 235th ACS National Meeting, New Orleans, LA (April, 2008, Oral)
2. “Rational Design of Metal-Organic Frameworks for H₂ Storage and Other Applications.” Chemical Sciences and Engineering Division, Argonne National Laboratory, Nov.12, 2007 (Invited talk)
3. “Syntheses and Characterizations of (3, 8)-connected Lanthanide Metal-Organic Frameworks.” 39th Central Regional Meeting, Covington, KY (May, 2007, Oral)
4. “The Application of Metal-Organic Frameworks in Hydrogen Storage.” University Clean Energy Alliance of Ohio (UCEAO) Inaugural Meeting, Columbus, OH (April, 2007, Poster)
5. “Syntheses and characterizations of mesh-adjustable molecular sieves (MAMSs) for gas separation.” The 233rd ACS National Meeting, Chicago, IL (March, 2007, Oral)
6. “Catenation Isomerism in Metal-Organic Frameworks (MOFs) and Its Impact on Hydrogen Uptake.” The 7th Annual Ohio Inorganic Meeting, Ohio University, Athens, OH (November, 2006, Oral)
7. “Syntheses and characterization of porous coordination networks with accessible unsaturated metal centers.” The 230th ACS National Meeting, Washington, DC (August, 2005, Poster)
8. “Rational Design of Porous Coordination Networks for Hydrogen Storage.” The 5th Annual Ohio Inorganic Meeting, University of Akron, Akron, OH (November, 2004, Oral)

Appendix

Tables of Crystal Structures

Table A1 Crystal data and structure refinement for PCN-6.

Identification code	PCN-6
Empirical formula	C ₄₈ H ₃₀ Cu ₃ N ₆ O ₁₅
Formula weight	1121.40
Temperature	293(2) K
Wavelength	0.71073 Å
Crystal system	Rhombohedral
Space group	<i>R</i> -3 <i>m</i>
Unit cell dimensions	<i>a</i> = 32.9680(13) Å = 90° <i>b</i> = 32.9680(13) Å = 90° <i>c</i> = 80.783(5) Å = 120°
Volume	76039(6) Å ³
<i>Z</i>	24
Density (calculated)	0.588 Mg/m
Absorption coefficient	0.528 mm ⁻¹
F(000)	13608
Crystal size	0.42 x 0.40 x 0.38 mm ³
Theta range for data collection	1.45 to 18.88°
Index ranges	-30 ≤ <i>h</i> ≤ 22, -29 ≤ <i>k</i> ≤ 30, -73 ≤ <i>l</i> ≤ 73
Reflections collected	73248
Independent reflections	7157 [R(int) = 0.0956]
Completeness to theta = 18.88	99.5 %
Absorption correction	None
Refinement method	Full-matrix least-squares on F ²
Data / restraints / parameters	7157 / 0 / 469
Goodness-of-fit on F ²	0.877
Final R indices [I > 2σ(I)]	R1 = 0.0530, wR2 = 0.1415
R indices (all data)	R1 = 0.0870, wR2 = 0.1508
Largest diff. peak and hole	0.635 and -0.268 eÅ ⁻³

Table A2 Crystal data and structure refinement for PCN-6'.

Identification code	PCN-6'	
Empirical formula	C ₈ H ₄ Cu _{0.50} NO _{2.50}	
Formula weight	185.89	
Temperature	250(2) K	
Wavelength	1.54178 Å	
Crystal system	cubic	
Space group	<i>Fm-3m</i>	
Unit cell dimensions	a = 46.636(5) Å	= 90°
	b = 46.636(5) Å	= 90°
	c = 46.636(5) Å	= 90°
Volume	101432(20) Å ³	
Z	96	
Density (calculated)	0.292 Mg/m ³	
Absorption coefficient	0.415 mm ⁻¹	
F(000)	8976	
Crystal size	0.12 x 0.12 x 0.12 mm ³	
Theta range for data collection	1.64 to 55.99°	
Index ranges	-50 ≤ h ≤ 50, -50 ≤ k ≤ 50, -50 ≤ l ≤ 50	
Reflections collected	284004	
Independent reflections	3248 [R(int) = 0.1904]	
Completeness to theta = 55.99	100.0 %	
Max. and min. transmission	0.9518 and 0.9518	
Refinement method	Full-matrix least-squares on F ²	
Data / restraints / parameters	3248 / 0 / 68	
Goodness-of-fit on F ²	1.153	
Final R indices [I > 2σ(I)]	R1 = 0.0650, wR2 = 0.1605	
R indices (all data)	R1 = 0.0886, wR2 = 0.1721	
Largest diff. peak and hole	0.216 and -0.940 eÅ ⁻³	

Table A3 Crystal data and structure refinement for Cu-HTB.

Identification code	Cu-HTB	
Empirical formula	$C_{36}H_{16}Cu_2N_{9.33}O_{10}$	
Formula weight	866.33	
Temperature	258(2) K	
Wavelength	1.54178 Å	
Crystal system	RHOMBOHEDRAL	
Space group	$R\bar{3}m$	
Unit cell dimensions	$a = 37.291(2)$ Å	= 90°
	$b = 37.291(2)$ Å	= 90°
	$c = 92.159(3)$ Å	= 120°
Volume	110988(9) Å ³	
Z	36	
Density (calculated)	0.467 Mg/m ³	
Absorption coefficient	0.611 mm ⁻¹	
F(000)	15672	
Crystal size	0.12 x 0.10 x 0.08 mm ³	
Theta range for data collection	1.67 to 25.99°	
Index ranges	-21 ≤ h ≤ 21, -11 ≤ k ≤ 21, -50 ≤ l ≤ 52	
Reflections collected	12274	
Independent reflections	1807 [R(int) = 0.0538]	
Completeness to theta = 25.99	68.4 %	
Max. and min. transmission	0.9527 and 0.9303	
Refinement method	Full-matrix least-squares on F ²	
Data / restraints / parameters	1807 / 611 / 547	
Goodness-of-fit on F ²	1.637	
Final R indices [I > 2σ(I)]	R1 = 0.1080, wR2 = 0.3272	
R indices (all data)	R1 = 0.1238, wR2 = 0.3451	
Largest diff. peak and hole	0.432 and -0.274 eÅ ⁻³	

Table A4 Crystal data and structure refinement for Cu-HTB'.

Identification code	Cu-HTB'	
Empirical formula	C ₉ H ₄ Cu _{0.50} N _{2.33} O _{2.50}	
Formula weight	216.58	
Temperature	295(2) K	
Wavelength	1.54178 Å	
Crystal system	CUBIC	
Space group	<i>Fm-3m</i>	
Unit cell dimensions	a = 52.993(6) Å	= 90°
	b = 52.993(6) Å	= 90°
	c = 52.993(6) Å	= 90°
Volume	148815(30) Å ³	
Z	96	
Density (calculated)	0.232 Mg/m ³	
Absorption coefficient	0.304 mm ⁻¹	
F(000)	10448	
Crystal size	0.15 x 0.15 x 0.15 mm ³	
Theta range for data collection	2.77 to 55.95°	
Index ranges	-52 ≤ h ≤ 52, -40 ≤ k ≤ 56, -55 ≤ l ≤ 55	
Reflections collected	81536	
Independent reflections	4665 [R(int) = 0.0837]	
Completeness to theta = 55.95	99.9 %	
Max. and min. transmission	0.9558 and 0.9558	
Refinement method	Full-matrix least-squares on F ²	
Data / restraints / parameters	4665 / 0 / 80	
Goodness-of-fit on F ²	0.951	
Final R indices [I > 2σ(I)]	R1 = 0.0417, wR2 = 0.0971	
R indices (all data)	R1 = 0.0659, wR2 = 0.1042	
Largest diff. peak and hole	0.042 and -0.189 eÅ ⁻³	

Table A5 Crystal data and structure refinement for PCN-9.

Identification code	PCN-9	
Empirical formula	$C_{64}H_{32}Co_4N_8O_{17}$	
Formula weight	1420.70	
Temperature	293(2) K	
Wavelength	0.71073 Å	
Crystal system	Cubic	
Space group	<i>Im-3m</i>	
Unit cell dimensions	$a = 25.4387(5)$ Å	= 90°
	$b = 25.4387(5)$ Å	= 90°
	$c = 25.4387(5)$ Å	= 90°
Volume	16462.1(6) Å ³	
Z	6	
Density (calculated)	0.860 Mg/m ³	
Absorption coefficient	0.638 mm ⁻¹	
F(000)	4296	
Crystal size	0.36 x 0.34 x 0.32 mm ³	
Theta range for data collection	1.13 to 25.04°	
Index ranges	-30 ≤ h ≤ 30, -30 ≤ k ≤ 25, -30 ≤ l ≤ 29	
Reflections collected	47359	
Independent reflections	1442 [R(int) = 0.0775]	
Completeness to theta = 25.04	99.5 %	
Absorption correction	None	
Refinement method	Full-matrix least-squares on F ²	
Data / restraints / parameters	1442 / 4 / 64	
Goodness-of-fit on F ²	1.218	
Final R indices [I > 2σ(I)]	R1 = 0.1031, wR2 = 0.3066	
R indices (all data)	R1 = 0.1233, wR2 = 0.3196	
Largest diff. peak and hole	0.911 and -0.599 eÅ ⁻³	

Table A6 Crystal data and structure refinement for PCN-13.

Identification code	PCN-13
Empirical formula	C ₄₈ H ₂₆ O ₁₆ Zn ₄
Formula weight	1120.17
Temperature	293(2) K
Wavelength	0.71073 Å
Crystal system	Cubic
Space group	<i>I</i> -43 <i>d</i>
Unit cell dimensions	a = 28.790(10) Å = 90° b = 28.790(10) Å = 90° c = 28.790(10) Å = 90°
Volume	23862(14) Å ³
Z	16
Density (calculated)	1.247 Mg/m ³
Absorption coefficient	1.645 mm ⁻¹
F(000)	8992
Crystal size	0.24 x 0.19 x 0.17 mm ³
Theta range for data collection	1.73 to 25.00°
Index ranges	-34 ≤ h ≤ 32, -11 ≤ k ≤ 34, -30 ≤ l ≤ 32
Reflections collected	30710
Independent reflections	3516 [R(int) = 0.1320]
Completeness to theta = 25.00	100.0 %
Absorption correction	None
Refinement method	Full-matrix least-squares on F ²
Data / restraints / parameters	3516 / 0 / 205
Goodness-of-fit on F ²	0.978
Final R indices [I > 2σ(I)]	R1 = 0.0578, wR2 = 0.1482
R indices (all data)	R1 = 0.0765, wR2 = 0.1546
Absolute structure parameter	0.04(3)
Largest diff. peak and hole	0.950 and -0.504 eÅ ⁻³

Table A7 Crystal data and structure refinement for PCN-14.

Identification code	PCN-14	
Empirical formula	C ₂₇₀ H ₁₆₂ Cu ₁₈ O ₉₀	
Formula weight	5989.9	
Temperature	90(2) K	
Wavelength	1.54178 Å	
Crystal system	Rhombohedral	
Space group	<i>R</i> -3 <i>c</i>	
Unit cell dimensions	a = 18.4530(4) Å	= 90°
	b = 18.4530(4) Å	= 90°
	c = 76.976(4) Å	= 120°
Volume	22699.7(14) Å ³	
Z	2	
Density (calculated)	0.871 Mg/m ³	
Absorption coefficient	1.323 mm ⁻¹	
F(000)	5976	
Crystal size	0.06 x 0.05 x 0.05 mm ³	
Theta range for data collection	2.99 to 68.10°	
Index ranges	-22 ≤ h ≤ 22, -22 ≤ k ≤ 22, -92 ≤ l ≤ 88	
Reflections collected	90758	
Independent reflections	4581 [R(int) = 0.0737]	
Completeness to theta = 68.10	99.1 %	
Absorption correction	SADABS	
Max. and min. transmission	0.9368 and 0.9248	
Refinement method	Full-matrix least-squares on F ²	
Data / restraints / parameters	4621 / 0 / 191	
Goodness-of-fit on F ²	1.071	
Final R indices [I > 2σ(I)]	R1 = 0.0518, wR2 = 0.1591	
R indices (all data)	R1 = 0.0597, wR2 = 0.1658	
Extinction coefficient	0.000003(2)	
Largest diff. peak and hole	0.839 and -0.384 eÅ ⁻³	

Table A8 Crystal data and structure refinement for PCN-15.

Identification code	PCN-15	
Empirical formula	C ₉₀ H ₅₄ ClFe ₆ O ₃₀	
Formula weight	1985.88	
Temperature	173(2) K	
Wavelength	0.71073 Å	
Crystal system	Rhombohedral	
Space group	<i>R</i> -3 <i>m</i>	
Unit cell dimensions	a = 27.1117(9) Å	= 90°
	b = 27.1117(9) Å	= 90°
	c = 16.5413(13) Å	= 120°
Volume	10529.6(10) Å ³	
Z	3	
Density (calculated)	0.940 Mg/m ³	
Absorption coefficient	0.674 mm ⁻¹	
F(000)	3021	
Crystal size	0.20 x 0.15 x 0.12 mm ³	
Theta range for data collection	1.50 to 23.27°	
Index ranges	-19 ≤ h ≤ 30, -29 ≤ k ≤ 30, -18 ≤ l ≤ 18	
Reflections collected	13516	
Independent reflections	1818 [R(int) = 0.0436]	
Completeness to theta = 23.27	99.8 %	
Refinement method	Full-matrix least-squares on F ²	
Data / restraints / parameters	1818 / 0 / 102	
Goodness-of-fit on F ²	1.636	
Final R indices [I > 2σ(I)]	R1 = 0.1088, wR2 = 0.3462	
R indices (all data)	R1 = 0.1143, wR2 = 0.3553	
Largest diff. peak and hole	2.140 and -0.562 eÅ ⁻³	

Table A9 Crystal data and structure refinement for PCN-17.

Identification code	PCN-17		
Empirical formula	$C_{72}H_{62}N_8O_{31}S_6Yb_4$		
Formula weight	2419.82		
Temperature	213(2) K		
Wavelength	0.71073 Å		
Crystal system	Cubic		
Space group	<i>Im-3m</i>		
Unit cell dimensions	$a = 26.2253(19)$ Å		= 90°
	$b = 26.2253(19)$ Å		= 90°
	$c = 26.2253(19)$ Å		= 90°
Volume	18037(2) Å ³		
Z	6		
Density (calculated)	1.337 Mg/m ³		
Absorption coefficient	3.247 mm ⁻¹		
F(000)	7044		
Crystal size	0.25 x 0.23 x 0.20 mm ³		
Theta range for data collection	1.10 to 24.99°		
Index ranges	-31 ≤ h ≤ 31, -25 ≤ k ≤ 31, -30 ≤ l ≤ 31		
Reflections collected	52100		
Independent reflections	1565 [R(int) = 0.0608]		
Completeness to theta = 24.99	100.0 %		
Absorption correction	Empirical		
Max. and min. transmission	1.000 and 0.457		
Refinement method	Full-matrix least-squares on F ²		
Data / restraints / parameters	1565 / 0 / 93		
Goodness-of-fit on F ²	1.094		
Final R indices [I > 2σ(I)]	R1 = 0.0969, wR2 = 0.2685		
R indices (all data)	R1 = 0.1106, wR2 = 0.2838		
Largest diff. peak and hole	1.323 and -1.496 eÅ ⁻³		

Table A10 Crystal data and structure refinement for MAMS-1.

Identification code	MAMS-1
Empirical formula	C ₃₆ H ₄₄ Ni ₄ O ₂₁
Formula weight	1047.55
Temperature	213(2) K
Wavelength	0.71073 Å
Crystal system	Monoclinic
Space group	<i>P</i> 2(1)/ <i>c</i>
Unit cell dimensions	a = 10.9606(16) Å = 90° b = 11.3002(17) Å = 96.769(3)° c = 38.373(6) Å = 90°
Volume	4719.6(12) Å ³
Z	4
Density (calculated)	1.474 Mg/m ³
Absorption coefficient	1.645 mm ⁻¹
F(000)	2160
Crystal size	0.23 x 0.08 x 0.08 mm ³
Theta range for data collection	1.07 to 18.91°
Index ranges	-9<= <i>h</i> <=9, -10<= <i>k</i> <=7, -34<= <i>l</i> <=34
Reflections collected	10507
Independent reflections	3742 [R(int) = 0.0691]
Completeness to theta = 18.91	99.8 %
Absorption correction	None
Refinement method	Full-matrix least-squares on F ²
Data / restraints / parameters	3742 / 2 / 546
Goodness-of-fit on F ²	1.024
Final R indices [I>2sigma(I)]	R1 = 0.0506, wR2 = 0.1366
R indices (all data)	R1 = 0.0700, wR2 = 0.1489
Largest diff. peak and hole	0.779 and -0.745 eÅ ⁻³

Table A11 Crystal data and structure refinement for MAMS-2.

Identification code	MAMS-2	
Empirical formula	$C_{18}H_{18}O_5Zn$	
Formula weight	379.69	
Temperature	293(2) K	
Wavelength	0.71073 Å	
Crystal system	Trigonal	
Space group	$P-3c1$	
Unit cell dimensions	$a = 18.6069(6)$ Å	= 90°
	$b = 18.6069(6)$ Å	= 90°
	$c = 22.6226(14)$ Å	= 120°
Volume	$6783.0(5)$ Å ³	
Z	12	
Density (calculated)	1.115 Mg/m ³	
Absorption coefficient	1.104 mm ⁻¹	
F(000)	2352	
Crystal size	0.20 x 0.18 x 0.15 mm ³	
Theta range for data collection	1.26 to 20.83°.	
Index ranges	$-15 \leq h \leq 18, -18 \leq k \leq 16, -22 \leq l \leq 22$	
Reflections collected	23787	
Independent reflections	2388 [R(int) = 0.1612]	
Completeness to theta = 20.83	100.0 %	
Absorption correction	None	
Refinement method	Full-matrix least-squares on F ²	
Data / restraints / parameters	2388 / 3 / 218	
Goodness-of-fit on F ²	1.060	
Final R indices [$I > 2\sigma(I)$]	R1 = 0.0746, wR2 = 0.2043	
R indices (all data)	R1 = 0.0900, wR2 = 0.2136	
Extinction coefficient	0.00035(16)	
Largest diff. peak and hole	0.473 and -0.722 eÅ ⁻³	

Table A12 Crystal data and structure refinement for MAMS-3.

Identification code	MAMS-3
Empirical formula	C ₁₈ H ₁₈ CoO ₅
Formula weight	373.25
Temperature	213(2) K
Wavelength	0.71073 Å
Crystal system	Trigonal
Space group	<i>P</i> -3 <i>c</i> 1
Unit cell dimensions	a = 18.9328(12) Å = 90° b = 18.9328(12) Å = 90° c = 22.307(3) Å = 120°
Volume	6924.7(11) Å ³
Z	12
Density (calculated)	1.074 Mg/m ³
Absorption coefficient	0.761 mm ⁻¹
F(000)	2316
Crystal size	0.18 x 0.15 x 0.10 mm ³
Theta range for data collection	1.24 to 20.80°
Index ranges	-18 ≤ h ≤ 17, -18 ≤ k ≤ 18, -21 ≤ l ≤ 22
Reflections collected	24266
Independent reflections	2427 [R(int) = 0.1489]
Completeness to theta = 20.80	99.9 %
Absorption correction	None
Refinement method	Full-matrix least-squares on F ²
Data / restraints / parameters	2427 / 0 / 217
Goodness-of-fit on F ²	1.064
Final R indices [I > 2σ(I)]	R1 = 0.0665, wR2 = 0.2030
R indices (all data)	R1 = 0.0832, wR2 = 0.2098
Largest diff. peak and hole	0.722 and -0.504 eÅ ⁻³

Table A13 Crystal data and structure refinement for MAMS-4.

Identification code	MAMS-4
Empirical formula	C ₁₈ H ₁₈ CuO _{5.33}
Formula weight	383.20
Temperature	293(2) K
Wavelength	0.71073 Å
Crystal system	Trigonal
Space group	<i>P</i> -3 <i>c</i> 1
Unit cell dimensions	a = 18.4472(4) Å = 90° b = 18.4472(4) Å = 90° c = 22.5760(12) Å = 120°
Volume	6653.3(4) Å ³
Z	12
Density (calculated)	1.148 Mg/m ³
Absorption coefficient	1.005 mm ⁻¹
F(000)	2372
Crystal size	0.21 x 0.18 x 0.14 mm ³
Theta range for data collection	1.27 to 20.87°
Index ranges	-18 ≤ h ≤ 18, -18 ≤ k ≤ 17, -22 ≤ l ≤ 11
Reflections collected	22294
Independent reflections	2353 [R(int) = 0.1469]
Completeness to theta = 20.87	100.0 %
Absorption correction	None
Refinement method	Full-matrix least-squares on F ²
Data / restraints / parameters	2353 / 0 / 220
Goodness-of-fit on F ²	1.146
Final R indices [I > 2σ(I)]	R1 = 0.0743, wR2 = 0.2236
R indices (all data)	R1 = 0.0945, wR2 = 0.2352
Largest diff. peak and hole	0.699 and -0.597 eÅ ⁻³